

Thalamocortical and corticothalamic interactions of
the auditory cortex in the Mongolian gerbil
(*Meriones unguiculatus*)

Dissertation

zur Erlangung des akademischen Grades

**doctor rerum naturalium
(Dr. rer. nat.)**

genehmigt durch die Fakultät für Naturwissenschaften
der Otto-von-Guericke-Universität Magdeburg

von **Dipl.-Biologin Katja Saldeitis**

geb. am 25.02.1985 in Hamburg

Gutachter: Prof. Dr. Frank Ohl
Prof. Dr. Manfred Kössl

eingereicht am: 28.04.2015

verteidigt am: 15.10.2015

Contents

Abbreviations	VI
1 Introduction	1
1.1 Background	1
1.2 Thalamocortical and corticothalamic processing streams	2
1.3 (Sub)divisions of the MGB of the Mongolian gerbil	4
1.4 The auditory cortex of the Mongolian gerbil	5
1.5 Motivation and objectives	6
1.6 Figures	10
2 Methods	14
2.1 Experimental animals	14
2.2 Anatomy of the auditory TC system	14
2.2.1 Surgical preparation for iontophoretic tracer injections	14
2.2.2 Electrophysiological recordings and acoustic stimulations.....	15
2.2.3 Iontophoretic injections of biocytin.....	16
2.2.4 Histology	16
2.2.5 Data analysis	17
2.3 Ultrastructural analysis of MGm terminals.....	18
2.3.1 Tracer injection	18
2.3.2 Cardiovascular perfusion	19
2.3.3 Immunohistochemical staining of labeled terminals	19
2.3.4 Electron microscopic embedding.....	20
2.3.5 Light microscopic examination	21
2.3.6 Electron microscopy	21
2.3.7 Data analysis	21
2.4 Change of cortical current source density patterns by selective apoptosis of auditory corticothalamic feedback projections	22
2.4.1 Establishment of the photolysis method	22
2.4.2 Preparation of the photolytic tracer (Chlorin e ₆ -conjugated retrobeads)	24
2.4.3 Tracer injection into MGB	24

2.4.4	Laser illumination of AI	24
2.4.5	Surgical preparation for CSD recording.....	25
2.4.6	Implantation of electrodes.....	26
2.4.7	Recording	26
2.4.8	Acoustic stimulation	27
2.4.9	Electrical stimulation	27
2.4.10	Pharmacological silencing	28
2.4.11	Perfusion of the animal and immunohistochemistry	28
2.4.12	Analysis of CSD data.....	29
2.4.13	Histological analysis	32
2.5	Figures	33
3	Results.....	35
3.1	Anatomy of the auditory thalamocortical system.....	35
3.1.1	MGv	35
3.1.2	MGd.....	39
3.1.3	MGm	41
3.1.4	Summary of the areal and laminar distributions of the auditory TC terminals in the Mongolian gerbil	42
3.1.5	Figures	43
3.1.6	Tables	53
3.2	Ultrastructural characterization of thalamocortical “giant“ and “normal” sized boutons from MGm	54
3.2.1	Qualitative analysis.....	54
3.2.2	Quantitative analysis.....	55
3.2.3	Summary of the ultrastructure of MGm boutons	57
3.2.4	Figures	58
3.2.5	Tables	62
3.3	Change of cortical current source density patterns by selective apoptosis of auditory corticothalamic feedback projections	64
3.3.1	Control experiments.....	64
3.3.2	Laminar origin of the auditory CT connections in Mongolian gerbils.....	66
3.3.3	Histological quantification of laser-induced neuronal loss in the animals used for CSD analysis	67
3.3.4	Acoustic stimulation	68
3.3.5	Intracortical microstimulation (ICMS).....	71
3.3.6	Summary of results.....	74
3.3.7	Figures	76

3.3.8	Tables	111
4	Discussion.....	114
4.1	Anatomy of the auditory thalamocortical system.....	114
4.1.1	MGv	114
4.1.2	MGd	122
4.1.3	MGm	126
4.2	Light and electron microscopic characterization of MGm terminals	128
4.3	Anatomy and influences of the corticothalamic system	133
4.3.1	Anatomy of CT connections	133
4.3.2	Effects of CT lesions on acoustically evoked activation (general activation patterns)	134
4.3.3	Effects of CT lesions on frequency tuning	136
4.3.4	Effect of layer VI CT lesions on the electrically evoked cortical activation	138
4.3.5	Effects of layer V CT lesions on the electrically evoked cortical activation	140
4.4	Interplay of TC and CT system	141
4.4.1	Model of CTC interactions upon acoustic stimulation	141
4.4.2	Model of CTC interaction upon ICMS.....	143
4.4.3	General principles governing auditory CT projections and functional implications for the CTC loops.....	145
4.5	Conclusion.....	146
4.6	Outlook and future directions.....	147
4.7	Figures	150
	References.....	VIII
	Appendix.....	XXVII
A	Buffer solutions.....	XXVII
B	Tracer solutions	XXVIII
C	Anesthetic solutions	XXIX
D	Perfusion solutions.....	XXIX
E	Protocol for the biocytin stain	XXX

F	Protocols for counterstains	XXXI
G	Protocol for Neuronal Nuclei (NeuN) stain	XXXI
H	Protocol for TEM pre-embedding	XXXIII
I	Brief theoretical background of CSD analysis.....	XXXV
J	Figures	XXXVI

	Summary of the doctoral thesis of Dipl.-Biol. Katja Saldeitis	XXXIX
--	--	--------------

	Zusammenfassung der Dissertationsschrift von Dipl.-Biol. Katja Saldeitis	XLI
--	---	------------

	Acknowledgements.....	XLIII
--	------------------------------	--------------

	Selbstständigkeitserklärung.....	XLIV
--	---	-------------

	List of publications	XLV
--	-----------------------------------	------------

Abbreviations

AAF	anterior auditory field
AC	auditory cortex
AI	primary auditory field
Ald	dorsal subfield of the primary auditory field
APT	anterior pretectal nucleus
AV	anteroventral auditory field
AVREC	averaged rectified CSD
BF	best frequency
BIC	brachium of the IC
c	caudal
CB+	calbindin-positive
CIC	central nucleus of the inferior colliculus
CPu	caudate-putamen
CSD	current source density (analysis)
CT	corticothalamic
d	dorsal
D	dorsal auditory field
DAB	diaminobenzidine
DCIC	dorsal cortex of the inferior colliculus
DD	deep dorsal nucleus of the MGd
DLG	dorsolateral geniculate body
DP	dorsoposterior auditory field
dv	dorsoventral
DZ	dorsal zone of the auditory cortex (cat)
ECIC	external cortex of the inferior colliculus
Gstim	granular ICMS
HF	hippocampal formation
hf	high frequency
ic	internal capsule
ICMS	intracortical microstimulation
IFC	isofrequency contour
IGstim	infragranular ICMS
I-VI	cortical layers

l	lateral
LesV	lesion of layer V CT neurons
LesV+VI	lesion of layer V and layer VI CT neurons
LesVI	lesion of layer VI CT neurons
lf	low frequency
LFP	local field potential
LGB	lateral geniculate body
LP	lateroposterior thalamic nucleus
LV	<i>pars lateralis</i> of the MGv
m	medial
MGB	medial geniculate body
MGd	dorsal division of the MGB
MGm	medial division of the MGB
MGv	ventral division of the MGB
ml	mediolateral
MZMG	marginal zone of the MGB
nwLes	no or weak lesion of CT neurons
OV	<i>pars ovoidea</i> of the MGB
PB	phosphate buffer
PBS	phosphate buffered saline
Po	posterior thalamic nucleus
PRh	perirhinal cortex
PV+	parvalbumin-positive
r	rostral
rc	rostrocaudal
RP	rostral pole of the MGv
Rt	reticular thalamic nucleus
SG	suprageniculate nucleus
SGstim	supagranular ICMS
TBS	TRIS-buffered saline
TEM	transmission electron microscopy
TC	thalamocortical
V	ventral auditory field
VLG	ventrolateral geniculate body

VM	ventromedial auditory field
VP	ventroposterior auditory field

1 Introduction

1.1 Background

Being positioned at the nexus between the ascending and descending auditory pathway, the higher order cortical systems, and multiple other sensory and non-sensory brainstructures, the auditory cortex (AC) represents the centralmost processing stage of auditory information along the auditory pathway. Thus, the AC holds a key role in bottom-up (ascending, feedforward, stimulus-driven) and top-down (descending, feedback, task-dependent) processing of auditory as well as of non-auditory information (e.g., Scheich *et al.*, 2007; Budinger *et al.*, 2008; Scheich *et al.*, 2011), and not just analyzes physical sound properties (for review, Budinger and Scheich, 2009).

The medial geniculate body (MGB) of the thalamus is the major source of subcortical input to the AC (for review see, e.g., Rouiller, 1997; Malmierca and Merchán, 2004; Budinger and Scheich, 2009; Winer, 2011). Thus, the neuronal spectro-temporal response properties of auditory cortical neurons depend highly on their frequency-specific (tonotopic) and frequency-unspecific (non-tonotopic) thalamocortical (TC) connectivities (for recent reviews see, e.g., Banks and Smith, 2011; Eggermont and Wang, 2011; Schreiner *et al.*, 2011; Wehr and Metherate, 2011), which originate and terminate in different divisions of the auditory thalamus and layers of the AC, respectively.

Thalamic neurons, however, are not only innervated by ascending (brainstem) inputs, but also receive extensive input from cortical neurons [corticothalamic feedback (CT) neurons] (e.g., Andersen *et al.*, 1980; Kelly and Wong, 1981; Winer *et al.*, 2001), which reflects their certain importance. By continuously communicating with the thalamus, the cortex is thus able to dynamically influence thalamic processing and ultimately adjust its own input via recurrent corticoefferent feedback. This concept is termed “egocentric selection” (Suga *et al.*, 1997; Zhang *et al.*, 1997). In this regard, several possible functional roles have been attributed to the CT projections, among them to affect receptive field properties of thalamic neurons (e.g., sharpen/adjust their frequency tuning: Zhang *et al.*, 1997; Zhang and Suga, 2000; He *et al.*, 2002), to increase the filtering properties of thalamic neurons (which might serve to improve the

saliency of specific sensory stimuli) (Villa *et al.*, 1991), to influence the TC gating (Destexhe, 2000; Kimura *et al.*, 2005), and to control the gain of the transmission of sensory signals from the thalamus to the cortex (e.g., Deschênes and Hu, 1990; He, 1997; Zhang and Suga, 1997; for review: Suga and Ma, 2003). An enhancement of transmission, for example, supplied by feedback could be accomplished by increasing the responsiveness of thalamic neurons to sensory stimuli, improving the reliability of thalamic responses, and/or altering the neuronal firing modes, and/or activity states (Steriade and Llinás, 1988; He *et al.*, 2002). The lastmentioned mechanisms may also play a role in cortically controlled synchronization of neuronal network oscillations associated with slow-wave sleep and epilepsies (e.g., Contreras and Steriade, 1996; Destexhe *et al.*, 1999; He, 2003). Furthermore, various studies provide evidence that the CT system is an essential substrate for sound-specific plasticity and adaptation in the auditory thalamus (e.g., Zhang and Yan, 2008; Antunes and Malmierca, 2011; Bäuerle *et al.*, 2011; for review: Xiong *et al.*, 2009; Suga and Ma, 2003; Suga, 2012; Malmierca *et al.*, 2015).

Despite the numerous influences the CT projections have demonstrated to exert over the auditory thalamus, many questions about how the cortically modulated thalamic activities in their turn influence the AC, i.e., how the complete transthalamic feedbackloop actually contributes to cortical activation patterns *in vivo*, are still unanswered.

In this work, we therefore had the following objectives: (1) to investigate the anatomy of the TC system in detail by means of anterograde tract tracing, (2) to characterize the ultrastructure of a specific type of TC terminals, which were discovered during (1), and (3) to examine the cortico-thalamo-cortical (CTC) interactions using current source density (CSD) analysis following a photolytic apoptosis of CT neurons.

1.2 Thalamocortical and corticothalamic processing streams

In general, it is largely agreed upon the literature that there are at least three TC processing streams (for review see, e.g., cat: Rouiller, 1997; Winer *et al.*, 2005; monkey: Hackett, 2011). Within the topographically, i.e. tonotopically organized lemniscal (core) part of the TC pathway, mainly frequency-specific information is relayed via parallel point-to-point connections between neurons of the ventral

division of the MGB (MGv) and neurons of the granular layer IV and supragranular sublayer IIIb of the tonotopically organized auditory fields of the ipsilateral side. As a consequence, the interconnected thalamic and cortical neurons have similar best frequencies (BFs) (Andersen *et al.*, 1980; Calford and Aitkin, 1983; Brandner and Redies, 1990; Hu, 2003; Hackett *et al.*, 2011a; Budinger *et al.*, 2013; Saldeitis *et al.*, 2014). In contrast, within the non-lemniscal part of the TC system, which in many species mainly originates in the dorsal division of the MGB (MGd) and terminates predominantly in granular but also in other layers of the non-primary AC, such a tonotopic organization has not been demonstrated and thalamic projections rather diverge across the tonotopic gradient if one is present at all of the cortical fields (for review see, e.g., Rouiller, 1997). Likewise, the multisensory part of the TC system, mainly originating in the medial division of the MGB (MGm), appears not to be topographically organized and its projections terminate in a widely distributed manner in the non-granular layers of the AC.

On the basis of their laminar source, intrathalamic terminal distribution, morphology of terminals, modes of synaptic transmission (Li *et al.*, 2003), and subcellular targets (distant vs. proximal dendrites), a dual pattern of CT projections was found, which is present across species and modalities (e.g., Rouiller and Welker, 1991; Ojima, 1994; Bajo *et al.*, 1995; Bourassa *et al.*, 1995; Hazama *et al.*, 2004; Rouiller and Durif, 2004; Takayanagi and Ojima, 2006; for review: Rouiller and Welker, 2000; Lee and Sherman, 2010). The first type of projection fibers, which are the more numerous (Ojima and Rouiller, 2011), arise from layer VI pyramidal neurons and bear exclusively small terminations (boutons, presynapses) in lemniscal thalamic nuclei (e.g., MGv). The second type, which originates from layer V pyramidal neurons, gives rise to large and small terminals in non-lemniscal thalamic nuclei (e.g., MGd). It is proposed that small terminals correspond to a system serving the feedback control of the cortex on the thalamic nucleus or division from which it receives its main afferents (allowing the cortex to modulate the inputs it receives from the thalamus, thus also termed “modulator”). Giant CT terminals, in contrast, are assumed to be involved in a feedforward projection system through which activity from one cortical area (e.g., AI) is securely delivered to other, remote cortical areas (e.g., secondary auditory fields) via the thalamus (also termed

“driver”) (Sherman and Guillery, 1998; Reichova and Sherman, 2004; Lee and Sherman, 2010; Theyel *et al.*, 2010).

In addition to providing excitatory monosynaptic input to ipsilateral thalamic principal neurons, the axons of CT neurons also provide polysynaptic inhibition, which is achieved by innervating local inhibitory neurons and through collaterals to the γ -aminobutyric acid (GABA)ergic neurons of the reticular nucleus of the thalamus (Rt). Layer VI, but probably not layer V CT cells branch to the Rt [Rouiller and de Ribaupierre, 1990; Rouiller and Welker, 1991; Bourassa and Deschênes, 1995 (visual)], while layer V CT neurons may supply axon collaterals to IC (Ojima 1994).

1.3 (Sub)divisions of the MGB of the Mongolian gerbil

We performed our experiments on the Mongolian gerbil (*Meriones unguiculatus*, Milne-Edwards 1867; see Thomas, 1908), that has become a highly valuable animal model for auditory research (for review see, e.g., Budinger and Klump, 2008; Budinger and Scheich, 2009). Gerbils have a good hearing capability, which ranges from low to ultrasound frequencies with a marked sensitivity at low frequencies (lf), similar to that of humans (Ryan, 1976; Gaese *et al.*, 2009; Klinge and Klump, 2009).

The main auditory thalamic nucleus (i.e., the MGB) of the gerbil consists of three major divisions, namely a ventral (MGv), dorsal (MGd), and medial (MGm) division (Budinger *et al.*, 2000b, Cant and Benson, 2007). At least the MGv and the MGd can be parcellated into further subdivisions on the basis of cyto- and fibroarchitectonic criteria (Budinger *et al.*, 2013; Mylius *et al.*, 2013; Saldeitis *et al.*, 2014).

The MGv represents the largest division and harbors small- to large-, but generally medium-sized neurons. Three subdivisions are apparent, namely a *pars lateralis* (LV) (Fig. 1.1 D), a *pars ovoidea* (OV) (Fig. 1.1 C-D), and a rostral pole (RP) (Fig. 1.1 B-D). In Nissl preparations, already the arrangement of the cell bodies in LV and OV reveals some kind of lamination; within the LV, the laminae are oriented from mediorostral to laterocaudal (indicated in Fig. 1.1 C), whereas in the OV, the laminae have a circular orientation (indicated in Fig. 1.1 D). These laminae most likely correspond to the fibrodendritic laminae of the principal bushy tufted neurons, which in turn might underlie the tonotopic

organization of the MGv (e.g., gerbil: Mylius *et al.*, 2013; rat: Winer *et al.*, 1999a). Based on results of recent electrophysiological (Bäuerle *et al.*, 2011) and anatomical tracing studies (Budinger *et al.*, 2013) on the gerbil's MGB it was suggested that the low-to-high frequency gradient within the MGv runs perpendicular to these cellular laminae, namely from rostralateral to caudomedial in LV and from central to peripheral in OV. The rostral part of the MGv comprises a cellular subdivision (RP), which has also been described in the cat (Winer *et al.*, 2001) and recently in the gerbil (Budinger *et al.*, 2013; Mylius *et al.*, 2013). RP displays no obvious lamination but comprises the same cell types as the other MGv subdivisions. Therefore and due to the rather rostroventral location of RP it was considered as a subdivision of MGv so far (Budinger *et al.*, 2000b; Cant and Benson, 2007; Budinger *et al.*, 2013; Mylius *et al.*, 2013).

The MGd (Fig. 1.1 A-B) covers the MGv dorsally. One subdivision, however, namely the deep dorsal nucleus (DD) extends further ventrally and abuts with the LV and RP (Fig. 1.1 C). In the Nissl-stain, DD is the only subdivision of the MGd, which could be consistently identified based on its higher cell density compared to the rest of the MGd. The latter we termed here MGd *proper*.

The MGm (Fig. 1.1 C-D) is an elongated structure in the medioventral MGB. It is the smallest of the three divisions with no obvious subdivisions. The MGm contains diverse neuronal cell types of different size and form, including some very large (probably the "magnocellular" neurons; Winer *et al.*, 1999a; Mylius *et al.*, 2013). There is no evidence for a tonotopic organization of the MGm or of the MGd (Ryan *et al.*, 1982).

1.4 The auditory cortex of the Mongolian gerbil

Within the gerbil's AC, eight fields can be distinguished on the basis of their architecture, anatomical connections, and frequency representation (Thomas *et al.*, 1993; Scheich *et al.*, 1993; Budinger *et al.*, 2000a, b; Fig. 1.2 A-B). At least five of them are tonotopically organized: The two koniocortical core fields, namely the primary auditory field (AI) and the anterior auditory field (AAF), have mirror-imaged tonotopic organizations around a common high frequency (hf) border. In both fields, the isofrequency contours (IFCs), formed by the neurons having similar BFs, run parallel in a roughly dorsoventral direction. Caudal to AI,

there are two smaller tonotopically organized fields, namely the dorsoposterior (DP) and the ventroposterior field (VP), that both share a lateral border with AI and with each other. The dorsal AC comprises the dorsal field (D) and a dorsal subfield of AI (Ald), both mainly comprising neurons that are usually broadly tuned to frequencies. Ventrally, the AI and AAF are bordered by the anteroventral (AV), ventral (V), and ventromedial field (VM). Field V shares a lateral border with AAF. Fields AV and VM are probably not tonotopically organized and belong to a transition area of the AC with the perirhinal cortex (Budinger *et al.*, 2000a).

1.5 Motivation and objectives

Detailed description of the TC system

A too general functional-anatomical scheme of the TC connections is not sufficient to understand the anatomical basis of recent physiological results about auditory cortical activity patterns obtained with high resolution recording and stimulation techniques such as two-photon calcium imaging (e.g., mouse: Bandyopadhyay *et al.*, 2010; Rothschild *et al.*, 2010; Grienberger *et al.*, 2012; Winkowski and Kanold, 2013; Issa *et al.*, 2014; for review: Kanold *et al.*, 2014), glutamate uncaging (e.g., mouse: Lee and Sherman, 2008) and multielectrode recording of laminar current source density (CSD; e.g., gerbil: Happel *et al.*, 2010; rat: Kaur *et al.*, 2005; Szymanski *et al.*, 2011; monkey: Lakatos *et al.*, 2005). For example, two-photon Ca^{2+} imaging challenged the traditional concept of topographic organization of AI, because the tonotopic arrangement was present in supragranular layers on a large scale but appeared to be fractured at the level of individual neurons (Bandyopadhyay *et al.*, 2010). Recent two-photon Ca^{2+} studies, however, showed that the local order of frequency representation is far more homogenous in layer IV (tonotopic) than in supragranular layers II/III (fractured) (Winkowski and Kanold, 2013; Kanold *et al.*, 2014). Thus, a detailed anatomical knowledge about the nuclear origin, layer-specificity and topography of TC projections will help to further disentangle the debate surrounding the dichotomous spatial organization of this sound property.

As another example, in the gerbil it was shown that the spectral integration in primary AC (AI) highly depends on the temporal convergence of TC and

intracortical afferents. Specifically, the spectral integration is most precise in close spectral neighborhood of the stimulated thalamic and cortical BF, i.e. in regions with the maximal overlap of both inputs (Happel *et al.*, 2010). However, even acoustic stimuli several octaves from the BF produce significant sinks and sources in AI (Kaur *et al.*, 2004; Kaur *et al.*, 2005), and it still remains obscure how the TC and intracortical connections contribute to this CSD patterns. Thus, again, a comprehensive anatomical knowledge about the nuclear origin and cortical field- and layer-specificities of the auditory TC inputs to the AC, including information about their possible tonotopy or divergence related to the cortical tonotopic maps, is required at all and for each experimental species (Hackett *et al.*, 2011a).

Therefore, we addressed several main questions respecting the anatomy of the TC system of the gerbil: How are the TC axons and their boutons distributed with regard to the auditory cortical fields, cortical layers and their origin in one of the subdivisions of the MGB? Do strict point-to-point connections exist between the tonotopic maps of the thalamus and cortex or do the projections terminate in a divergent manner across the cortical frequency-gradient?

We approached these questions by means of iontophoretic injections of the sensitive anterograde tracer biocytin into the MGB in order to juxtacellularly label small populations of electrophysiologically characterized neurons (BF, latency, on-off response characteristics) and their distinct cortical projections (fields, layers).

The results complement those obtained by pressure injections (to study the general cortical projection patterns of the thalamic subdivisions), and by part of the iontophoretic injections, which were presented in my Diploma thesis. The results from both approaches were published in Saldeitis *et al.*, 2014.

Ultrastructural investigation of hitherto unknown “giant” boutons from MGm

In course of our tracing studies on the TC connections we discovered a hitherto unknown population of very large (“giant”) boutons arising from the MGm (see also Saldeitis *et al.*, 2014). The auditory system comprises some other very large axonal terminals, among them the endbulb and the calyx of Held in the brainstem (for review: Ryugo and Spirou, 2009) and those formed by CT

pyramidal neurons originating in layer V (referred to as “drivers”, e.g., Lee and Sherman, 2010, see also 1.2). Specific features, such as rapid, high-fidelity transmission, of the so far known “giant” terminals have been related to their size (“form fits function”). Therefore, and due to their specific projection pattern in the AC, we speculate that the giant synapses from MGm play an important role in auditory processing. As a first step towards an understanding of these giant MGm terminals we will give here a first description of their ultrastructure combining tracing and transmission electron microscopy (TEM), which will provide insights about their putative functions.

Influence of CT projections on recurrent cortical activity patterns

The AC integrates sensory (e.g., spectral) information by temporally precise interactions of TC inputs and intracortical networks, as for example revealed by dissociating their respective contributions to cortical activity patterns by means of pharmacological intracortical silencing (Kaur *et al.*, 2004; Happel *et al.*, 2010), or by investigating the spread of excitation in AC following MGv stimulation in the TC slice (Kaur *et al.*, 2005).

It was also shown that layer-specific infragranular and granular intracortical microstimulation (ICMS) evoke a cross-laminar CSD pattern of activation comparable to acoustic stimulation, i.e., a granular sink followed by subsequent extragranular sinks (Jeschke, 2006; Happel *et al.*, 2014). During pharmacological cortical silencing, only the initial sinks in the main thalamorecipient layers, especially in layer IV, appear upon both acoustic stimulation and ICMS, indicating that the later components are (mainly) generated intracortically.

Based on the similarities between the acoustically and electrically evoked CSD profiles it has been hypothesized that ICMS produces them via a cortico-thalamo-cortical (CTC) loop (Jeschke, 2006; Happel *et al.*, 2014). More precisely, ICMS may activate CT pyramidal neurons in layers V/VI, which are potentially contributors to a fast-acting recurrent CT loop activation, by which (infragranular) output layers and (granular) input layers of the AC are connected via the thalamic relay (MGv). To test our hypothesis and to identify further possible contributions of this feedback loop to cortical activity patterns we used a combination of anatomical, physiological, and pharmacological techniques.

First, we selectively eliminated CT neurons projecting from layer V/VI of the primary AC (field AI) to the MGB using a chromophore-targeted laser photolysis method (Madison and Macklis, 1993; Bajo *et al.*, 2010) (Fig. 1.3). In course of this experiment, retrobeads injected into different MGB divisions retrogradely labeled distinctive CT projection neurons in the AC. This information was also used to further investigate their areal and laminar location. Following the selective apoptosis, the activity patterns in the ipsilateral lesioned AC evoked by acoustic stimulation and by electrical layer-specific ICMS were investigated using CSD analysis (for a brief theoretical background of the CSD analysis see appendix). This was done before and after cortical silencing with muscimol (GABA_A agonist).

1.6 Figures

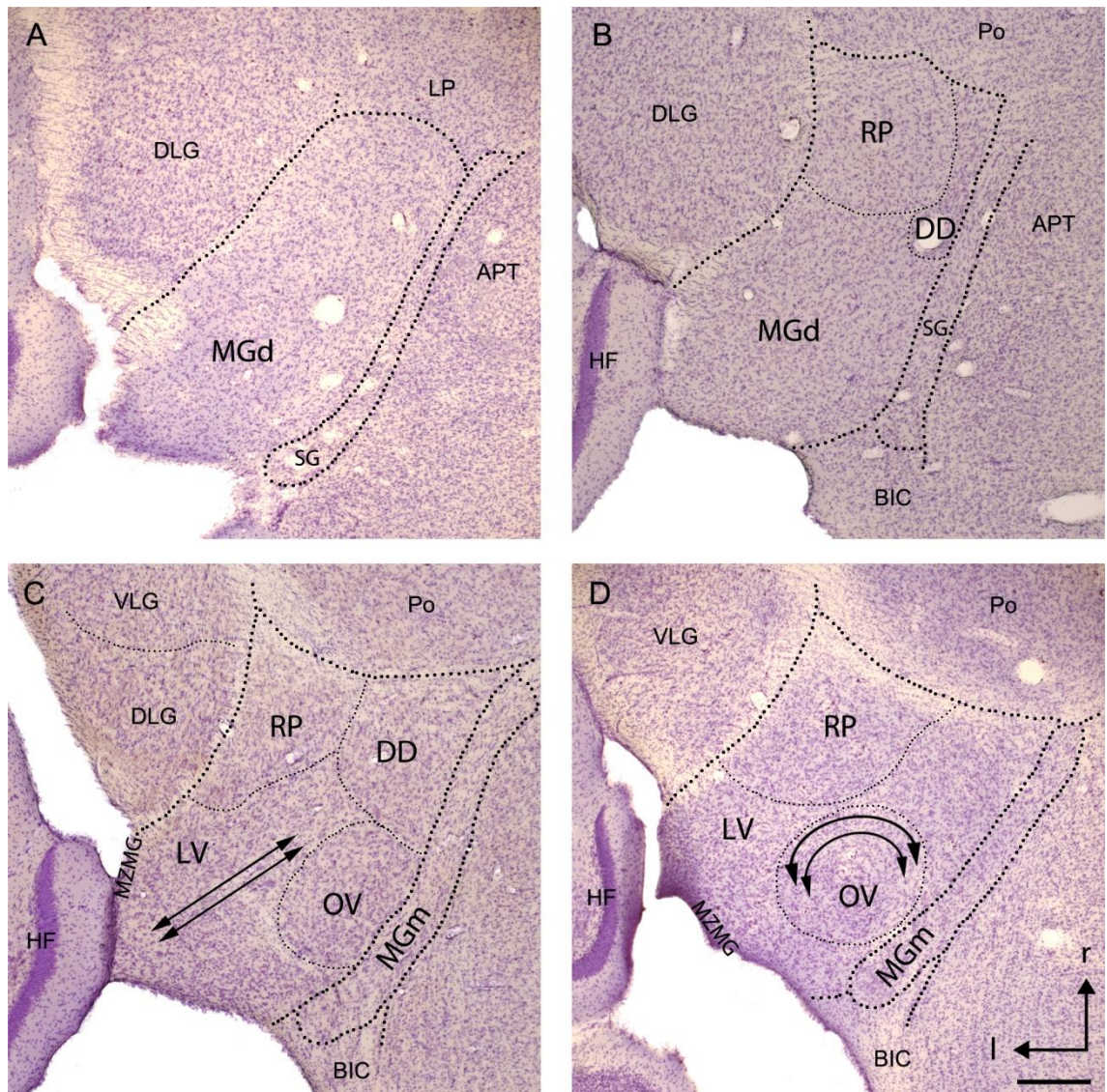


Figure 1.1: Cytoarchitecture of the medial geniculate body (MGB) as seen in Nissl-stains at different horizontal levels from dorsal (**A**) to ventral (**D**). The MGB consists of a dorsal (MGd), ventral (MGv), and medial (MGm) division. The MGd harbors at least one subdivision, namely the deep dorsal nucleus (DD); the remaining MGd we termed MGd *proper*. The MGv has three subdivisions, namely the *pars lateralis* (LV), *pars ovoidea* (OV), and rostral pole (RP). The orientation of the cellular laminae of LV and OV are indicated by the solid black lines and arrows. For all other abbreviations see list. Scale bar: 300 μ m.

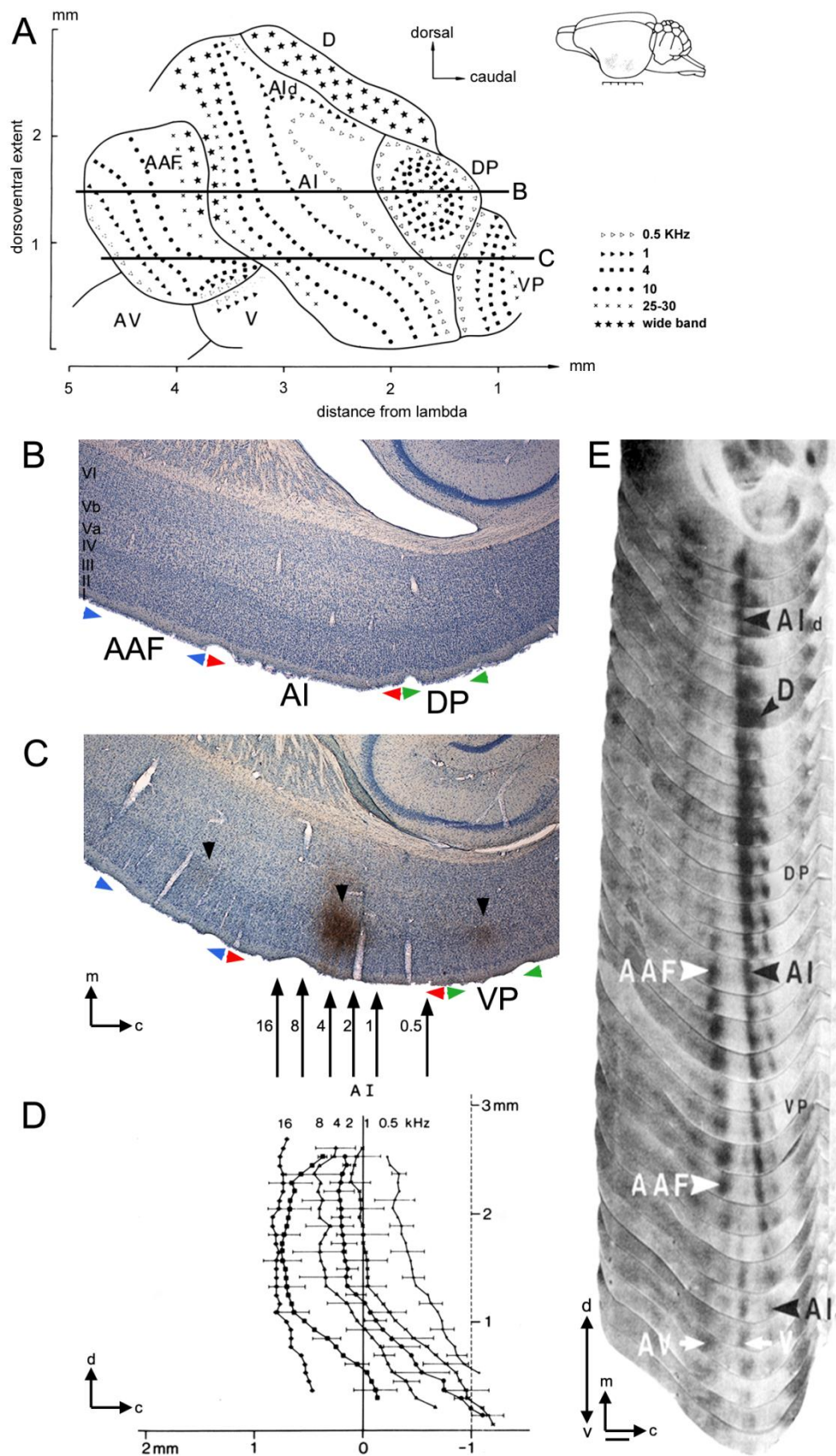


Figure 1.2 (preceding page): **(A)** Frequency organization (tonotopic map) of the AC of the Mongolian gerbil derived from numerous fine-grained electrophysiological recordings during acoustic stimulation with pure tones (modified from Thomas *et al.*, 1993). Note the expanded representation of low frequencies (≤ 1 kHz) in AI. Section levels of B and C are indicated. **(B)** Horizontal section through the gerbil's AC at a rather dorsal level (see A) showing its cytoarchitecture as seen using the Nissl-stain. Note the koniocortical architecture (particular high cell density in layer IV) of AI and AAF. Moreover, cells of layer V are not so densely packed in AI as in AAF. In DP (and VP, see C), cells are more loosely distributed across the cortical layers. Field borders are indicated by blue, red and green arrowheads, respectively. **(C)** Horizontal section at a rather ventral level (see A) stained for cell bodies (Nissl) and labeled TC axons following an injection of biocytin into LV at middle frequencies. Note the strong anterograde labeling in AI and the weaker labeling in VP and AAF (black arrowheads). Locations of different BF representations within AI are indicated at the bottom as derived from metabolic 2-deoxyglucose (2-DG) studies (see D and E). **(D)** Rostrocaudal location (with respect to the rostral tip of the hippocampus) and dorsoventral extent of isofrequency contours in the gerbil's AC as derived from 2-DG-labeling following tonal stimulation of the animals (modified from Scheich *et al.*, 1993). The results of the 2-DG experiments and fine-grained electrophysiological recordings (see A) did show that the spatial resolution for frequencies along the horizontal dimension (i.e., across the tonotopic gradient) in the gerbil's AI is 400 μm per octave for frequencies below 1 kHz and 200 μm per octave for frequencies above 1 kHz. **(E)** Montage of the left hemisphere from 2-DG autoradiographs of horizontal brain sections showing high metabolic activity in the gerbil's auditory cortical fields following the acoustic stimulation with frequency-modulated tones of 1-2 kHz (modified from Scheich *et al.*, 1993). The knowledge about the location and bandwidth of such 2-DG-labeled isofrequency contours enabled the assignment of cortical biocytin-labeling in this study. Scale bar: 1 mm. Figure reproduced from Saldeitis *et al.*, 2014.

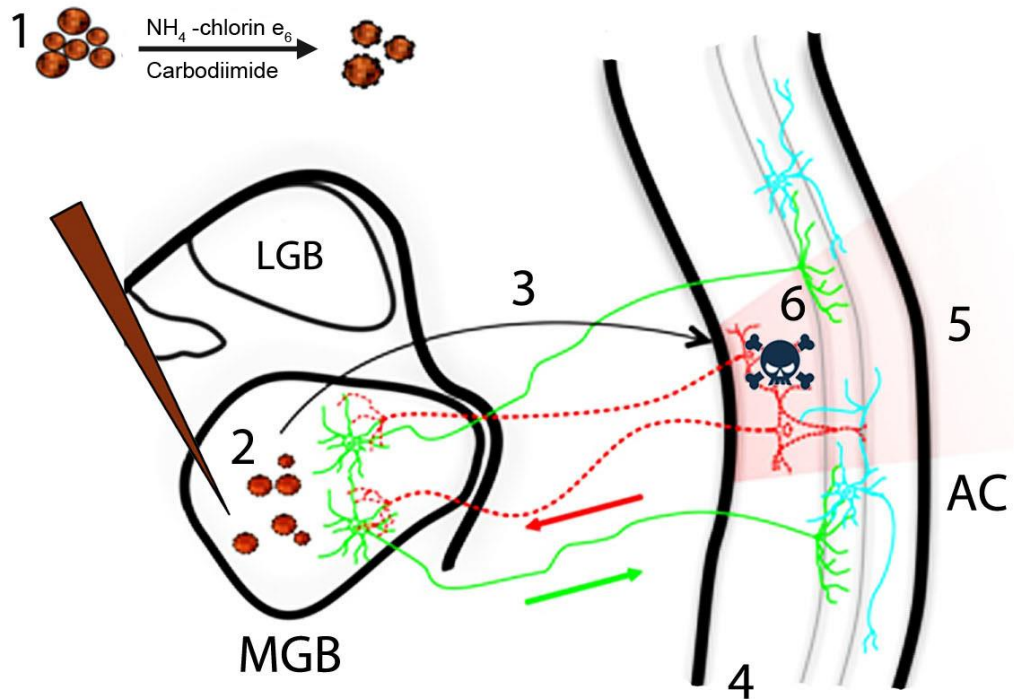


Figure 1.3: The photolytic apoptosis technique. **(1)** Preparation of the tracer solution: conjugation of red retrobeads with chlorin e₆. **(2)** Unilateral injection into the medial geniculate body (MGB). **(3)** Retrograde transport to the auditory cortex (AC). **(4)** Fluorescent labeling of corticothalamic (CT) projection neurons. **(5)** Laser illumination of the ipsilateral AC (670 nm, 10 days after injection) induces a photolytic apoptosis of CT projection neurons by the release of reactive oxygen species **(6)**. The template for this figure was kindly provided by Dr. Max Happel.

2 Methods

2.1 Experimental animals

The anatomy of the thalamocortical (TC) connections was examined on 11 young adult male Mongolian gerbils (*Meriones unguiculatus*) (Charles River, USA). For electron microscopy, 2 animals were used. 3 animals were used for establishment of the photolytic apoptosis technique. CSD experiments were performed on 15 gerbils. The animals were 4-6 months old and weighed 65-85 g. All experiments were approved by the ethics committee of Sachsen-Anhalt, Germany (No.43.2-42502/2-2-1103 IFN MD and 42502-2-825), in accordance with the Guide for the Care and Use of Laboratory Animals (NIH, 2011).

2.2 Anatomy of the auditory TC system

2.2.1 Surgical preparation for iontophoretic tracer injections

In order to investigate the TC projection patterns of small neuronal populations we performed iontophoretic tracer experiments. General initial anesthesia was induced with a combination of ketamine (10 mg/100 g body weight, i.p., Ratiopharm GmbH, Germany) and xylazine (0.5 mg/100 g body weight, i.p., Bayer, Germany) prepared in isotonic sodium chloride solution. The level of anesthesia was controlled by monitoring the hindlimb withdrawal reflex and respiratory rate and maintenance doses were given as needed. Body temperature was maintained at 37°C using a heating blanket. Initially, animals were mounted in a stereotaxic apparatus (Stoelting, USA). To make the MGB accessible for later electrophysiological recordings and iontophoresis, the cranial skin was disinfected, locally anesthetized with Gingicain (Tetracain, Sanofi Aventis, Germany) and removed. Thereafter, an opening (diameter approx. 2 mm) was drilled bilaterally into the skull perpendicular over the location of the MGB. The center of the hole was placed 3.9-4.0 mm caudal and 2.9-3.0 mm lateral from Bregma. Then, a gold-plated pin (diameter 1 mm, Amphenol, Germany) was implanted into the frontal bone of the animal with good contact to the *dura mater* to serve later as a reference electrode. Finally, insect pins were stuck along the parietal bone and an aluminum bar was

mounted on the frontal skull with dental cement (Paladur, Keraeus Kulzer, Germany) for later head fixation during recordings and iontophoresis.

2.2.2 Electrophysiological recordings and acoustic stimulations

The animals were transferred to an acoustically and electrically shielded recording chamber. Throughout the experiments, anesthesia was maintained by subcutaneous infusion of ketamine and xylazine and body temperature was kept at 37°C by a controlled heating blanket.

Prior to the iontophoresis, action potential (spike) and local field potential recordings, obtained with a single tungsten electrode (1 M Ω , WPI, USA), were performed in order to roughly map the MGB and thus to find an appropriate position for later micropipette insertion. Recording positions (spaced about 200 μ m apart) were chosen based on stereotaxic coordinates (previously established by pressure injections, Saldeitis *et al.*, 2014) and were related to the cortical vasculature to allow the retrieval of the selected position for the glass pipette used for microiontophoresis. The electrode was lowered into MGB (3.7-4.5 mm deep from the cortical surface) by means of a motorized stepping microdrive (WPI). Multi- and single-unit activity was recorded using a multichannel recording and amplification system (Multichannel Acquisition Processor; Plexon, USA). Action potentials were band pass filtered between 400 Hz and 4 kHz and digitized at 40 kHz. Local field potentials were bandpass filtered between 3 and 170 Hz and digitized at 2 kHz.

Acoustical stimuli were digitally synthesized and controlled using Matlab software (MathWorks, USA). Stimuli were delivered free field via an attenuator (g.PAH, Guger Technologies, Austria), amplifier (STAX SRM-3, Hongkong), and an electrostatic loudspeaker (STAX Ltd., Hongkong); the latter positioned 5 cm in front of the animal's head. Speaker output was measured prior to an experiment using a 0.5 inch condenser microphone (Brüel & Kjær, Denmark). Animals were stimulated with pseudorandomized series of pure tone frequencies with a logarithmic (iso-octave) frequency spacing from 125 Hz to 16 kHz as well as with clicks, all with 15 repetitions of each stimulus and inter-stimulus intervals (ISI) of 0.8 to 1.2 s. Stimuli were presented at a constant intensity of 60 to 70 dB SPL for 200 ms and with a 5 ms sinusoidal rising and falling ramp.

2.2.3 Iontophoretic injections of biocytin

Microiontophoretic administration of the tracer was performed with an IONOPHOR 3 iontophoresis unit (Science Products, Germany) via three-barrel micropipettes (tip diameter broken to 4-10 μm , impedance 4-15 $\text{M}\Omega$, WPI, USA), which were pulled using an electrode puller (Narishige Scientific Instruments, Japan) and mounted (as the tungsten recording electrode) on a stereotaxic device (Märzhäuser, Germany). Micropipettes barrels were filled with 3% biocytin dissolved in a 1.5 M NaCl solution for tracing and recording and with 3 M KCl for pure recording, respectively. Positive ejecting currents ranged from 450 nA to 850 nA using a pulsed signal (5 s on, 2 s off; A 310 Accupulser, WPI) and were applied over a period of 20-30 min.

Under microscopic control, the micropipette was vertically inserted at the preselected position (Fig. 2.1). In order to physiologically characterize the neurons to be labeled, we performed acoustic stimulation and recordings as described above. Following the injection, the animals were given postoperative care and they were allowed to survive for 24 h.

2.2.4 Histology

Animals were reanesthetized (20 mg ketamine/100 g body weight, 1 mg xylazine/100 g body weight) and perfused transcardially with 20 ml of 0.1 M phosphate buffered saline (PBS, pH 7.4, for recipe see appendix), followed by 200 ml of 4% paraformaldehyde (PFA) and 0.1% glutaraldehyde (pH 7.4). The brains were removed, postfixated overnight in 4% PFA at 4°C, and cryoprotected for 48 h in 30% sucrose solution. Then, they were shock-frozen in isopentane, which was cooled to -50°C in a nitrogen bath, and afterwards cut on a freezing microtome (Leica CM 1950, Germany) into 50- μm -thick horizontal sections, which were collected in 0.1 M PBS.

Biocytin was visualized using the avidin-biotin-peroxidase reaction (ABC-kit, VECTOR Laboratories, USA). To prevent false-positive stainings, the sections were pretreated by several blocking steps: Reactive aldehyde groups were blocked with sodium borohydride (1% in PBS, Sigma-Aldrich, USA), endogenous peroxidase with methanol (1:1 with PBS) and hydrogen peroxide (0.03%), and nonspecific antibody binding sites with bovine serum albumin (5% in 0.1 M PBS plus 0.3% triton, ROTH, Germany). Thereafter, sections were

incubated in the ABC-antibody solution, including 0.3% triton (Sigma-Aldrich, USA), overnight and then biocytin was visualized using 3,3-diaminobenzidine (DAB, Sigma-Aldrich) as the chromogen.

Sections were then mounted on gelatine-coated slides and consecutive sections were either counterstained for cell nuclei with methyl green (Sigma-Aldrich; for protocol see appendix) or for cell bodies with cresyl violet (Nissl stain; every sixth section; Sigma-Aldrich; for protocol see appendix) and finally coverslipped with Merckoglas (Merck, Germany).

2.2.5 Data analysis

The sections were examined light microscopically (Zeiss Axioskop 2, Germany) and regions of interest were photographed (Leica DFC 500, Germany) and processed for illustrations using the Adobe Photoshop software (Adobe Systems, USA). The distribution of anterogradely labeled presynapses (boutons) was reconstructed using a microscope system with motorized stage (Leica DMRX and Märzhäuser, Germany) and the Neurolucida software (MicroBrightField, Europe). Graphically reconstructed consecutive sections were stacked so that the more dorsal section covered all but the cortex of the more ventral section (e.g., Fig. 1.2 G-H). The rostral tip of the hippocampus, a reliable internal anatomical landmark, was used for rostrocaudal alignment. Such montages enable the comparison of autoradiographs showing functional metabolic 2-deoxyglucose (2-DG) labeling after acoustic stimulation (e.g., Scheich *et al.*, 1993) with histological sections showing neuronal tracer labeling (e.g., Budinger *et al.*, 2000a) and thus facilitate the identification of biocytin-labeled auditory fields and estimation of the BF at a given cortical site (Fig. 1.2). In addition, cytoarchitectonic criteria such as koniocortical features were used for the identification of the auditory fields (Fig. 1.2 B; see also Budinger *et al.*, 2000a).

Tonotopy of the TC connections was additionally underpinned by the measurement of distances between the center mass of boutons in layer IV of the different labeled fields (using the "Quick measure" tool of the Neurolucida software; Fig. 3.4 B). This was done because we expected in cases of tonotopic TC connections a correlation of the distances between the bouton clusters in AI, AAF, and DP/VP, respectively, with the BF at the thalamic injection site. In other

words, due to their mirror-imaged tonotopic organization the distances between the center mass of boutons in AI and AAF should be longest in lf injection cases and shortest in hf cases (see Fig. 3.4). For the distances between AI and DP/VP, the opposite should be true. For this analysis, also results from pressure injections were included (Saldeitis *et al.*, 2014).

For the quantitative analysis of the layer and field specific distribution of synaptic boutons we used the NeuroLucida software including the Neuroexplorer program (MicroBrightField) and the Excel spreadsheet application (Microsoft, Germany) (e.g., Fig. 3.2 Ac-e). Herefore, we basically analyzed sections counterstained with cresyl violet, i.e., sections of 300 μm interval.

The identification and nomenclature of brain structures correspond to the stereotaxic atlases of the rat (Paxinos and Watson, 2007), mouse (Franklin and Paxinos, 2008), and gerbil (Loskota *et al.*, 1974; Thiessen and Yahr, 1977) as well as to related publications on gerbils (Scheich *et al.*, 1993; Thomas *et al.*, 1993; Budinger *et al.*, 2000b, 2013; Cant and Benson, 2007; Mylius *et al.*, 2013; Saldeitis *et al.*, 2014) and rats (e.g., Winer *et al.*, 1999a). The cortical layers were identified according to standard features such as type, size, and packing density of neurons (Winer, 1992; Zilles and Wree, 1995).

Action potentials were displayed as rasterplots (1 dot represents an action potential at a certain time point as response to the given frequency and intensity; e.g., Fig. 3.1) and the neuronal response characteristics were analyzed with respect to latencies and BFs using Matlab (Mathworks). The BF of a unit was determined from its response to isointensity tones and was defined as the frequency, which evoked the highest spike rate.

2.3 Ultrastructural analysis of MGm terminals

2.3.1 Tracer injection

In order to characterize the ultrastructure of different types of TC terminals arising from the medial division of the MGB (MGm) we anterogradely labeled them by stereotaxic or iontophoretic injections of biocytin. Iontophoretic injections were performed as described above.

For the stereotaxic pressure injections, animals were anesthetized as described above. The cranial skin was disinfected, locally anesthetized, and incised. A small hole was drilled bilaterally with a dental drill into the skull according to the

stereotaxic coordinates of the MGB established previously (see 2.2.2, i.e., 3.9-4.0 mm caudal and 2.85-2.9 mm lateral from Bregma) and 20 nl of 5% biocytin (Sigma-Aldrich, USA), dissolved in 0.05 M Tris-HCl buffer (Tris, pH 7.6), was injected over a period of two minutes. The injection was performed with the help of a fine glass micropipette (outer diameter 1.2 mm, inner diameter 0.68 mm, WPI, USA), which was pulled (Sutter Instruments, USA), broken (tip diameter: 20 μ m), and then mounted on an oil hydraulic nanoliter delivery system (WPI). The micropipette was advanced vertically into the brain. The depth of the tip, measured from the cortical surface, was 4.1-4.5 mm for injections into MGm. Following the injections, the cranial opening was closed with bone wax (Ethicon, Germany), the surgical sore was treated with an anti-inflammatory ointment (Volon A, Dermapharm GmbH, Germany), and the skin over the cranial opening was closed with a tissue adhesive (Histoacryl, Braun, Germany). Thereafter, the animals were allowed to recover and survive for 24 hours.

2.3.2 Cardiovascular perfusion

24 h following tracer injection, animals were reanesthetized (20 mg ketamine/100 g body weight, 1 mg xylazine/100 g body weight) and perfused transcardially with 20 ml physiological saline followed by 250 ml fixative solution consisting of 4% PFA, 0.26% picric acid, and 1% glutaraldehyde in phosphate buffer (PB, 0.1 M, pH 7.4; 10 ml/min; for recipe see appendix). The brains were removed from the skulls and postfixed in 4% PFA overnight at 4°C.

2.3.3 Immunohistochemical staining of labeled terminals

Staining and electron microscopic embedding was adapted from a protocol previously established by Riedel *et al.* (2013). Horizontal sections (60 μ m) were cut on a vibratome (VT 1000S; Leica, Germany) and collected in PB (0.1 M PB; pH 7.4) at 4°C. They were rinsed 3 x in PB and incubated in PB at 4°C overnight. On the next day, sections were again rinsed in PB (3 x 30 min), incubated in 1% sodium borohydride (NaBH₄) in double-distilled water for 30 min, quickly rinsed in PB (3 x), and afterwards washed in PB (3 x 30 min). Then, the sections were cryoprotected in PB (0.05 M, pH 7.4), containing 25% sucrose and 10% glycerol, for 20-30 min and subsequently freeze-thawed for 4-

5 times to gently break the cell membrane and thus allow later penetration of the antibody. Cryoprotection solution was washed out using PB (3 x 30 min).

To block nonspecific antibody binding sites, sections were pretreated with 5% bovine serum albumin (ROTH, Germany) in TBS for 40 min (after washing 2 x 20 min in TBS). Thereafter, sections were rinsed in TBS (3 x 30 min) and incubated in the ABC-solution (1:500) for two days at 4°C. Sections were rinsed in TBS (3 x 20 min) and Tris (0.05 M, pH 7.6; 2 x 10 min) and then incubated in 0.05% DAB in Tris for 20-30 min. Visualization was performed by adding 1% H₂O₂ to the DAB solution. The reaction was stopped after 10 min by applying Tris (3 x 30 min); then the sections were stored in PB at 4°C.

2.3.4 Electron microscopic embedding

On the next day, sections were rinsed in PB (2 x 20 min) and treated with 1% osmiumtetroxide (OsO₄) in PB for 1 h at room temperature in the dark, washed again in PB (2 x 10 min), and quickly rinsed in double-distilled water. Then, sections were dehydrated in 50% ethanol for 10 min, 1% uranyl acetate in 70% ethanol for 40 min, 90% ethanol for 10 min, 94% ethanol for 10 min, absolute alcohol for 2 x 10 min, and propylene oxide for 2 x 10 min (to remove residual ethanol used for dehydration).

OsO₄ serves a secondary fixative (preventing coagulation of proteins by alcohols during dehydration) and also creates contrast between membranes and the neighboring cytoplasm by binding to phospholipid head regions. Uranyl acetate adds electron density and thus image contrast to the internal structures. The uranyl ions bind to proteins and lipids with sialic acid carboxyl groups such as glycoproteins and ganglioside and to nucleic acid phosphate groups. Hence, it delivers good contrasting results of membranes, nucleic acids (DNA, RNA), and ribosomes.

Subsequently, sections were transferred to Durcupan (Electron microscopy sciences, EMS, USA) and left there overnight at room temperature. On the next day, i.e., after polymerization of Durcupan, sections were mounted onto glass slides and covered with glass cover slips pre-treated with liquid release agent (EMS).

2.3.5 Light microscopic examination

The sections were examined with a light microscope (Zeiss Axioskop 2, Germany) to verify the injection site (MGm) and to identify labeled normal and large sized terminals in AI. Regions of interest (ROIs) were selected and photographed (Leica DFC 500, Germany).

2.3.6 Electron microscopy

Cover slips were removed and selected areas of the AI were excised from the section, remounted on resin blocks (EMS), and fixed with ethyl 2-cyanoacrylate containing superglue (Quick Bond, Aron Alpha CE-471, Science Services, Germany).

Ultrathin sections (approx. 70 nm thick) were cut with an ultramicrotome (EM UC6; Leica, Germany) using a diamond knife (Ultra, Diatome, Switzerland) and collected on Formvar (Plano, GmbH, Germany; 1.5% in chloroform) film-coated nickel slid grids (G2500C; Plano GmbH, Germany). The ultrathin sections were examined with a transmission electron microscope (EM-900 TEM, Zeiss, Germany) using an acceleration voltage of 80 kV. Labeled boutons were photographed (with an integrated TRS USB camera) at different magnifications (12000 x, 20000 x, 30000 x; exposure: 1280 ms).

2.3.7 Data analysis

Image processing (brightness and contrast) and figure layout were done with Photoshop (Adobe, Germany). The cross-section areas and perimeters of terminals and mitochondria as well as the number and length of synaptic contacts were quantitatively analyzed using SPIImage Viewer (TRS & SysProg, Germany) for outlining the boutons and mitochondria and tracing synaptic densities, and Matlab (R2012a; MathWorks) for statistical analyses and graphical representations (using a custom-written program). Per labeled bouton, one image was used for analysis. For comparison, the same number of randomly selected non-labeled cortical boutons was also analyzed. In detail, we tested labeled vs. non-labeled boutons for differences in boutons area, bouton perimeter, mitochondrial fraction (i.e., summed mitochondrial area divided by bouton area), synaptic length, synaptic fraction (i.e., summed synaptic length divided by bouton perimeter), and number of synaptic contacts. Differences in

bouton size (area and perimeter) were tested using a t-test assuming unequal variances. To test for possible between group differences in mitochondrial and synaptic fraction we applied an analysis of covariance (ANCOVA) (IBM SPSS Statistics 20), because it accounts for the effect of the covariate (bouton size) on the dependent variable.

We further tested for each group (labeled and non-labeled independently) whether synaptic or mitochondrial fraction correlates with bouton size computing Pearson's linear correlation coefficient.

The distributions of bouton area, mitochondrial fraction, and synaptic fraction were also tested for unimodality using the Hartigan's dip test (Hartigan and Hartigan, 1985; Matlab code: HartigansDipSignifTest by F. Mechler, 2002) in order to define (or exclude the existence of) putative subpopulations based on the examined characteristics. If a distribution was not uniform, clusters were separated using a kmeans algorithm (Matlab R2012a). The optimal number of clusters was thereby obtained by determining the number that maximizes the mean silhouette value over all points.

2.4 Change of cortical current source density patterns by selective apoptosis of auditory corticothalamic feedback projections

2.4.1 Establishment of the photolysis method

The photolytic apoptosis of chromophore-targeted neuronal populations has been described elsewhere using mice, rats, and ferrets (Macklis, 1993; Madison and Macklis, 1993; Bajo *et al.*, 2010), but has never been conducted in gerbils before. Thus, the method had to be adjusted to our needs as described in the following:

As the photolytic chromophore, we selected Chlorin e_6 (-monoethylenediamineamide) disodium (Frontier Scientific, USA). The same (chemical) compound was used before by Madison and Macklis (1993), and also worked well here as determined from the tests described below.

Regarding the the agent needed for conjugation, we first tested two carbodiimides we had in storage. 1-Ethyl-3-(3-dimethylaminopropyl)carbodiimid (used by Madison and Macklis) resulted to be too old and was not longer

commercially available, and N,N'-Dicyclohexyl carbodiimide did not dissolve well. We finally favored newly ordered N-Cyclohexyl-N'-(2-morpholinoethyl)carbodiimide metho-p-toluenesulfonate (used by Bajo *et al.*, 2010).

Then, we had to determine appropriate time periods; the first between injection and laser illumination, and the second between illumination and further experiments that reveal the consequences of the elimination of specific neuronal populations. Periods should be long enough to ensure the tracer transport as well as laser-induced apoptosis being complete, but on the other hand, not be extremely long to exclude the decomposition of tracer solution, or the occurrence of massive regenerative processes. The reported time periods between injection and laser illumination amounted to at least 4 weeks (Madison and Macklis, 1993; Bajo *et al.*, 2010). Since retrobeads are reliably transported within one week (Kobbert *et al.*, 2000; Vercelli *et al.*, 2000) over long distances, we tested a time interval of approx. 10 days between injection and lasering, which worked well as it resulted in strong labeling of the AC, as tested in some animals not listed here.

Because degenerating neurons, visualized by using silver stain methods were seen over a wide range of survival times (4 h to 7 d; Madison and Macklis, 1993), we decided to wait at least 10 d to ensure that the apoptotic process had been largely completed by the time of the electrophysiological experiments.

Another critical parameter to adjust was the laser power. We found a power of approximately 50 mW and a exposure time of 12 min, which corresponds to a total energy dose of 1250 J/cm² (which ranges between the energy dosages reported earlier using mice, rats, and ferrets), to be appropriate for transcranial illumination of the cortex (see below) since the lesion efficacy was good (posthoc evaluation); higher power led to spontaneous seizures.

Respecting the surgery technique we dismissed our first strategy of thinning the cranial bone before illumination (which was first done in order to optimize penetration) because the skull tended to break after a while, and instead switched to transcranial illumination through the intact (i.e., unthinned) skull, since it protected the brain (undamaged dura), while the laser was still effective. Control experiments to approve the method are described in section 3.3.1.

2.4.2 Preparation of the photolytic tracer (Chlorin e₆-conjugated retrobeads)

An 1 mM solution of Chlorin e₆-(monoethylenediamineamide) (Phytochlorin, Frontier Scientific, USA, CAS# 19660-77-6, MW 596.68) was made up with 3 ml of 0.01 M PB (pH 7.4) and was activated with 5 mg N-Cyclohexyl-N'-(2-morpholinoethyl)carbodiimide metho-p-toluenesulfonate (Sigma-Aldrich, Switzerland, CAS# 2491-17-0) for 30 min at 4°C on a rocker table (70 rpm). 50 µl Red Retrobeads™ IX (Lumafuor, USA, excitation: 530 nm, emission: 590 nm) were diluted in 300 µl PB and added to the solution. Chlorin e₆ was then attached to the latex surface of the fluorescent microbeads by gentle agitation on a rocker table at 4°C. The reaction was stopped after 60 min with 335 µL 0.1 M glycine buffer (pH 8.0) and this mixture was pelleted by a series of high-speed centrifugations (Optima MAX Ultracentrifuge, Beckman Coulter, USA, 60 min each, 140,000 g, 45,000 rpm; MLA-80 rotor, Beckman Coulter; 10 ml Centrifuge Tubes, Beckman) until the supernatant was fully clear (about 4 times). Following each round, the supernatant was removed and the pellet resuspended in 3 ml PB. The final pellet was resuspended in 50 µl PB and stored at 4°C. Conjugated beads were injected within 14 days (as proven to be stable for at least 2 weeks by Madison and Macklis, 1993).

2.4.3 Tracer injection into MGB

Immediately before using, the tracer solution was put into an ultrasound bath (Sonorex Super 10P, Bandelin, Germany, 15 min) to prevent clotting. Glass pipettes (outer diameter 1.2 mm, inner diameter 0.68 mm, WPI, USA; tip diameter broken to 20 µm) were filled backwards using a 28 gauge MicroFil needle (WPI, USA). Unilateral stereotaxic pressure injections of conjugated microbeads (40 nl) into the MGB of gerbils were made as for biocytin injections (see section 2.3.1).

2.4.4 Laser illumination of AI

10 days following the injection, photolytic apoptosis of retrogradely labeled cortical neurons was induced by ipsilateral exposure of AI to laser light. To this aim, gerbils were reanesthetized [ketamine (10 mg/100 g body weight) and xylazine (0.5 mg/100 g body weight) in saline, i.p.], and the skin and the

temporal muscle overlaying the AC were deflected laterally. The exposed AI, which can be identified by its vasculature landmarks (e.g. Thomas *et al.*, 1993; Sugimoto *et al.*, 1997) was illuminated transcranially with a 670-nm wavelength near-infrared light from a tunable 300 mW laser diode (Flatbeam-Laser 670, Schäfter + Kirchhoff, Germany). The laser light was adjusted with beam-shaping optics to create a 1.35-mm spot focused at the level of layer V/VI (1-1.5 mm deep) and the laser intensity was tuned to 50 mW (surface energy doses of approx. 1250 J/cm², exposure area approx. 2.86 mm²) and maintained for 10-12 min (5-6 min at two cortical sites). Following illumination, the skin was closed using surgical thread and tissue adhesive (Histoacryl, Braun, Germany), and the animal was allowed to recover.

2.4.5 Surgical preparation for CSD recording

2-3 weeks after laser exposure, animals were prepared for the electrophysiological experiment. Before surgery, ear canals and tympanic membranes were controlled using a surgical microscope. General anesthesia was induced and monitored as described above and was then switched to a subcutaneous anesthesia. Depending on the status of anesthesia, 0.02-0.04 ml of the anesthetic cocktail was supplied roughly every 20 minutes. Body temperature was kept at 37°C by a controlled heating blanket.

The animal's head was shaved and additionally anesthetized locally with Gingicain in the region of the incision. An incision into the skin was cut over the *Sutura interparietoparietalis*. An additional incision was done in a 90° angle to the first one, ending at the connection line between eye and external ear. Connective tissue and parts of the temporal muscle (ipsilateral to injection and illumination side) were carefully removed. Then, the AC was exposed by craniotomy (3-4 mm), thereby preserving the dura mater.

A stainless steel wire (Science Products, Germany) was implanted in the contralateral parietal bone with good contact to the dura mater and was used as a reference electrode. Stereotaxic fixation was achieved by an aluminum bar attached to the frontal bones with dental cement (Paladur; Heraeus Kulzer).

After finishing the preparation, the animal was transferred to an electrically and acoustically shielded recording chamber (Fig. 2.2). Body temperature of the animal was kept constant at 37°C by means of a regulated heating blanket. 0.02

ml Robinul (0.2 mg/ml Glycopyrronium, Eumedica, Switzerland) was administered (s.c.) to minimize pulmonary secretions.

2.4.6 Implantation of electrodes

Cortical activity was recorded by 32-multichannel silicon polytrodes (interelectrode distance: 50 μm ; NeuroNexus Technologies, USA). With this multiprobe, a radial depth profile of field potentials and action potentials of smaller groups of neurons (multi units), located in different cortical depths, can be recorded simultaneously. Recording positions were chosen based on vasculature landmarks and the well established tonotopic organization of AI (Thomas *et al.*, 1993; Schulze *et al.*, 1997, Sugimoto *et al.*, 1997). Immediately before insertion of the multichannel shaft electrode into AI (region of the laser-treatment), a cut was made in the dura using a small cannula needle. With the help of a 3D micromanipulator (HS6, WPI Inc., USA), we positioned the shaft-electrode perpendicular to the cortical surface and inserted the electrode until the topmost recording channels were barely visible.

Electrical stimulation was applied by a stimulation electrode array of three wires (platin-iridium, 40 μm diameter, ends cut blank, interelectrode distances along z-direction: 500 μm , lateral distances 70 μm) aimed to stimulate cortical layers I/II, III/IV, and V/VI. The stimulation electrodes were glued together with dental acrylic to a rigid wire, which was connected to a micromanipulator (Stoelting, USA). The electrode array was perpendicularly inserted into AI as close as possible (approx. 300-400 μm ventrally) to the recording electrode, in the (proposed) same isofrequency contour (IFC). Electrodes were then connected to the stimulus generator (STG-2008, Multichannel-Systems, Germany) and to the reference and ground.

2.4.7 Recording

Neuronal signals of the 32-channel electrodes were conveyed through an impedance converter ("headstage", Plexon, USA) and fed into a preamplifier (Plexon) where they were amplified by a factor of 500 and split into a low frequency (3-170 Hz) and a high frequency range (400-4000 Hz) by means of bandpass filters. Then, all signals were routed to a multichannel recording system (Multichannel Acquisition Processor; Plexon) where they again were

amplified (with a variable amplification factor), digitized with a sampling rate of 2 kHz and 40 kHz for the low and high frequency range, respectively, and stored on a PC for later analysis. Low pass filtered signals were used for the acquisition of the field potentials needed for the subsequent calculation of the CSDs, high pass filtered signals were used for action potentials to have an additional means for observing online the effect of muscimol (see 2.4.10).

2.4.8 Acoustic stimulation

Acoustic stimuli were digitally generated with a PC containing a signal processing card (National Instruments, Germany). Stimuli were routed via an attenuator (g.PAH, Guger Technologies, Austria) and an audioamplifier into a loudspeaker (Tannoy Arena 5.0, UK), which was positioned about 100 cm in front of the animal's head. Sound pressure intensities were calibrated prior to the experiments by means of a reference signal (0 dB attenuation corresponds to 94 dB SPL). We presented pseudo-randomized series of pure tones with different sound pressure levels and a logarithmic (i.e. iso-octave) frequency spacing spanning 7-8 octaves from 250/500 to 32 kHz (34-74 db SPL), tone duration: 200 ms, rise and fall time: 5 ms, ISI: 600 ms, 50 repetitions. If the cortex was responsive to the acoustic stimuli we could conclude that the MGB was not damaged by the tracer injection and thus relayed sensory information to the AC.

2.4.9 Electrical stimulation

Electrical stimuli were generated with a PC and a programmable electrostimulation device (STG2008, Multichannel Systems, Germany). The shape of the stimuli was generated using Matlab and sent to the stimulus generator. For synchronizing purposes and the ease of later data processing, the trigger was not only transferred to the stimulator but also to the recording system (to mark the beginning of a stimulation trial).

Intracortical microstimulation of biphasic (current-balanced), monopolar, cathodic-first single pulses were applied (50 repetitions, phase duration: 100 ms, inter phase interval 50 ms, ISI: 500 ms) in three different cortical layers. Stimulation amplitudes were varied from 40-160 μ A.

2.4.10 Pharmacological silencing

After recording of acoustically and electrically evoked CSD patterns of pharmacologically untreated animals, the GABA_A-agonist muscimol (7.5-8.4 mM, 20-30 µl, Tocris, USA) was applied onto the cortical surface for pharmacological blocking of intracortical transmission. Axonal conductance should not be influenced; electrical stimulation of the cortex should therefore be able to excite for example CT projection fibers. Inputs with their neuronal generators outside of the pharmacologically inhibited region, like TC projections, should also still be excitable. The volume and concentration of muscimol used in this study has been shown to be an appropriate dosage for effective cortical silencing in gerbil AC (Happel *et al.*, 2010, Happel *et al.*, 2014). During diffusion of muscimol, acoustic stimuli (pure tones at 40 db attenuation) were presented to monitor which layers have been silenced so far. After complete diffusion of muscimol across all cortical layers (takes approximately 0.5-1 h) the same set of acoustic and electrical stimuli were repeated.

2.4.11 Perfusion of the animal and immunohistochemistry

Following the electrophysiological experiments, the gerbils were perfused transcardially with 20 ml of 0.1 M PBS (pH 7.4) followed by 4% PFA (200 ml). Brains were postfixated in 4% PFA overnight, cryoprotected in 30% sucrose dissolved in PBS, frozen and cut into 50 µm thick horizontal slices. Every third section was mounted on slides and coverslipped using Immu-Mount (Thermo Scientific, Germany) to analyze the injection site and retrograde transport of beads under a fluorescence microscope.

In addition, every third section was stained to visualize neuronal nuclei (NeuN) to verify the efficacy of the laser treatment indicated by reduction of cell number in layers VI (and V). To this aim, sections were incubated in a solution containing a monoclonal mouse antibody to NeuN (1:500 or 1:1000, Chemicon Europe), 0.1-0.3% Triton, and 1% BSA for two days. To ensure specificity of the later secondary antibody, control probes without primary antibodies were also made. After blocking against unspecific binding sites (see section 2.2.4), appropriate secondary biotinylated antibodies were used (anti-host IgG 1:200, Vector Labs). The reaction product was visualized by incubating the sections in the ABC-solution (Vectastain Elite ABC Kit, Vector Labs) and using 3,3'-

diaminobenzidine (0.4 mM of DAB, Sigma-Aldrich) as chromogen in the presence of 0.015% H₂O₂. After rinsing with TRIS-HCl (1 x) and PBS (2 x), the sections were mounted on gelatine-coated slides. The sections were dehydrated in isopropanol (2 min) and Rotoclear (ROTH, Germany, 3 x 5 min) and then coverslipped using Merckoglass (Merck, Germany).

2.4.12 Analysis of CSD data

Recorded raw data were imported into the Matlab programming environment and were further processed by custom written programs (fundamental routines for conversion and analysis of the electrophysiological data were kindly provided by Dr. Marcus Jeschke. Additional Matlab codes meeting our specific needs were written by me).

The converted raw data of the field potentials were averaged over the particular stimulus repetitions relative to the stimulus onset.

Before CSD calculation, the averaged field potentials were spatially filtered with a weighted average (Hamming window) across $n=9$ sampling points, corresponding to a spatial filter kernel width of 450 μm (kernel width/interchannel distance = $450\mu\text{m}/50\mu\text{m} = 9$ sampling points). To avoid the loss of sampling points (upper and lower boundary sites) due to the running average, we used a linear extrapolation procedure (Happel *et al.*, 2010) by which at each point in time $k = (n-1)/2$ virtual spatial sampling points were added. This offered the advantage that no further spatial curvatures are added during filtering, which would be interpreted as current sinks and sources during CSD analysis.

We calculated the one-dimensional CSD profile from the second spatial derivative of the laminar LFP according to the following formula (for every spatial and temporal sampling point) (Pitts, 1952; Nicholson and Freeman, 1975; Mitzdorf, 1985; Steinschneider *et al.*, 1992) (Eq. 1):

$$- \text{CSD} \approx \frac{\delta^2 \varphi(z)}{\delta z^2} = \frac{\varphi(z + n\Delta z) - 2\varphi(z) + \varphi(z - n\Delta z)}{(n\Delta z)^2} \quad (1)$$

where φ is the field potential, z is the spatial coordinate perpendicular to the cortical layers, (δz) is the sampling interval (50 μm), and n is the differentiation grid (Mitzdorf, 1985; Happel *et al.*, 2010).

We analyzed acoustically evoked responses with an intensity of 54 dB SPL. This relatively low intensity was chosen because it revealed the bandwidth of frequency tuning particularly clearly.

For each animal and stimulus condition (i.e., acoustic stimulation before and after muscimol; ICMS before and after muscimol), onset latencies (OL), peak amplitudes (PA), and peak latencies (PL) were determined for the different sinks from the CSD signals averaged across the channels within the layers corresponding to the sink.

We classified the observed sinks as follow: early granular sink (S1), early infragranular sink (iS1), supragranular sink (S2), late infragranular sink in layer V(a) (S3), and late infragranular sink in layer Vb/VI (S4). Not all sinks were visible in each animal and only those which could be identified were analyzed (with exception of the electrically evoked granular sink, see below). For analysis of tone-evoked sink components, we averaged those channels that displayed the shortest onset latencies of the respective sink and/or displayed the highest amplitude. For analysis of ICMS-evoked activity, channels attributed to individual sinks were identical to the sink locations defined in previous pure-tone stimulation, or shifted (maximal) one channel up or down. The number of channels per sink was kept constant when comparing responses in untreated cortex vs. after application of muscimol. If an animal displayed no granular sink during ICMS, its theoretical location (channel numbers) was derived from the location of the acoustically evoked granular sink after cortical silencing, and was also analyzed.

PAs were defined as the highest amplitude of an individual sink. PLs were determined by the latency of the PA after stimulus onset. OLs of the sinks were defined as the intersection of a line, which was fitted around the point at which a given curve surpasses 3 SDs below baseline (based on the prestimulus period of 200 ms). For control of this automated processing, all plots were additionally inspected and, if necessary, corrected by hand. Offsets were defined as the next crossing with the baseline or as the first inflection of the curve for at least 5 ms. In addition, integrals (INT) were calculated for all identified acoustically evoked sinks. For this we used the time period between onset and offset latency as time window.

The BF was defined as the frequency of the pure tone stimulus in our stimulus set that elicited the maximum peak in the initial granular sink. The sharpness of frequency tuning was estimated by dividing the response strength (PA, INT) at BF by the response strength at nonBF (BF +/- 2 octaves).

The averaged rectified CSD (AVREC) was calculated by averaging the absolute values of the CSD across all of the n channels. While information on the direction and laminar location of transmembrane current flow is lost by (full-wave) rectification, the AVREC waveform provides a useful measure of the temporal pattern of the overall strength of transmembrane current flow (Schroeder *et al.*, 1998) (Eq. 2).

$$\text{AVREC} = \frac{\sum_{i=1}^n |\text{CSD}_i(t)|}{n} \quad (2)$$

Onset latencies of AVREC were defined as for the CSD sinks. To facilitate comparison of activation (PA, PL, INT) between animals and/or conditions, we decided to always use the same time windows for analysis of the AVREC curves. In the acoustic condition, we analyzed the data from 18 ms (which approximately correspond to the onset latency in most animals) to 300 ms, and additionally subdivided them into an early (18-60 ms) and a late phase (60-300 ms). Sharpness of frequency tuning was determined as described above for the CSD sinks. The ICMS data were analyzed from 6-300 ms (6 ms correspond to the duration of the stimulus artifact), as well as from 6-36 ms (early phase) and from 36-300 ms (late phase).

For comparison of different animal groups (non/weakly lesioned, layer VI lesioned, layer VI plus layer V lesioned, for definition see Tab. 3.4), CSD profiles of animals belonging to the same group were averaged (Szymanski *et al.*, 2009). Before averaging, profiles were aligned with respect to layer IV (granular sink). In electrically evoked CSD patterns, its location was determined with the help of the acoustically evoked pattern (post muscimol condition) and supported by histological examination. We performed this analysis with and without normalization (dividing the CSD values by the maximum absolute CSD value before averaging so that the maximum value is 1). Since normalized and

non-normalized patterns resembled each other in most cases, we decided to present the actual values only.

Similarly, AVREC curves obtained from acoustic (BF) and electric stimulations (160 μ A, all stimulation depths) were averaged and plotted including standard deviations.

2.4.13 Histological analysis

Light and fluorescence microscopic analyses and photography (to verify injection sites and determine lesion efficacy) were carried out using a microscope (Zeiss Axioskop 2, Germany), fitted with the appropriate filters for fluorescence and a digital camera (Leica DFC 500, Germany).

Calculations of neuronal cell loss were made using ImageJ (<http://imagej.nih.gov/ij/>). To this aim, color photographs of NeuN-stained sections were converted to 16 bit images (gray scale), and then to binary (black/white) images by choosing a specified threshold. The same threshold was applied for all sections of a given animal. Then, layers V and VI, which are well discernible in NeuN stained tissues, were outlined in both the ipsilateral lesioned and the contralateral non-lesioned AI, and the percentual area occupied by particles (i.e., NeuN stained nuclei) was determined in at least three sections per hemisphere surrounding the electrodes on the lesioned side and for comparison at similar dorsoventral levels on the contralateral side of AI. The percentual neuronal loss in the infragranular layers relative to the contralateral side was calculated for each animal. In addition, a correlation analysis was performed (Pearson, Spearman) to test whether lesions in layer V and VI occur independently.

2.5 Figures

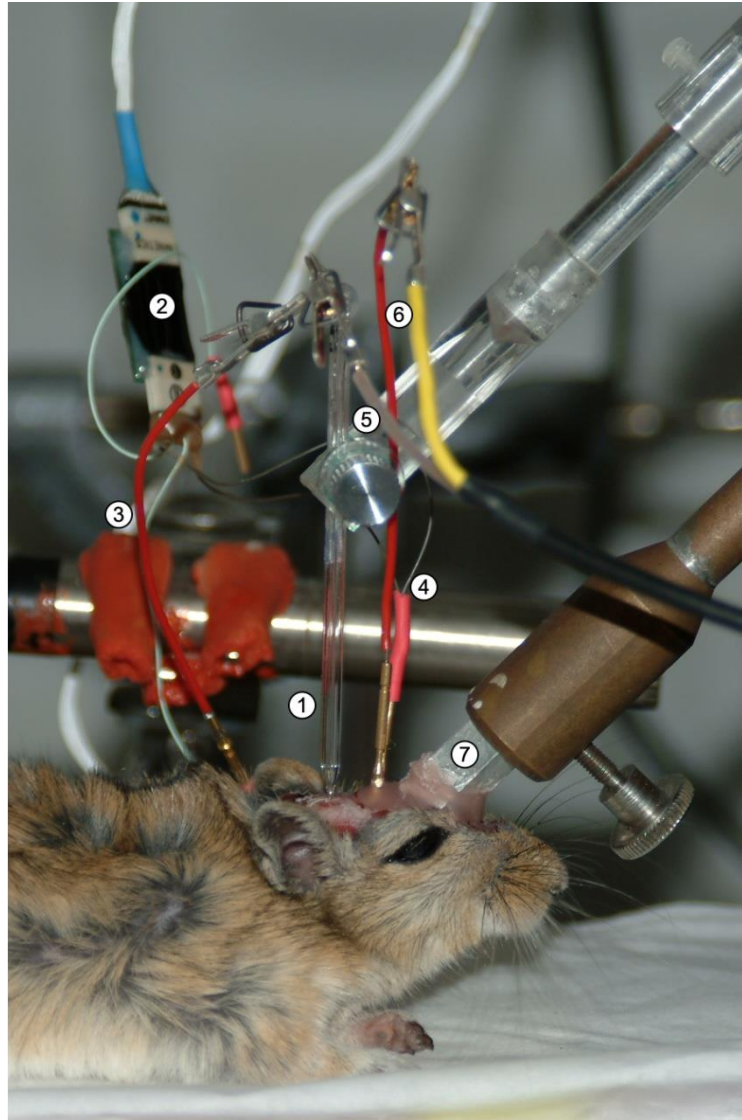


Figure 2.1: Animal in the electrophysiological setup prepared for iontophoresis. **(1)** Three-barrel glass pipette filled with biocytin and saline. **(2)** Impedance converter (headstage). **(3)** Cable connecting silver wire in saline with headstage (for extracellular recording). **(4)** Connection between headstage and reference electrode/ground. **(5)** Current supply to eject the tracer. **(6)** Connection between iontophoretic lead-wire and ground. **(7)** “Headmount” for head fixation.

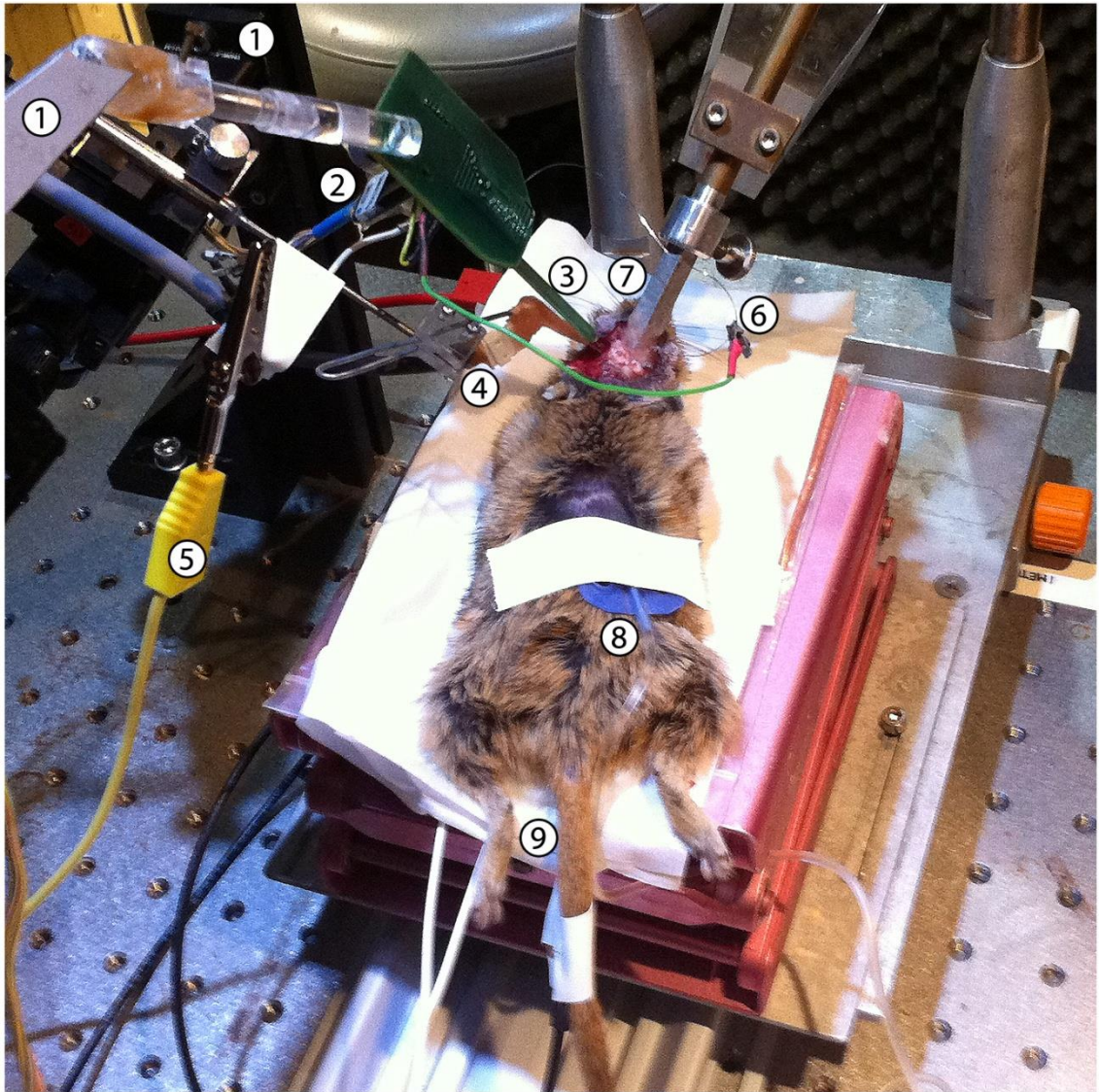


Figure 2.2: Animal in the electrophysiological setup prepared for CSD-analysis. (1) Micromanipulators. (2) Impedance converter (headstage). (3) 32-channel recording electrode, (4) 3-channel stimulation electrode, both inserted into left AI. Connections to ground (5) and reference (6) electrode. (7) “Headmount” for head fixation. (8) Indwelling cannula for s.c. administration of the anesthetic cocktail. (9) Regulated heating blanket (rectal probe).

3 Results

3.1 Anatomy of the auditory thalamocortical system

In the following, the results from iontophoretic injections of biocytin into each of the cytoarchitecturally identified subdivisions of the MGB will be presented. We will describe and illustrate for each subdivision the typical neuronal responses to acoustic stimuli (pure tones and clicks) (Fig. 3.1) and projection patterns of one representative case of injections (Figs. 3.2, 3.3, 3.5, 3.6). Summaries and statistical analyses are depicted in Figures 3.4, 3.7, and 3.8. For an overview of all iontophoretic injection sites see Table 3.1.

3.1.1 MGv

Auditory responses of MGv neurons

Neurons of the LV generally displayed clear frequency selectivity and showed robust, transient short latency onset responses (about 12-15 ms) to tonal stimuli (60-70 dB SPL, 50 repetitions) at their respective BFs (Fig. 3.1). OV neurons also responded with short onset latencies (about 13 ms) frequency-specifically to pure tones, but stimulus frequencies remote from the BF often elicited weak spike activity as well (i.e., some neurons had multipeaked tuning curves). In RP, we generally recorded strong burst-like discharges to a wide range of frequencies. Elicited responses occurred after 10-12 ms latency, which then sustained for about 15-20 ms. Click responses had very short latencies down to 6 ms. Although we recorded from different locations of RP (Tab. 3.1), we could not detect a tonotopic organization of RP as reported for the cat (Imig and Morel, 1985a; Barone *et al.*, 1996). In all MGv subdivisions, acoustically evoked spikes were often followed by a suppression of spontaneous activity.

Labeled cell types of MGv

Following biocytin injections into MGv, labeled cells of all subdivisions were mainly medium-sized and had a bitufted or rather radiate arrangement of their tufted dendrites (Fig. 3.1 b); thus, they probably correspond to the principal bushy tufted neurons of the gerbil (Mylius *et al.*, 2013) and rat (Clerici *et al.*, 1990; Bartlett and Smith, 1999; Winer *et al.*, 1999a).

Projections of MGv-LV

In the presented case (G-05-l, Tab. 3.1, Fig. 3.2 A) axonal labeling was identified in the caudal (lf) part of AI (82.0% of all counted boutons) as well as in the rostral (lf) part of DP/VP (18.0%). The (rostro)lateral location of the injection site and the response properties of the juxtacellularly labeled neurons were in agreement with the recorded frequency selectivity of the neurons (BF 500 Hz, in Fig. 3.1 labeled with an asterisk). Thus, the location of the labeled cortical axons and their terminals suggest a tonotopic organization of the connections between LV and AI, and DP/VP, respectively. Within the target fields, labeled axons formed multiple terminal patches. For example, in AI the most prominent terminal patch was accompanied rostrally and/or caudally by smaller patches (which were mainly formed by axon collaterals from axons diverging in layer V), together having a rostrocaudal extent of about 700-800 μm . This corresponds to approx. 2 octaves in the low frequency region of AI (Scheich *et al.*, 1993; Thomas *et al.*, 1993). The most caudal cluster was additionally discontinuous in the dorsoventral direction (Fig. 3.3 A). In AI as well as in DP/VP, labeling was most prominent in layer IV (59.0% in AI, 61.4% in DP/VP) followed by layer III (22.8% in AI, 31.2% in DP/VP) and layer V (14.5% in AI, 5.8% in DP/VP).

The mean distributions of labeled boutons in the cortical layers of AI and DP/VP of all iontophoretic cases are depicted in Figure 3.7. Also, the percentages of all labeled boutons in fields AI and DP/VP across all iontophoretic cases are depicted in this figure. The distances between the centers of mass of boutons (case G-05-l: AI-DP/VP $430.0 \pm 46.5 \mu\text{m}$) in these fields are illustrated in Fig. 3.4 B.

Projections of MGv-OV

Labeled neurons from the OV innervated preferentially the ventral part of the AC (including ventral part of AI, VP, and ventral fields), whereas the dorsal part of the AC (including D, Ald, dorsal part of AI, DP) was virtually free of labeled terminals. In the case illustrated here (G-06-r, Tab. 3.1, Fig. 3.2 B), axonal labeling was identified in AI (82.4% of all counted terminals), V (14.9%), and AAF (2.7%). Two distinct terminal patches were identified in AI, which differed in their laminar profile and rostrocaudal width. Both were composed of several clusters or columns. The more dorsal patch (Fig. 3.2 Bc; approx. 450-500 μm wide) was formed by several slender vertically orientated columns, being

identifiable best in superficial layers (three terminal dense units of approx. 50 μm in diameter, separated by terminal sparse regions of approx. 50 μm). The more ventral patch (Fig.3.2 Bd; approx. 750-800 μm total width) consisted of several adjacent clusters centered in middle layers. In layer IV, terminals formed up to four clusters (approx. 200 μm width each). The presence of two distinct terminal patches in the AI, which differed in their laminar profile and rostrocaudal width, was a common feature also seen in the previous studies using pressure injections (see Saldeitis *et al.*, 2014).

Since the BF at the injection site in OV was at 16 kHz (Fig 3.1) and the projections were primarily seen in the rostral high frequency (hf) portion of AI, we conclude that OV projects to AI in a tonotopic fashion; however, the labeled region encompassed approx. 3-4 octaves (200 μm per octave in the hf region of AI; Scheich *et al.*, 1993; Thomas *et al.*, 1993).

The quantitative analysis of the laminar terminal distribution revealed that in AI the layers III (31.3%), IV (26.4%), and V (25.2%) were almost equally innervated. The more dorsal patch had more terminals in layers II and Va compared to the ventral patch, which had more terminals in layer Vb. Projections to AAF terminated predominantly in layers IV (41.1%) and V (39.3%). In field V, most of the labeled boutons were also found in layer IV (98.7%). The distances between the centers of mass of boutons are illustrated in Fig. 3.4 B (AI-AAF $634.4 \pm 143.1 \mu\text{m}$).

Projections of MGv-RP

RP neurons preferentially sent their axons to dorsal portions of the AC, namely to D, Ald, and dorsal parts of AI. Some axonal branches reached AAF. In two cases (G-07-r, G-10-l), some labeling could also be observed in DP (layer IV). In the case illustrated in Figures 3.2 C and 3.3 B (G-10-r), 28.4% of all presynaptic terminals were identified in D, 26.2% in Ald, 37.3% in AI, and 8.1% in AAF. Generally, the cortical projection patterns of RP matched the broad frequency-tuning of its neurons (Fig. 3.1) by terminating in broad-band frequency regions of the gerbil's AC (D, Ald) and over a wide range of the rostrocaudal frequency gradient in the other fields (AI, AAF, DP).

Terminals were located predominantly in middle layers IIIb-Va. In the presented case, the quantitative analysis of the laminar distribution of synaptic boutons revealed that in D and in AAF layer IV was predominantly targeted by the RP

neurons (56.4% and 61.8%, respectively), whereas in AId layers III, IV, and V were roughly equally targeted (31.0%, 33.8%, and 28.6%, respectively). In AI, projections to layer V (45.0%) even outnumbered those to layer IV (34.4%). Projections to layers I and II were sparse in all innervated fields. Layer Va terminals were frequently found on collaterals that interconnected different clusters (that could be located in either the same or adjacent auditory cortical fields, e.g., between AI and AAF). The mean distributions of labeled boutons in the layers and fields of all RP cases are depicted in Figure 3.7.

Summary of the topography of the cortical projections of MGv

In general, we observed two kinds of topographic relationships of the projections from the MGv to the AC that are summarized and illustrated in Figure 3.4.

First, we could determine frequency-specific, i.e., tonotopic connections between LV and OV and the tonotopically organized auditory fields AI, AAF, and DP/VP (Fig. 3.4 A-C). Here, neurons of the laterorostral lf and mediocaudal hf laminae of the LV (Ryan *et al.*, 1982; Bäuerle *et al.*, 2011; Budinger *et al.*, 2013) projected to the respective lf and hf representation areas of the cortical target fields (compare with Fig. 1.2). For OV we suggest a similar tonotopic organization of its TC connections on the basis of the circular arrangement of its laminae. In OV, lower frequencies are represented in its central laminae, higher frequencies in its peripheral laminae (gerbil: Budinger *et al.*, 2013; cat: Imig and Morel, 1985b). In order to further underpin these topographic relationships we calculated the distances between the centers of mass of boutons in layer IV of fields AI, AAF, and DP/VP and analyzed them with respect to the measured (or, in cases of pressure injections, assumed) frequency-selectivity of the injected thalamic neurons. The distances between the centers of bouton clusters in these fields are illustrated in Figure 3.4 B. According to the mirror-imaged tonotopic organization of these fields, the distances between the bouton clusters in AI and DP/VP (common lf border) were shortest in lf LV and OV injection cases and longest in hf cases. The opposite was true for the distances between AI and AAF (common hf border).

We found most neurons of the (non-laminated) RP to be broadly tuned to frequencies. Accordingly, their main projections were to the fields D and AId as well as diverging across the tonotopic gradient of the other fields (Fig. 3.4. A;

compare also rather focused bouton distributions for LV and OV in Figs. 3.2 A and 3.2 B, respectively, with rather diverging bouton distribution for RP in Fig. 3.2 C). We therefore conclude that the TC connections of RP with the AC of the gerbil are non-tonotopically organized.

Second, we revealed an unexpected topographic relationship between the position of the injection site within the subdivisions of the MGv and the focus of the TC projections along the dorsoventral axis of the gerbil's AC (Fig. 3.4 D). Thus, RP neurons sent most of their axons to the dorsal half of the AC including D, Ald, and DP. LV neurons projected predominantly to middle (central) parts of the AC. Rostrally localized neurons center their cortical terminals somewhat more dorsally than caudomedially localized neurons. Finally, neurons of the OV sent their main projections preferentially to the ventral AI and the ventral fields V and VM.

3.1.2 MGd

Auditory responses of MGd neurons

Within the MGd *proper*, we could not record acoustically evoked responses at all sites. Neurons located in the mediorostral part of the MGd responded weakly and unreliably to pure tones. Responses were characterized by poor frequency selectivity, long first spike latency (approx. 35 ms) and great variability in spike timing (Fig. 3.1).

Auditory responses of DD neurons were similar to those of the MGd *proper* in terms of poor frequency selectivity, but neurons responded more reliably, i.e., with a lesser spike variability and with shorter latencies (9-15 ms). Neurons exhibited a (bursting) activity of 20-30 ms duration with (slight) preferences for tones of either lower (125 Hz-1 kHz) or higher (2-16 kHz) frequencies.

Labeled cell types of MGd

In the MGd *proper*, biocytin labeled neurons of different size, but usually with bitufted, multipolar tufted or radiate dendrites (Fig. 3.5 Ab). They probably correspond to the "principal tufted", "radiate", or "stellate" cells (gerbil: Mylius *et al.*, 2013; rat Clerici *et al.*, 1990; Bartlett and Smith, 1999; Winer *et al.*, 1999a). The iontophoretic injections of biocytin into DD labeled neurons predominantly of the bitufted type (Fig. 3.5 Bb) (Clerici *et al.*, 1990; Bartlett and Smith, 1999; Winer *et al.*, 1999a; Mylius *et al.*, 2013).

Projections of MGd proper

Labeled neurons of the illustrated case (G-11-r; Fig. 3.5 A) sent their axons mainly to field V (77.5% of all counted boutons) whereas AI (12.0%), AAF (8.3%), and DP (2.2%) received less innervation. This is to some part in contrast to a previous pressure injection (Saldeitis *et al.*, 2014), after which DP received strong input. In field V of the presented animal, axons terminated to a large degree in layer IV (72.5%) and the remaining terminals were mainly found in layer I (14.1%). In AI, the boutons were mainly identified in the infragranular layers V (37.4%) and VI (29.3%) and in superficial layer I (27.2%). Most of the projections to AAF were located in the ventral part of AAF and terminated predominantly in layer V (57.1%) and layer I (22.9%). In DP, the main recipient layers were layers IV (31.8%), I (20.5%), V (20.5%), and VI (15.9%). All of the innervated auditory fields received only a little input into layers II and III.

Projections of MGd-DD

Projection targets of the presented DD case (G-14-l; Fig. 3.5 B) were AI (73.4% of all counted boutons), AAF (2.8%) and DP/VP (23.8%). In one experimental case (G-13-r; not illustrated), fields V/VM were also labeled. In AI, labeled terminals spanned almost the entire rostrocaudal frequency range of the field, but there were local maxima. In all cases of DD, we observed a match between the preferred frequencies of DD neurons and the sites of these local maxima in AI. However, due to the high divergence of the projections emerging from a very restricted area in the DD, a tonotopic organization of the connections between DD and AI is not as evident as for the connections between LV/OV and AI. In AI and DP/VP, layer V, and here in particular sublayer Va (Fig. 3.5 Bd-e) received most of the labeled afferents arising from DD (63.4% and 59.8%, respectively). In AI, layer I (25.0%) and in DP/VP layer VI (34.5%) contained the second largest proportion of labeled terminals. In AAF, presynaptic boutons were exclusively found in infragranular layers (70.0% in layer VI, 30.0% in V). In all labeled auditory fields, layers II, III, and IV received just a few inputs from DD. Mean distributions of labeled boutons in the layers and fields of all DD cases are depicted in Figure 3.7.

3.1.3 MGm

Auditory responses of MGm neurons

Neurons of the MGm usually responded to a wide range of frequencies with burst or tonic activity. As shown for the case presented in Figure 3.1 (case G-15-r), spikes could be elicited using pure tones covering several octaves favoring low frequencies (250 Hz-2 kHz, 60 db SPL) and clicks. The first spike latency was short (7-10 ms).

Labeled cell types of MGm

Following the iontophoretic injections of biocytin, a variety of cell types was labeled in MGm. The most conspicuous neuron had a large soma with several irregularly radiating dendrites (Fig. 3.6 B) and corresponds most likely to the "magnocellular" neuron described in gerbils (Mylius *et al.*, 2013) and several other species (for review see, e.g., Winer, 1992).

Projections of MGm

Projections from the MGm diverged in a non-tonotopic manner over large areas in several auditory fields. The tuning (see above) was typically narrower than the distribution of terminals, which covered the whole frequency gradient. In the case shown (G-15-r, Tab. 3.1, Fig. 3.6), terminals were found in AI (48.4% of all counted boutons), AAF (29.6%), D (15.3%), and DP/VP (6.7%).

In AI, AAF, and DP/VP, many terminals were identified in the deep infragranular layers V(b) (39.9%, 38.3%, and 50.8%, respectively) and VI (22.2%, 9.7% and 16.9%, respectively). Besides that, layer III (IIIb) was a substantial target layer in AAF (31.7%) and AI (18.3%), even outnumbering layer IV (19.2% and 9.1%, respectively), whereas in DP layer IV contained more terminals than layer III (22.4% and 3.8%, respectively). In D, terminals were found primarily throughout layer V (81.3%). Mean distributions of labeled boutons of all MGm cases are depicted in Figure 3.7.

In layers Vb/VI of AAF, AI, and DP/VP, MGm axons ran perpendicular to the cortical layers (i.e., parallel to the cortical surface) thereby forming small terminal patches spaced 500-700 μm apart (e.g., Fig. 3.6 E, case G-16-r). In addition, most of the labeled axons ascending from the middle layers to superficial layer I were arranged in a column-like fashion. Thus, a columnar arrangement of TC projections of the MGm was apparent by the regular spacing

of terminal patches in deep infragranular layers as well as by the ascending fibers towards supragranular layers.

In addition to this conspicuous projection pattern, MGm projections were also characterized by a morphological feature that was exclusively found after injections into the MGm. Besides “normal” synaptic boutons of a diameter of approximately 1 μm , we found very large boutons, whose diameter ranged from 2.5 to 3 μm and which appeared as boutons *en passant* and boutons *terminaux* in the AC (Fig. 3.6 G). These “giant” boutons were localized mainly in deep infragranular layers but also in other layers (Fig. 3.6 F) and constituted on average 4.5% of all TC boutons emerging from the MGm to the AC. For the investigation of their ultrastructure, see chapter 3.2.

3.1.4 Summary of the areal and laminar distributions of the auditory TC terminals in the Mongolian gerbil

The auditory TC connections of the gerbil show highly specific features regarding their origin in one of the subdivisions of the MGB as well as their termination patterns in the auditory cortical fields and layers.

The relative overall (i.e., summarized for all auditory fields) and field-specific laminar distributions of the gerbil's TC terminals in the AC after iontophoretic injections of biocytin into the diverse subdivisions of the MGB are illustrated in Figures 3.7 and 3.8. Every subdivision of the MGB has a characteristic laminar profile of its input to the AC. Regarding the MGv, layer IV is the preferential target layer of all three subdivisions. However, for LV this dominance is much more pronounced and to a higher degree due to projections to AI than for OV and RP. In addition, the three subdivisions contribute differentially to the TC inputs of layers III and V (dashed line in Fig. 3.8) and vary with respect to the cortical divergence and patchiness of their projections. In the MGd *proper*, projections to layer IV also dominate, but projections to the other layers (except layer I) are much sparser than for MGv. For DD, the main target is layer V (in particular sublayer Va) in all fields except field V. Projections from DD and the MGd *proper* have in common that both have a larger proportion of terminals in layer I than all other divisions and subdivisions of the MGB. Main target layers of the MGm are the deep infragranular layers (Vb and VI, all fields) followed by the middle layers (IIIb and IV, in AI and AAF).

3.1.5 Figures

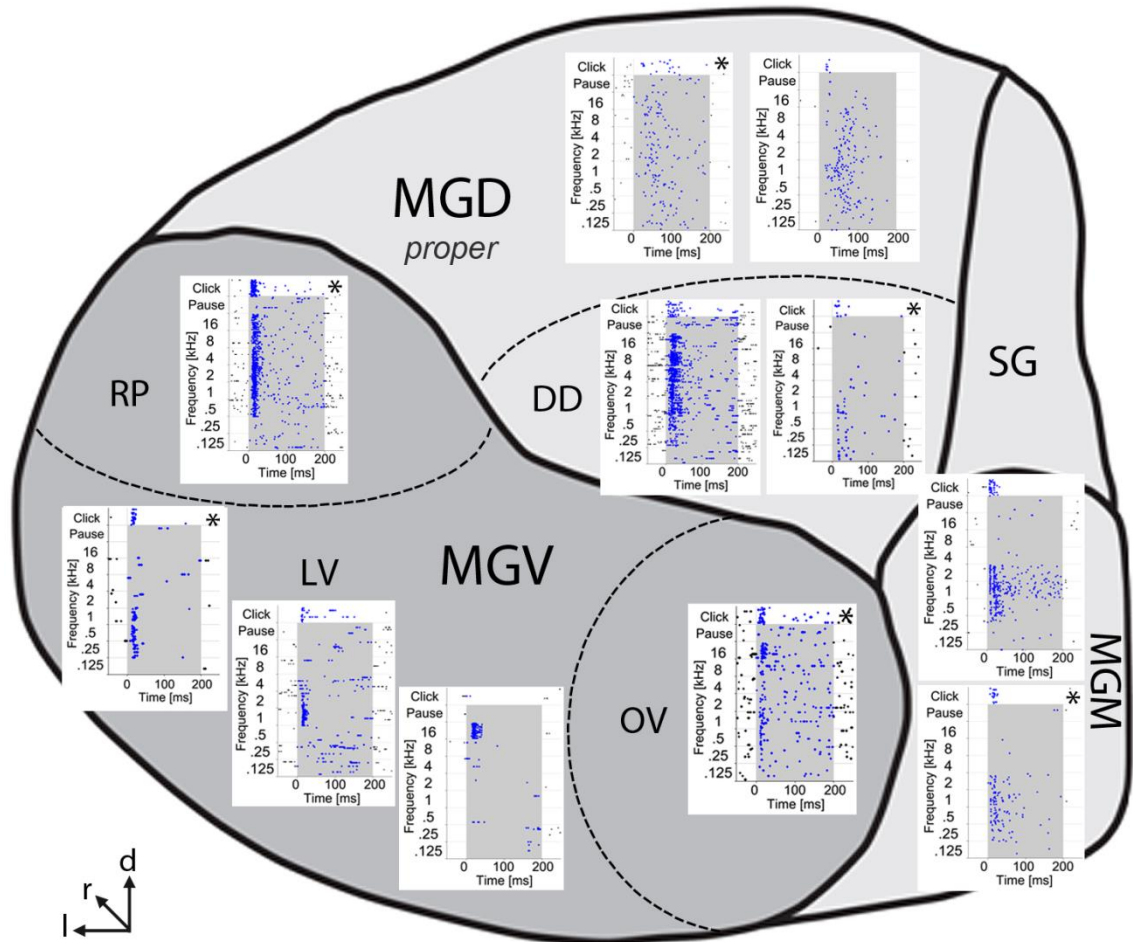


Figure 3.1: Electrophysiological responses of the different subdivisions of the MGB. Schematic representation of the MGB showing rasterplots of spike events following stimulation with pure tones and clicks at 60-70 db SPL. Neurons in the LV and OV of the MGv responded with short onset latencies to pure tones. LV neurons were tonotopically arranged with lf represented laterally, and hf represented medially. In OV, hf were represented peripherally. Neurons from RP showed burst activity with weak frequency selectivity. Neurons from MGd *proper* responded weakly, were broadly tuned and had long and variable response latencies (25-50 ms), while DD neurons had shorter onset latencies. MGm neurons responded typically with bursts across several octaves with an average response latency of 7-10 ms. Rasterplots of the representative cases of injections whose cortical projections are described in 3.1.1-3.1.3 are labeled by asterisks.

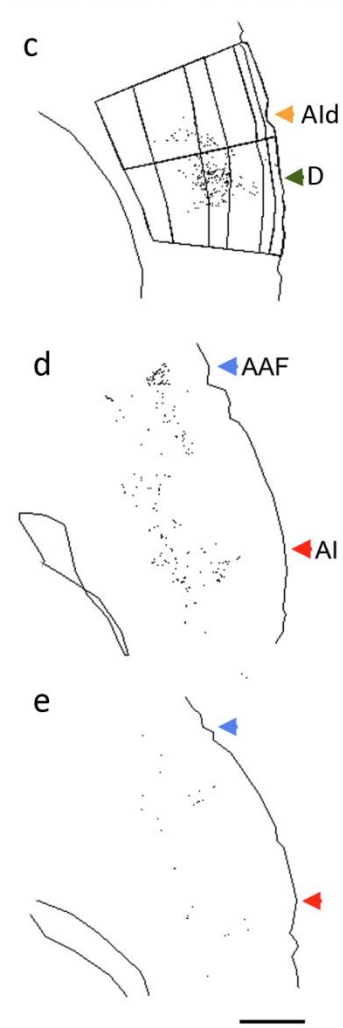
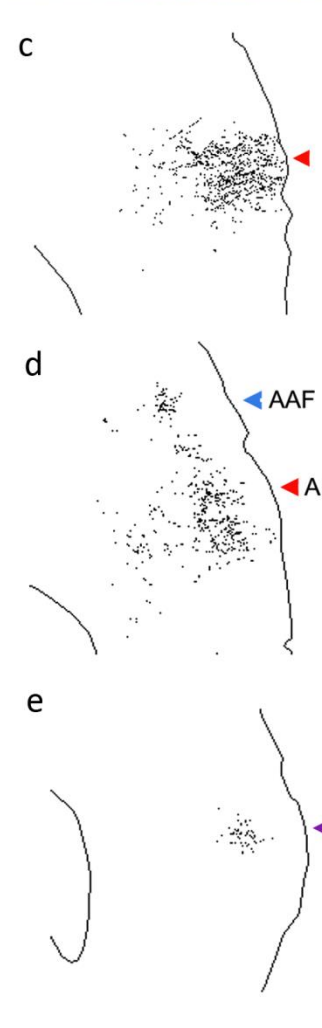
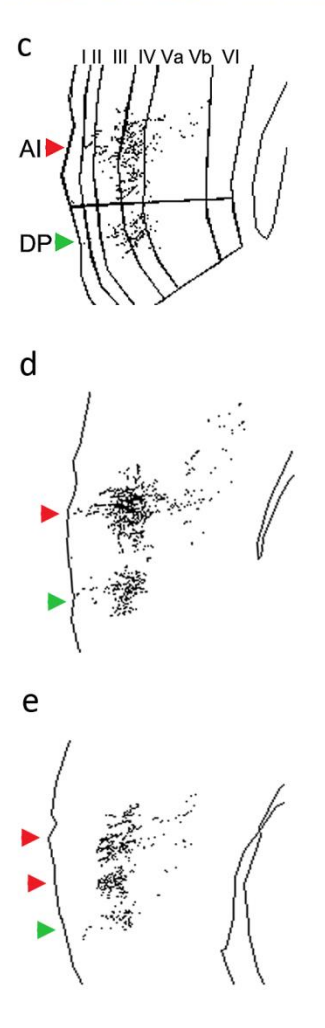
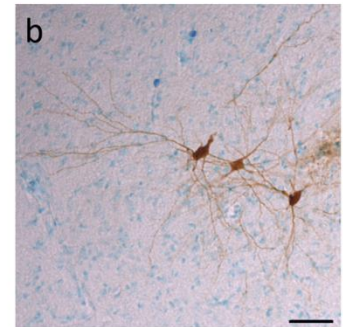
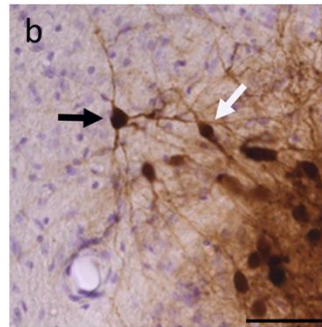
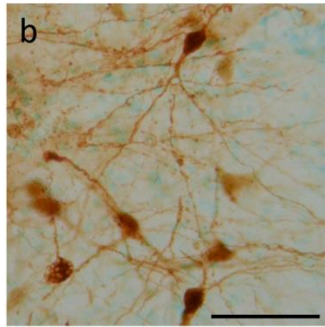
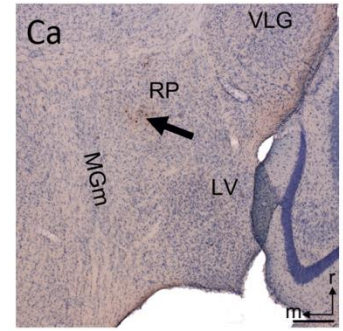
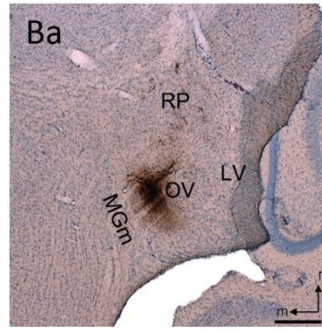
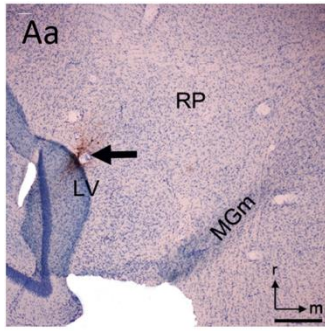


Figure 3.2 (preceding page): Results of iontophoretic injections of biocytin into the MGv (LV: case G-05-l, OV case case G-06-r, RP case G-10-r). **(Aa)** Nissl-counterstained sections showing the iontophoretic injection sites in the rostromedial part of the LV (arrow). **(Ab)** Methyl green-counterstained section representing principal bitufted neurons of the LV juxtacellularly labeled at the iontophoretic injection site. **(Ac-e)** Samples of NeuroLucida-reconstructed sections showing the areal and laminar distribution of TC terminals in AI and DP following the iontophoretic injection into LV. Lines parallel to the cortical surface in panel Ac indicate the borders of cortical layers I-VI. **(Ba)** Iontophoretic injection site in OV. **(Bb)** Principal tufted neurons of the OV with bitufted (white arrow) and radiate dendrites (black arrow). **(Bc-e)** Samples of reconstructed sections arranged from dorsal (c) to ventral (e) showing the distribution of TC terminals in AI, AAF, and V following the injection into OV. **(Ca)** Section showing the injection site in the RP (arrow). **(Cb)** Principal bitufted neurons with rather radiate dendrites of the RP. **(Cc-e)** Samples of reconstructed sections showing the distribution of TC terminals in AI, Ald, AAF, and D. All sections are in the horizontal plane. Orientation in Aa also applies to panels Ab-e, orientation in Ba also applies to Bb-e and C. Scale bars: 50 μm (Ab, Bb,Cb), 300 μm (Aa, Ba, Ca), 500 μm (Ac-e, Bc-e, Cc-e). For abbreviations see list.

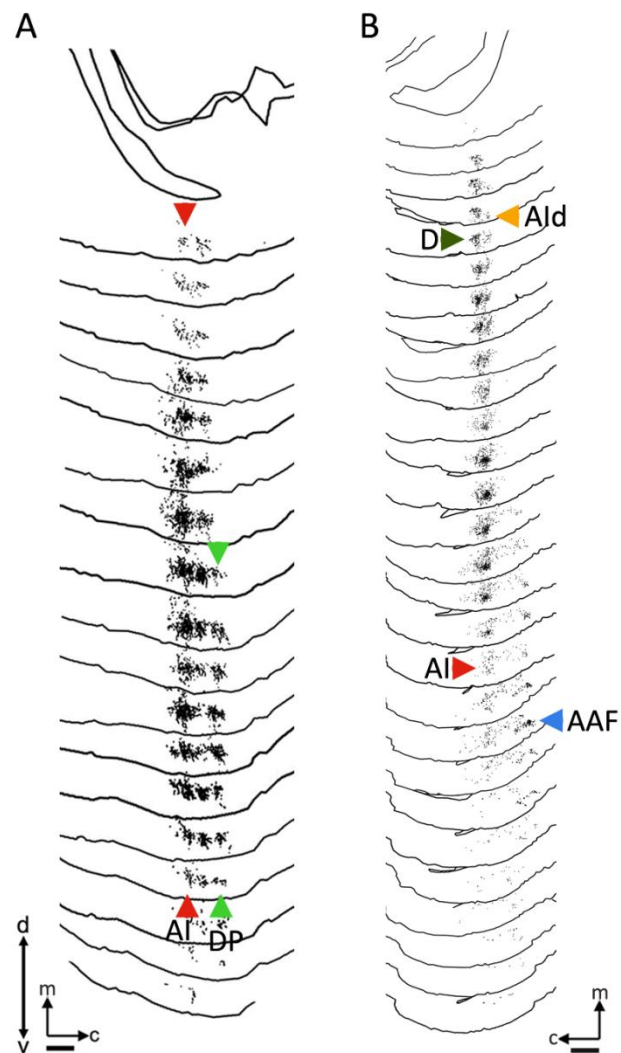


Figure 3.3: Montages from Neurolucida-reconstructed hemispheres following injections into MGv. **(A)** Montage of the left hemisphere illustrating the labeling in AI (red arrowheads) and DP/VP (green arrowheads) following injections into LV (case G-05-l). **(B)** Montage of the right hemisphere illustrating the labeling in D (dark green arrowheads), Ald (yellow arrowheads), AI, and AAF (blue arrowheads) following injections into RP (case G-10-r). For comparison of labeling with 2-DG activity see Fig. 1.2 E. Scale bars: 500 μm (A), 1 mm (B).

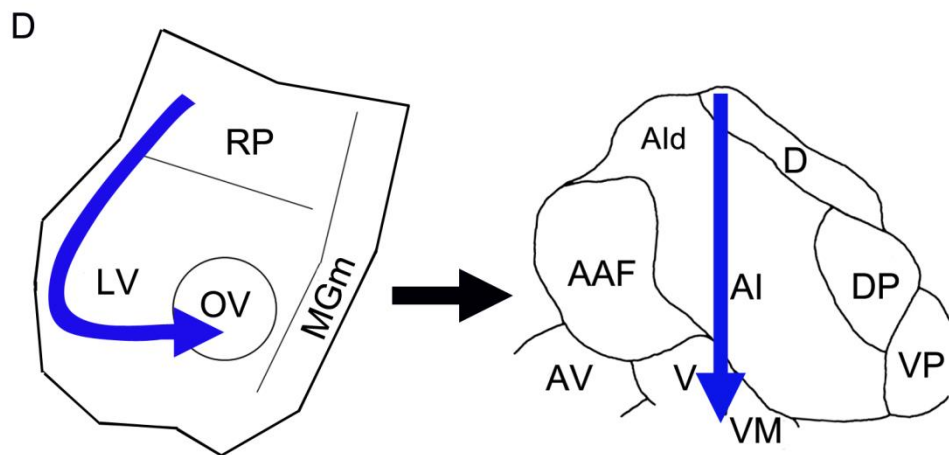
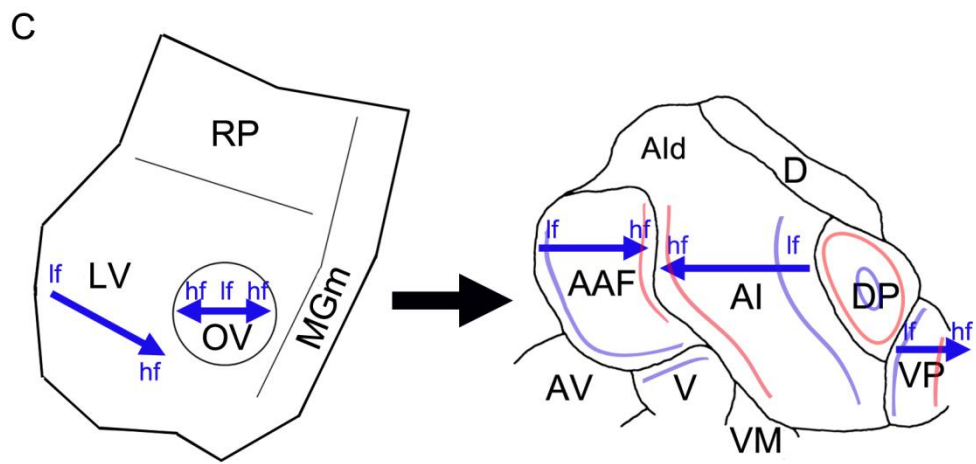
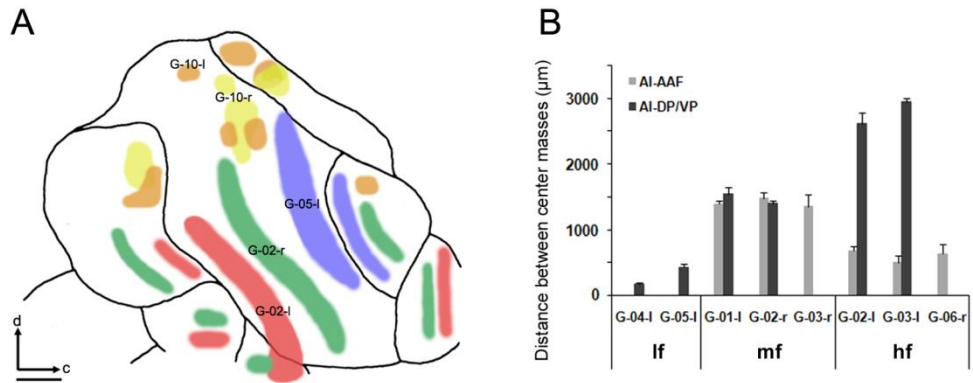


Figure 3.4 (preceding page): Topography of TC connections of MGv. **(A)** Map of cortical bouton distribution in a standardized auditory cortex (see also Fig. 1A) for selected injection cases into LV, OV, and RP (see also Fig. 3, Tab. 1). Note that the location of the cortical bouton distribution matches the topographic frequency-representation within the auditory cortical fields and the (measured or assumed) response properties of the injected thalamic neurons. Scale bar: 500 μm . **(B)** Distances between the centers of mass of boutons in cortical layer IV of fields AI, AAF, and DP, respectively, for selected injection cases into lf, mf, and hf regions of LV and OV. Note that consistent with the mirror-imaged tonotopy of these auditory cortical fields, distances between labeling in AI and DP/VP are shortest in lf and longest in hf injection cases; the trend is opposite for center-to-center distances between AI and AAF. Values are means (3 slices per case) \pm standard deviation (SD). **(C-D)** Summary diagrams about the topography of the cortical projections of the MGv to the AC in the Mongolian gerbil. Frequency-selective neurons of LV and OV project in a frequency-specific (tonotopic) manner to the tonotopically organized auditory cortical fields AI, AAF, and DP/VP **(C)**. Neurons of the RP, however, respond to a wide range of frequencies and project non-tonotopically to the AC. A rostro-caudal gradient of injection sites within the MGv corresponds to a dorsoventral gradient of preferential thalamic inputs across the AC **(D)**.

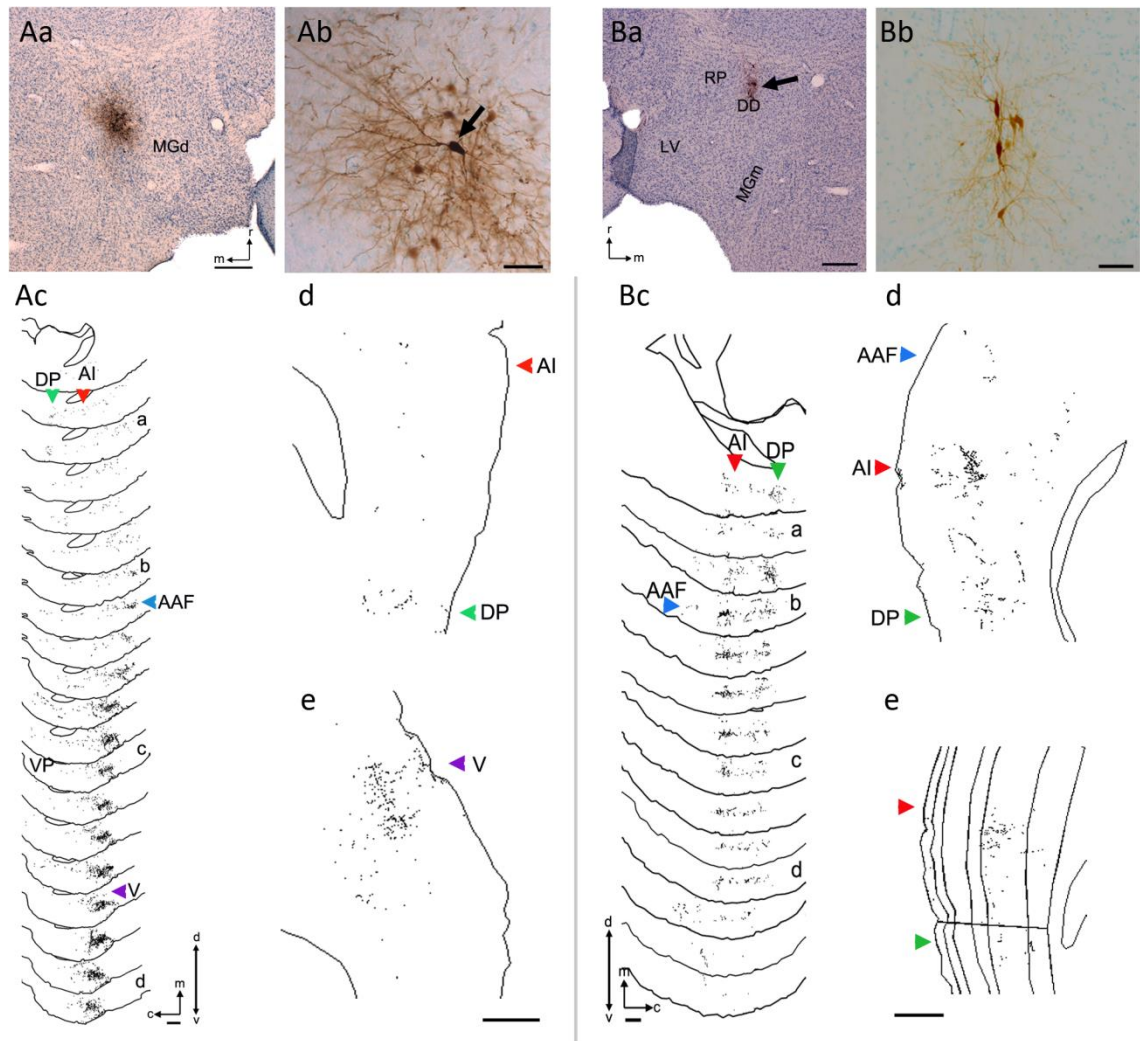
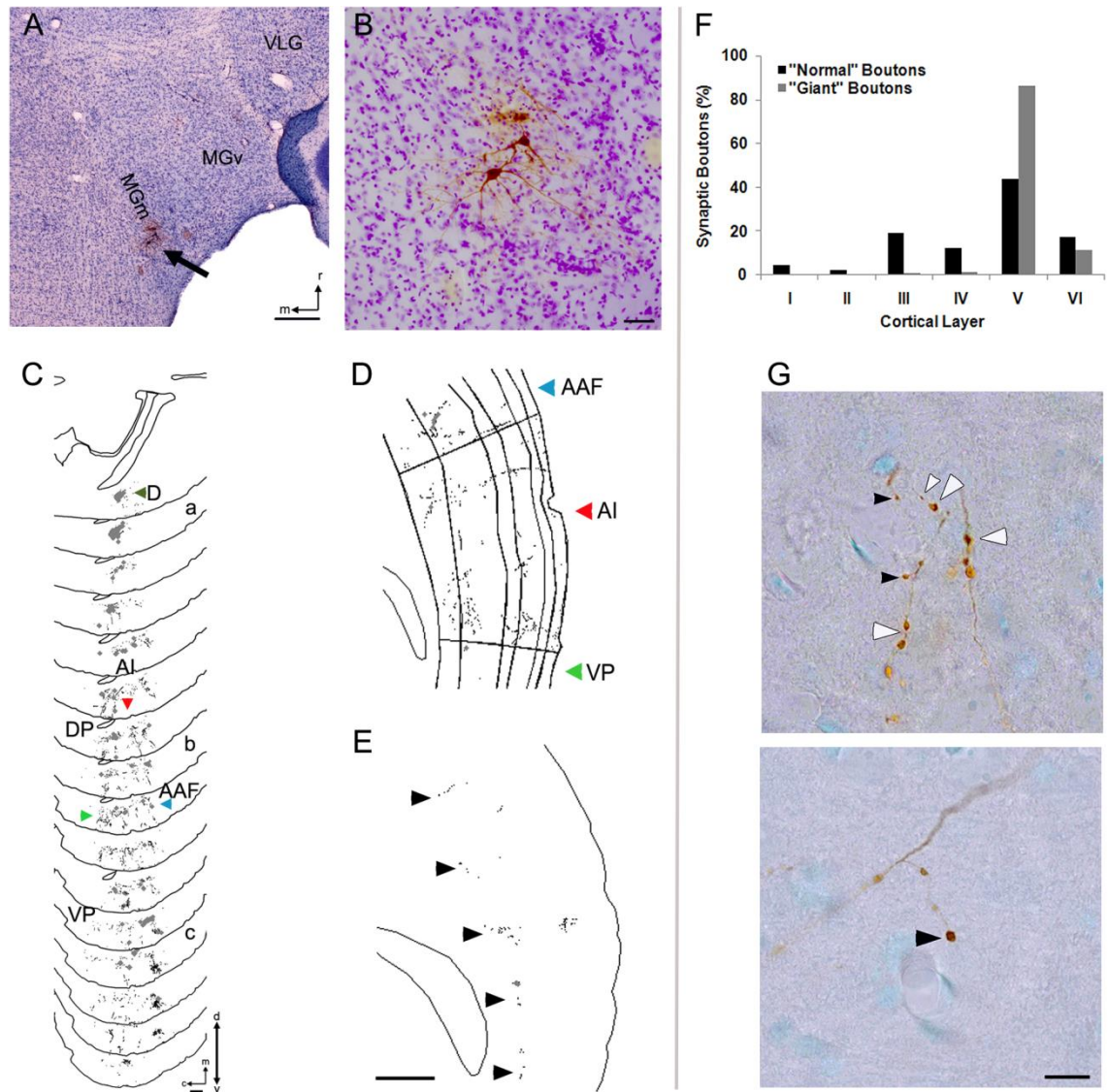


Figure 3.5: Results of iontophoretic injections into the MGd (MGd *proper* case G-12-r, DD case case G-14-l). **(Aa)** Nissl-counterstained section showing the iontophoretic injection site in the medio-rostral part of MGd. **(Ab)** Methyl green-counterstained section showing a principal tufted neuron of the MGd-proper (arrow), surrounded by several radiate neurons, juxtacellularly labeled at the injection site. **(Ac)** Montage of the right hemisphere from *NeuroLucida*-reconstructed hemisections illustrating the labeling in AI, AAF, DP/VP, and V. **(Ad-e)** Samples of reconstructed sections showing the areal and laminar distribution of TC terminals in the different auditory fields. **(Ba)** Injection site in the rostral part of DD. **(Bb)** Principal bitufted neurons of the DD. **(Bc)** Montage of the left hemisphere from reconstructed hemisections illustrating the labeling in AI, AAF, and DP/VP. **(Bd-e)** Samples of reconstructed sections showing the distribution of TC terminals. The majority of labeled synaptic boutons identified in layer V were located in sublayer Va. Orientation in Aa applies to panels Ab-e, orientation in Ba applies to panels Bb-e. Scale bars: 50 μm (Ab, Bb), 300 μm (Aa, Ba), 500 μm (Ac-e, Bc-e). All other conventions as in Fig. 3.4.



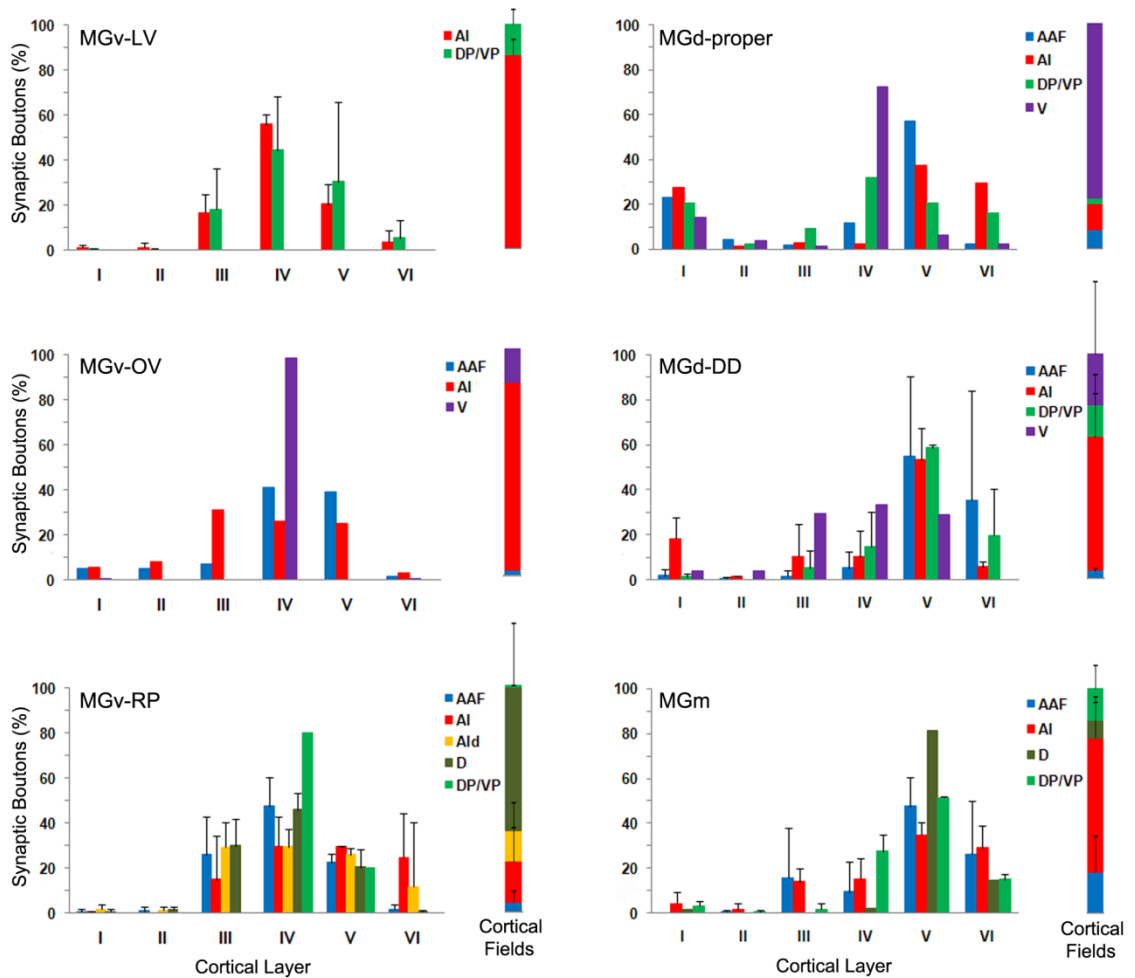


Figure 3.7: Quantitative analysis of the field specific laminar distribution of TC terminals in the AC of the Mongolian gerbil following iontophoretic injections of biocytin into the MGB, illustrated for each thalamic subdivision ($n_{LV}=2$, $n_{OV}=1$, $n_{RP}=5$, $n_{MGdproper}=1$, $n_{DD}=2$, $n_{MGm}=2$).

In each of the targeted auditory fields, values sum up to 100%. Mean values are given ± 1 SD. On the right-hand side of each diagram, the field-specific input ratio of the respective thalamic subdivision into the AC as derived from the counted numbers of boutons (mean ± 1 SD) is provided.

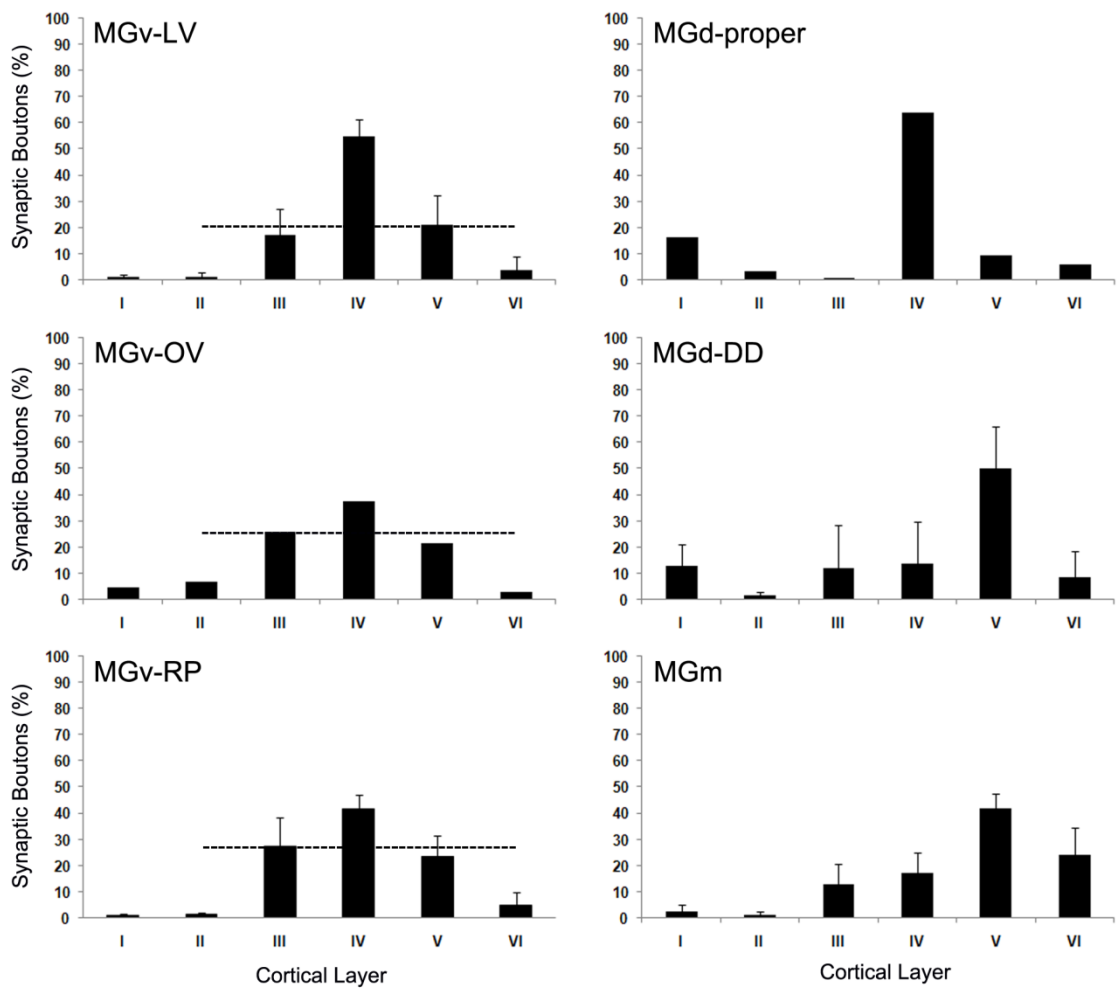


Figure 3.8: Quantitative summary of the overall laminar distribution of TC terminals in the AC of the Mongolian gerbil following iontophoretic injections of biocytin into the MGB, illustrated for each thalamic subdivision ($n_{LV}=2$, $n_{OV}=1$, $n_{RP}=5$, $n_{Mgdproper}=1$, $n_{DD}=2$, $n_{MGm}=2$).

Dashed lines in the left-hand diagrams illustrate the different percentages of MGv-LV, -OV and -RP projections to layer III and V. In DD, the majority of labeled synaptic boutons identified in layer V were located in sublayer Va. In MGm, boutons were mainly located in sublayer Vb. Mean values are given ± 1 SD.

3.1.6 Tables

Table 3.1: Experimental animals¹

Case	Hemi-sphere	MGB subdivision	Number of labeled neurons	Physiological properties (frequency tuning; onset latency)
G-04-l	left	MGv-LV (lateral)	88	BF 0.5 kHz 30 ms
G-05-l	left	MGv-LV (laterorostral)	50	BF 0.5 kHz 12 ms
G-06-r	right	MGv-OV (medial periphery)	73	BF 16 kHz; 13 ms
G-08-l	left	MGv-RP (caudal)	10	BF around 1 kHz 8 ms
G-09-l	left	MGv-RP (center)	93	broad; 15 ms
G-09-r	right	MGv-RP (lateral)	86	broad; 15-20 ms
G-10-l	left	MGv-RP (center)	60	broad; 10-18 ms
G-10-r	right	MGv-RP (center/caudal)	68	broad; 10-12 ms
G-12-r	right	MGd (mediorostral)	120	broad, weak; 25-50 ms
G-13-r	right	MGd-DD (caudal)	37	0.25-1 kHz and 16kHz; 14-20 ms
G-14-l	left	MGd-DD (rostral)	13	broad; 9-15 ms
G-15-r	right	MGm (caudal)	22	0.25-2 kHz; 7-10 ms
G-16-r	right	MGm (caudal)	46	0.25-2 kHz; 7-10 ms

¹Case number, hemispheric side, and exact location of biocytin injections into the subdivisions of the MGB as well as the numbers of the labeled cells at the injection sites and their electrophysiological properties, respectively, listed for each of the 11 experimental animals.

3.2 Ultrastructural characterization of thalamocortical “giant” and “normal” sized boutons from MGm

During the anterograde light microscopic labeling studies (described above) we detected so far unknown large synaptic terminals arising from MGm. Here we analyzed their ultrastructure in order to get some information about their possible role. To this aim, we performed additional injections of biocytin into MGm, processed the slices according to a pre-embedding protocol for electron microscopy (see Riedel *et al.*, 2013, methods, and appendix), and then analyzed the labeled boutons qualitatively and quantitatively, and also compared them with non-labeled cortical boutons of unknown origin.

From a total of four MGm injections (2 processed for light microscopy, 2 processed for electron microscopy) all displayed giant boutons in the deep layers of the AC, suggesting that these terminals represent a common feature of MGm projections. The electron microscopic results presented below are derived from one animal, because it delivered the best results in terms of conserved ultrastructure and contrast.

3.2.1 Qualitative analysis

As giant boutons comprise only a small fraction of MGm boutons, we found also many small and medium-sized (“normal”) labeled boutons. Figure 3.9 A provides a direct comparison of their ultrastructure including their relative sizes and forms. Giant boutons (labeled with a G) were obviously larger than the other, i.e., labeled normal (N) and non-labeled (exemplarily labeled by green asterisks) boutons located in infragranular layers of AI. Further, giant boutons appeared rather elongated than round.

In the bottom of the same figure, further photographs of a giant bouton *terminaux* (Fig 3.9 B), a giant bouton *en passant* (Fig. 3.9 C), and a normal bouton (Fig 3.9 D) are shown. In most cases, synaptic contacts were made on dendritic spines (blue asterisks), and many boutons had multiple contacts with the same or different spines. A very few synapses terminated on dendritic shafts (Fig. 3.10 D), but we did not observe contacts with somata; they were spared out even if the terminal touched on a soma (Fig 3.9 B). We further noted that the mitochondrial fraction (see methods) was higher in labeled than in non-labeled boutons (green stars in Fig. 3.9). For quantitative validation of these

observations (i.e. differences in bouton size and mitochondrial fractions between labeled and non-labeled boutons) see 3.2.2 and Figure 3.11.

Both giant and normal sized labeled boutons (Fig. 3.10 A, B) formed asymmetric synaptic contacts. However, we could not always make a clear assignment to one of the synaptic types according to the commonly used classification of Gray (i.e., type I, asymmetric, glutamatergic/excitatory; type II, symmetric, GABAergic/inhibitory) (Gray, 1959).

Vesicles were mainly small (about 30 nm in diameter), clear, and round. Some terminals from MGm, however, additionally contained larger electron-lucent (occasionally slightly oval) vesicles (50-100 nm in diameter) (Fig. 3.10 C).

3.2.2 Quantitative analysis

We quantified bouton areas and perimeters, mitochondrial and synaptic fractions (see 2.3.7) as well as the number of synaptic contacts and tested then for differences between and within the labeled and non-labeled groups of boutons.

Based on Hartigan's dip test for unimodality (Hartigan & Hartigan, 1985), none of the evaluated properties (bouton area, mitochondrial, and synaptic fraction) displayed a bi- or multimodal distribution in the labeled group of boutons (Fig. 3.11 A). The same was true for the non-labeled boutons, except for their synaptic fraction, which was bimodal (tested by one-dimensional kmeans clustering using the mean silhouette value to determine whether 2 or more clusters fit best) (Fig. 3.11 A, mean of the centroids (0.082) is indicated by an arrow). Hence, both the labeled and the non-labeled boutons form mostly uniform (within-group) populations, implicating that no clear-cut distinction can be made between normal (small) and giant sized subpopulations of labeled boutons (based on their size and/or the other features investigated so far). However, as expected from the qualitative analysis, the distinctive intergroup distributions indicate that the labeled and non-labeled boutons differ with respect to areal size and mitochondrial fraction and therefore belong to distinguishable populations of boutons (Fig. 3.11 C).

Cross-section areas of labeled boutons varied from 0.310 to 5.228 μm^2 in a rather continuous fashion, which is in accord to the results from the dip test and histogram, whereas the areas and their range were much smaller in the non-

labeled population of boutons from infragranular layers of AI (0.091-0.805 μm^2 (Fig. 3.11 A, C, D). Statistical analysis (t-test assuming unequal variances) of labeled and cortical non-labeled boutons indeed revealed that the former were significantly larger than the latter (labeled mean area \pm 1 SD: $1.636 \pm 1.102 \mu\text{m}^2$, non-labeled: $0.302 \pm 0.149 \mu\text{m}^2$, $p < 0.001$, Fig 3.11 B).

The labeled and non-labeled boutons had average mitochondrial fractions of 0.266 ± 0.094 and 0.032 ± 0.063 , and average synaptic fractions of 0.089 ± 0.049 and 0.080 ± 0.070 , respectively (Fig. 3.11 B). Statistically, the effect of group (independent variable) on either mitochondrial or synaptic fractions or synaptic numbers (dependent variable) was tested using an ANCOVA to account for possible influence of the bouton size (area or perimeter; covariate) on the outcome. As the assumption of homogenous regression coefficients (slopes), which indicates that no interaction exists between the categorical (groups: labeled vs. non-labeled) and continuous (bouton areas) predictors, was not satisfied, we analyzed only those boutons whose cross-section area was between the minimum areal size of labeled boutons and the maximum size of non-labeled boutons. This procedure appeared justifiable, since the positive correlation between mitochondrial fraction and areal size in the non-labeled group (Fig 3.11 D left) may be an “artifact” of the general very small size of the non-labeled boutons favoring the lack of mitochondria, and because we expect the linearity to be limited as otherwise the fractions would rapidly exceed 100%. By doing so, there was no significant interaction (bouton area x mitochondrial fraction) anymore, but still a significant main effect, showing that (at least within the defined areal range) labeled boutons from MGm have a higher mitochondrial fraction independently of their size (Tab. 3.2), which underpins our qualitative observations. Synaptic fractions and numbers of synaptic contacts did not differ across groups following adjustment for covariates (Tab. 3.3).

Considering the whole areal range again, the number of synaptic contacts increased with the perimeter ($r = 0.585$, $p = <0.001$) and area ($r = 0.494$, $p = <0.001$) of labeled boutons (Fig 3.11 D right), and was in average higher in labeled than in non-labeled boutons (labeled mean \pm 1 SD: 1.948 ± 1.248 , non-labeled: 0.724 ± 0.586 , $p = <0.001$). However, as aforesaid, no differences were present when taking their sizes (as covariate) into account (Tab. 3.2).

3.2.3 Summary of the ultrastructure of MGm boutons

Qualitative and quantitative ultrastructural analyses revealed that boutons arising from MGm can reach much larger sizes than other, non-labeled cortical boutons. Also the average area of labeled cortical boutons was larger than that of non-labeled terminals, as was their mitochondrial fraction. The synaptic fractions did not differ between labeled and non-labeled boutons. The labeled boutons originating from MGm neurons represent a population of boutons that was fairly homogeneous respecting ultrastructural characteristics such as mitochondrial and synaptic fractions, type of synaptic contacts (asymmetric), and postsynaptic target (dendritic spines). In contrast, they were very heterogeneous in size, but nevertheless uniformly distributed. Thus, based on the characteristics investigated so far, “normal” and “giant” labeled boutons did not belong to clearly distinguishable subpopulations of terminals.

3.2.4 Figures

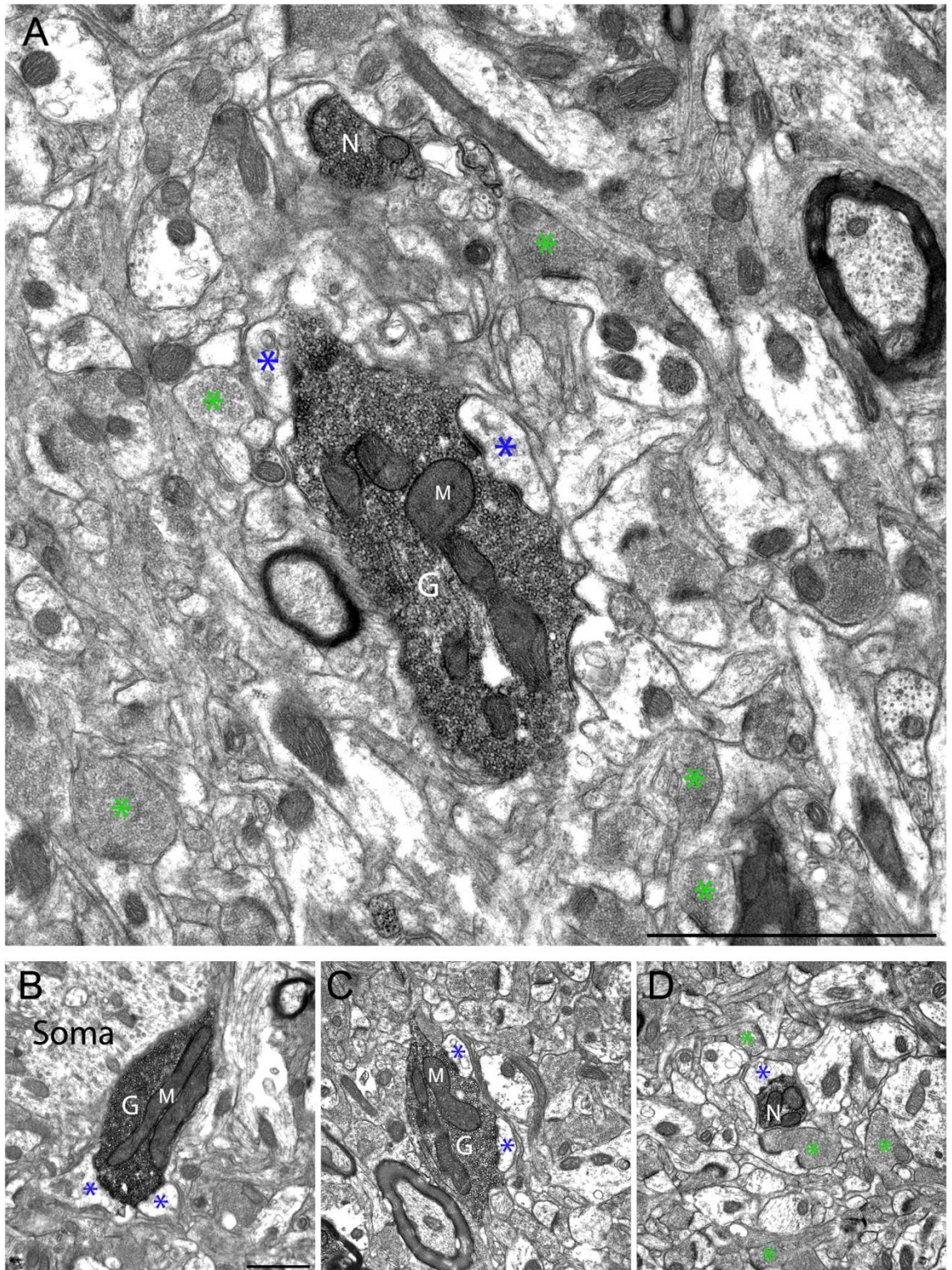


Figure 3.9 (preceding page): TEM photographs. **(A)** Direct comparison between labeled giant (G, area $5.22 \mu\text{m}^2$), labeled normal/small (N, area $0.53 \mu\text{m}^2$) and surrounding non-labeled boutons (exemplarily labeled by green stars). **(B)** Giant bouton *terminaux* (area $3.34 \mu\text{m}^2$) **(C)** Giant bouton *en passant* (area $2.76 \mu\text{m}^2$). **(D)** Small bouton (area $0.54 \mu\text{m}^2$). Note that synaptic contacts were made on dendritic spines (blue asterisks) but not on somata (as seen in **B**), and that the mitochondrial (M) fraction was higher in labeled than in non-labeled boutons (exemplarily marked by green asterisks in **C**, quantitative validation see Fig. 3.11 and Tab. 3.2). Images taken at 12000 x (A) and at 20000 x (B) magnification. Scale bars: $2.5 \mu\text{m}$ (A), $1 \mu\text{m}$ (B), scalebar in (B) also applies to (C) and (D).

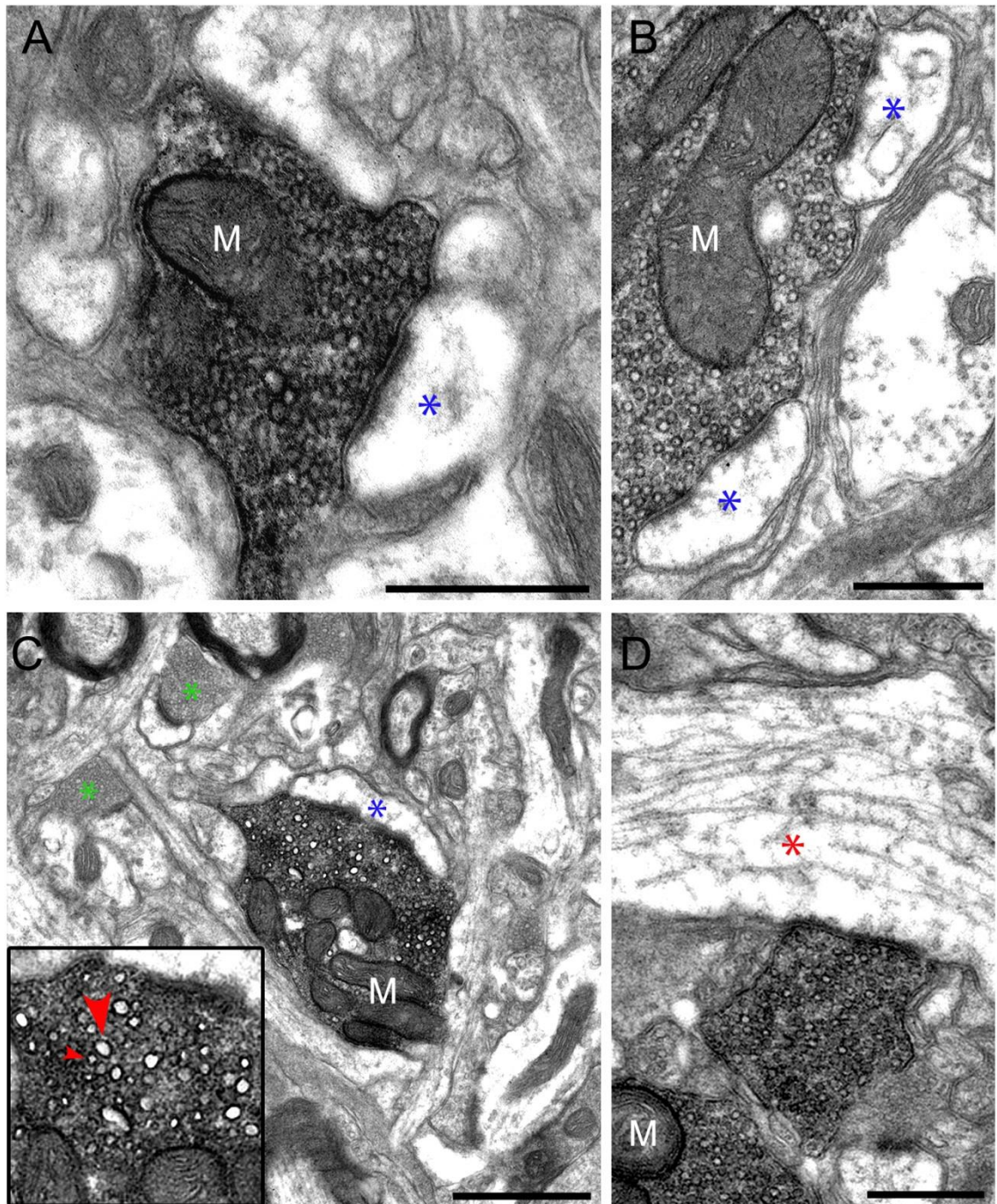


Figure 3.10: TEM photographs. Both the normal **(A)** and giant **(B)** boutons formed asymmetric, probably glutamatergic, synaptic contacts. **(C)** Some terminals from MGm contained large clear round or oval vesicles (large red arrowhead, ~60 nm diameter), in addition to small (small red arrowhead, ~25 nm diameter) round vesicles. **(D)** A very few labeled boutons targeted dendritic shafts (red asterisk). Photographs were taken at 20000 x (B-D) and 50000 x (A) magnification. Scale bars: 1 μm (C), 0.5 μm (A, B, D). All other conventions as in Figure 3.9.

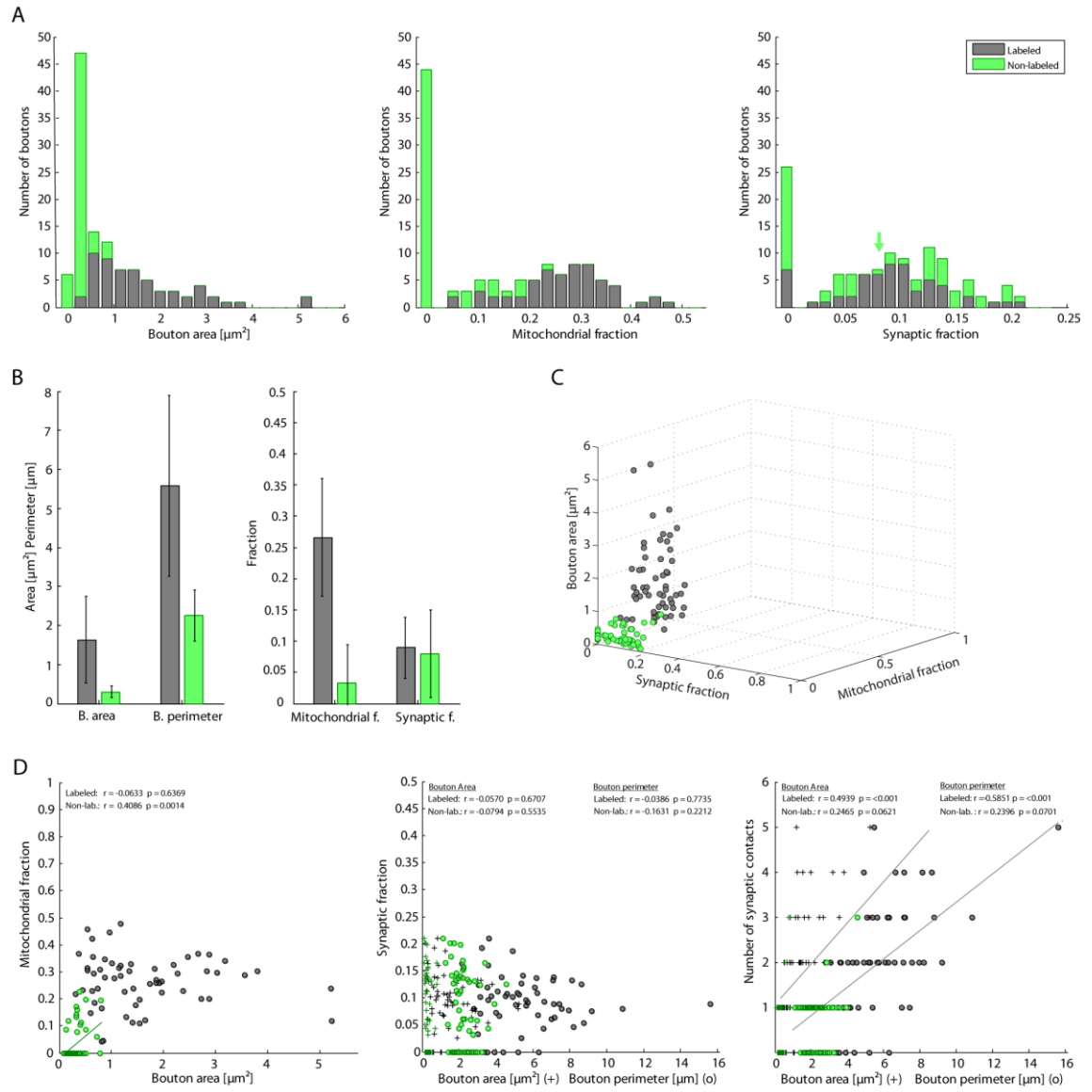


Figure 3.11: Quantitative analysis of labeled ($n=58$; grey) and non-labeled ($n=58$; green) boutons. **(A)** Histograms showing distributions of bouton areas, mitochondrial fractions, and synaptic fractions of both labeled and non-labeled boutons. All distributions were unimodal, with the exception of the synaptic fraction of the non-labeled boutons, which was bimodally distributed. The mean between the both centroids was 0.0820 (green arrow). The histograms also suggest differences regarding size and mitochondrial fractions between the groups. **(B)** Comparison of boutons size, mitochondrial, and synaptic fractions between both groups (values are means \pm 1 SD). Labeled boutons were larger ($p = <0.001$; two sample t-test assuming unequal variances) and had higher mitochondrial fractions than non-labeled boutons. For statistical analysis of mitochondria and synapses, an ANCOVA for the overlapping areal range was used (see Tab.3.2). **(C)** 3D plot indicating that labeled and non-labeled boutons represent different populations, but do not comprise various subpopulations. **(D)** Correlation analyses between mitochondrial fraction, synaptic fraction or number, and bouton sizes. The mitochondrial fraction increased in the non-labeled, but not in the labeled boutons. The number of synaptic contacts grew significantly with bouton size in the labeled boutons, while the synaptic fraction remained constant.

3.2.5 Tables

Table 3.2: ANCOVA¹

Dependent variable	Source	F	p	Group mean diff. of adj. dep. var.
Mitochondrial fraction	Group	45.476	<0.001	0.216 ± 0.032
		4.924	0.033	
	Bouton area	0.149	0.702	
		0.041	0.841	
	Group x B. area	0.178	0.676	
Synaptic fraction	Group	0.264	0.611	0.012 ± 0.023
		0.480	0.493	
	Bouton area	1,358	0.252	
		0.748	0.393	
	Group x B. area	0.332	0.568	
Synaptic fraction	Group	0.756	0.391	0.019 ± 0.022
		0.140	0.710	
	B. perimeter	0.544	0.466	
		0.452	0.506	
	Group x B. perimeter	0.045	0.834	
Synaptic number	Group	0.150	0.701	0.093 ± 0.240
		0.382	0.541	
	B. perimeter	7.918	0.008	
		6.884	0.013	
	Group x B. perimeter	0.307	0.583	
Synaptic number	Group	0.009	0.923	0.026 ± 0.263
		0.117	0.735	
	Bouton area	5.739	0.022	
		4.339	0.045	
	Group x B. area	0.108	0.745	

¹ANCOVA to test for group differences respecting mitochondrial fraction, synaptic fraction, and synaptic number with bouton size (area or perimeter) as covariate. To meet the assumption of homogeneity of regression coefficients (slopes), only the boutons within the overlapping areal range [i.e., between the smallest labeled bouton (0.310 μm^2) and the largest non-labeled bouton (0.805 μm^2)] were analyzed. Within the defined range, mitochondrial fraction was significantly higher in labeled than in non-labeled boutons. The groups did not differ in synaptic fraction or number. The rightmost column depicts the differences between means (labeled boutons – non-labeled boutons) of the adjusted dependent variables (the means are shown in Tab. 3.3). Levene's test results were n.s. ($p > 0.01$) indicating that the assumption of equality of error variances across groups was not violated. Values obtained from statistical models including the interaction term ($p > 0.05$ indicates homogeneity of slopes) are depicted in blue, values calculated without the interaction term in black.

Table 3.3: Unadjusted and adjusted means of mitochondria and synapses²

Dep. Var.	Covariate	Group	Unadj. mean \pm SD	Adj. mean \pm SD
Mito. frac.	Bout. area	Labeled	0.291 \pm 0.089	0.288 \pm 0.024
		Non-labeled	0.069 \pm 0.080	0.072 \pm 0.018
Syn. frac.	Bout. area	Labeled	0.087 \pm 0.061	0.079 \pm 0.018
		Non-labeled	0.062 \pm 0.062	0.067 \pm 0.013
Syn. frac.	Bout. peri.	Labeled	0.087 \pm 0.061	0.084 \pm 0.017
		Non-labeled	0.062 \pm 0.062	0.064 \pm 0.013
Syn. num	Bout. area	Labeled	1.071 \pm 0.730	0.885 \pm 0.200
		Non-labeled	0.750 \pm 0.737	0.859 \pm 0.148
Syn. num	Bout. peri.	Labeled	1.071 \pm 0.730	0.927 \pm 0.187
		Non-labeled	0.750 \pm 0.737	0.834 \pm 0.141

²Unadjusted and adjusted means of mitochondrial fractions, synaptic fractions and numbers after ANCOVA with boutons size as covariate. For further explanations and conventions see Table 3.2.

3.3 Change of cortical current source density patterns by selective apoptosis of auditory corticothalamic feedback projections

In this section, the electrophysiological consequences of lesioning the CT connections were investigated by CSD analysis following acoustic and electrical stimulation. This was done before and after cortical silencing with muscimol to dissociate the TC from polysynaptic intracortical inputs.

3.3.1 Control experiments

Injections of physiological saline plus laser treatment to show the general harmlessness of the laser as well as tracer injections without laser treatment to exclude that possible measured effects are due to alterations of the injection site, were conducted in the course of behavioral experiments which are not part of this work (Saldeitis *et al.*, 2013). In the experiments described here, cortical CSD patterns of animals that had no or only weak CT cell loss, but were likewise exposed to the laser, served to prove that the laser illumination did not unspecifically interfere with cortical physiology. In addition, (using 3 test animals not listed here) we tested the responsiveness of thalamic neurons near the injection site, determined the most suitable stain for histological quantification of neuronal loss, and confirmed the specificity of the photolytic apoptosis, as described in the following.

NeuN stain provides a suitable histological assay to quantify lesion efficacy

To prove the efficacy and specificity of the laser apoptosis, we tested three immunohistochemical stains, namely antibodies against Neuronal nuclei (NeuN), SMI-32, and active Caspase 3 (Casp3). For this we always compared the lesioned cortical side with the non-lesioned side.

NeuN is a neuron-specific DNA-binding nuclear protein in vertebrates, and thus, we could determine cortical cell loss by a reduction of staining density of labeled somata in the correspondent, i.e., infragranular layers. In addition, it was appropriate to verify the overall integrity of cortical tissue (Fig. 3.12 A). Antibodies against NeuN allowed us to easily quantify the lesion efficacy,

because stained somata were clearly distinguishable against the background (neuropil), and were therefore chosen for this purpose.

Antibodies that recognize a nonphosphorylated epitope of neurofilament H (SMI-32) (used by Bajo *et al.* (2010)) visualize neurons, preferentially pyramidal neurons (Ouda *et al.*, 2012), in a Golgi-like manner (neuronal cell bodies, dendrites and some thick axons in the central and peripheral nervous systems). This marker showed a reduction of staining in the infragranular layers of the lesioned vs. the non-lesioned side (Fig. 3.12 B), but quantification was difficult due to staining of fine neuronal processes.

Caspase 3 is a key enzyme involved in the apoptotic cascade. Casp3 stain, however, provides a snapshot in time during the ongoing process of degeneration by capturing only a subset of apoptotic cells rather than displaying the total number of dead cells. Thus, staining would be strongest at timepoints shortly after laser illumination. This staining method revealed no significant visible differences in staining intensity between lesioned and non-lesioned cortical side (Fig. 3.12 C), suggesting that Casp3 activity had again reached background levels by the time of sacrifice. Hence, Casp3 was inappropriate because we had the aim to perform the recordings at a timepoint with as many as possible cells degenerated.

The photolytic apoptosis specifically eliminates targeted neurons

To assure the specificity of the method we had to show that the tracer is being retrogradely transported (red fluorescent label in infragranular layers), that the photolytic component has been successfully attached to the beads, and that it is activated upon illumination, which should become evident through cell degeneration after laser exposure (reduction of cells as seen in NeuN stains) and bleaching of the fluorescent beads.

Non-labeled cells (in other layers and in the same layers outside the labeled region) provide controls for laser exposure alone and should not be affected by laser illumination. Likewise, cells that incorporated the tracer but were not exposed to the laser should be preserved. This was demonstrated by comparing fluorescent slices with NeuN-stained slices in a complementary way. On the left side of Figure 3.13, the fluorescent patterns of retrogradely labeled cells are shown in the example of two animals. On the right, corresponding NeuN stained slices exhibit different strengths of apoptosis (lighter regions in

layer VI). Note that regions with lesion effects (labeled by a 1) show no or weak corresponding fluorescent labeling, indicating that the tracer underwent photolytic bleaching. Areas showing neither reduction of cell density nor fluorescent labeling (2) indicate that no (or only a small fraction of) cells have been retrogradely labeled. On the other hand, areas with high cell density and simultaneous fluorescent labeling (3) suggest that no photolysis has occurred, because this region (which in this example corresponds to AAF) was outside the beam spot, whereas remaining retrograde labeling along with neuronal cell loss points to incomplete bleaching (4). Also note that the electrodes were well placed within the lesion regions (arrow).

Thalamic neurons near the injection site still respond to pure tones

To make sure that the conjugated beads do not interfere with the activity of nearby thalamic neurons and that they are still responsive after laser exposure, we recorded from thalamic neurons following acoustic stimulation. The tungsten electrode used for these recordings were dipped into a solution containing the tracer Fast Blue (to label the recording sites). This enabled us to histologically determine the distance between recording (identifiable by Fast Blue) and injection sites (chlorin e₆ conjugated retrobeads). Figure 3.14 shows that neurons adjacent to (i.e., medially and laterally of) the injection site (Fig. 3.14 C) respond tonotopically to pure tones (44 db SPL, 10 repetitions) (Fig. 3.14 B). In the AC, layer VI of mid frequency regions of the ipsilateral AI is less densely stained than layer VI of border regions of AI as well as of AAF and DP/VP (Fig. 3.14 D). Thus, in animals with successfully eliminated CT projections nearby thalamic (MGv) neurons are still responsive and still respond tonotopically. Very large injection volumina, however, led to thalamic necrosis and loss of neuronal responsiveness.

3.3.2 Laminar origin of the auditory CT connections in Mongolian gerbils

The laminar origins of auditory corticothalamic cells in gerbils were layer VI, and to a lesser extend, layer V. This was shown by retrograde labeling with the fluorescent beads (as well as by the layer-specific lesions effects). Labeling in Layer VI was particularly strong after injections into MGv (Fig. 3.15 A), while labeling or apoptosis in layer V (of AI and AAF) was observed especially if terminals in MGd or MGm (Fig. 3.15 B) incorporated the tracer, but some layer

V cells were also labeled after pure MGv injections (Fig. 3.15 Ab). In the posterior fields, prominent labeling in layer V was frequently seen following tracer deposits into any of the MGB divisions (Fig. 3.15 Ac, Bc).

Due to the well intracellular distribution of the beads, many cells could be identified as pyramidal neurons by their characteristic shape including the basal and apical dendrites (Fig. 3.15 C).

The topography of projections from AI to MGv was largely tonotopic but appeared to be more divergent and convergent than the TC projections, as large MGB injections labeled and/or resulted in photolytic apoptosis of cortical neurons across the entire frequency gradient, and even confined injections were associated with considerable labeling or neuronal loss across the cortical representation of several octaves.

Finally, thalamic neurons did not only receive (direct) descending projections from the cortex, but also from the reticular thalamic nucleus (Rt, Fig. 3.15 D).

3.3.3 Histological quantification of laser-induced neuronal loss in the animals used for CSD analysis

To assess potential relationships between lesion strengths of CT connections and their possible electrophysiological consequences it was necessary to verify the thalamic injection sites (see Tab. 3.5) and to measure the reduction of cell density or numbers in infragranular layers of AI. Images of brain slices stained for NeuN were used to determine the lesion efficacy, the contralateral side serving as the interindividual reference. Moderate to strong neuronal loss, as frequently present in layer VI, was already clearly visible by eye (Fig. 3.16 A-B), whereas the rather weak lesions in layer V (Fig. 3.16 B) were less obvious. Thus, a quantification of neuronal cell loss in layers V and VI was performed by determining the percentual area occupied by neurons in both the ipsi- and the contralateral AI (Fig. 3.16 A and B, lower row), and a subsequent calculation of their ratio. Figure 3.16 C depicts the lesion strengths of each experimental animal. Positive values represent neuronal loss, while negative values indicate that more cells were found ipsilaterally than contralaterally. However, this apparent gain most likely corresponds to a natural variability and/or to staining differences. We attributed the animals to different lesion groups (non- or weakly lesioned (nwLes), layer V lesioned (LesV), layer VI lesioned (LesVI), layer V

plus layer VI lesioned (LesV+VI) (for definition see Tab. 3.4). The lesion strengths in layer V and VI did not correlate (Fig. 3.16 D), indicating that layer V lesions did not result from unspecific lesion of non-labeled cells induced by the laser light (and that there may be independent connections).

3.3.4 Acoustic stimulation

CSD profiles

Acoustic stimulation with pure tones evoked a canonical cross-laminar activation pattern seen in prior studies using gerbils (Happel *et al.*, 2010, Happel *et al.*, 2014) in most of the animals, irrespective of their lesion level (Fig 3.17 A). In detail, a short latent (early) prominent granular sink (referred to as S1) was followed by several sinks in supra- (S2) and infragranular (S3 and S4) layers. In agreement with the above cited studies, an early sink in deep infragranular layers (Vb/VI) could also be observed repetitively (referred to as iS1). After pharmacological blocking of intracortical activity, chiefly the early sinks in the main recipient TC layers remained present (but were reduced in amplitudes), while the later sinks and sources were largely abolished (Fig. 3.17 A, lower panels). As expected due to blocking of recurrent excitatory activity (Happel *et al.*, 2010) muscimol led to general reduction of S1 amplitudes (mean reduction of PAs: 78.68% ($21.32 \pm 8.87\%$ of the pre-value); see also the results from repeated measures ANOVA, Tab. 3.6), and its effect was independent of lesion strength (Spearman's rho = -0.3297, $p = 0.2715$ (for lesion in layer VI); see also Tab. 3.6). The late (S2, S3, S4), albeit weak extragranular sinks and sources after the initial source-sink-source triplet during the silenced condition reflect repolarization currents being observable because they are not superimposed by other CSD components attributable to active intracortical processes during later time points after stimulus onset. Figure 3.17 A represents the means of CSD profiles of the groups defined according to their lesion levels (nwLes: $n=3$; LesVI: $n=4$; LesV+VI: $n=5$) at BF. The three averaged profiles as well as the individual CSD profiles of animals with pure layer V lesions (see appendix, Fig. J.2) look similar in their general activation patterns. However, iS1 appeared to be strongest in non/weakly lesioned animals, both before and after cortical silencing.

A significant rank (Spearman) and linear (Pearson) correlation between lesion strength in layer VI and the integral (INT) of iS1 confirmed the above described observation that this sink is stronger in weakly than in strongly lesioned animals (Fig. 3.19). After application of muscimol, the INT was not significant anymore, but instead the peak amplitude (PA). In addition, the peak latency (PL) became tendentially shorter with increasing lesion efficacy in layer VI before silencing. The integrals of S1 were also stronger in animals with lesions in layer VI before, but not after cortical silencing (Fig. 3.18). At nonBF (two octaves distant from BF), there were no significant relationships neither (not illustrated). The strength of lesion in layer V did not influence any of the parameters (PL, PA, INT) of S1 at BF and nonBF (not illustrated).

Possible influences of the lesions on later intracortical processing were investigated by analyzing the relative strengths (PA, INT) of the extragranular sinks S2 and S3 compared to granular sink S1 (i.e., PAs and INTs of S2 and S3, respectively, divided by PA and INT of S1). While the relative contributions of the later extragranular components were generally higher at nonBF than at BF (and largely independent of lesion strength), at BF they increased with increasing cell loss in layer VI (Fig. 3.20).

We then asked whether the elimination of CT neurons affects the sharpness of frequency tuning. To this aim, the relationships between the BF/nonBF ratios of the different parameters and the respective lesion strengths were analyzed. Latencies (OL, PL) did not change with lesion strength. For both INTs and PAs of S1, however, this approach delivered a strong (negative) correlation with lesion strength in layer VI (Fig. 3.22 A 1st row, and Fig. 3.21, right column, 1st and 3rd row, lesion strength is indicated by color), i.e., the frequency tuning was less sharp in animals with stronger apoptosis in layer VI. After application of muscimol, the relationships were less tight (n.s.) (Fig. 3.22 A, 2nd row, and Fig. 3.21, right column, 2nd and 4th row). However, there was no effect towards the direction of change, as ratios decreased, increased, or remained the same (Fig. 3.22 B). The narrower bandwidth during the silenced condition also entailed very high BF/nonBF ratios. Representative examples of CSD profiles at BF and nonBF are shown in Figure 3.23 (to visualize the less reduced nonBF response in strongly lesioned animals compared to weakly lesioned animals). Respecting iS1 the influence of the lesion on the frequency tuning did not reach significance

(not shown; Spearman's rho: -0.4011, $p = 0.1758$). The sharpness of frequency tuning of the other sinks did not correlate with lesion strength in layer VI, as was the case for all sinks if lesion strength in layer V was used as predictor (Fig. 3.21, left column). Notably, the influence of layer VI on the frequency tuning appeared first at 2 octaves away from BF. Compared to the nearBF/BF ratio, where the values were still close together and distributed irrespective of their lesion level, the BF/nonBF ratios dispersed and ranked among the values according to their lesion efficacy (ordered color-coded values in Fig 3.21, right column).

AVRECs

The time course of the AVREC curves, which reflect the overall activation strength, was characterized by a first steep rise and subsequent fall, which correspond to the TC onset response (peak at approx. 30 ms, similar to the PL of the granular sink). The first high peak was followed by long latent elevations, which were smaller in amplitude and correspond to the late sinks and sources (produced by intracortical activity). This general form of the curves was very similar across all animal groups (Figs. 3.17 B and 3.24). Animals with (additional) lesions in layer V tended to have a more pronounced intermediate activation (about 40-90 ms after stimulus onset), which sometimes appeared as a plateau (see also Fig. 3.24, rightmost panel) and probably reflects a longer S1 and supragranular source (So1). After blocking intracortical activity only the first peak remained present, but its amplitude was reduced (Tab. 3.6). There were no significant correlations between any of the AVREC parameters (OL, PL, PA, INT) and lesion strength, both before and after cortical silencing and considering all time windows (total: 16-300 ms, early phase: 16-60 ms, late phase: 60-300 ms). The seemingly higher PA in the non/weakly lesioned animals (Fig. 3.17 B) is partly due to the strong response of one case (GLA21) and to stronger iS1 in these animals.

The above described effect of layer VI CT lesions on the frequency tuning of S1 was also discernible in the AVREC curves. Note that the amplitudes at nonBF were relatively higher in lesioned than in non-lesioned animals (Fig. 3.24, see also Fig. 3.26).

Consistent with the results for S1, the "spreading" of the data points leading to the less sharp frequency tuning in layer VI lesioned animals first occurred at 2

octaves away from BF (Fig. 3.25; values ordered according to color, representing lesion strength). Likewise, sharpness of frequency tuning was not affected by layer V lesions, neither before nor after cortical silencing.

Statistical analysis of their PAs and INTs confirmed this observation: The sharpness of frequency tuning (BF/nonBF) declined significantly with increasing lesion strength in layer VI in the early, but not in the late phase of the AVRECs (Fig. 3.26 A) in the pharmacologically untreated cortex. Post-silencing, the significant correlation dissolved, but the data seemed not to be completely uncorrelated. Regarding the early phase of the PAs, we could not determine whether frequency tuning was sharper before or after application of muscimol, as changes in both directions were observed, independent of lesion strength (Fig. 3.26 B, lesion strength is color-coded). With respect to the integrals, however, the average value and the variance were lower after silencing (Fig. 3.25; lesion layer VI, early phase), and the results from the repeated measures ANOVA (Tab. 3.6) indicate that the pharmacological treatment has an effect on the tuning sharpness depending on the lesion strength in layer VI. In particular, as shown by Figure 3.26 B (INT early), animals with weak, but not those with strong lesions have a lower BF/nonBF ratio after silencing.

3.3.5 Intracortical microstimulation (ICMS)

CSD profiles

In non/weakly lesioned animals, infragranular ICMS (IGstim) evoked a cross-laminar activation pattern similar to that seen after acoustic stimulation, i.e., a strong granular sink (S1), followed by sinks in supragranular (S2) and infragranular (S3) layers, as well as the early deep infragranular sink (iS1) (Fig. 3.27, averaged CSD profiles). In these animals, IGstim provoked the strongest activation pattern during the untreated condition compared to other stimulation depths and lesion levels. Granular ICMS (Gstim) was less effective and produced no or only weak granular sinks. Instead, sinks in layers bordering layer IV (IIIb, Va) and iS1 were present. Supragranular ICMS (SGstim) was the least effective stimulus depth and evoked a pattern similar to that after Gstim. In lesioned animals, the location of sinks varied more and was not always assignable to one of the previously defined sinks. So we here describe, if applicable, the location rather than the name of the sink. Gstim was at least as

effective as IGstim. Some animals had sinks in layer IV, particularly after Gstim, while infragranular sinks were present in most animals. For all stimulation depths, averaging the CSD profiles (Fig. 3.27) reveals that animals with lesions in layer VI received input mainly in middle layer V, while in animals with additional layer V lesions, the infragranular sink was located a little higher (Va). Supragranular sinks were also present, especially in animals with lesions in layer VI only.

Following application of muscimol (Fig. 3.28, averaged CSD profiles), IGstim still evoked prominent sinks in the main lemniscal thalamic input layers (S1 and iS1), Gstim produced a weaker activation essentially in layers Vb/VI (iS1), and SGstim evoked weak activation in layer III in non/weakly lesioned animals. In lesioned animals, no or very weak S1 appeared, but still the different supra- and infragranular sinks, which had similar spatiotemporal locations as before silencing. This suggests that no polysynaptic intracortical connections are essential for their generation. Noticeably, animals with lesions in both infragranular layers had a stronger and prolonged pattern of sinks and sources than the other two groups. This applied to all stimulation depths, but was strongest following Gstim, particularly with respect to the evoked sink in layer Va. The experimental case with cell loss in layer V only (see appendix, Fig. J.2), also displayed a kind of “blurry” activation but had, given its intact layer VI projection neurons, still a S1, indicating that the observed effect was due to a loss of layer V CT neurons.

Averaging swallows small incongruent activations, but it can also reveal the dominant input sites concealed in the variable data, and overcomes the problem emerging especially in the CSD profiles of the layer V lesioned animals after silencing, which were characterized by a long lasting, stripy activation that was not clearly separable from stimulus artifact. By averaging, we could demonstrate that this strange pattern underlies a physiological activation that is approximately within the same cortical depth as before silencing. The apparent stronger sources compared to sinks may be due to a better spatiotemporal matching across animals.

As expected by the qualitative results, statistical analysis of S1 after IGstim revealed that PAs and INTs decreased with increasing lesion strength in layer VI both before and after application of muscimol (Figs. 3.29 and 3.30 A).

Thereby, S1 was generally smaller after silencing (see Tab. 3.6 and Fig. 3.30 B). PLs did not correlate but tended to be shorter after silencing (Fig. 3.30), and neither did any of the measures (PA, PL) at other stimulus depths (SGstim, Gstim) (Fig. 3.29).

The strength of S1 after IGstim did not correlate with lesion strength in layer V (unordered color-coded values in Fig 3.29), but SGstim did.

AVRECs

Averaging the AVREC curves of the different groups revealed that before cortical silencing, strongest activation (among all groups and stimulation depths) was seen after IGstim and in non/weakly lesioned animals (Fig. 3.31, bottom left, indicated by an arrow). In the groups that included lesions in layer VI, Gstim and SGstim were at least as effective as IGstim, and the mean PLs of their curves were longer (Fig. 3.31, top left (arrow), 13-17 ms after stimulus onset) than those after IGstim in non/weakly lesioned animals (9 ms).

After cortical silencing (Fig. 3.31, right column), IGstim produced a very short activation in non/weakly lesioned animals (barely separable from the stimulus artifact). In animals with lesions in layer VI only, the activation strength was similar or even smaller. Curves of animals that included lesions in layer V, however, showed a more sustained slowly decaying activation that had similar or slightly higher amplitudes than the curves of these animals before silencing.

The above described observation that in the untreated cortex IGstim activates the cortices of non/weakly lesioned animals more than those with higher cell loss is evidence of the correlation between PA and INT of the AVREC and lesion strength of layer VI (Figs. 3.32, right column: ordered color-coded values, and 3.34). The comparably weak, but more sustained cortical activation in layer V CT lesioned animals after silencing may explain that the PAs (early phase), but not the INTs remain significant during this condition. The activation strength upon Gstim and SGstim did not reach significant correlations (Fig. 3.32, right column: less ordered color-coded values).

Figure 3.32 (left column) also clearly shows that the overall activation strength does specifically depend on neuronal loss in layer V during the silenced, but not in the untreated condition. In detail, before application of muscimol, PA and INT values were unordered with respect to the color-coded lesion strength. Afterwards, animals with lesions in layer V had higher INT and PA values than

animals without lesions in layer V, which applied for all stimulation depths (see also Tab. 3.6). Colors, on the other hand were unordered, if lesion strengths in layer VI were considered (Fig. 3.32, right column), suggesting that lesions in layer VI did not contribute to the elevated activation after silencing. Correlation analyses between lesion strength in layer V and the PA and INTs of AVREC underpin the observations based on Figures 3.31 and 3.32, namely that animals with layer V lesions had higher activations than those without after cortical silencing (Fig. 3.32: significant correlations labeled by asterisks, and Fig. 3.33). Corresponding to the baseline range defined for grouping our animals, values increased from lesion strength of 5% upwards. Due to the large baseline range compared to the range above threshold for effective lesioning we actually do not deal with a monotonic or linear relationship, even if the analysis produced significant p-values.

3.3.6 Summary of results

The selective elimination of CT projection neurons by photolytic apoptosis resulted in layer-specific consequences of acoustically and electrically evoked activity patterns of AI.

Animals with and without loss of CT neurons had generally similar acoustically evoked CSD profiles, namely a sequential cross-laminar activation pattern before, and an initial source-sink-source triplet after pharmacological silencing. However, lesioning layer VI neurons led to slightly reduced strengths (PA, INT) of initial sinks S1 (before silencing) and iS1 (before and after silencing) at BF, and to increased relative strengths of the extragranular sinks S2 and S3. Furthermore, a broadening of frequency tuning was observed in S1 and AVRECs of layer VI lesioned animals (stronger correlation than for S1 at BF alone).

Respecting ICMS, non/weakly lesioned animals had the strongest activation after IGstim compared with other stimulation depths and lesion groups. We observed that in the post-silencing condition S1 remained present in weakly lesioned animals after IGstim, whereas the already weaker S1 in lesioned animals vanished almost completely. Instead, lesioned animals rather displayed sinks in layer V upon electrical, particularly Gstim, which did not disappear after drug application, implying that no polysynaptic intracortical connections are

essential for their generation. Furthermore, following cortical silencing, strongest activation was seen in the animals having layer V lesions, which was also reflected by the higher and more long-lasting amplitudes and integrals in the overall activation (AVRECs).

3.3.7 Figures

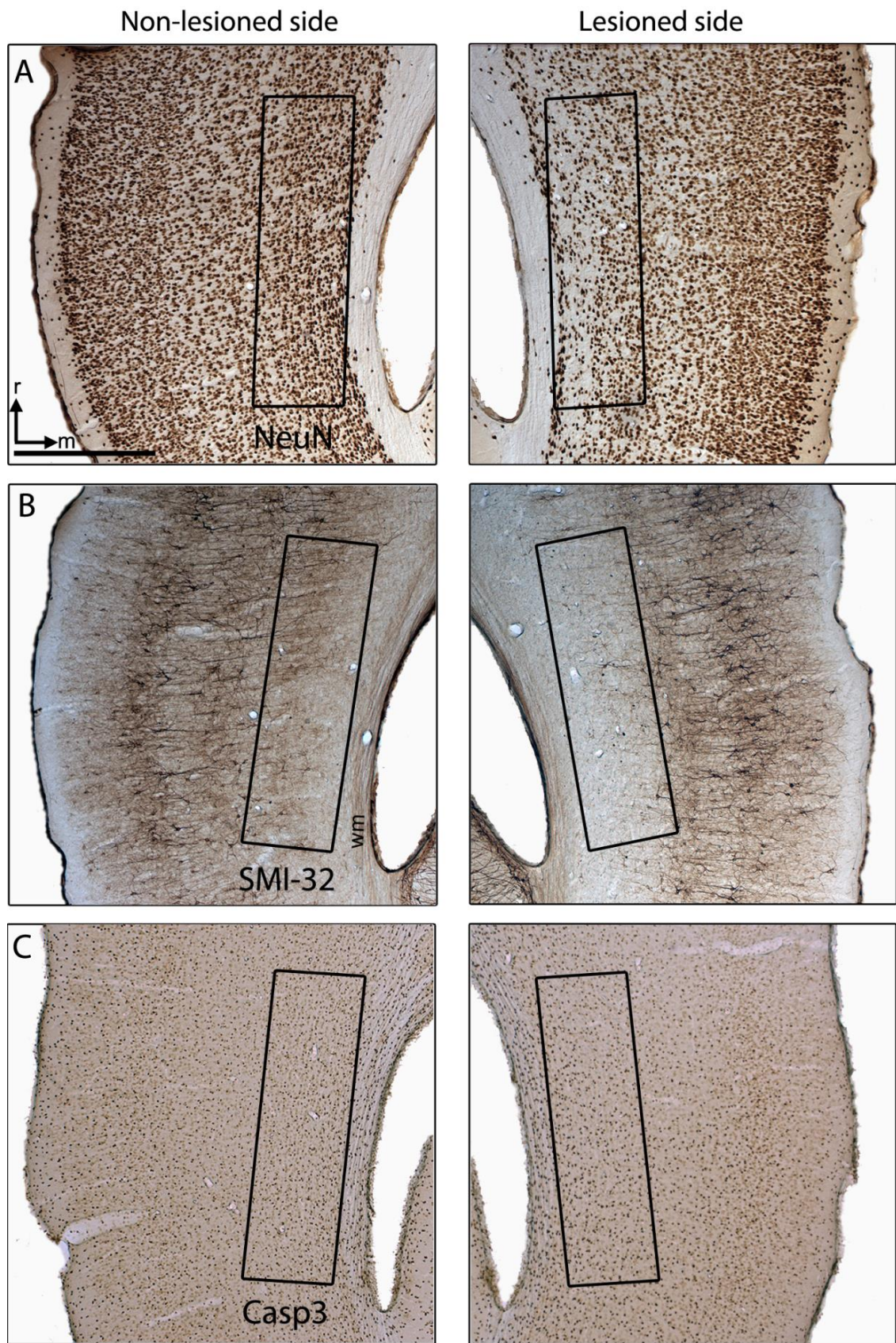


Figure 3.12 (preceding page): Three immunohistochemical stains to display apoptotic cells or neuronal cell loss, evaluated by comparing the non-lesioned (left) with the lesioned (right) cortical sides of AI. **(A)** The NeuN (neuronal nuclei) stain we regarded the best assay for quantification of neuronal cell loss based on its visualization of nuclei/somata. **(B)** Antibody against SMI-32 reveal neuronal loss in deep infragranular layers of the lesioned AI, particularly seen by the reduction of dendritic and axonal arbors, and of axons within the white matter (wm). **(C)** Active Casp3 stain did not provide clear differences between both cortical sides, because photolytically induced apoptosis was already completed. Scale bar: 500 μm .

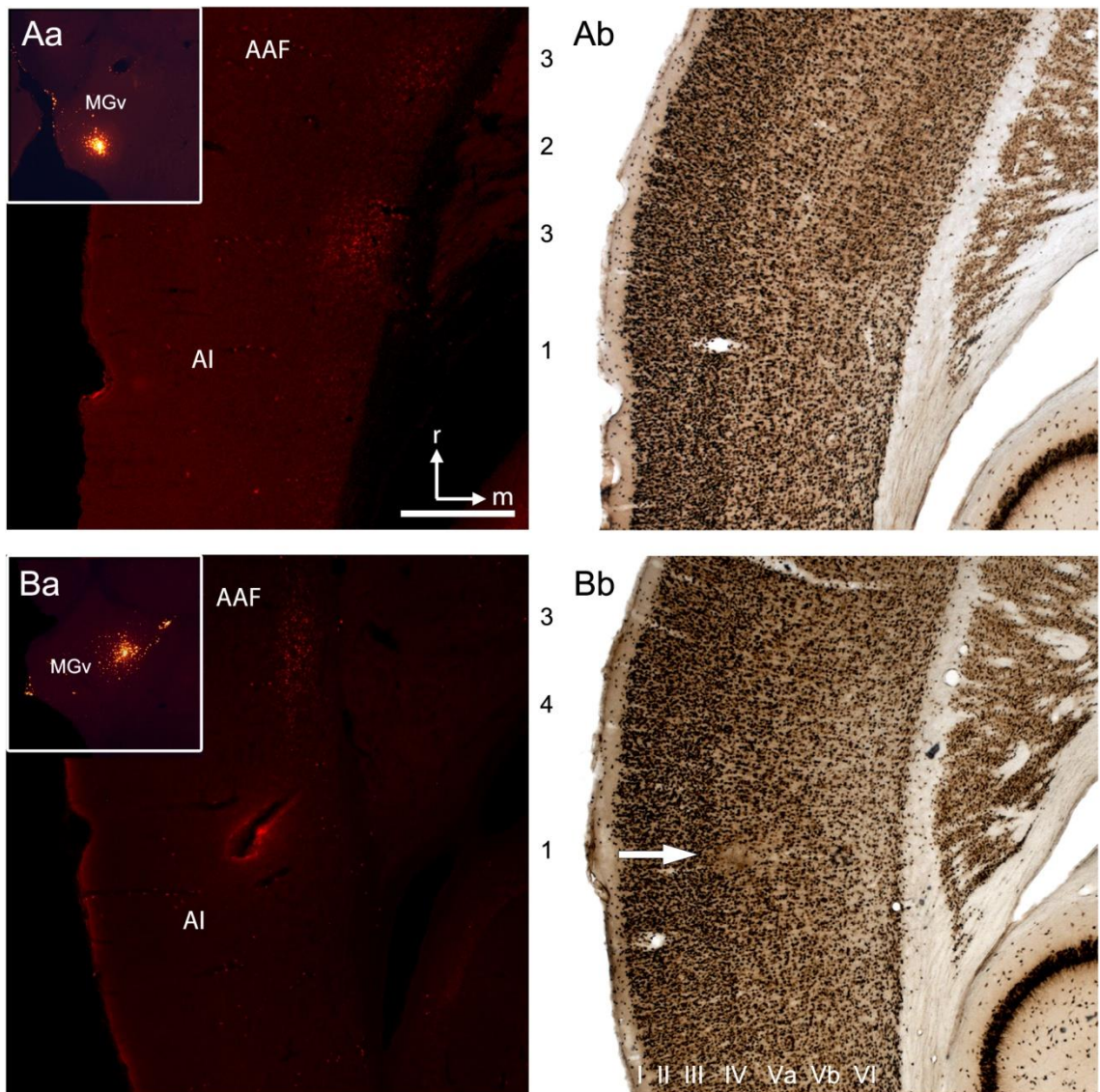


Figure 3.13: The specificity of the photolytic apoptosis was approved by complementary analyses of fluorescent and NeuN-stained slices of the AC. Regions that were labeled (such as the AAF in Aa and Ba, zone 3), but not illuminated, did not show neuronal degeneration (high cell density in layer VI in AAF of Ab and Bb). Cells within regions that were not labeled (Aa, rostral AI, zone 2), were also preserved. Neuronal loss (zones with reduced cell density in layer VI of Ab and Bb) was generally accompanied by bleaching in the correspondent fluorescent slices (zone 1), but bleaching was not always complete (rostral AI in Ab, zone 4). Scale bar: 500 μ m.

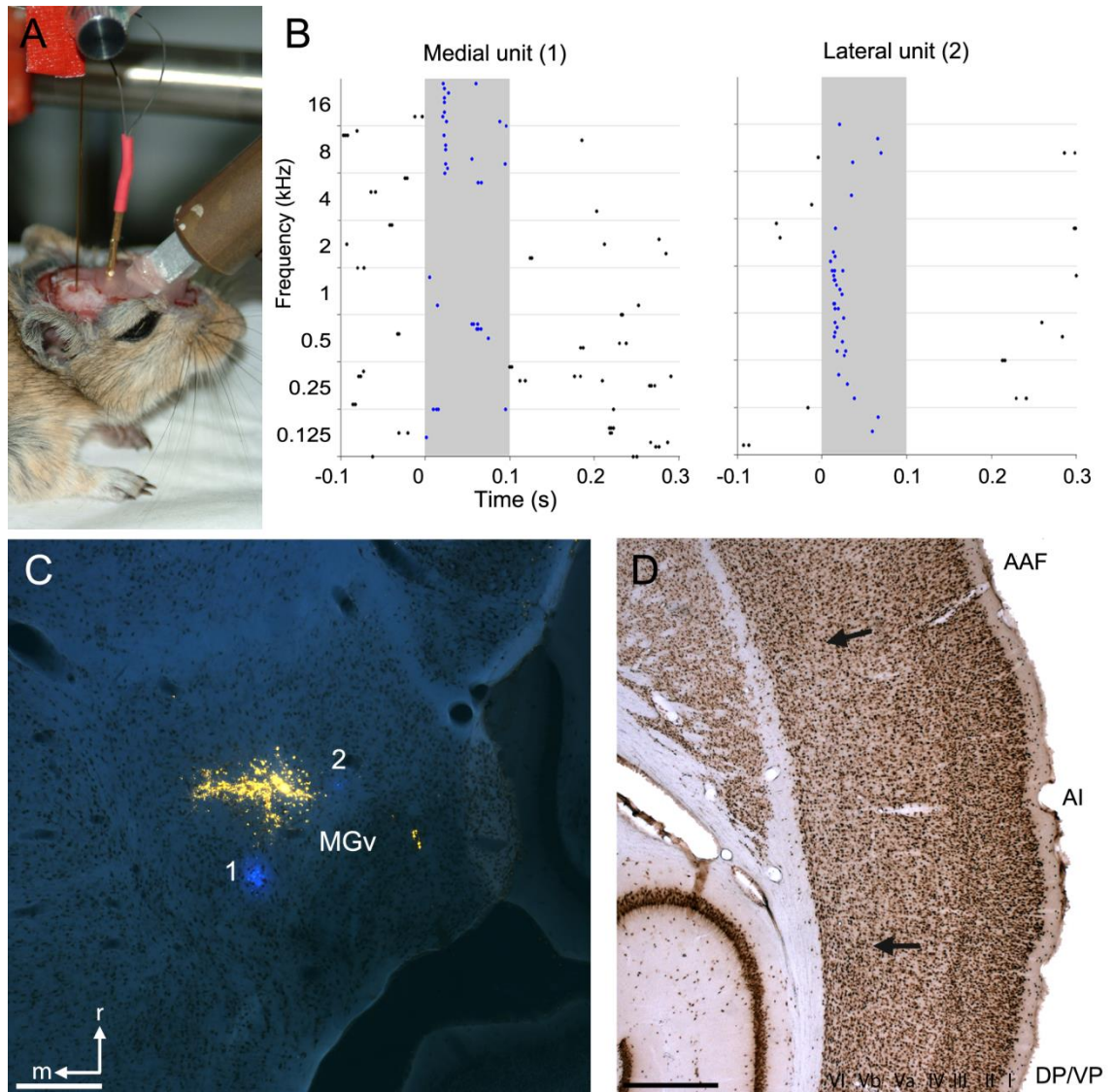


Figure 3.14: (A) Thalamic responsiveness to acoustic stimuli after photolytic apoptosis of CT neurons was tested by recordings using a tungsten electrode. MGv neurons adjacent to the injections site (C) still respond tonotopically to pure tones (B) (medial unit (1): 8-16 kHz, lateral unit (2) 0.5-1 kHz, 54 dB, duration 100 ms). (C) NeuN-stained horizontal slice showing the recording sites (1 and 2, labeled by Fast Blue), and the injection site (chlorin e_6 conjugated retrobeads, appearing yellowish due to the applied filter set (F31-013, AHF Analysentechnik AG, Germany)). (D) NeuN-stained slice representing moderate neuronal loss in AI (area enclosed by arrows) of the same animal. Scale bars: 300 μ m (C), 500 μ m (D).

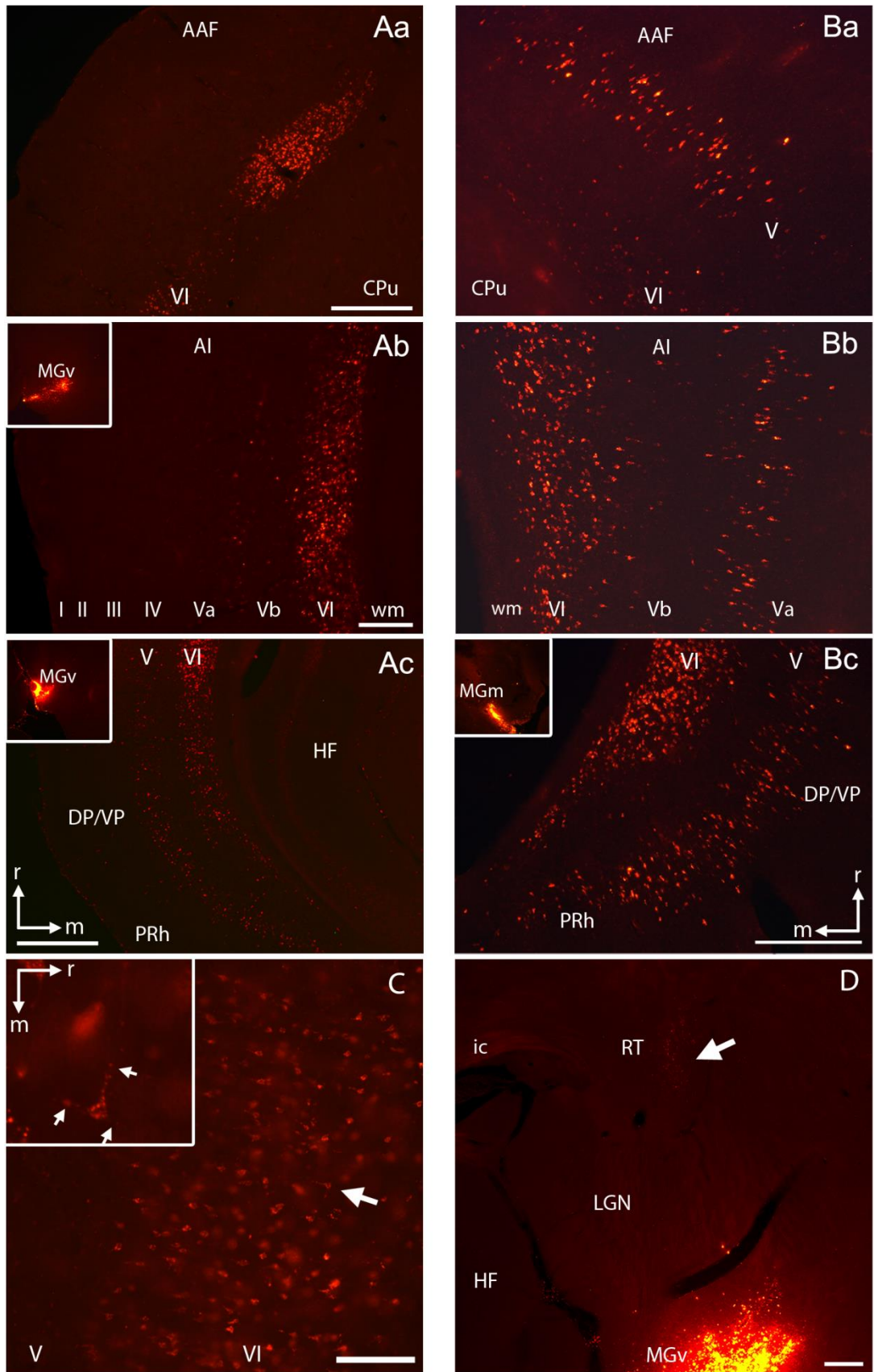


Figure 3.15 (preceding page): Retrograde labeling of CT neurons. Fluorescence photographs showing examples of injection sites into the MGv (**A**, insets) and MGm (**B**, inset) of the MGB, and the correspondent retrograde labelings in layers VI and V of the AC. MGv receives cortical input mainly from layer VI, but also from layer V (especially of DP/VP). Cortical neurons from layers VI (particularly of AI) and V (particularly of AAF and DP/VP) project to MGm. (**C**) Higher magnification shows that labeled cells are pyramidal neurons. (**D**) MGB neurons are also innervated by the Rt. Scale bars: 100 μm (B), 200 μm (Ab, C, D), 500 μm (Aa, Ac). The respective injection sites are represented in small insets (Ab also applies to Aa, C, and D; Bc also applies for Ba-b).

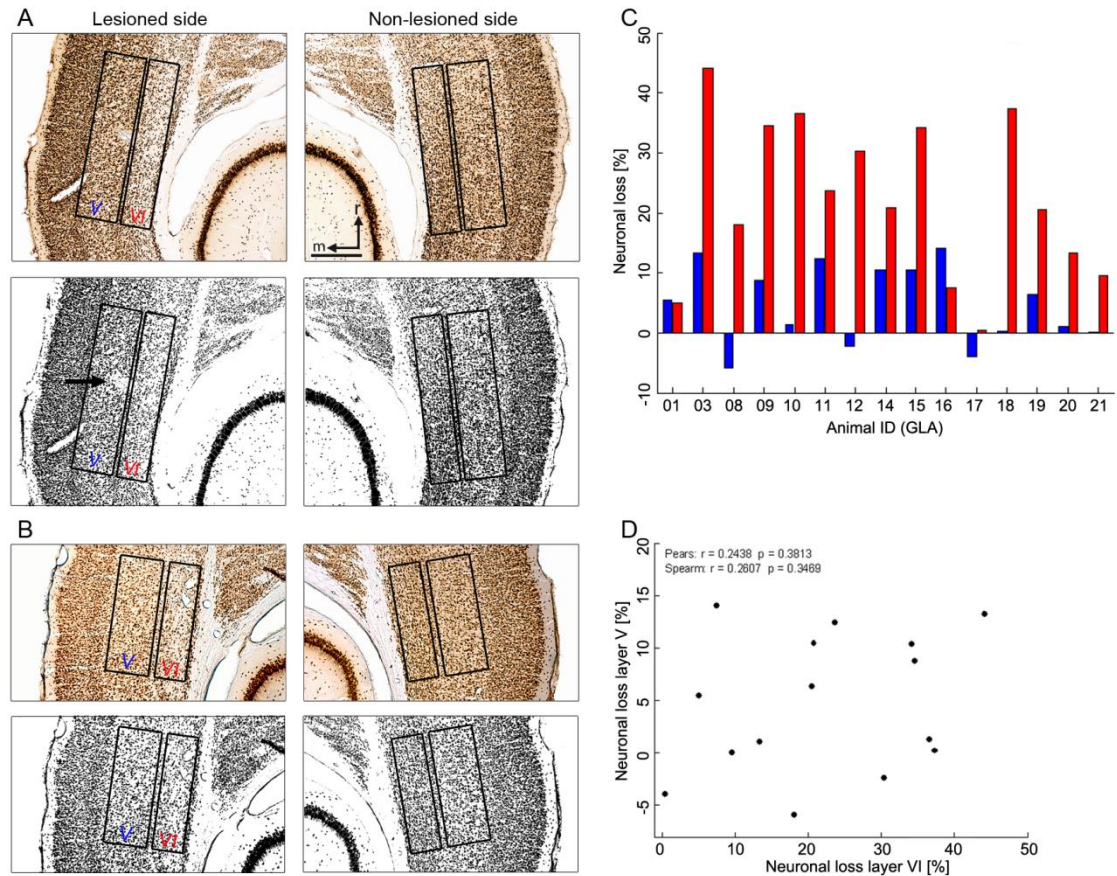


Figure 3.16: Histological quantification of neuronal loss of the animals used for CSD analysis. **(A)** Top: NeuN-stained section showing neuronal apoptosis in layer VI of the ipsilateral, i.e., illuminated cortical side of AI (case GLA18). Cellular density is much lower than in the contralateral (non-lesioned) side. The black arrow points to the electrode track within the region of laser treatment. Bottom: For quantitative analysis of cell loss, photographs were converted to binary format. For details see methods. **(B)** NeuN-stained section (top) and its binary equivalent (bottom) showing neuronal apoptosis in layers V and VI of the illuminated cortical hemisphere (case GLA03). Lesions in layer V were not as strong and clearly visible as layer VI lesions. **(C)** Bar diagram representing the percentual neuronal loss (positive values) or gain (negative values) compared to the contralateral side in layers V and VI of the individual animals. **(D)** There is no correlation between lesion strengths in layers V and VI (suggesting the absence of unspecific lesion effects).

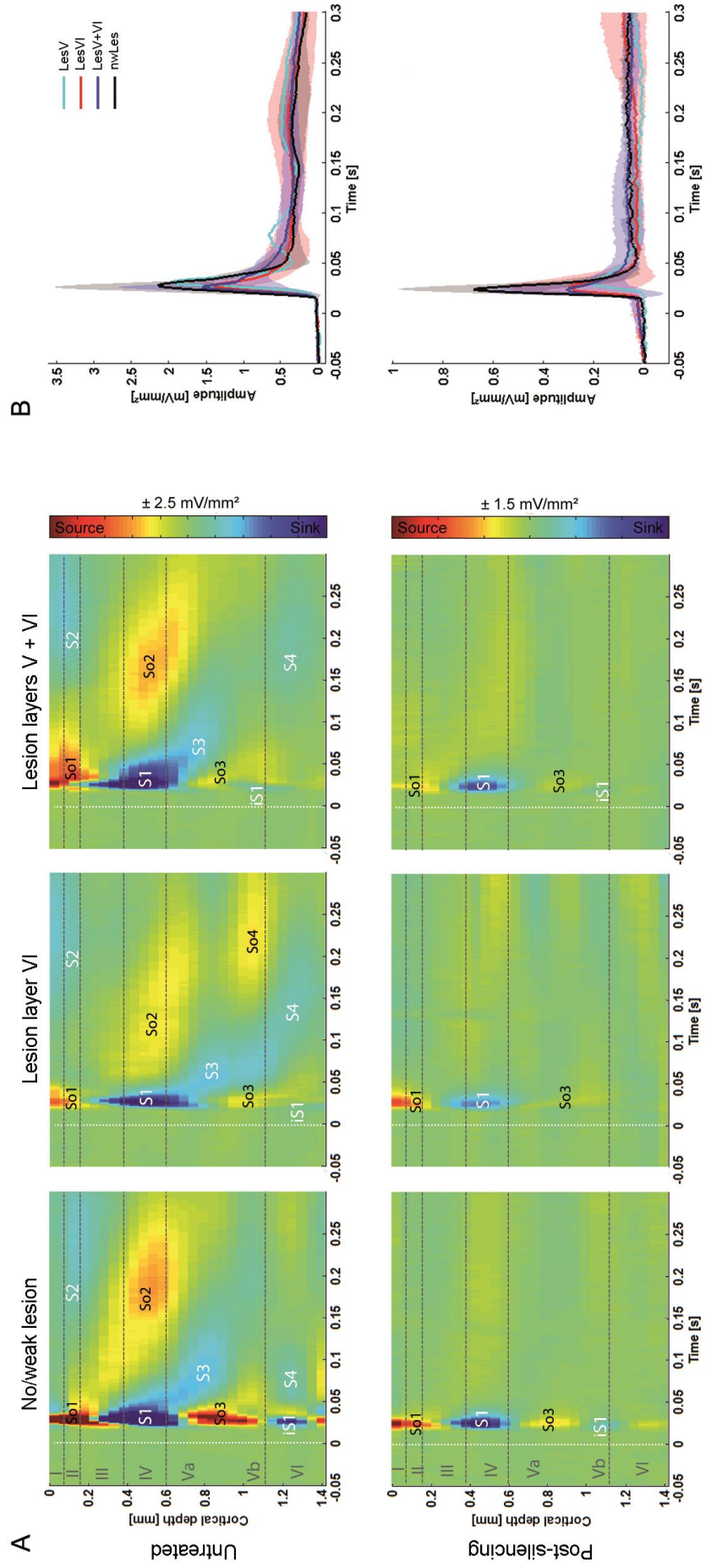


Figure 3.17 (preceeding page): (A) Averaged acoustically evoked CSD profiles at BF (54 dB SPL), before (top), and after (bottom) cortical silencing with muscimol. All lesion groups [nwLes, LesVI, LesV+VI, LesV (see appendix, Fig. J.2)] had comparable general activation patterns of current sinks (S1, S2, S3, iS1) and sources (So1, So2, So3), shown in red and blue, respectively. Color shading indicates sink and source amplitudes. However, non/weakly lesioned animals displayed a stronger early infragranular sink (iS1). **(B)** Averaged AVREC traces at BF during the untreated condition, showing means (solid lines) and SD (shaded areas) of the different lesion groups. Curves were similar across all groups. For averaging, only those animals with available post-muscimol data were used. $n_{nwLes} = 3$, $n_{LesV} = 1$, $n_{LesVI} = 4$; $n_{LesV+VI} = 5$.

CSD S1 at BF - Lesion layer VI

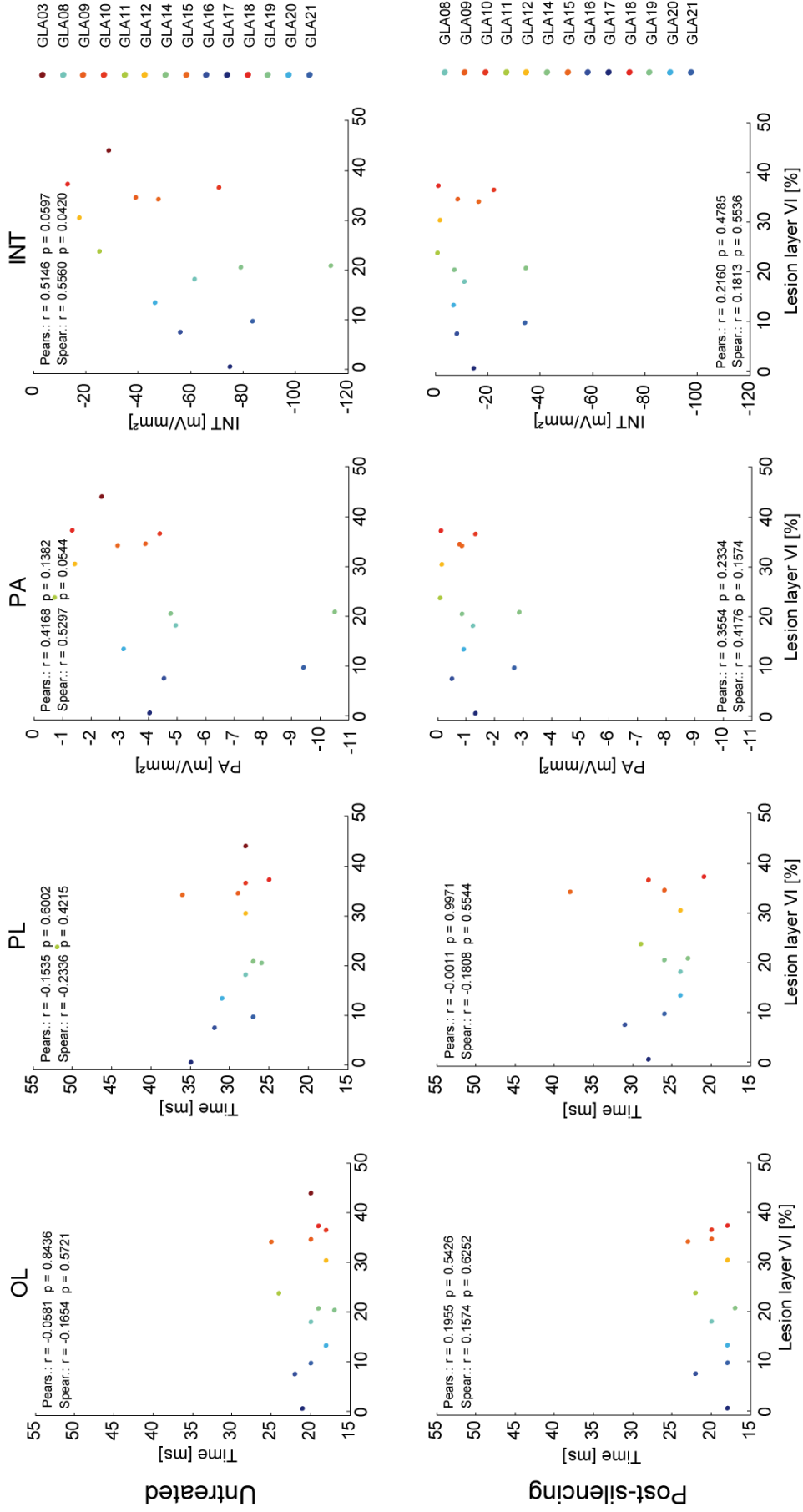


Figure 3.18 (preceeding page): Relationships between lesion strength in layer VI and the OL, PL, PA and INT in S1, before (top) and after (bottom) application of muscimol at BF (54 dB SPL). There were no significant correlations except for the INT of S1 before cortical silencing, which became less strong with increasing lesion efficacy. Abbreviations: OL, onset latency; PL, peak latency; PA, peak amplitude; INT, integral.

CSD iS1 at BF - Lesion layer VI

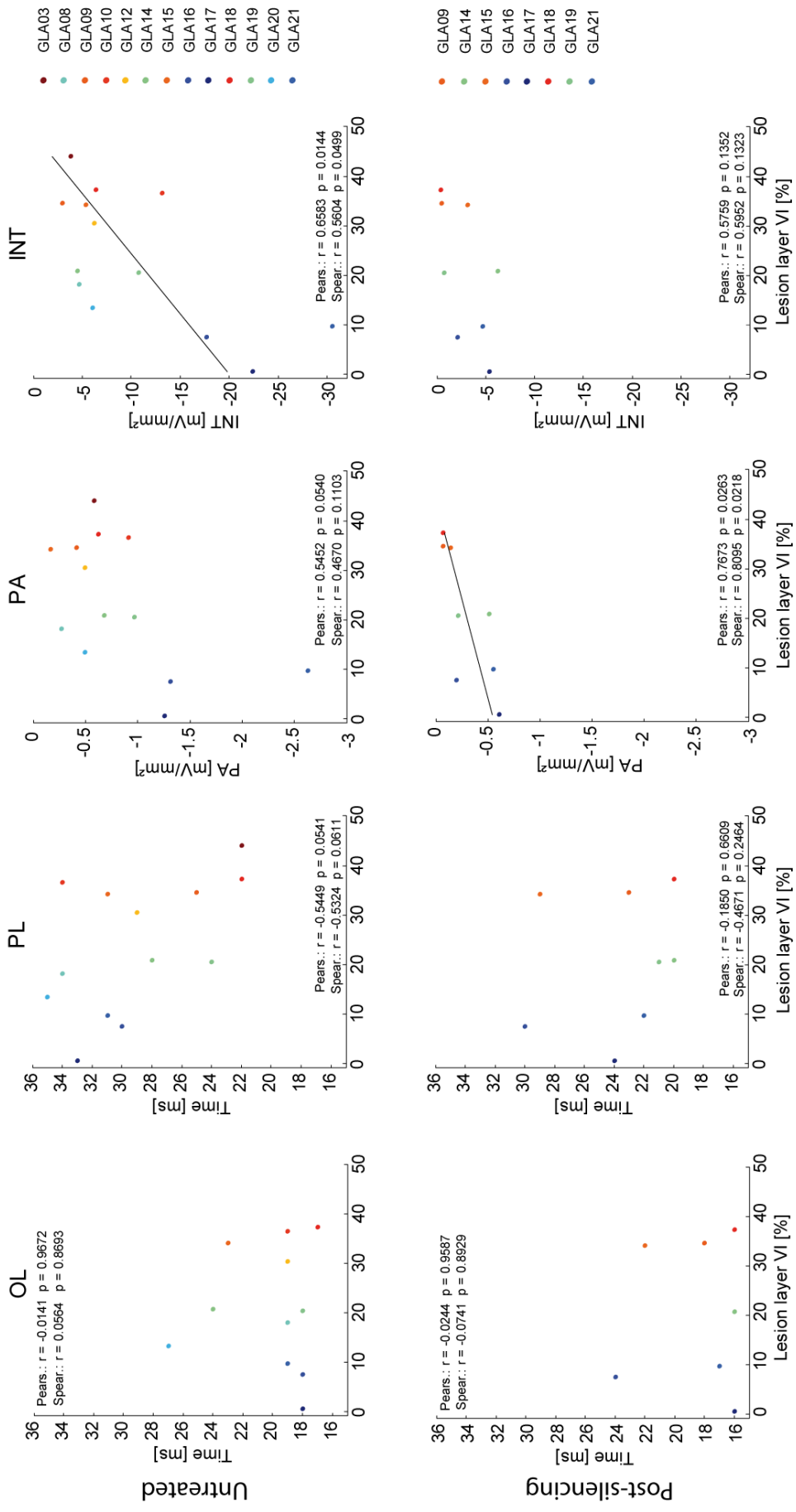


Figure 3.19 (preceding page): Relationships between lesion strength in layer VI and OL, PL, PA, and INT in the early infragranular sink (iS1) before (top) and after (bottom) application of muscimol at BF (54 dB SPL). Significant correlations (i.e., reduction of response strength with increasing lesion strength) were present for the INT before, and for the PA after cortical silencing.

Relative strengths of late extragranular sinks

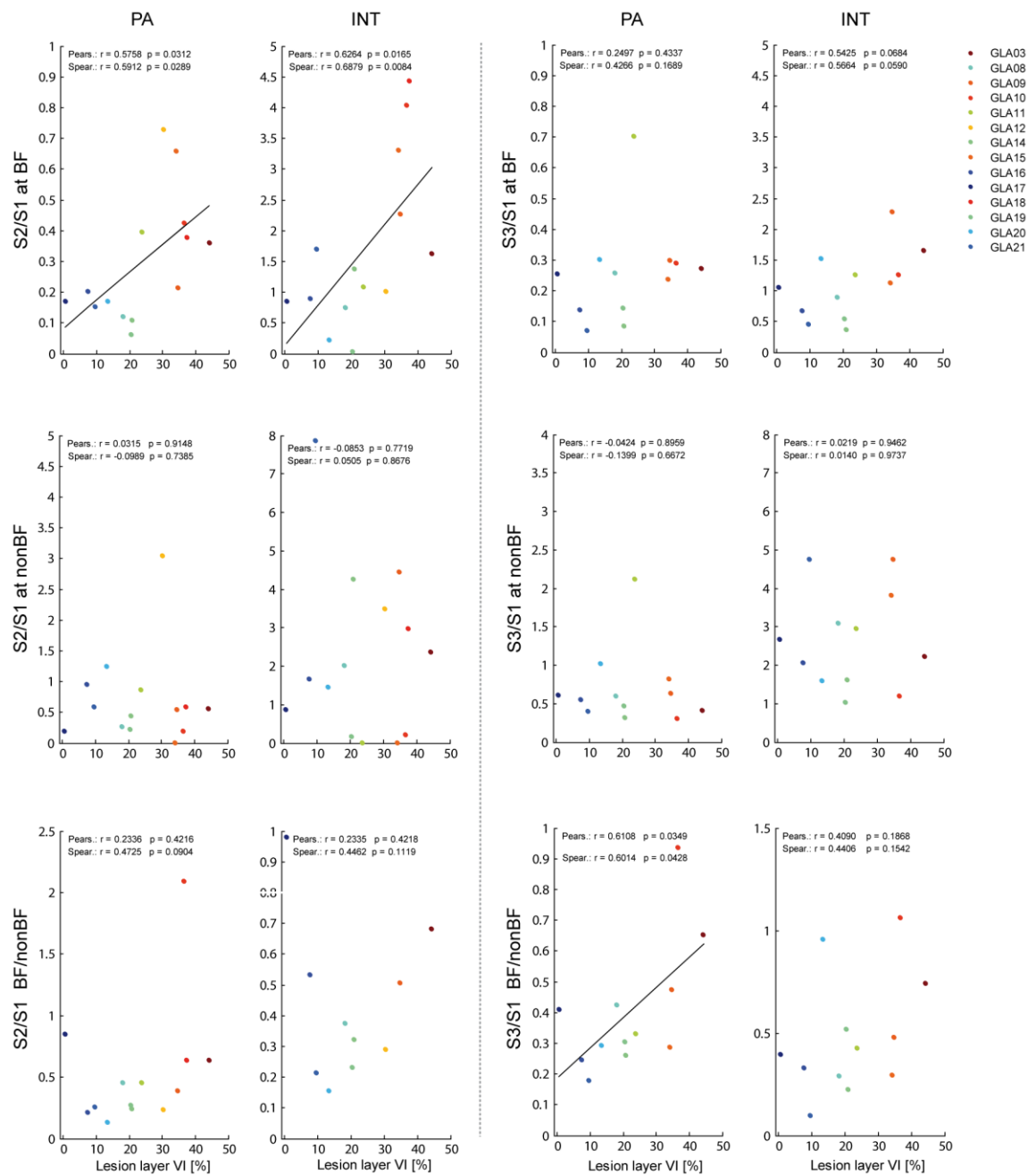


Figure 3.20: Comparative analysis of relative amplitude strengths of extragranular sinks S2 and S3 versus granular sink S1 (PAs or INTs of S2 and S3, respectively, are divided by PAs or INTs of S1) in the untreated cortex, both at BF and nonBF (2 octaves distant to BF). Comparing the ratios at BF and at nonBF reveals that the relative contributions of extragranular components are higher at nonBF than at BF. Notably, the extragranular sinks become relatively stronger with increasing lesion of layer VI CT neurons, which is mainly due to intracortical processing at BF.

CSD S1 Frequency tuning

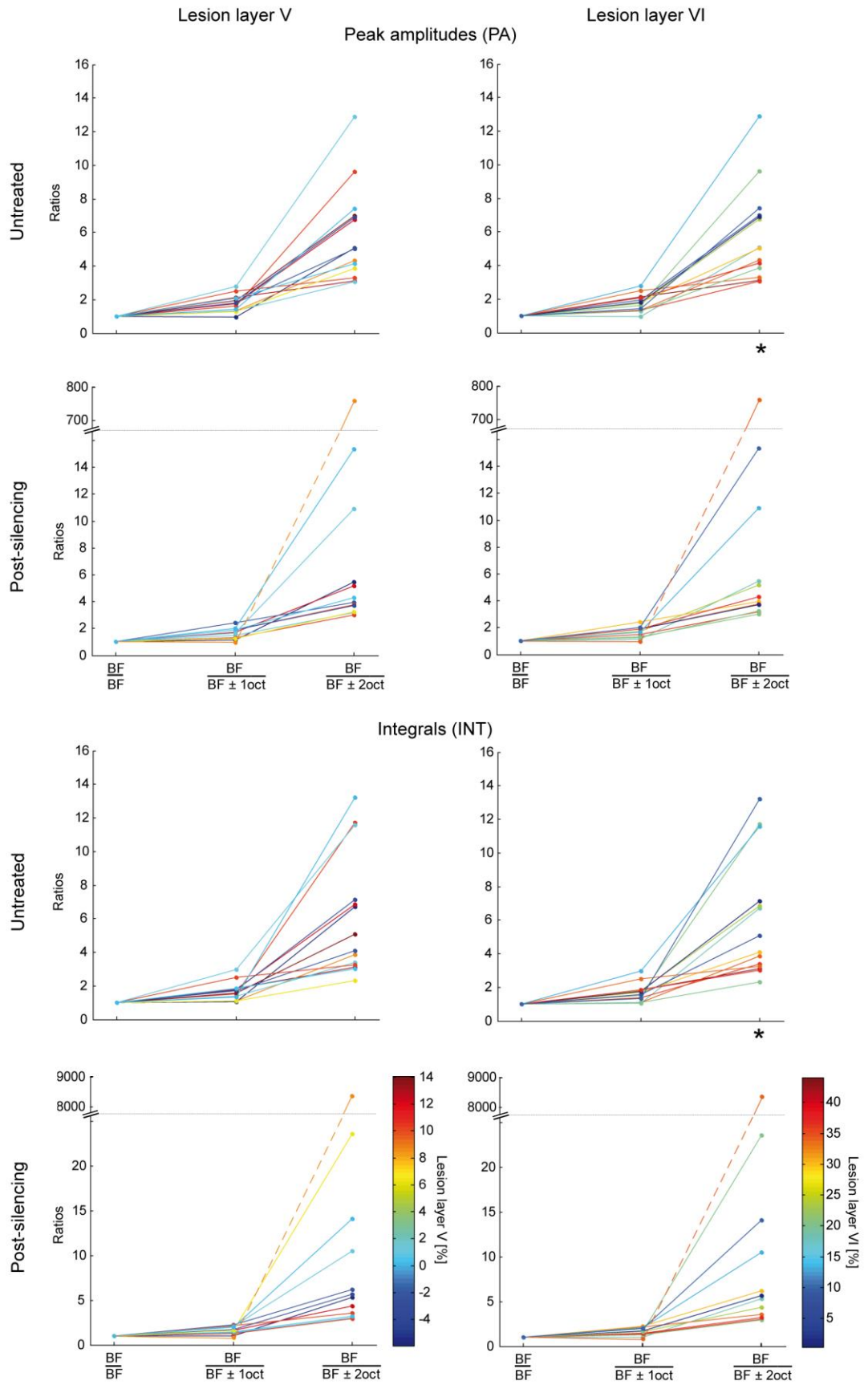


Figure 3.21 (preceding page): Ratios of BF to nearBF (BF \pm 1 octave) and BF to nonBF (BF \pm 2 octaves) at 54 dB SPL, displayed for both peak amplitudes and integrals of S1, before and after cortical silencing. Individual lesion strengths of either layer V (left column) or VI (right column) are color-coded. In the untreated cortex, sharpness of tuning (BF/nonBF) correlated with lesion strengths in layer VI (matching of color arrangement), but not layer V. At nearBF, ratios were still low and did not depend on lesion strength. Post-silencing, the relationship between S1 and lesion in layer VI was less straight (n.s.). Significant rank (Spearman) and linear (Pearson) correlations are labeled by asterisks.

Frequency tuning S1 - Lesion layer VI

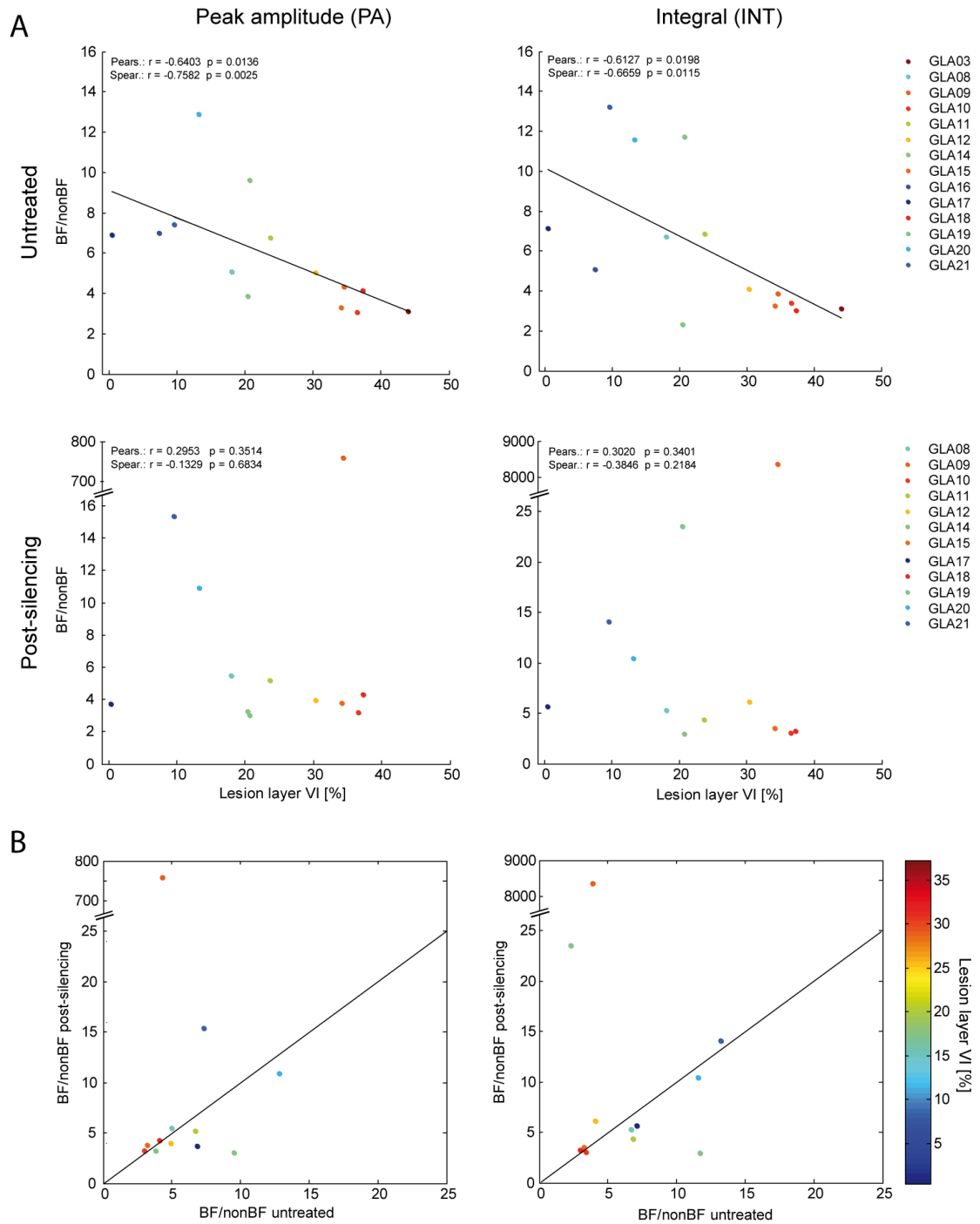


Figure 3.22: (A) Relationship between sharpness of frequency tuning in S1 (defined by calculating BF/nonBF) and lesion strength in layer VI before and after cortical silencing with muscimol (54 dB SPL). Lesion of layer VI CT neurons results in less sharp frequency tuning before, but not after cortical silencing. Post-silencing, some nonBF values became very small leading to very high ratios. **(B)** To facilitate comparison between the two treatment conditions, post-values were plotted versus pre-values. No clear trend was visible.

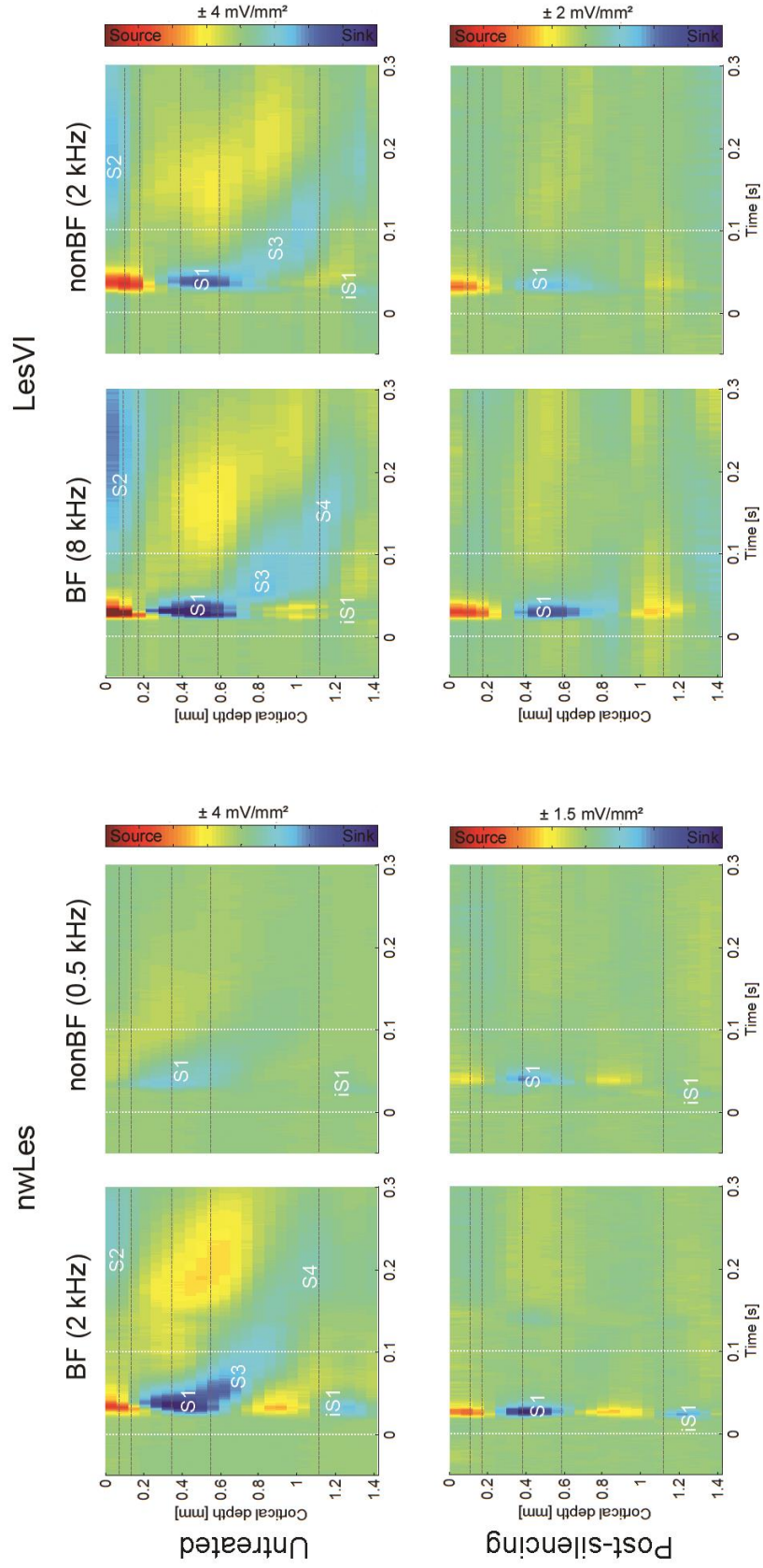


Figure 3.23 (preceeding page): Representative examples of CSD profiles at BF and nonBF (at 54 dB SPL) showing a weakly lesioned (GLA17) and a strongly lesioned (GLA10) animal, before and after application of muscimol. Note that the activation at nonBF is stronger in the stongly lesioned compared to the weakly lesioned case.

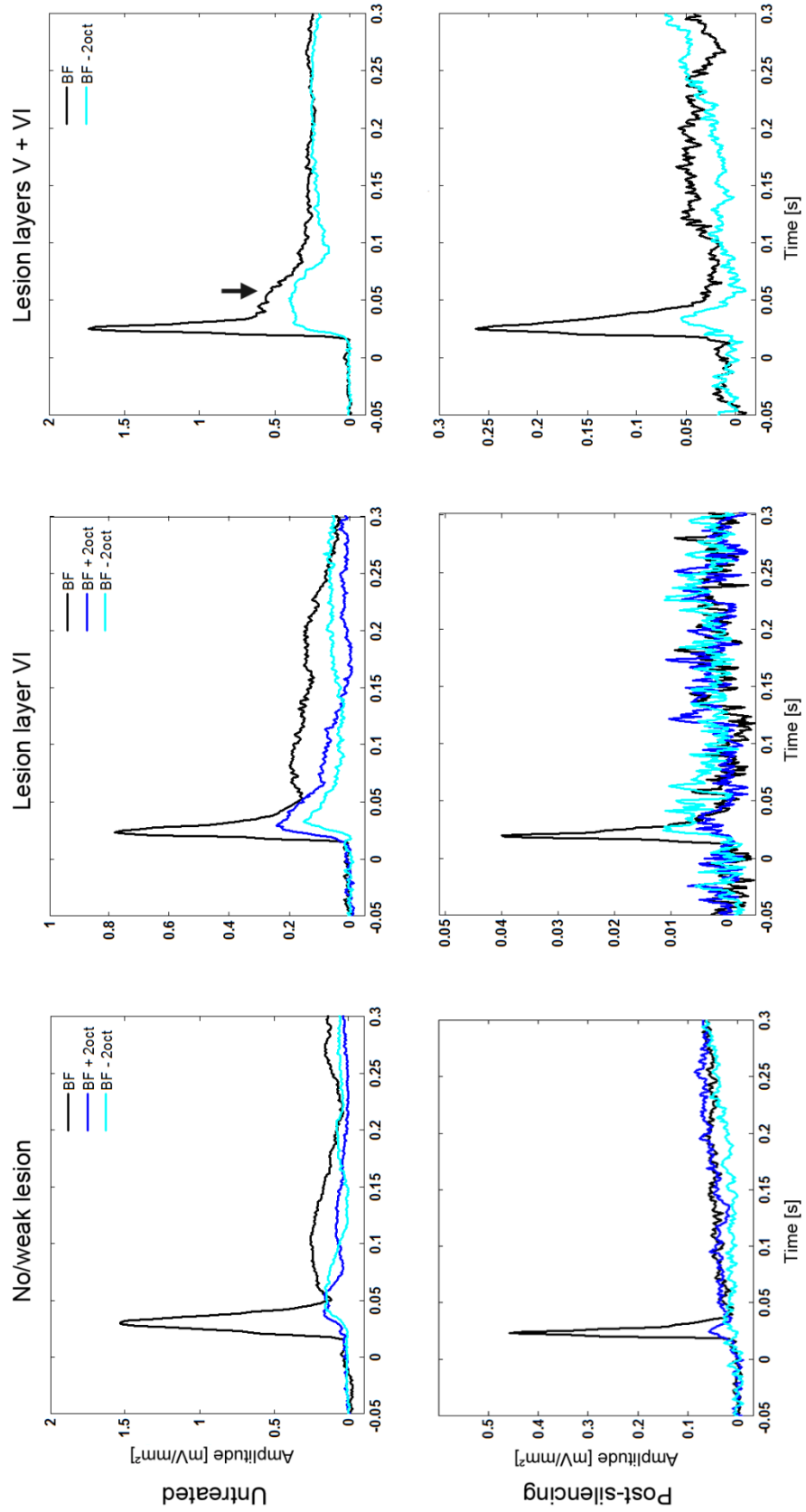


Figure 3.24 (preceding page): Examples of individual AVREC curves at BF and nonBF (cases from left to right: GLA20, GLA18, GLA19) (54 dB SPL). In strongly lesioned animals, the amplitude of the curve at nonBF (compared to that at BF) was relatively higher than in non/weakly lesioned animals. Note also the second activation (about 40-90 ms after stimulus onset, arrow), which seemed to be more prominent in animals that included a lesion in layer V.

AVREC frequency tuning

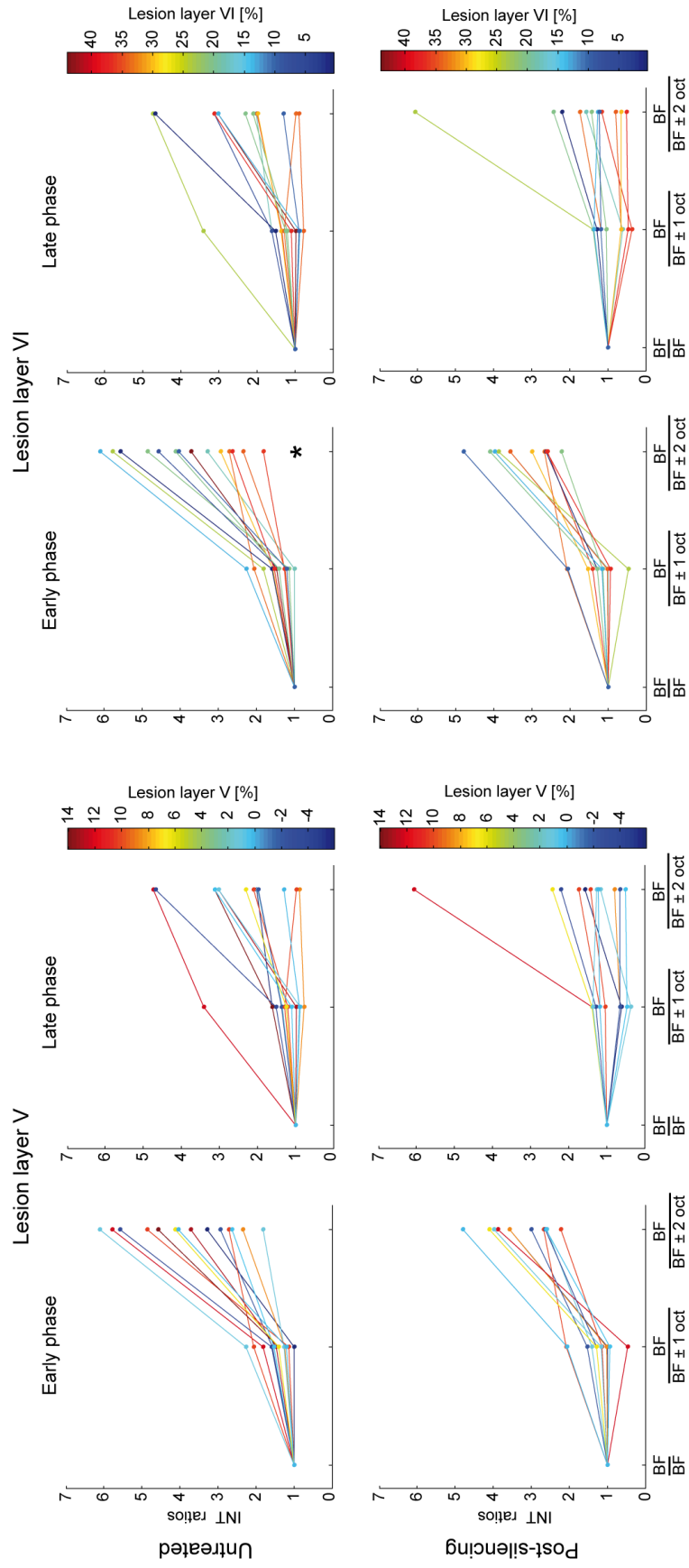


Figure 3.25 (preceding page): Sharpness of frequency tuning in AVRECs. Ratios of BF to nearBF (BF \pm 1 octave), and BF to nonBF (BF \pm 2 octaves) (54 dB SPL), displayed for the early (16-60 ms after stimulus onset) and late (60-300 ms after stimulus onset) phases of AVREC integrals, before and after cortical silencing. Individual lesion strengths of either layer V (left panels) or VI (right panels) are color-coded. During the untreated condition, BF/nonBF of early phase AVREC integrals correlated with lesion strength in layer VI (matching of color arrangement), but not in layer V. Late phases did not correlate with lesion strengths. At nearBF (both phases), the ratios were still small and were not dependent on lesion strength. Post-silencing, the dispersion of the points (BF/nonBF vs. lesion in layer VI) during the early phase was closer together (and now n.s.), as tuning was now solely determined by the TC input. Late phase BF/nonBF ratios distributed around 1, because activity measured after cortical silencing is unlikely to be stimulus driven. Significant correlations are labeled by asterisks.

AVREC Tuning - Lesion layer VI

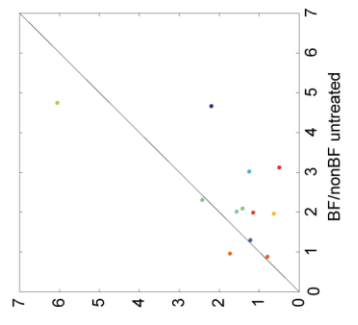
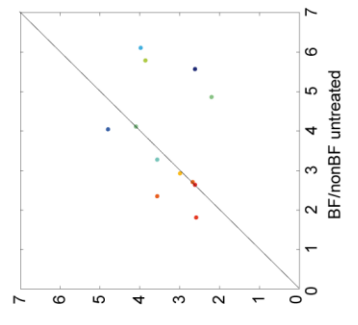
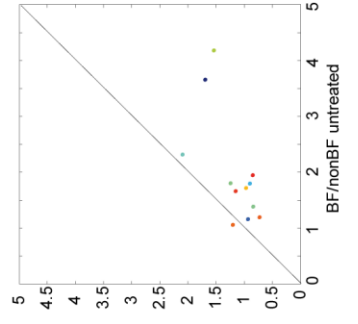
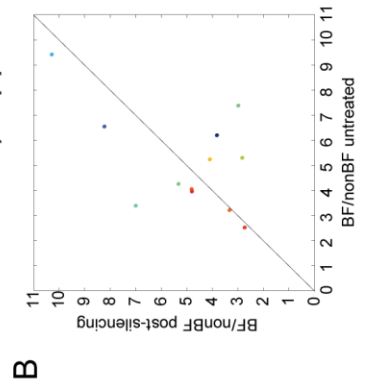
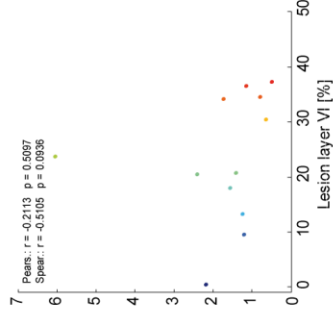
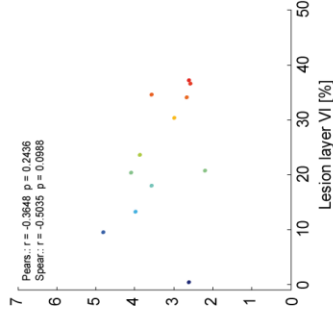
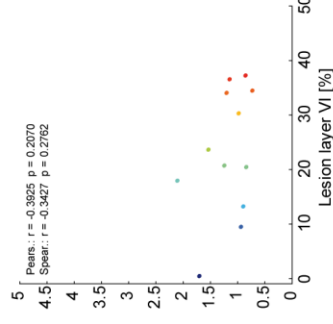
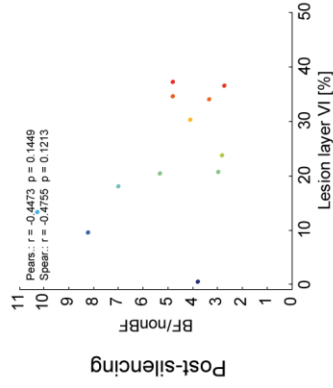
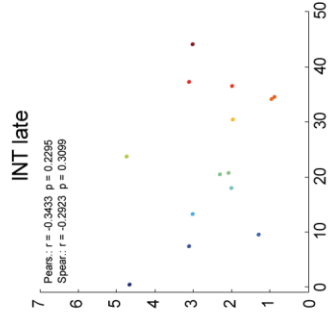
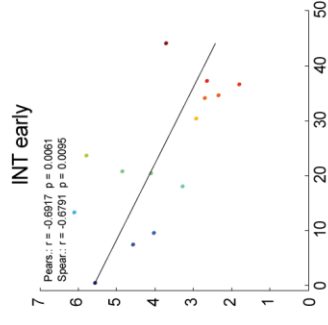
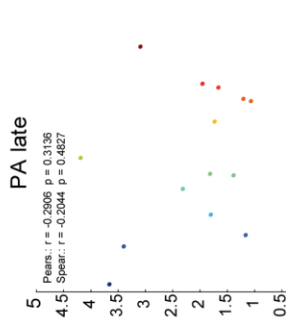
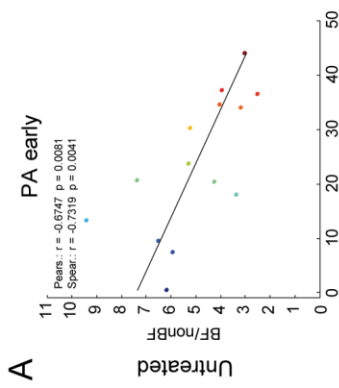


Figure 3.26 (preceding page): (A) Relationship between sharpness of frequency tuning of AVRECs (defined by calculating BF/nonBF) at 54 dB SPL and lesion strength in layer VI before and after cortical silencing with muscimol. Lesion of layer VI CT neurons results in less sharp frequency tuning in the early phase (18-60 ms after stimulus onset) of the AVREC before, but not after drug application. The tuning of the late phases (60-300 ms after stimulus onset) was not influenced by lesions of CT neurons. **(B)** With regard to the early phases, no clear change of the ratios could be seen after silencing, even though the tuning of the INT tended to decrease in the weakly, and to remain unchanged in strongly lesioned animals. The late phases were generally broader tuned after silencing (ratio around 1) due to the overall reduction of intracortical activity.

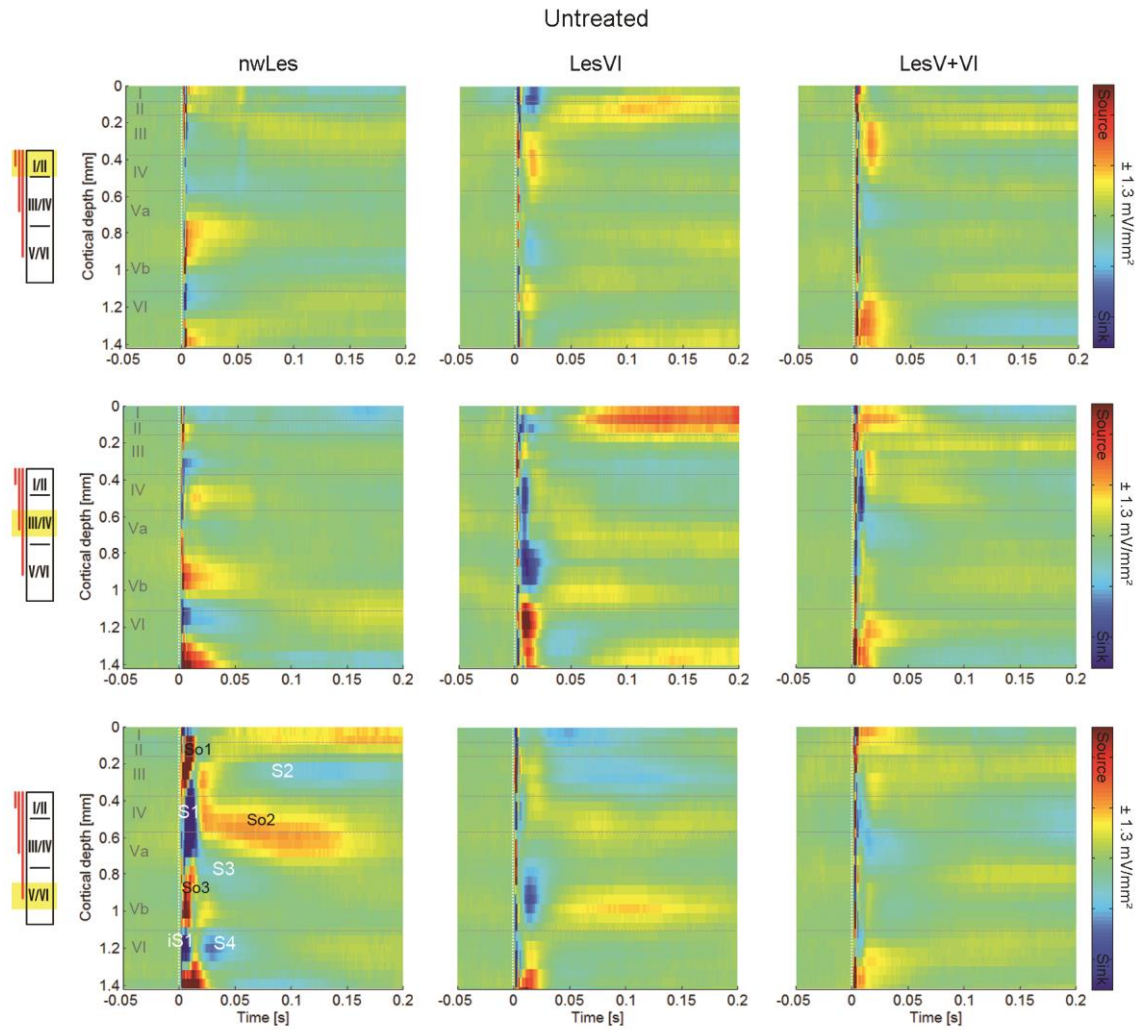


Figure 3.27: Averaged CSD profiles of three lesion groups (nwLes, LesVI, LesV+VI) evoked by layer-specific ICMS ($160 \mu\text{A}$), in the untreated condition. In general, but in particular upon IGstim, non/weakly lesioned animals show a cross-laminar activation pattern similar to that evoked by acoustic stimulation. In more strongly lesioned animals, sinks in layer V dominated over S1. For averaging, only those animals with successful cortical silencing were used. $n_{\text{nwLes}} = 3$, $n_{\text{LesVI}} = 4$; $n_{\text{LesV+VI}} = 5$.

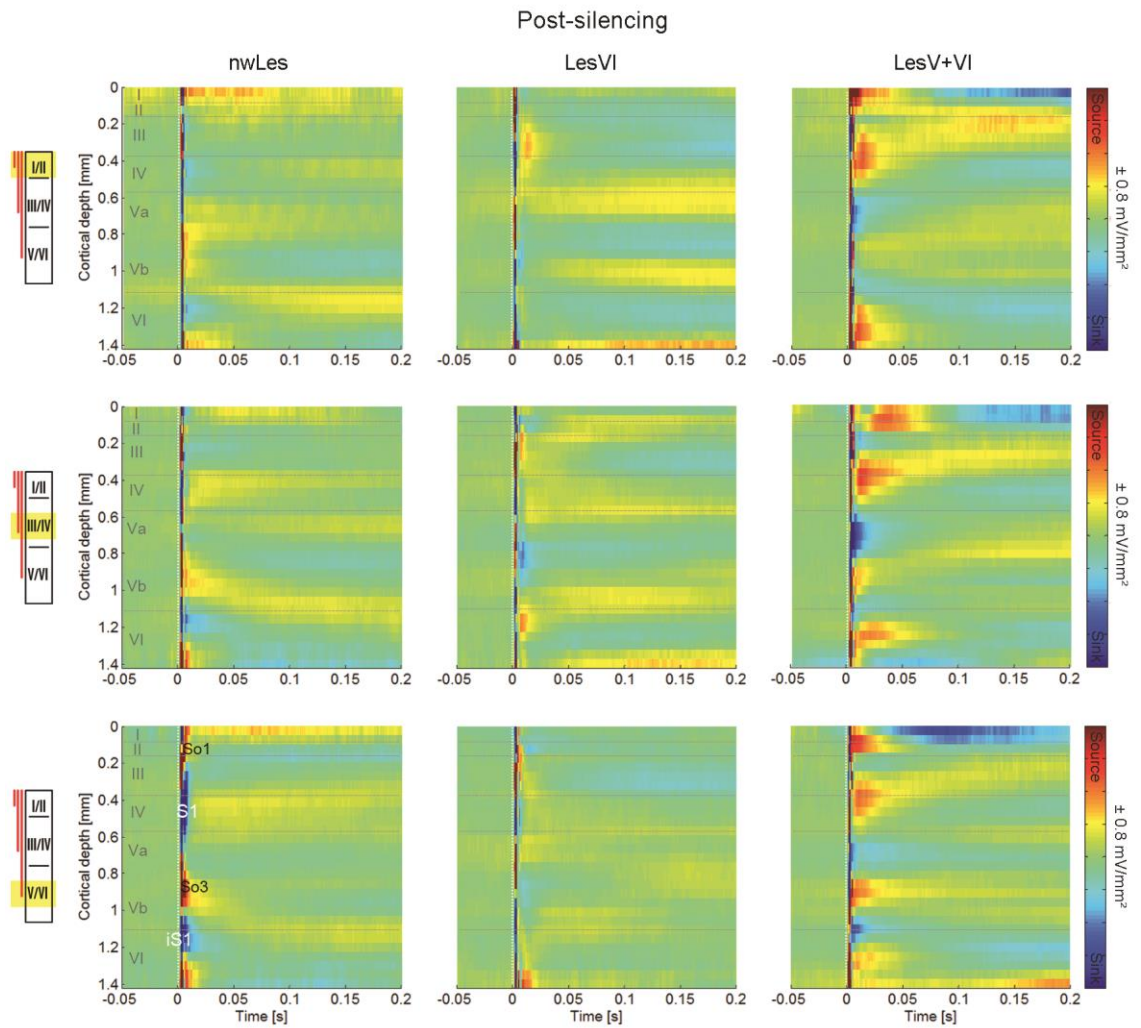


Figure 3.28: Averaged CSD profiles of three lesion groups evoked by layer-specific ICMS (160 μ A), after cortical silencing with muscimol. After infragranular stimulation, non/weakly lesioned animals display the two initial sinks (S1, iS1) also seen upon acoustic stimulation in the silenced cortex. In contrast, more strongly lesioned animals lack or have only very small S1. In layer VI only lesioned animals, rather weak sinks in layers V and I/II remained present, while in animals with additional loss of layer V neurons, a stronger and longer lasting pattern of sinks and sources was observed. $n_{nwLes} = 3$, $n_{LesVI} = 4$; $n_{LesV+VI} = 5$.

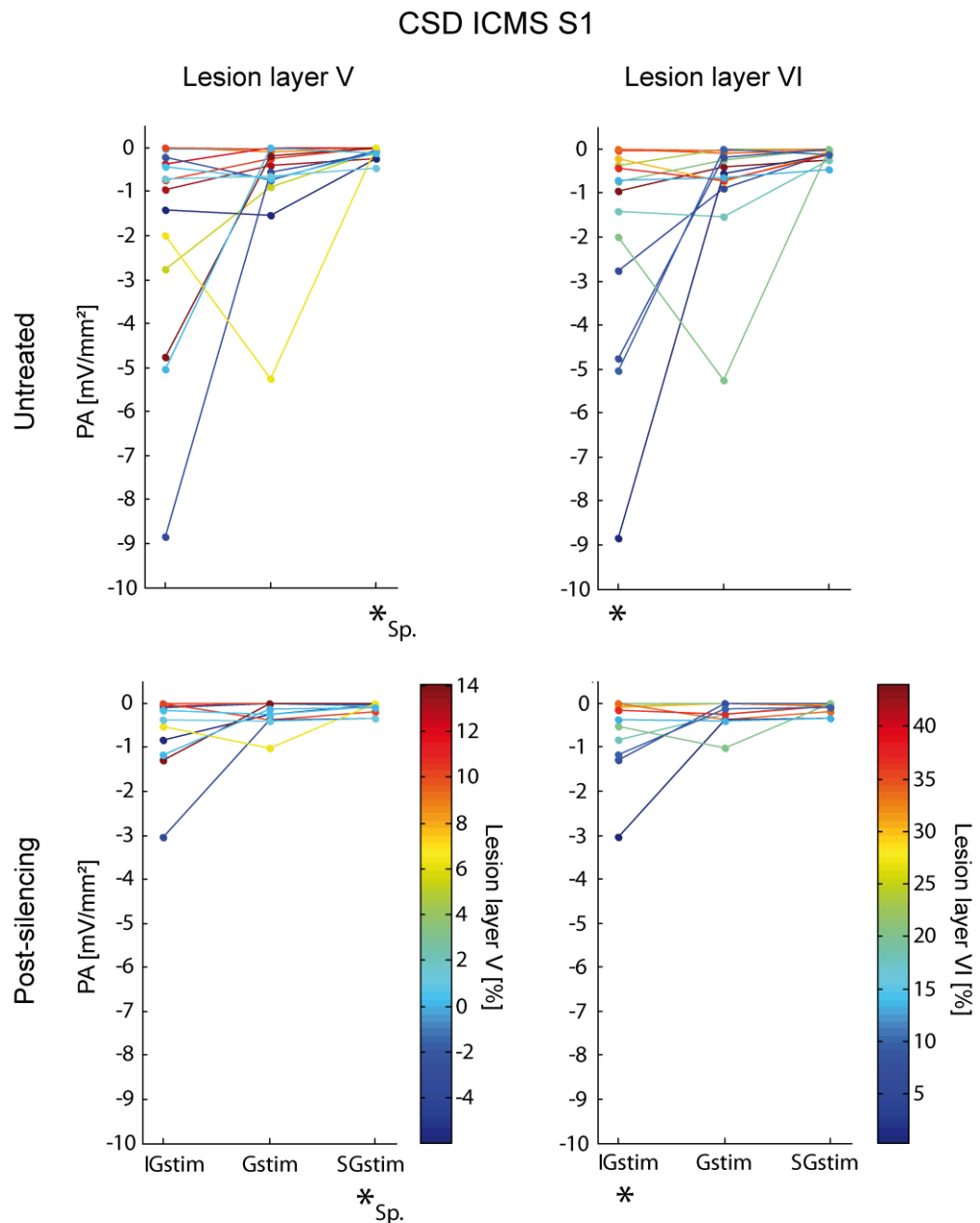


Figure 3.29: Diagrams depicting the PA of S1 evoked by layer-specific ICMS (160 μ A), before and after cortical silencing. Data points are color-coded according to their respective lesion strength in layers V (left column) or VI (right column). IGstim evoked highest amplitudes and integrals in animals with cell loss in layer VI, both before and after application of muscimol. The strength of S1 did not depend on lesions in layer V. Conditions with significant correlations are labeled by an asterisk (“Sp.” indicates that only Spearman’s, but not Pearson’s correlation coefficient, was significant).

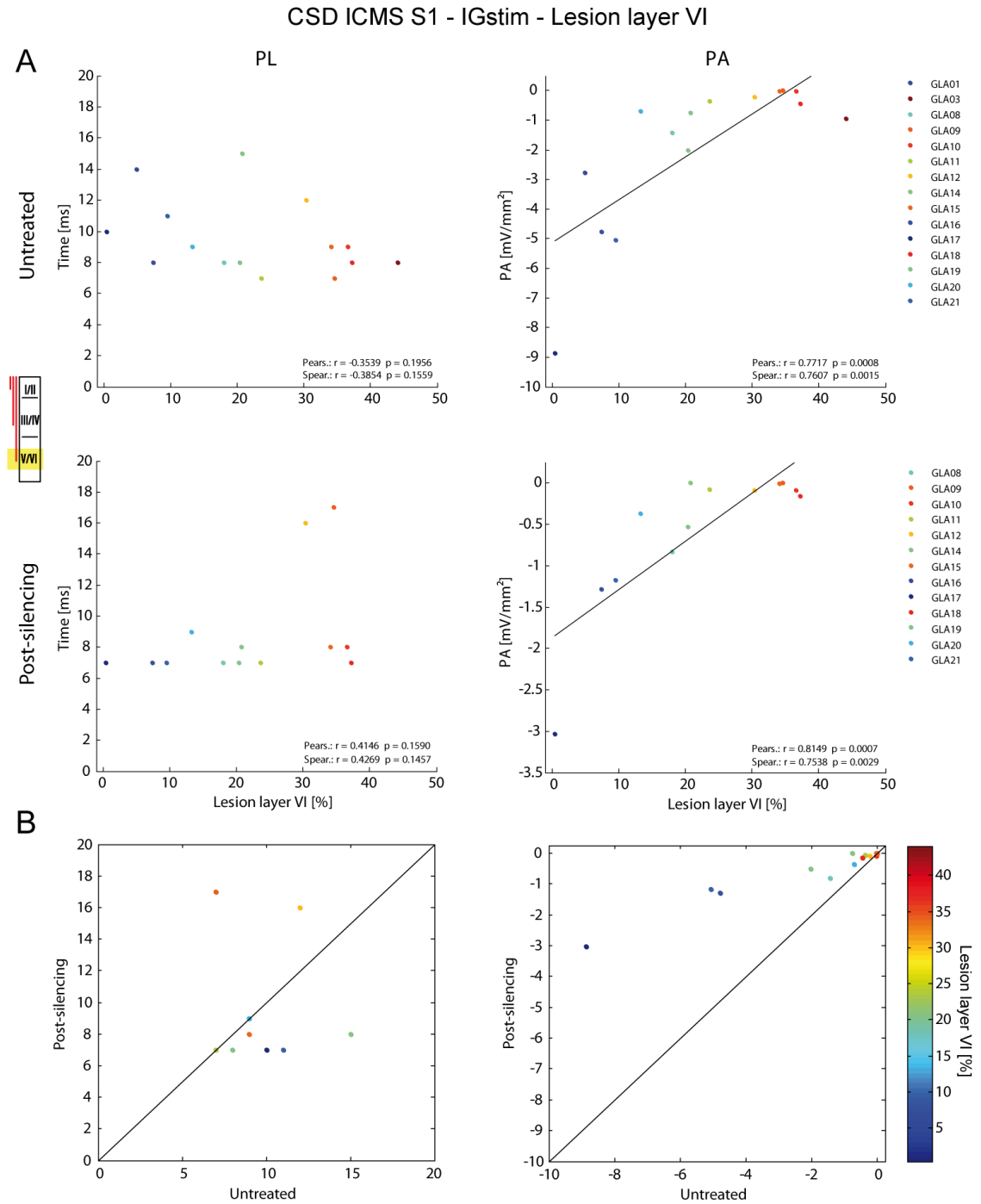


Figure 3.30: (A) Correlation between lesion strength in layer VI and PL and PA of S1 after IGstim. First row shows data before, second row after cortical silencing. The strengths (PA, INT) of the sinks decreased with higher lesion efficacy in both treatment conditions. **(B)** Post-values plotted against pre-values. Muscimol led to shorter PL, and weaker PA and INT in almost all animals. Lesion strength is color-coded.

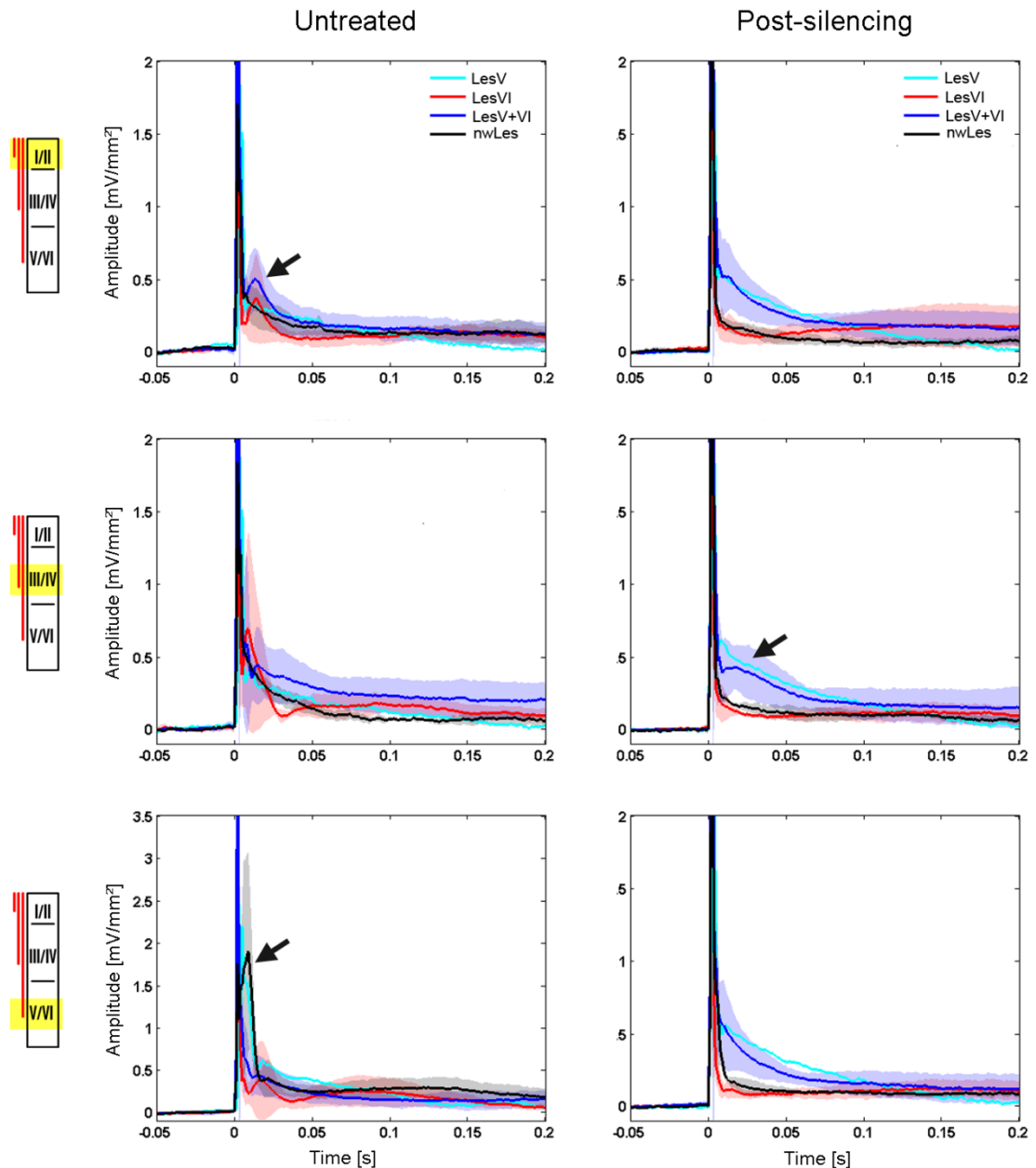


Figure 3.31: Averaged AVREC curves evoked by layer-specific ICMS (160 μ A) in the untreated (left) and silenced (right) condition, showing means (solid lines) and standard deviations (shaded areas) of the different lesion groups. The first short peak represents the stimulus artifact. Before cortical silencing, strongest activation was seen after IGstim and in non/weakly lesioned animals (arrow in bottom-left panel). PL evoked by SGstim was longer in lesioned animals (arrow in top-left panel). After application of muscimol a more sustained activation was seen in animals that involved lesions in layer V (the arrow applies for all stimulation depths), while curves of animals with no/weak lesions or lesions in layer VI only declined rapidly to very low values.

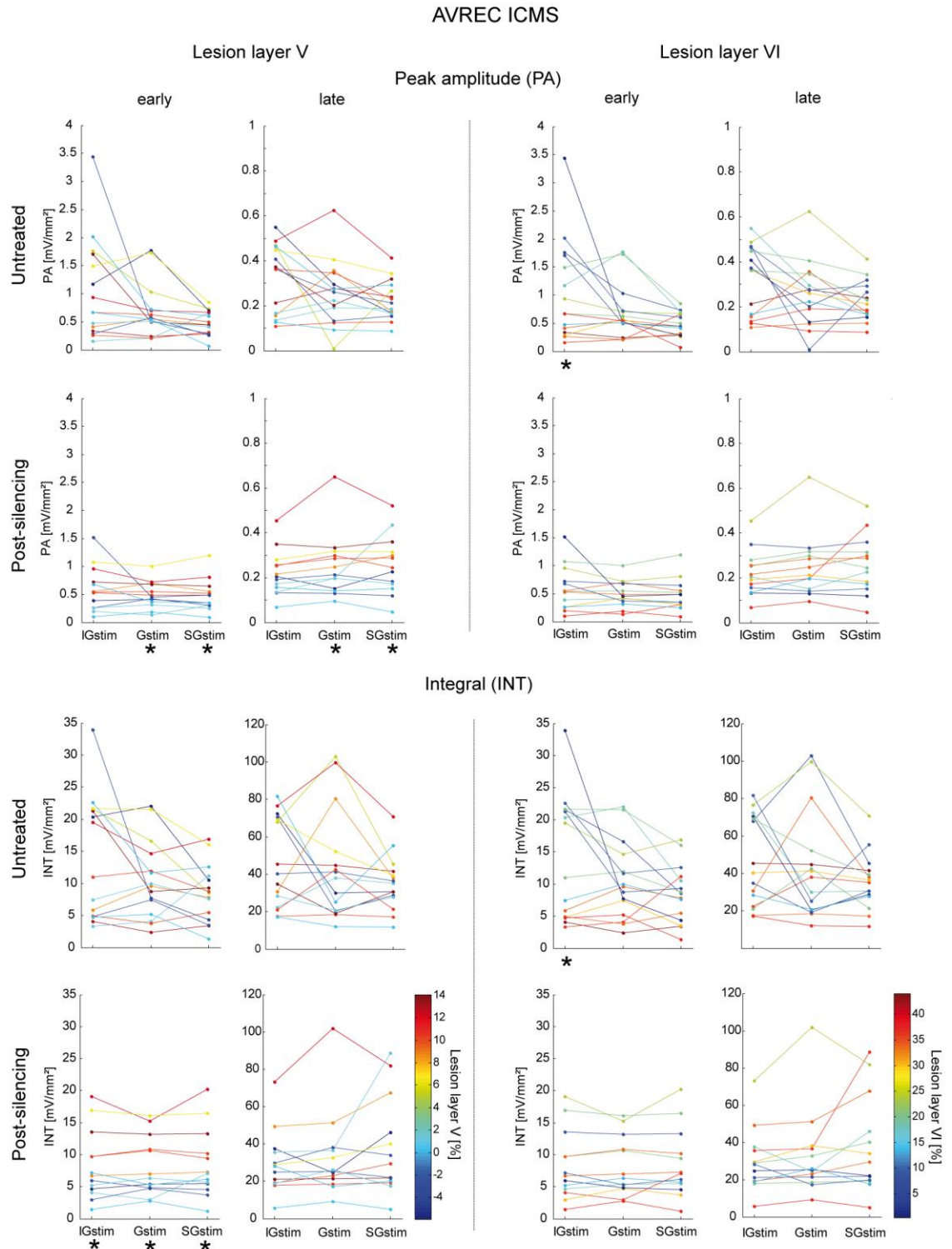


Figure 3.32: Diagrams depicting the PA and INT of the AVRECs evoked by layer-specific ICMS (160 μ A) before and after cortical silencing. Data points and lines are coded by colors according to their respective lesion strength in layers V or VI. Note that before silencing, IGstim evoked highest activation in animals without cell loss in layer VI. After application of muscimol, ICMS (especially in granular and supragranular layers) produced highest activity in animals having lesions in layer V. Conditions with significant correlations are labeled by an asterisk.

AVREC ICMS - Gstim - Lesion layer V

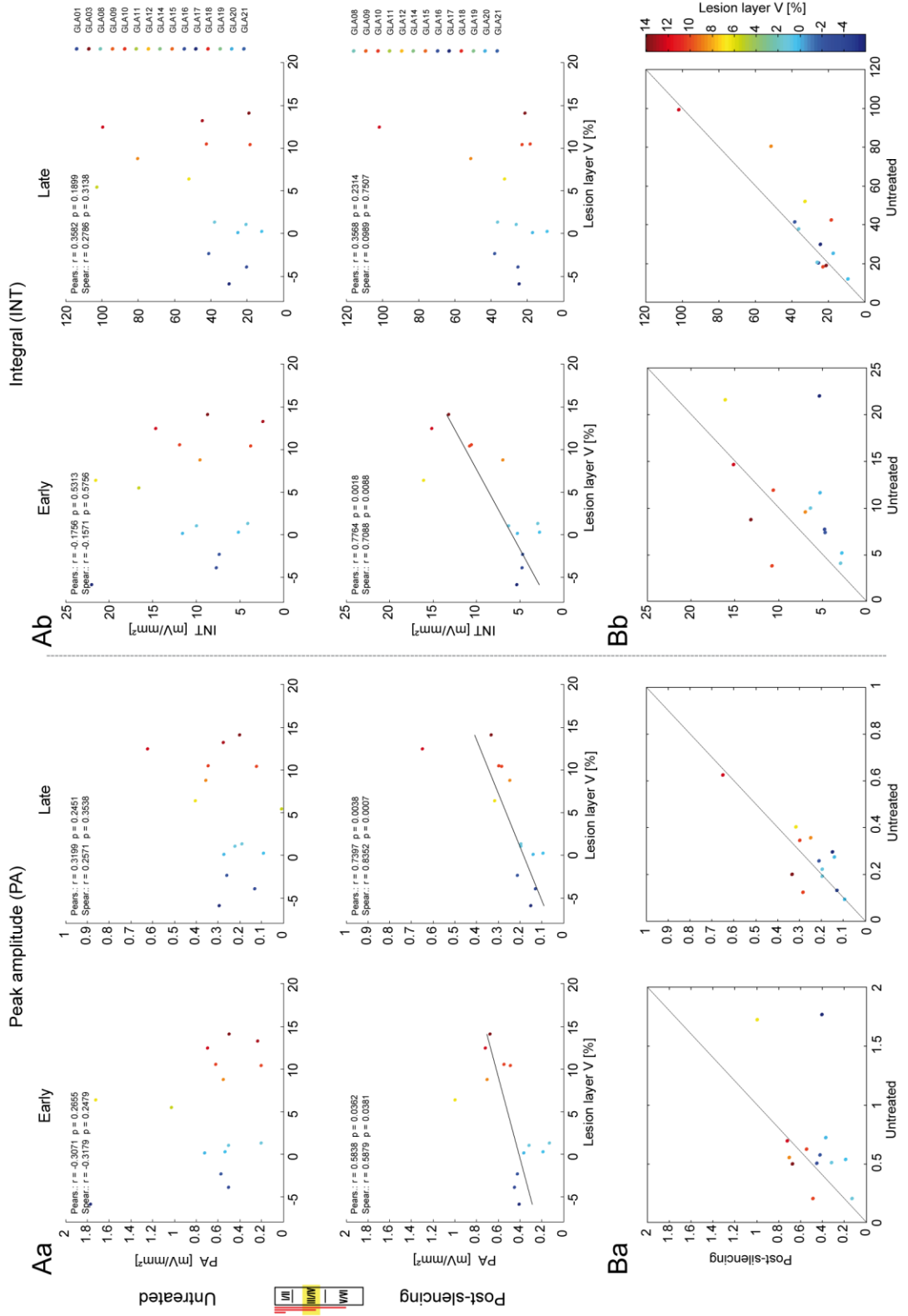


Figure 3.33 (preceding page): (A) Relationship between lesion strength in layer V, and PA (Aa) and INT (Ab) of AVRECs after Gstim (160 μ A). First row shows data before, second row after cortical silencing. The strengths of the sinks correlated with lesion efficacy in layer V after silencing. **(B)** Pre-post plot showing that AVRECs were smaller after muscimol in animals without, but remained similar or increased in animals with layer V lesions.

AVREC ICMS - IGstim - Lesion layer VI

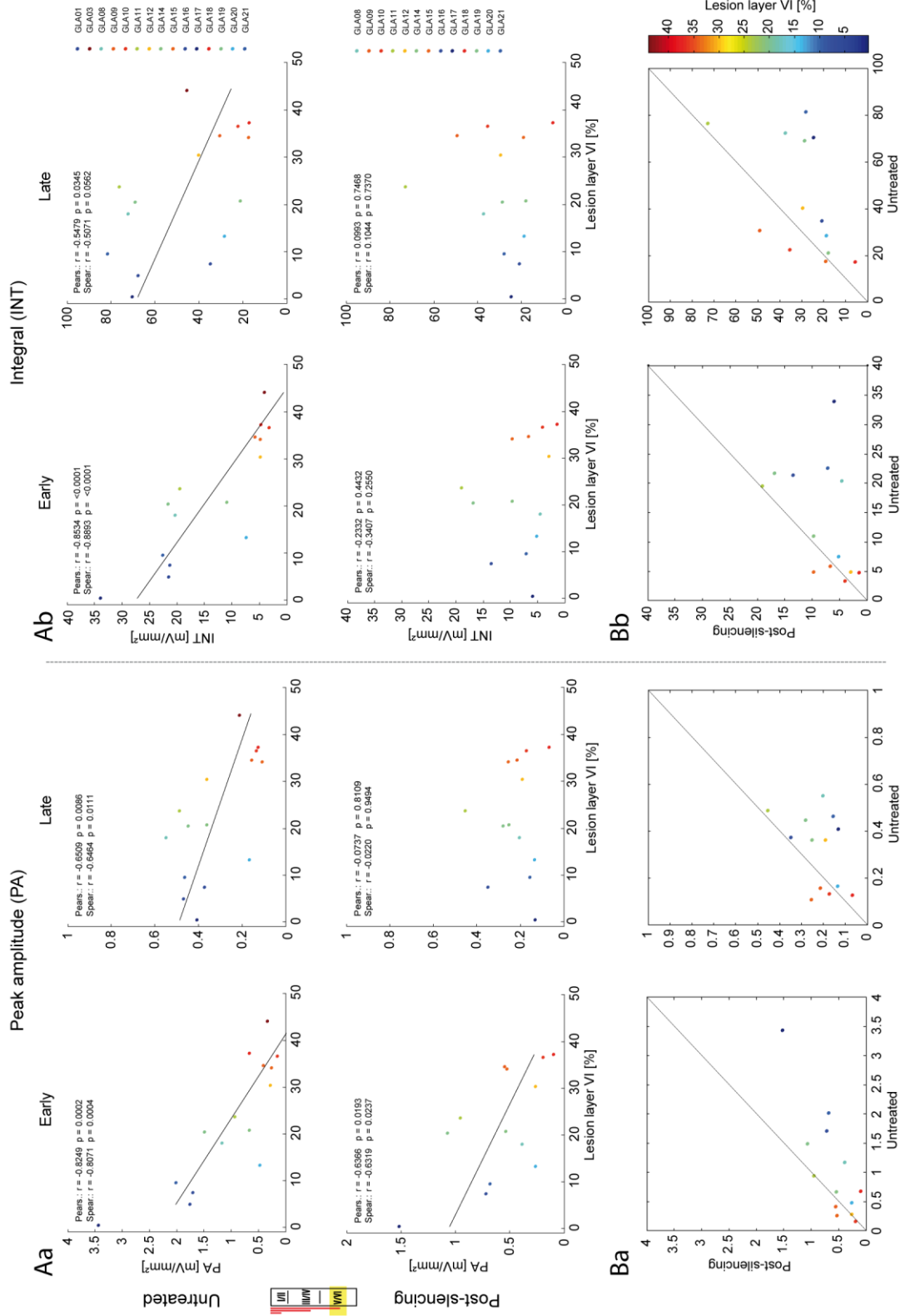


Figure 3.34 (preceding page): (A) Relationship between lesion strength in layer VI, and PA (Aa) and INT (Ab) of AVRECs after IGstim (160 μ A). First row shows data before, second row after cortical silencing. The strengths of the sinks decreased with higher lesion efficacy in both treatment conditions. **(B)** After muscimol, PAs and INTs remained equal in animals with very low values already in the unsilenced condition, and otherwise decreased.

3.3.8 Tables

Table 3.4: Definition of lesion groups¹

Lesion group	Neuronal loss [%]		N
	Layer V	Layer VI	
nwLes	≤ 5	≤15	3
Les V	> 5	≤15	1 (2)
Les VI	≤ 5	>15	4
Les V+VI	> 5	>15	5 (6)

¹Criteria (i.e. percentages of neuronal loss in layers V and VI) applied for the assignment of the individual cases to the respective lesion groups, and numbers of animals (N) assigned to these groups. Cases GLA01 and GLA03 were not included into the averaged CSD and AVREC profiles and to two-way repeated measures ANOVA (see Tab. 3.6) due to lacking muscimol data.

Table 3.5: Experimental animals used for CSD analysis²

Case	Hemi-sphere	Injection site	Cortical BF	Comments
GLA17	le	Caudomedial MGv	4 kHz	Very small injection
GLA20	le	Caudal MGv	1 kHz	
GLA21	le	(Rostro)ventrolateral MGv	1 kHz	Labeling very ventral, i.e. out of laser focus
GLA01	le	MGd	~1 kHz	Small injection; Incomplete muscimol effect; BF could not be reliably defined ; ICMS amplitudes: -40, -100, -120 μ A
GLA16	le	MGd	2 kHz	No nonBF data available for the post-silencing condition
GLA08	ri	Rostromedial MGB (RP)	2 kHz	
GLA10	le	(Rostro)central MGv	8 kHz	
GLA12	ri	Rostral MGm and MGv	1 kHz	
GLA18	le	Caudal MGv	1 kHz	
GLA03	le	MGv, partly MGd	1 kHz	No muscimol applied; ICMS amplitude: -120 μ A Large injection, lateral part of MGB necrotic
GLA09	le	Central MGv	0.5 kHz	
GLA11	le	Medial MGv, MGm and MGd-DD	0.5 kHz	
GLA14	le	Lateral MGv	1 kHz	
GLA15	le	MGB	1 kHz	Large injection, Caudal part of MGB necrotic
GLA19	le	Cental MGv	16-32 kHz	

² For each case, the injected and illuminated hemisphere, intrathalamic location of the injection site, and the BF encountered at cortical recording site are depicted, and, where required, comments. Background colors indicate the respective group assignments defined by the lesion strengths (see Tab. 3.4).

Table 3.6: Two-way repeated measures ANOVA³

Stimulus or stim. ratio	CSD sink or AVREC phase	Measure	Treatment	Treatm. x Les V	Treatm. x Les VI	Les V	Les VI
BF	S1	PA	0.004 ↓	0.590	0.198	0.827	0.220
BF	S1	INT	<0.001 ↓	0.615	0.064	0.747	0.178
BF	early	PA	0.002 ↓	0.829	0.273	0.836	0.230
BF	early	INT	<0.001 ↓	0.603	0.094	0.688	0.253
BF	late	PA	<0.001 ↓	0.865	0.231	0.758	0.434
BF	late	INT	0.002 ↓	0.988	0.380	0.825	0.527
nonBF	S1	PA	0.078	0.882	0.690	0.971	0.974
nonBF	S1	INT	0.220	0.751	0.934	0.610	0.768
nonBF	early	PA	0.130	0.279	0.305	0.730	0.851
nonBF	early	INT	0.143	0.257	0.212	0.636	0.610
nonBF	late	PA	0.037 ↓	0.734	0.752	0.739	0.818
nonBF	late	INT	0.176	0.741	0.561	0.798	0.634
BF/nonBF	S1	PA	0.697	0.576	0.502	0.564	0.534
BF/nonBF	S1	INT	0.700	0.567	0.503	0.566	0.508
BF/nonBF	early	PA	0.602	0.101	0.357	0.833	0.065
BF/nonBF	early	INT	0.019 ↓	0.206	0.028 ↓/↓	0.08	0.001 ↓/→
BF/nonBF	late	PA	0.042 ↓	0.545	0.316	0.956	0.216
BF/nonBF	late	INT	0.169	0.027 ↓/→	0.831	0.233	0.149
SGstim	S1	PA	0.873	432	0.858	0.064	0.159
SGstim	early	PA	0.981	0.056	0.536	0.137	0.364
SGstim	early	INT	0.265	0.010 ↓/↑	0.985	0.031 →/↑	0.361
SGstim	late	PA	0.206	0.311	0.076	0.025 →/↑	0.665
SGstim	late	INT	0.096	0.942	0.034 ↓/↑	0.607	0.573
Gstim	S1	PA	0.376	0.759	0.900	0.724	0.799
Gstim	early	PA	0.102	0.042 ↓/→↑	0.811	0.856	0.429
Gstim	early	INT	0.043 ↓	0.011 ↓/→↑	0.637	0.179	0.231
Gstim	late	PA	0.337	0.081	0.968	0.038 →/↑	0.826
Gstim	late	INT	0.980	0.542	0.493	0.219	0.544
IGstim	S1	PA	<0.001 ↓	0.739	0.001 ↓/→	0.359	0.001 ↓/↓
IGstim	early	PA	<0.001 ↓	0.067	0.001 ↓/→	0.931	0.002 ↓/↓
IGstim	early	INT	<0.001 ↓	0.006 ↓/→	<0.001 ↓/→	0.124	0.002 ↓/↓
IGstim	late	PA	<0.001 ↓	0.007 ↓/→	0.015 ↓/→	0.255	0.079
IGstim	late	INT	<0.001 ↓	0.063	0.005 ↓/→	0.897	0.277

³ The effect of the pharmacological treatment and apoptosis of CT cells in either layer V and/or VI as well as their interactions on the acoustically or electrically evoked sink S1 or the two phases of the AVREC. Interactions between LesV and LesVI were always n.s., and thus not included into the statistical model. The visually estimated direction of change is indicated by the orientation of the arrow. In treatment x lesion columns, the two arrows represent treatment changes in non-lesioned and lesioned (separated by a slash) animals. In lesion columns, the two arrows represent the changes seen in lesioned animals (compared to non-lesioned animals) before and after cortical silencing, respectively. ↓ - reduction; → - no change; ↑ - increase; →↑ - increase or no change.

4 Discussion

In this thesis, the anatomy and function of the thalamocortical (TC) and corticothalamic (CT) systems in the Mongolian gerbil were investigated by a combination of several anatomical, physiological, and pharmacological techniques. Using anterograde and retrograde tract tracing, we revealed a complex and specific anatomy of TC (and CT) connections regarding their nuclear origin in the MGB and their termination patterns in the auditory cortical fields and layers (4.1). Thereby, we characterized the ultrastructure of a so far unknown type of very large (“giant”) terminals, which arises from the MGm (4.2). Furthermore, using current source density (CSD) analysis following a photolytic apoptosis of CT neurons, both before and after cortical silencing with muscimol, we found the CT system to substantially modulate acoustically and electrically evoked cortical activity patterns (4.3, 4.4).

4.1 Anatomy of the auditory thalamocortical system

By electrophysiologically guided iontophoretic injections of an anterograde tract tracer, we here investigated the precise cortical distribution of terminals of smaller neuronal populations (summarized in Figs. 3.4 C-D, 3.7, 3.8). The projections of the MGB subdivisions to the diverse auditory fields, the relative strengths of these projections and their main target layers are illustrated in Figure 4.1 (for the construction of these diagrams, cases of pressure injections were also included; Saldeitis *et al.*, 2014).

The results derived from this approach extend previous knowledge about the anatomical organization of the auditory TC connections in gerbils from our and other laboratories and reveal new remarkable, but complex characteristics and functional implications of this network. Together with the results from other species, which will be discussed in detail below, we are now able to draw a more extended and refined picture of the mammalian auditory TC system.

4.1.1 MGv

We parcellated the gerbil's MGv into LV, OV, and RP. The question about the assignment of the region around the rostral pole of the MGB (RP) either to diverse nuclei of the metathalamus (including the MGB) or to the posterior thalamic group, respectively, has been discussed by various authors (Jones

and Powell, 1971; Imig and Morel, 1985a; Winer *et al.*, 1999a; Cant and Benson, 2007), but was not resolved conclusively. In the gerbil, a recent study described RP using Golgi- and Nissl-stained material (Mylius *et al.*, 2013) and assigned it to the MGv as a third subdivision based on the similarity of the cell types within these subdivisions. This classification is also in accordance with previous studies on the MGB of the gerbil using markers for cellbodies and myelinated fibers (Budinger *et al.*, 2000b; Cant and Benson, 2007), calcium-binding proteins (Budinger *et al.*, 2000b), and cytochrome oxidase activity (Cant and Benson, 2007), which already allocated the region corresponding to the RP to the MGv. Here, we provide first detailed information about the physiology and cortical connections of the RP region in this species.

In the gerbil, the primary target of the LV is AI, but other auditory fields (AAF, posterior and ventral fields) are also innervated. Notably, the LV does not innervate all parts of the core AC in a strong way, since field AAF, which is considered primary in the Mongolian gerbil (Scheich *et al.*, 1993; Thomas *et al.*, 1993; Budinger *et al.*, 2000a; b) and in other species (e.g., mouse: Llano and Sherman, 2008; cat: Lee and Winer, 2008) receives only minor inputs from LV. In contrast, the posterior fields DP and VP, which are not primary but still tonotopically organized, contained a large amount of labeled terminals. Therefore, the prevailing view that the MGv/LV projects almost exclusively to primary AC (derived from key studies, e.g., mouse: Llano and Sherman, 2008; rat: Vaudano *et al.*, 1991; Kimura *et al.*, 2003; cat: Mitani *et al.*, 1987; monkey: Hashikawa *et al.*, 1995; for review: Lee, 2012) is too simplistic. This conclusion is also supported by other, often more recent studies, demonstrating, for example, substantial MGv-LV projections to posterior and ventral auditory fields (rat: Romanski and LeDoux, 1993; Smith *et al.*, 2012; cat: Andersen *et al.*, 1980; Rodrigues-Dagaëff *et al.*, 1989; Huang and Winer, 2000; Winer *et al.*, 2005; Lee and Winer, 2008; Hackett, 2011). Interestingly, in cats, the projections to AAF were also found to be outnumbered by those directed to posterior auditory fields (Huang and Winer, 2000). It was also shown that cells projecting to AI and AAF belong to separate thalamic populations of the LV, the former group being larger than the latter one (Lee *et al.*, 2004a; Lee and Winer, 2005). A possibly similar organization in gerbils could account for the low number of projections to AAF as observed after small iontophoretic deposits of

the tracer. Thus, our results would be consistent with the hypothesis of two, largely independent TC processing channels towards AI and AAF (cat: Imaizumi *et al.*, 2004; Lee *et al.*, 2004a).

Neurons of the OV in the gerbil project to the same fields as the LV, namely to AI, AAF, posterior, and ventral fields. In contrast to LV projections, however, the terminal focus is shifted towards more ventral parts of the AC, i.e., to middle and ventral parts of AI, and to the ventral fields. Comparisons to other mammals are difficult, because to our knowledge, most tracing studies did not distinguish between LV and OV projections. In rat, however, it was reported that both the OV and the LV project heavily to primary AC (Te1) and more sparsely to its ventral part Te1v (Romanski and LeDoux, 1993).

Following tracer injections into RP, labeled axons could be preferentially found in dorsal auditory areas including D, Ald, and the dorsal part of AI whereas in central parts of AI, terminals were rare and scattered. Comparing our results with those of other species, we found remarkable similarities in particular with cats. In that species, RP has been shown to project to the broadly tuned dorsal zone (DZ) (Middlebrooks and Zook, 1983; Winer and Lee, 2007; Lee and Winer, 2008), dorsal AI, and weakly to the remaining AI (Lee *et al.*, 2004a; Lee and Winer, 2011a; Read *et al.*, 2011). In contrast, the cat's AAF is at least as strongly innervated by the RP as the DZ (Lee *et al.*, 2004b; Winer and Lee, 2007; Lee and Winer, 2008), which is not the case in gerbils, whose AAF is generally very sparsely innervated. With respect to that, it seems noteworthy to mention that in cats neurons projecting to either AAF or DZ were topographically segregated within RP (Lee and Winer, 2008). Such an organization could in principle also exist in gerbils. However, since in our experiments the tracer was confined to various locations within RP, but never resulted in strong labeling of AAF, the RP of cat and gerbil seem to be not completely homologous.

Axons from the LV form dense plexuses centered in cortical layer IV, some collaterals terminating also in infra- (Vb) and supragranular (I) layers, which largely agrees with the classic view of thalamic input layers (mouse: Frost and Caviness, 1980; Llano and Sherman, 2008; rat: Romanski and LeDoux, 1993; Kimura *et al.*, 2003; Smith *et al.*, 2012; cat: Mitani *et al.*, 1984; Huang and Winer, 2000; monkey: Jones and Burton, 1976; Hashikawa *et al.*, 1995). While

in our study infragranular terminals were mainly located in layer Vb, in others they were found to be denser slightly deeper, i.e., at the junction of layers Vb and VI (Jones and Burton, 1976; Romanski and LeDoux, 1993) or in (upper) layer VI (Hashikawa *et al.*, 1995; Kimura *et al.*, 2003; Llano and Sherman, 2008, Smith *et al.*, 2012). The overall laminar profile of the OV is in accordance with the classical view of MGv projections (see above) since layers IV and III(b) contained the highest percentages of terminals. Notably, compared to the LV, injections into the OV produce a higher proportion of layer III terminations, particularly in AI. We assume that this may be also the case in other mammals but has not been reported in previous studies probably because the LV and OV projections were not considered separately. We could also identify two distinct cluster types along what appeared to be the same IFC in AI, located in central and ventral parts of AI, respectively. They differ in both shape and terminal laminar distribution, namely that the dorsal cluster is composed of parallel aligned ascending axons with terminals in layers I-Va, being centered in layer Va, whereas the ventral cluster forms the more commonly found densely branched structure focused in layers IV and Vb. The question whether distinct cell types or neuronal populations with different frequency response properties are the source of the different laminar projection patterns in AI as well as of the projections to ventral fields still remains unanswered and requires further investigations. The laminar projection patterns of RP observed in the current study correspond largely to the general view of middle cortical layers being preferentially targeted by core (lemniscal) thalamic inputs and further support its belonging to the MGv. In comparison to LV projections, however, RP terminals are less restricted to layer IV, i.e., the overall laminar profile is more balanced between layers III, IV, and V(a) and thus closely resembles the overall cortical layer-specific projection pattern of OV (Fig. 3.8). Nevertheless, in several fields (AAF and D), layer IV is still the dominant target layer.

We observed two kinds of topographic relationships of TC connections between MGv and AC. The first one involves the tonotopic organization of the projections of the laminated subdivisions LV and OV to the AC. As expected from previous anatomical tracing (gerbil: Budinger *et al.*, 2000b, 2013; Cant and Benson, 2007; Budinger and Scheich, 2009; rabbit: Cetas *et al.*, 2001; cat: Andersen *et al.*, 1980; Morel and Imig, 1987; for review: Rouiller, 1997; Lee and Winer,

2011b) and electrophysiological studies (gerbil: Bäuerle *et al.*, 2011; rabbit: Cetas *et al.*, 2001; cat: Aitkin and Webster, 1972; Calford and Webster, 1981; for review: Rouiller, 1997; Edeline, 2011) we found a tonotopic organization of the LV and its connections with the tonotopic fields of the AC (especially with AI, but also with AAF, and DP/VP). In LV, the tonotopic organization is in parallel with the orientation of its fibrodendritic laminae as seen in Golgi preparations (Mylius *et al.*, 2013). Specifically, neurons located in rostromedial laminae of the LV respond best to low frequency (lf) tones and project to the caudal AI, which is known to represent lf tones as well (Scheich *et al.*, 1993; Thomas *et al.*, 1993), whereas neurons located in caudomedial laminae of the LV are rather tuned to high frequencies (hf) and project preferentially to the rostral hf AI. The width (300-600 μm) and appearance of the cortical terminal clusters correlate with the frequency-specific columnar activity patterns in the AC as visualized using metabolic 2-DG (Scheich *et al.*, 1993) and thallium-autometallography (Goldschmidt *et al.*, 2004, 2010) following an acoustic stimulation of gerbils with pure tones. This indicates that the TC input of LV may essentially account for the frequency-specific patterns of cortical neuronal activity. Our findings that most of the tonotopic input to AI is confined to layer IV while layer II is almost devoid of terminals may explain the local (fine-scale) vs. global (fractured on a small scale) tonotopic gradients in layers IV and II, respectively (e.g., Bandyopadhyay *et al.*, 2010; Rothschild *et al.*, 2010; for review: Kanold *et al.*, 2014). In addition to their precise tonotopic projections, TC axons originating from the LV also diverge into neighboring frequency-representation areas (at least of AI) mainly by forming axon collaterals, which branch out in infragranular layers and form small terminal patches rostral and caudal to the tonotopic labeling. Such a patchy divergence across the tonotopic gradient correlates well with recent studies on gerbils (Budinger *et al.*, 2013) and cats (Lee *et al.*, 2004a, b). These studies investigated the distribution of retrogradely labeled somata in the MGB after simultaneous injections of different retrograde tracers into different frequency representation areas of AI. Here, a few single-labeled somata at non-frequency-matched regions (as well as some double-labeled cells) were always identified in the LV.

The circular structure of OV, which is most obvious in Golgi preparations and characteristic for this subdivision (gerbil: Mylius *et al.*, 2013; rat: Clerici *et al.*,

1990; Clerici and Coleman, 1990; Winer *et al.*, 1999a; rabbit: Cetas *et al.*, 2002; Cetas *et al.*, 2003; cat: Morest, 1965; for review: Winer, 1992), underlies also the circular tonotopic organization of OV. According to a recent retrograde tract tracing study in gerbils (Budinger *et al.*, 2013) and electrophysiological studies in, e.g., rabbits (Cetas *et al.*, 2001) and cats (Calford and Webster, 1981; Imig and Morel, 1983; Imig and Morel, 1985b; Rouiller and de Ribaupierre, 1985), OV comprises a separate tonotopic map, in which the frequency gradient runs from central (lf) to peripheral (hf). Our results are in accordance with these findings since neurons, for example, located in the periphery of the OV responded best to hf tones and projected to the rostral hf region of AI. The observation that the terminals from OV cover several octaves in AI may be explained by either the spread of the tracer into several frequency-laminae, by a less strictly ordered arrangement of frequency representations in OV compared to LV (e.g., rat: Clerici *et al.*, 1990; rabbit : Cetas *et al.*, 2001; cat: Aitkin and Webster, 1972; Calford and Webster, 1981; Calford, 1983; Rouiller and de Ribaupierre, 1985; Morel *et al.*, 1987), by a more broadly tuned resp. multi-peaked responsiveness of OV neurons (see also Cetas *et al.*, 2001), or by a higher cortical divergence of individual thalamic axons (Budinger *et al.*, 2013). Unlike in the LV and OV, we could not identify any structural lamination nor frequency selectivity in the RP (see also Mylius *et al.*, 2013). However, we do not see that these characteristics are sufficient enough to consider RP as an extension of MGd (bat: Wenstrup and Grose, 1995). A non-laminated region in the anterior pole of the MGv without a systematic frequency gradient has also been reported in rabbits (Cetas *et al.*, 2001) but not cat (e.g., Imig and Morel, 1985b). In the gerbil, the weak frequency-selectivity of the RP neurons corresponds also to their cortical projections in that their terminals were either located in non-tonotopically organized auditory cortical areas (D, Ald) and were distributed over large regions of the tonotopic map of AI and AAF.

The second topographic relationship involves a gradient of inputs, which is oriented perpendicular to the cortical frequency gradient, i.e., parallel to the IFCs (Fig. 3.4 D). Specifically, the rostrocaudal position of the injection sites within the MGv corresponds to the dorsoventral position of preferential thalamic inputs across the entire AC including all fields. In the gerbil, this topography has not been described before, though results of previous tracing studies of this

species can be easily included into this scheme (Budinger *et al.*, 2000b; Budinger and Scheich, 2009). However, a rostrocaudally orientated topography within the MGv that is based on its tectal afferents has been demonstrated (Cant and Benson, 2007). According to this study, the rostral part of the MGv receives preferential input from rostromedial parts of the inferior colliculus (IC), whereas the caudal part is mostly innervated by caudomedial parts of the central nucleus of the IC (CIC). These two areas of the CIC receive, in turn, different inputs from the brainstem (Cant and Benson, 2006). Taken together, these results support the notion of segregated and functionally different pathways within the lemniscal (core) part of the ascending auditory system. Indeed, growing evidence suggests that topographic relationships other than tonotopic organization exist in the mammalian TC system. For example, as in gerbils also in rats (Roger and Arnault, 1989; Polley *et al.*, 2007; Storace *et al.*, 2010), guinea pigs (Redies *et al.*, 1989), and cats (Andersen *et al.*, 1980; Imig and Morel, 1983; Brandner and Redies, 1990; Read *et al.*, 2011), the rostrocaudal position of MGv (LV/OV) neurons correlates with the dorsoventral position of their terminal fields in the AC. Likewise, a considerable number of studies reported that the cat DZ is preferentially innervated by the RP (Middlebrooks and Zook, 1983; Huang and Winer, 2000; Winer and Lee, 2007; Lee and Winer, 2008). Interestingly, there is also a rostrocaudal gradient in the expression of molecular markers, such as vesicular glutamate transporters, in the MGv of rats and mice (Ito *et al.*, 2011; Storace *et al.*, 2012). The functional roles of the here mentioned topographic relationships within the TC auditory core pathway are uncertain, but they are consistent with segregated streams, e.g., for the processing of temporal and spatial (Middlebrooks and Zook, 1983; Kimura *et al.*, 2007) or broadly and narrowly tuned spectral (Read *et al.*, 2001; Storace *et al.*, 2011) information.

A modular organization of LV projections to AI in particular is not only evident in the rostrocaudal direction, but also in the dorsoventral direction in the form of small terminal patches along the IFC. These patches could correspond to clusters of neurons with similar binaural properties (gerbil: Caird *et al.*, 1991; cat: Imig and Adrian, 1977; Middlebrooks *et al.*, 1980; for review: Schreiner and Winer, 2007), tuning characteristics (Read *et al.*, 2001), periodicity preferences (gerbil: Schulze and Langner, 1997; Schulze *et al.*, 2002), or reflect zones of

alternating callosal and TC inputs (rat: Vaughan, 1983; cat: Imig and Brugge, 1978; monkey: Pandya and Rosene, 1993).

All together, the largely tonotopic projections to layer IV of the primary AC strongly support the notion that the LV in gerbils belongs to the central (core, lemniscal) ascending auditory system as reported so far for all other mammals (for review: Malmierca and Merchán, 2004; Rouiller, 1997). It acts as a “specific” thalamic nucleus suited to drive cortical activity and to contribute to the spectral analysis of the acoustic stimuli (Sugimoto *et al.*, 1997; Happel *et al.*, 2010). The diverging projection fibers indicate that spectral information conveyed to cortex by its TC input is not relayed in a strict point-to-point (or -stripe) manner as suggested previously (rat: Scheel, 1988; rabbit: Velenovsky *et al.*, 2003; guinea pig: Redies *et al.*, 1989; cat: Andersen *et al.*, 1980; Calford and Aitkin, 1983; Brandner and Redies, 1990; Calford and Aitkin, 1983; Lee and Winer, 2005; review: Hu, 2003), but rather that the LV mediates cortical responses to BF and near BF stimuli (Metherate *et al.*, 2005). The MGv has also been shown to evoke tone specific plasticity in the AC (e.g., Ma and Suga, 2009), which could be based on the diverging heterotopic projections from the LV (Lee *et al.*, 2004b; Liu *et al.*, 2011), but may also be attained in collaboration with the corticofugal system, as are further possible functions treated in context of bidirectional interactions with the auditory cortex (see 1.1, 4.3, and 4.4).

OV and LV are usually suggested to serve similar functions in the physiological literature (e.g., Aitkin and Webster, 1972). Functional differences of OV and LV have been proposed only in one study on guinea pigs based on the simpler firing patterns of OV neurons (only phasic ON-reponses) compared to LV neurons (Zhang *et al.*, 2008). Although OV shares many properties with LV, such as similar cell types, laminated (though circular) structure, tonotopic organization, and similar target fields (Mylius *et al.*, 2013; Budinger *et al.*, 2013; present study), and it most likely belongs to the central (core, lemniscal) auditory pathway, we expect substantial functional differences between LV and OV, especially with respect to the stronger OV projection to ventral parts of the AC, their differential laminar innervation of AI, and their tuning properties. Via its strong projections to V and VM, which have been suggested to operate on a higher hierarchical level of cortical processing than AI (gerbil: Thomas *et al.*, 1993; Budinger *et al.*, 2000a; rat: Kimura *et al.*, 2007; but see also Storace *et*

al., 2010; Storace *et al.*, 2011, who designate the rat ventral auditory field to the core), OV may influence directly (and without temporal delay due to intracortical processing) associative functions.

The functional role of the RP and its influence on the AC is still unknown. Based on the present results we suggest that the RP is less engaged in the spectral analysis of tones but provides a strong feedforward input into the AC because the acoustically evoked responses are very strong, reliable, and fast, and because many terminals can be found in layers IV/IIIb. The RP may therefore represent a main source of driving inputs to D and Ald, which could play specific roles in sound localization (DZ cat: Stecker *et al.*, 2005; Malhotra *et al.*, 2008) or in the integrative analysis of broadband stimuli (Ald cat: Schreiner and Sutter, 1992; Ehret and Schreiner, 1997).

4.1.2 MGd

On the basis of our results and previous anatomical studies (Budinger *et al.*, 2000b; Mylius *et al.*, 2013) we subdivided the MGd into two parts: the DD and the "remaining" MGd (MGd *proper*). Labeled axons and terminals, arising from the MGd *proper*, terminate in primary (AI, AAF) and non-primary (DP, V/VM) auditory fields. Projections to the primary fields are weak and rather diffuse (likewise in other mammals, e.g., mouse: Llano and Sherman, 2008; rat: Vaudano *et al.*, 1991; Winer *et al.*, 1999b; Kimura *et al.*, 2003; cat: Huang and Winer, 2000; Winer and Lee, 2007; monkey: Hashikawa *et al.*, 1995; Molinari *et al.*, 1995); however, in addition to this diffuse labeling we found also a large number of terminals at the rostral edge of AI, which most likely belongs to the transition zone between AI and AAF. This region has been shown to exhibit physiological features distinct from those found in other parts of AI and AAF (e.g., broad frequency-tuning: Thomas *et al.*, 1993; Schulze *et al.*, 1997). However, the posterior (DP) and the ventral fields (V/VM) are the main cortical targets of the gerbil's MGd (Budinger *et al.*, 2000b; present study). In rats, the two presumably equivalent auditory fields, namely the posterodorsal field (PD) and the ventral auditory field (Te3v/VA) likewise have connections with the MGd (Kimura *et al.*, 2003; Kimura *et al.*, 2004; Donishi *et al.*, 2006; Kimura *et al.*, 2007; Polley *et al.*, 2007; Smith *et al.*, 2012). Also in mice (Llano and Sherman,

2008) and cats (e.g. Huang and Winer, 2000), the MGd was found to project to auditory areas, which are located posterior and ventral (All) to AI.

In the gerbil, the DD projects similar to MGd *proper* to AI, DP/VP, V/VM, and sparsely to AAF. Its projections to AI, however, are considerably stronger. Compared to other mammalian species, there are variances in the reports: Some authors found the DD of cats to be connected with tonotopically organized fields such as AI, AAF, P, VP (Andersen *et al.*, 1980; Imig and Morel, 1983), similar to the MGv, whereas others found more similarities with other MGd subdivisions through preferred projections to non-tonotopically organized fields (Winer, 1985; Huang and Winer, 2000; Lee and Winer, 2005). In rats (Kimura *et al.*, 2003), in addition to field PD, the (rostro)ventral margin of Te1/AI was found to be strongly innervated by DD neurons. This is similar to one of our cases (G-13-r, not illustrated), where many terminals could be identified in ventral fields and the adjacent (rostro)ventral AI.

The specificity of targeted fields and layers may be related to the cell type in DD. In one case (Fig. 3.6), no labeling was found in V/VM, but instead a very large proportion of terminals in layer Va of AI, AAF, and DP. In that case, most of the labeled neurons were bitufted (Mylius *et al.*, 2013). In the other DD injection, the labeled neuronal population was more heterogeneous and projections were also found to V/VM and less restricted to layer Va in ventrorostral parts of AI.

Axons from the gerbil's MGd *proper* terminate in middle layers (non-primary fields and AI-AAF border region), infragranular layers (mainly primary fields), and layer I (all innervated fields). The descriptions available respecting the laminar targets of the MGd in non-primary fields of other mammals are in large agreement with our findings, as they report the terminals to be located in layers IIIb/IV (focalized), layer I, and sometimes in infragranular layers (diffuse) (Huang and Winer, 2000; Kimura *et al.*, 2003; Llano and Sherman, 2008; Smith *et al.*, 2012). In monkeys, the bulk of terminals assemble in layer IIIb rather than layer IV (Jones and Burton, 1976; Hashikawa *et al.*, 1995).

With respect to their laminar targets the two MGd subdivisions share a relatively high proportion of terminals located in layer I (especially in AI) in comparison to other divisions and subdivisions of the MGB. In contrast, a very conspicuous feature of the DD projections is that most of its terminals can be found in layer

Va of the AC (except V/VM). In cats, the DD was shown to send its projections preferentially to layers IV and I (Huang and Winer, 2000) and in rats, its terminals were found in layers IIIb/IV and upper layer VI, but not in Va (Kimura *et al.*, 2003). During CSD experiments performed in rats (Kaur *et al.*, 2005) and also in some of our recordings, however, short latency sinks appeared in layer Va of non-CF regions, which could be mediated by the DD innervations described here. Respecting the CSD recordings made within the frame of this work, ICMS in animals whose CT projections had been eliminated often evoked a sink in layer Va as well (see Figs. 3.27 and 3.28), which did not disappear after silencing of polysynaptic intracortical connections. Potentially, these sinks could be caused by a CTC-loop involving the DD.

We showed that in the gerbil, as in most other species, MGd neurons are broadly tuned, have long latencies, and are frequently less responsive to pure tones (mouse: Anderson and Linden, 2011; rat: Bordi and LeDoux, 1994a; Hu, 1995; guinea pig: Anderson *et al.*, 2007; Zhang *et al.*, 2008; cat: Calford and Webster, 1981; Calford, 1983; Imig and Morel, 1985b; Rouiller and de Ribaupierre, 1985; Morel *et al.*, 1987). A possible tonotopic organization of the MGd has been suggested; a tonotopic map, however, is most likely less exact, regular, or complete than in the MGv (discussed by, e.g., Winer, 1985; Budinger *et al.*, 2013). In the gerbil, the electrophysiological properties of DD neurons differ from those of other parts of the MGd with respect to their response strengths and latencies, but also from those of the MGv (LV, OV) in having a poorer frequency-selectivity. These properties largely agree with findings in cats. The strength of auditory responses in DD is higher compared to units from other subdivisions of the MGd, onset latencies are usually a little bit longer than those in the MGv, and DD units are just moderately tuned to frequencies (Calford, 1983; Calford and Aitkin, 1983; Imig and Morel, 1985b). A possible tonotopic organization of DD has been suggested by several authors (gerbil: Budinger *et al.*, 2006; Budinger *et al.*, 2013; rat: Roger and Arnault, 1989; Clerici *et al.*, 1990; cat: Andersen *et al.*, 1980; Imig and Morel, 1983) but could not be confirmed by others (cat: Calford, 1983; Calford and Aitkin, 1983). In the present study, local terminal maxima, whose positions on the tonotopic map of AI correspond to the frequency-range of the injected DD neurons, were indeed

found. This would suggest a certain degree of tonotopic connections between DD and AI and thus also to a coarse tonotopy of DD.

Together, our anatomical and physiological findings fully agree with the idea that the MGd is part of the non-lemniscal auditory pathway. By means of its connections with hierarchically higher auditory fields, which, in turn, are substantially connected with higher-order integration and association areas (e.g., Budinger *et al.*, 2000a; Kimura *et al.*, 2004; Kimura *et al.*, 2007), it is conceivable that the MGd is involved in various associative functions including multisensory integration (Calford and Aitkin, 1983; Bordi and LeDoux, 1994b; Budinger *et al.*, 2006; Henschke *et al.*, 2015) and spatial as well as emotional auditory processing (Stecker *et al.*, 2003; Kimura *et al.*, 2004; Kimura *et al.*, 2007). The functions of the DD are largely unknown in gerbils as well as in other species. Considering its unique laminar targets (especially Va), we expect the DD to activate cortical circuits different from those activated by other MGB subdivisions (which rather project to deep infragranular layers). For example, neurons of the DD could be strongly involved in the modulation of transcallosal projections since a significant portion of the commissural neurons as well as their contralateral axonal terminations are located within sublayer Va (gerbil: Budinger *et al.*, 2000a; rat: Games and Winer, 1988). Based on the finding that both neurons of the DD and of the posteromedial thalamic nucleus (POm) of the paralemniscal trigeminal system (e.g., Wimmer *et al.*, 2010) terminate mainly in cortical layer Va (and I), the DD could represent an important thalamic structure of an analogous pathway in the auditory system. Physiological investigations in non-lemniscal or in border regions between lemniscal and non-lemniscal thalamic divisions of the MGB revealed that they are specifically involved in the coding of lf temporal information including slow TC oscillations (He, 2003, Abrams *et al.*, 2011). This resembles the processing scheme proposed for the paralemniscal trigeminal pathway (e.g. Ahissar *et al.*, 2000: temporally encoded information in the lf range is decoded by the paralemniscal system). Whether the neurons of the gerbil's DD have similar temporal coding properties remains to be elucidated.

4.1.3 MGm

Labeled neurons of the MGm project to all auditory fields except V/VM. Compared to MGv and MGd, MGm has a higher proportion of projections to AAF. The axons tend to diverge and distribute widely within and across these fields, which coincides with a number of studies made in several species (mouse: Caviness and Frost, 1980; rat: Ryugo and Killackey, 1974; Winer *et al.*, 1999b; Kimura *et al.*, 2003; Polley *et al.*, 2007; guinea pig: Redies *et al.*, 1989; Redies and Brandner, 1991; tree shrew: Oliver and Hall, 1978; cat: Imig and Morel, 1983; Morel and Imig, 1987; Rouiller *et al.*, 1989; Huang and Winer, 2000; Lee and Winer, 2005; Lee and Winer, 2008; monkey: Burton and Jones, 1976; Hashikawa *et al.*, 1995; Molinari *et al.*, 1995).

In our study, MGm terminals were mainly found in deep infragranular (Vb, VI) and supragranular (IIIb) layers. Regarding the laminar destination of the terminals there are no consistent data in the literature. Some authors identified layers I and VI (mouse: Caviness and Frost, 1980; cat: Winer and Lee, 2007), especially layer I, as the main recipient layer (rat: Herkenham, 1980; cat: Mitani *et al.*, 1984; Mitani *et al.*, 1987; monkey: Burton and Jones, 1976; Jones and Burton, 1976). Other authors reported middle and superficial (monkey: Hashikawa *et al.*, 1995), middle and deep layers (tree shrew: Oliver and Hall, 1978), layers I, III/IV, and VI (cat: Huang and Winer, 2000), or all layers (rat: Ryugo and Killackey, 1974) to be mainly innervated by the MGm. Notably, our findings correlate well with those from two studies on rats (Linke and Schwegler, 2000; Kimura *et al.*, 2003).

The projections from the MGm are widely distributed across the AC; thus, the connections between the AC and MGm are most likely not matched in frequency. Accordingly, our study as well as several other electrophysiological studies show that MGm neurons are usually tuned to a wider range of tones than neurons in the MGv (rat: Bordi and LeDoux, 1994a; guinea pig: Redies and Brandner, 1991; Anderson *et al.*, 2007; Zhang *et al.*, 2008; cat: Phillips and Irvine, 1979; Calford, 1983; Rouiller *et al.*, 1989), with no (guinea pig: Anderson *et al.*, 2007; Zhang *et al.*, 2008; cat: Phillips and Irvine, 1979; Calford, 1983) or a moderate tonotopic organization of the MGm (mouse: Hackett *et al.*, 2011a; rat: Bordi and LeDoux, 1994a; cat: Imig and Morel, 1984; Morel *et al.*, 1987; Rouiller *et al.*, 1989). In addition, MGm neurons process other sensory stimuli

as well (e.g. rat: Bordi and LeDoux, 1994b; Komura *et al.*, 2005; cat: Wepsic, 1966; Khorevin, 1978).

Due to its extremely short response latencies (present results; Bordi and LeDoux, 1994a; Malmierca *et al.*, 2002; Malmierca and Merchán, 2004; Wallace *et al.*, 2007; Anderson and Linden, 2011; Hackett *et al.*, 2011a), which could be partly result from a short direct (e.g., cochlear nucleus complex to MGm) pathway bypassing the IC (Malmierca *et al.*, 2002; Malmierca and Merchán, 2004; Wallace *et al.*, 2007), and to its multisensory response properties, the MGm could play a role in the fast integration of auditory and other information at the subcortical level (e.g., Bordi and LeDoux, 1994b; Komura *et al.*, 2005; Budinger *et al.*, 2006; Anderson and Linden, 2011), for example, in order to mediate rapid behavioral responses (e.g., eyeblink: Campolattaro *et al.*, 2007).

An interesting characteristic of the MGm projections in the gerbil is the repetitive arrangement of small terminal clusters along the rostrocaudal axis of the AC, which arise from the same axon. Because they obviously link certain cortical modules or columns (maybe with similar functional properties), individual MGm neurons might be able to orchestrate and synchronize the activity of multiple columns as seen in form of, e.g., stimulus-evoked, stimulus-induced, and inherent oscillations (e.g., Jeschke *et al.*, 2008; Brosch *et al.*, 2013). This linkage would also allow for processing of harmonic structures in natural sounds, an important cue for sound source segregation and communication (e.g., Fishman and Steinschneider, 2010).

A further compelling anatomical feature of MGm projections is that they bear extremely large (“giant”) synaptic boutons (up to 5 μm^2 cross-section area), which were not observed in the AC after injections into any of the other divisions of the MGB. To our knowledge, this morphological characteristic of TC terminals has not been described before, which motivated us to investigate their ultrastructure. Findings on and implications of the light and electron microscopic examinations of these boutons are discussed in the next section.

4.2 Light and electron microscopic characterization of MGm terminals

Giant boutons were found in fields AI, AAF, DP/VP, and D after injections into MGm. The main target field of the terminals differed from case to case and they were mainly found in deep infragranular layers, particularly in layer Vb (Fig. 3.6). In field D, their sublaminar restriction to layer Vb was not as evident (i.e., the boutons occupied the entire layer V of D). Due to their restriction to axons from the MGm we suggest that one or more specific neuronal cell types form these giant boutons. Whether there are different types of neurons forming giant boutons but having different areal and laminar target preferences, or whether there is one cell type projecting to various fields, has to be investigated further (see 4.6). The most likely candidate is the magnocellular neuron (gerbil: Mylius *et al.*, 2013; rat: Winer, 1985; Winer, 1992), which was in the majority among the labeled cells of the MGm.

The giant boutons observed by light microscopic examination had diameters of 2.5-3 μm (occasionally up to 4-5 μm) and were found in addition (i.e., on the same axons) to the “normal”, smaller terminals (diameter approx. 1 μm). Electron microscopically, we identified labeled boutons having cross-section areas of about 0.5-5 μm^2 (0.310 - 5.228 μm^2), which largely corresponds to the sizes observed by light microscopic examination¹.

The mean cross-section area of the MGm boutons (1.64 μm^2) far exceeds that of non-labeled cortical boutons (0.30 μm^2), as well as the areas reported so far for MGv [Kharazia and Weinberg, 1994: 0.43 μm^2 (layer IV); Smith *et al.*, 2012: 0.42 μm^2 (overall), 0.45 μm^2 (layer IV)]; MGd (Smith *et al.*, 2012: about 0.48 μm^2), and SG (Smith *et al.*, 2010: 0.29 μm^2) TC terminals. Therefore, the terminals emanating from the MGm probably comprise the largest of the auditory TC system. At other stations of the ascending auditory pathway, e.g.,

¹ Our measurements may underestimate the real bouton sizes due to the cutting plane. On the other hand, the average size of labeled boutons derived from our data set may be biased towards overestimation due to the preselection of ROIs. I.e., because of the rarity of very large boutons, ultrathin slices were excised only from cortical areas that contained those boutons. Nevertheless, the sizes of boutons determined by light (where all labeled boutons of the brain were analyzed) and electron microscopic examination did generally match, and also the much smaller size of intracortical boutons within the same specimen indicates that the boutons of MGm are in average unusually large.

endbulb and calyx of Held (for review: Ryugo and Spirou, 2009; approx. $10 \mu\text{m}^2$) and the descending auditory pathway, e.g., some CT terminals (e.g. Rouiller and Welker, 1991; Bartlett *et al.*, 2000; 2-10 μm in diameter), however, large endings are well-known and generally associated with rapid and reliable transmission of information (Ryugo and Spirou, 2009; Taschenberger and von Gersdorff, 2000; Petrof and Sherman, 2013).

Typically, single neurons integrate information from many thousands of converging synapses (e.g., projections arising from MGv and terminating in layer IV; Schoonover *et al.*, 2014). The MGm, however, provides sparse, but orderly distributed projections across several fields of the AC. To simultaneously activate and possibly boost synchronization of many cortical columns by only a few afferents, there may emerge the need for a high fidelity transmission system, which could be accomplished by powerful terminals such as the here described boutons arising from potential “master neurons” of MGm. Our ultrastructural analyses of these boutons provide a first step towards understanding how they could mediate this. As terminal size is thought to be a clear predictor of its potential power in influencing the postsynaptic target (Petrof and Sherman, 2013), their large size including multiple synaptic contacts may predestine them to meet these demands (only a few afferents needed for suprathreshold activation). One additional indication of having a high impact on postsynapses provides our observation that boutons from the MGm had a significantly higher proportion of mitochondria than non-labeled terminals (mitochondrial fractions: 0.266 vs. 0.032), suggesting they consume much energy. The fact that high mitochondrial proportions were present in MGm boutons of all sizes indicates that even smaller boutons may have a higher impact on postsynapses than other cortical boutons of comparable size.

Other studies have shown that layer IV TC boutons are also relatively rich in mitochondria (mitochondrial fraction: 0.21; Kharazia and Weinberg, 1994) and were, in contrast to layer II boutons, considered as „drivers” (Viaene *et al.*, 2011a). However, according to Schoonover *et al.* (2014), TC synapses from MGv are rather weak in transmission.

Possibly, the high speed (turnover) is also a characteristic of transmission of MGm (giant) boutons, whose action may complete a fast-acting ascending pathway from periphery up to the cortex (discussed in 4.1.3), considering that

MGm cells responded with very short onset latencies to acoustic stimuli. Whether they are able to follow prolonged input with hf repetition rates as the calyx of Held (Taschenberger and von Gersdorff, 2000) remains to be shown. In any case, the abundant mitochondria may support both operations at high speed and in a sustained manner (i.e., without succumbing to synaptic depression) by enabling, for example, a fast recycling of neurotransmitter.

The vast majority of labeled boutons synapsed onto dendritic spines, suggesting that the innervated cell type is a pyramidal neuron. The probability that the contacted cell is a spiny inhibitory interneuron is low given their rarity (for review: Markram *et al.*, 2004). In addition, other TC projections have been reported to terminate onto (non-GABAergic) spines of pyramidal neurons as well (Kubota *et al.*, 2007; Smith *et al.*, 2012). Therefore, and due to their columnar innervations pattern MGm synapses may mediate intracortical pyramidal-interneuronal gamma oscillations. This model involves the interplay of pyramidal cells and interneurons, triggered by an external stimulus driving the output of pyramidal neurons onto interneurons (Traub *et al.*, 1996), that in their turn inhibit pyramidal cells. This would implicate their involvement in binding of information to represent global features of a stimulus pattern, of arousal, and of short- and long-term memory processes (Gray *et al.*, 1989; Engel *et al.*, 2001; Engel and Singer, 2001; Herrmann *et al.*, 2004; Kaiser and Lutzenberger, 2005; Jensen *et al.*, 2007; Lakatos *et al.*, 2008; Ainsworth *et al.*, 2011), among others associated with gamma oscillations. Non-lemniscal thalamic input to cortex has indeed been shown to modulate oscillations (Barth and MacDonald, 1996) and synchronized gamma oscillations with near zero phase lag have been found over several millimeters (Engel *et al.*, 1991). The here described putative powerful, widely distributed synapses from MGm may therefore provide a neuronal mechanism explaining the generation of stimulus-induced (large scale) synchronization and oscillation across spatially separate columns (Gray *et al.*, 1989).

Taking the preferred infragranular localization of MGm boutons into account, they might also be suited to rapidly influence feedback projections by the innervation of strategically advantageous (effective) compartments (e.g., proximal dendrites) of corticofugal pyramidal neurons (Romanski and LeDoux, 1993; Thomson, 2010; Smith *et al.*, 2012; Viaene *et al.*, 2011b).

Boutons from MGm form multiple asymmetric synapses (Gray type I; Gray, 1959) with their postsynaptic targets, suggesting an excitatory (DeFelipe *et al.*, 1988; Conti *et al.*, 1989), probably glutamatergic transmission, as in other TC pathways (Kharazia and Weinberg, 1994). However, we could not always identify the type of synapse. This may be due to the preparation, e.g. cutting plane. Alternatively, rising evidence suggests that a simple classification into Gray type I and II synapses (Gray, 1959) is not always possible (Klemann and Roubos, 2011). Labeled boutons had round clear vesicles of about 30 nm in diameter, which are common features of glutamatergic vesicles (e.g., Harris and Sultan, 1995; Qu *et al.*, 2009; Harris and Weinberg, 2012). However, we found some terminals that had in addition also larger vesicles (50-100 nm in diameter), which could also have an oval shape. Those vesicles may either represent variations in glutamatergic vesicles size, possibly influenced by activity or other physiological conditions, or could contain cotransmitters (Ogawa *et al.*, 1989; Whitworth *et al.*, 2002). The large vesicles could also represent endosomal-like compartments, which appear during the reformation of synaptic vesicles after exocytosis (e.g., Takei *et al.*, 1996; Paillart *et al.*, 2003).

Despite the numerous indications that the labeled boutons from the MGm may form driver-like synapses, their identification as Class 1 (drivers) or 2 (modulators) (Lee and Sherman, 2011) should not be assumed purely on their anatomical features, since the synaptic properties of many glutamatergic pathways have not been explored so far. TC synapses are generally considered to be glutamatergic (e.g., Kharazia and Weinberg, 1994). With this in mind it would be interesting to know more about their pre- and postsynaptic receptor and transporter types. The differential expression of vesicular glutamate transporters (vGLUTs) (Hackett *et al.*, 2011b; Ito *et al.*, 2011; Lee and Sherman, 2012; Storace *et al.*, 2012) or the engagement of different types of glutamate receptors (GluRs) could implicate different functions of giant vs. normal boutons. As a result, these synapses could be characterized either as drivers, which allow the principal conduit of information flow by synapsing on ionotropic GluRs (iGluRs) only, or as modulators of neuronal activity by activating both iGluRs and metabotropic GluRs (mGluRs) (Lee and Sherman, 2009).

As discussed above, (labeled) MGm terminals display distinct features compared to (non-labeled) corticocortical and other synapses. However, with our methods, within the group of MGm boutons no clear cut distinction could be made between small and large boutons. Also, the coexistence of small and large boutons may be explained by a possible potential of the small terminals to grow, meaning that the wide range of sizes reflects differential plastic, e.g., activity dependent (Becker *et al.*, 2008) effects, which again suggests an involvement of MGm in memory processes.

4.3 Anatomy and influences of the corticothalamic system

4.3.1 Anatomy of CT connections

Retrograde labeling in the AC following tracer injection (retrobeads) into the MGB was confined to layers VI and V. Speaking for AI, CT cells originating from layer VI outnumbered those from layer V, which is in agreement with the literature (for review: Ojima and Rouiller, 2011). However, our injections did not include large deposits into non-lemniscal thalamic nuclei, especially MGd, which is likely to be an important target of layer V projections (e.g., Rouiller and Welker, 1991; Ojima, 1994; Bajo *et al.*, 1995; Takayanagi and Ojima, 2006). MGm was innervated from both layer VI and V neurons of AI, in agreement with a prior study in cats (Ojima, 1994), though larger proportions of layer V projections originated from other fields (DP/VP, AAF). Interestingly, also a few neurons of layer V appear to project to MGv - a finding that does not fully match the common view of the organization of the CT system. However, giant boutons (which are considered to originate from layer V) in MGv were occasionally reported (Rouiller & Durif, 2004; Budinger *et al.*, 2006), and a few layer V neurons probably project to MGv (Kelly and Wong, 1981). Thus, the MGv may also receive driver-like input from AI and the posterior auditory fields.

We had the impression that despite the largely topographic projection scheme of connections between AI and MGv, the degree of divergent and convergent connections (divergence: the axon of a CT neuron branches to affect multiple neurons along the tonotopic gradient of the MGB; convergence: innervation of a MGB neuron by many CT neurons from different frequency representations in AC) in gerbils is somewhat higher in the CT than in the TC system. According to a study in the gerbil using bidirectional tracers (Budinger *et al.*, 2013), the region of the anterograde labeling slightly exceeded the region of retrograde labeling in MGv after injections into AI, and there were also a few labeled somata at non-matched locations, in agreement with our observations. Similar findings in spite of a general high degree of reciprocity were also reported elsewhere (rat: Winer and Larue, 1987; mouse: Llano and Sherman, 2008; cat: Winer *et al.*, 2001; Lee *et al.*, 2004a, b; Rouiller and de Ribaupierre, 1990).

The portion of infragranular cortical neurons that project to the thalamus is not entirely known for the auditory system. It has been estimated that CT cells

account for about 50% of all neurons in layer VI [Prieto and Winer, 1999, Fig. 14; Kelly and Wong, 1981 (auditory system); Gilbert and Kelly, 1975 (visual); Zhang and Deschênes, 1997 (somatosensory)]. Taking this number as benchmark, the maximum cell loss achieved by the photolysis method in the animals used for CSD analysis may amount to 80-90% of layer VI CT neurons.

4.3.2 Effects of CT lesions on acoustically evoked activation (general activation patterns)

Based on connectivity strength, laminar target, onset latency and frequency specificity (see 3.1), the acoustically evoked sinks are supposed to mainly reflect the input of MGv neurons. Contributions from MGd and MGm following pure tone stimulation could not be identified with certainty. MGm instead of MGv could have evoked the very short latent deep infragranular sink (being earlier and stronger than granular activation) occasionally observed after nonBF stimuli (Fig 4.2). This suggestion would substantiate the hypothesis of a large-scale rapid activation of AC by MGm fibers (see 4.2). The sometimes pronounced initial sink in layer Va could have been produced by DD projections.

The fact that in the lesioned animals acoustic stimulation provoked interlaminar activation patterns generally resembling those seen in normal animals (Happel *et al.*, 2010) proves that tracer injections and laser treatment did not unspecifically disturb thalamic input and intracortical processing. Still, the loss of CT neurons, particularly those of layer VI caused changes in the acoustically evoked cortical CSD profiles.

First, the strengths of the initial granular (S1) and infragranular (iS1) sinks were slightly reduced in lesioned animals. Respecting S1, the effect disappeared after blocking of intracortical activity, suggesting that the granular activation is not only amplified by local (intralaminar) recurrent loops (Liu *et al.*, 2007), but also by CT neurons, probably via CTC loops. Thus, the loop is likely to hold a gain function, which is consistent with previous studies investigating the influence of CT projections on thalamic neurons (e.g., Deschênes and Hu, 1990; He, 1997; Zhang and Suga, 1997). The correlation between strengths of iS1 and lesion, on the other hand, remained significant after drug application. Speculating that (under normal conditions) the thalamic projections to deep infragranular layers (Saldeitis *et al.*, 2014; see 3.1) synapse onto CT cells, they

could modulate directly and fast, that means by bypassing the interlaminar cascade of information processing, the activity of corticofugally projecting pyramidal cells (Romanski and LeDoux, 1993; Thomson, 2010; Smith *et al.*, 2012; Viaene *et al.*, 2011b). Accordingly, the reduction of the iS1 in lesioned animals may be explained by the loss of these postsynaptic target cells.

In this context, the direct and rapid activation of CT pyramidal cells by TC axons may be also critical for stimulus-specific adaptation in the thalamus, which has been demonstrated to be a result of fast frequency-specific habituation regulated by the corticofugal system (Bäuerle *et al.*, 2011).

The elimination of layer VI CT neurons had also consequences for the later cortical processing (i.e., the sequential interlaminar cascade). The relative strengths of the extragranular sinks S2 and S3 compared to S1 (i.e. S2/S1 and S3/S1) increased with lesion strength in layer VI in the untreated cortex. This relationship was particularly observed at BF. At nonBF, the relative contributions of the extragranular components were not noticeably related to lesion strength and were generally higher than at BF, consistent with the results reported previously (Happel *et al.*, 2010)². The fact that both S2 and S3 were relatively stronger in lesioned animals indicates that they rely on common (intracortical) processes, which were interfered by the apoptosis of CT neurons. Layer VI CT neurons comprise vertically oriented intrinsic axons reaching up to layer III/IV [Ojima *et al.*, 1992 (auditory); Prieto and Winer, 1999 (auditory); Zhang and Deschênes, 1997 (somatosensory)], thereby being suitable for locally influencing cortical processing, i.e., within a cortical column. The mode of action of these recurrent intracortical collaterals is not unequivocally solved, and current hypotheses include both inhibitory and facilitatory mechanisms [Lee and Sherman, 2008 (auditory and somatosensory); Lee and Sherman, 2012 (auditory); Bolz and Gilbert, 1986; Bortone *et al.*, 2014 (visual); Kim *et al.*, 2014 (visual and somatosensory); Staiger *et al.*, 1996 (somatosensory)]. Our observations indicate a net inhibitory effect of these collaterals on later local cortical processing (a loss of layer VI cells resulting in a disinhibition). Whether that holds true for more complex stimuli and during wakefulness remains to be

² In the present work, probably a different (i.e., later) supragranular sink than by Happel *et al.* (2010) was analyzed due to the lack of the earlier one in many of our animals.

investigated. In any case, they are supposed to have a local modulatory role (Lee and Sherman, 2009).

4.3.3 Effects of CT lesions on frequency tuning

Spectral integration in AC has shown to be accomplished by a precise interaction of TC and intracortical networks (Wallace *et al.*, 1991; Miller *et al.*, 2001; Kadia and Wang, 2003; Kaur *et al.*, 2004, 2005; Metherate *et al.*, 2005; Liu *et al.*, 2007; Kurt *et al.*, 2008; Happel *et al.*, 2010; Moeller *et al.*, 2010), which are differentially recruited in time and space. In detail, TC or intracortical inputs, respectively, were found to be the dominant generators of the initial cortical activation, depending on whether a cortical site was stimulated with a tone frequency corresponding to its BF or to a spectrally distant frequency (Kaur *et al.*, 2005; Happel *et al.*, 2010).

In this study, we identified the CT projection neurons representing a further integral part of spectral processing insofar as they were critically involved in modulating sharpness of cortical frequency tuning. Specifically, we revealed that the tuning sharpness (here defined as the ratio between responses at BF and nonBF) of the initial components of the signal (S1, early phase of AVRECs) is reduced in animals with loss of layer VI CT neurons. This suggests a significant involvement of a fast-acting CTC loop, though we cannot exclude that local recurrent loops from CT intracortical collaterals to layer IV also play a role.

Notably, the responses one octave apart from BF were only slightly weaker than at BF, and their strength did not depend on lesion efficacy, which may be attributed to the finding from our confined iontophoretic injections that TC projections originating from the MGv (LV) (which do not run in a strict point-to-point manner) mediate responses to BF and nearBF stimuli (see also de Venecia and McMullen, 1994; Cetas *et al.*, 1999; Happel *et al.*, 2010). Thus, in the nearBF region, where TC and intracortical connections have their greatest overlap, the CT projections may play a subordinate role during spectral processing.

Although the relationship between strength of S1 and lesion level was (partly) abolished after pharmacological silencing, as one would expect under the assumption that then the acoustically evoked cortical activation should be

determined solely by the TC projections in all animals, we obtained inconsistent results of BF/nonBF ratios respecting the direction of change. This may be in part due to the narrower bandwidth after silencing (Kaur *et al.*, 2004; Happel *et al.*, 2010) and the therefore very small, even subthreshold signals at nonBF. However, the integrals of the AVRECS showed that after silencing the BF/nonBF ratio decreased in weakly, but not in strongly lesioned cases. Thus, the similar ratio before and after muscimol in strongly lesioned animals suggests that their tuning was barely influenced (i.e., sharpened) by CT feedback projections already in the untreated condition. Data from a previous study using normal animals (Happel *et al.*, 2010) also indicate that the BF/nonBF ratio (of S1 peak amplitudes) usually decreases after application of muscimol (untreated: 4.77, post-silencing: 3.27). The lower ratios compared to ours may be explained by the higher stimulus intensities used in that study (65-75 db SPL).

Together, we suggest the following influence of the cortical feedback projections on the thalamus upon acoustic stimulation: since S1 at BF, though less tightly correlated with lesion efficacy than the BF/nonBF ratio, was weaker in lesioned animals, the amplification of BF responses seems to contribute more to the sharpening of tuning than the suppression of nonBF responses. This suggests that CT neurons may particularly enhance thalamic responses at BF. However, also intra- and interlaminar short and long range connections influence tuning curves of cortical neurons, which means that the representation of frequencies is not exclusively inherited from afferent thalamic input. In addition, since thalamo-reticulo-thalamic interaction could attenuate a possible suppressive effect (which would lack in lesioned animals) onto thalamic nonBF responses, the effect of CT projections on the spectral responsiveness of thalamic cells could still be compatible with a model of center-surround inhibition (Zhang *et al.*, 1997; Miller *et al.*, 2002; for review: Alitto and Usrey, 2003). According to that CT feedback would amplify both excitatory responses (at BF) and inhibitory responses (at nonBF) to sharpen receptive fields. For instance, inactivating cortical regions outside the BF of a MGB neuron (in bats) has been shown to shift the tuning of thalamic neurons towards the inactivated frequency, which could be due to a release of cortically induced surround suppression (Zhang *et al.*, 1997). Complementary, electrical stimulation of an AI site whose BF

matches a MGv recording site has been demonstrated to elicit mainly facilitatory responses to pure tones. In contrast, if the stimulated site is frequency unmatched, a suppressive modulation results (Zhang and Suga, 2000). However, studies using guinea pigs (He *et al.*, 2002) and cats (He, 1997) reported strong facilitatory and only weak inhibitory effects of corticofugal modulation, similar to our results. The relative amounts of modulation that center vs. surround receive, may additionally be state-dependent (burst or tonic mode of thalamic neurons) (Destexhe, 2000).

To conclude, the results from our approach attempting to study the CTC loop complement a row of previous studies on the capability of CT projections to sharpen auditory thalamic receptive fields by demonstrating that the thalamic inputs re-entering the cortex have been modified by CT projections, leading to measurable differences in cortical responses. This is consistent with the concept of 'egocentric selection', which refers to the ability of cortical neurons 'to adjust and improve their own inputs' (Suga *et al.*, 2000). That means, by amplifying the responses of thalamic neurons that best encode the predicted signal (BF) and eventually suppressing the responses of neurons that do not (nonBF), the AC sharpens its own response profile.

Notably, the same manipulation method (photolytic apoptosis) was applied to investigate the CTC loop in the visual system (Eyding *et al.*, 2003). Using EEG to assess the effect of CT loss on cortical activity (V1), that study revealed an increase in receptive field size - a further indication for the general organisation principles across systems.

4.3.4 Effect of layer VI CT lesions on the electrically evoked cortical activation

Based on the observations that in normal animals the electrically evoked CSD pattern in AI looks similar to the acoustically evoked pattern, and that the granular sink S1, which is likely to reflect lemniscal TC input, can still be provoked by (granular and infragranular) ICMS after cortical silencing, it was hypothesized that ICMS triggers a local CTC loop (Jeschke, 2006; Happel *et al.*, 2014).

The consequences of eliminating layer VI CT pyramidal cells of AI, which mainly connect to MGv, are evidence of such recurrent feedback loop activation by

ICMS and of the necessary involvement of these neurons, as the respective CSD profiles were characterized by a complete or nearly complete absence of S1. The appearance of a granular sink during the untreated condition in some of the lesioned animals, however, suggests that also polysynaptic intracortical connections contribute to this sink.

The apparent contradiction with regard to the driver-modulator theory, according to that feedback projections from layer VI to lemniscal thalamus are modulatory rather than driving, can be explained by the strong electrical stimulation eliciting a simultaneous firing of thalamic neurons, sufficient to activate cortex by recurrent TC input.

Interestingly, in lesioned animals infragranular sinks were still observed before and after cortical silencing, particularly in cortical depths that were free of sinks in non/weakly lesioned animals, such as upper or middle layer V. Possible neural generators of these activations could either be CTC loops via subcortical structures (e.g., non-lemniscal thalamic nuclei), or monosynaptic intracortical projections. As the analysis of relative residues (Harding, 1992), which should be zero in the case of extracortical activation, is very susceptible to noise (which was stronger after ICMS than after acoustic stimulation), we could not reliably test the hypothesis of monosynaptic (vs. transthalamic) transmission by residual analysis. Because, however, the intracortical collaterals of layer VI CT pyramidal cells extend rather vertically than horizontally (Ojima *et al.*, 1992; Prieto and Winer, 1999), and thus probably do not rise above the site of the recording electrode, and because of the close match respecting the laminar locations of electrically and acoustically evoked sinks (in non-lesioned cases), we favor a model including thalamic structures to explain the granular sink usually evoked by ICMS. In addition, in a recent CSD study (Happel *et al.*, 2014) proximal supragranular ICMS (300 μm) did not evoke considerable sinks and sources at the recording site after cortical silencing. Thus, the before seen activation pattern is a result of polysynaptic horizontal transmission.

The question why the extragranular sinks emerging after lesioning layer VI cells are not already seen in non/weakly lesioned animals arises. The imaginable scenario that other neurons, e.g., layer V corticofugal neurons projecting to non-lemniscal thalamus, are less strongly activated in the presence of layer VI CT cells is rather unlikely as we assume all cells being excited independently of

their activity state by the high stimulus amplitude applied in our experiments. Possibly, an input via a (non-lemniscal) CTC loop targeting extragranular layers (or a monosynaptic intracortical transmission) is likewise, but latently present in non-lesioned animals. This might be due to extinction through sources which counterbalance the prominent granular sink evoked by the relatively stronger lemniscal thalamic input (caused by stimulation of layer VI CT neurons). Alternatively, the (recurrent TC) sink evoked by layer V CT cells may be quenched by inhibitory neurons being excited by the lemniscal TC afferents (disynaptic inhibition), but this mechanism does not explain for the silenced condition. Last but not least, a change of the excitation-inhibition balance due to lacking layer VI CT projections could occur already in the thalamus, leading to an enhanced activation of thalamic neurons whose cortical target layers are outside layer IV. For example, layer VI CT projections to Rt sectors which innervate MGd/MGm, or to Rt neurons that target more than one thalamic division (Crabtree, 1998) could indirectly suppress non-lemniscal divisions, which are released from inhibition after elimination of layer VI CT cells (this hypothesis has been included into the model of electrically induced activation, section 4.4., Fig. 4.3). Assuming that the observed extragranular sinks actually represent non-lemniscal thalamic inputs, those terminating in layers Va and I of AI may particularly arise from DD, while other infragranular sinks may be provoked by MGm (see 3.1.3 and 3.1.3).

In animals with layer VI CT lesions the cortical activation strength was less dependent on stimulation depth than in animals with intact layer VI CT neurons (in which IGstim evoked much stronger sinks than other stimulation depths). This may be due to the longer apical dendrite of layer V corticofugal cells (up to layer I) compared to layer VI CT cells (up to layer IV) (e.g., Games and Winer, 1988; Llano and Sherman, 2009).

4.3.5 Effects of layer V CT lesions on the electrically evoked cortical activation

As discussed above, layer VI CT cells were found to be necessary for the emergence of the granular sink after ICMS in the silenced cortex. Cases that (additionally) exhibited loss of layer V CT neurons differed from the others in that their overall activation during cortical silencing was more persistent and not

reduced compared with the untreated condition. Even in the case that had a lesion in layer V only, the (because of the intact layer VI CT connections) still present granular sink was blurred, indicating that indeed the loss of CT neurons located in layer V was specifically responsible for this effect.

Though speculative, the most plausible explanation for the mechanisms behind these activations is the release from inhibition, i.e., the neuronal population targeted by layer V CT cells may normally contribute to inhibit certain brain regions, so that their elimination leads to a disturbance of the balance between excitation and inhibition (shifts towards excitation), and in consequence to a more long-lasting activation of synapses in the AC. This activation, considering that there are different populations of (layer V) corticofugal cells [e.g., Ojima, 1994; Wong and Kelly, 1981; Bajo and Moore, 2005 (IC); Doucet *et al.*, 2002 (SOC); Weedman and Ryugo, 1996 (cochlear nucleus); Budinger *et al.*, 2000b, 2013 (various brainstem nuclei, CPu, amygdala); for review: Winer, 2006] is probably caused by the now dominant action of a corticofugal cell population that has been preserved and hence is still excitable by ICMS (see 4.4.2 and Fig. 4.4).

Since to our knowledge no distinct projections from layer V neurons to MGv have been characterised so far, it remains to be investigated whether the here probably observed minor connections from layer V are MGv-specific, or whether they represent collaterals of axons predominantly targeting other subcortical structures (e.g., MGd).

4.4 Interplay of TC and CT system

Our results obtained by the detailed layer-, field-, and frequency-specific analysis of TC connections and the effect of selective elimination of CT neurons on electrically and acoustically evoked cortical activity patterns reveal new aspects of how these two systems interact and influence each other.

4.4.1 Model of CTC interactions upon acoustic stimulation

Figure 4.3 illustrates how TC, intracortical, and CT connections may contribute and interact during processing of pure tones and spectrotemporal integration in AI, based on the current tract tracing and electrophysiological results as well as on results from literature.

The minimal network includes afferent TC input to granular and to deep infragranular layers, mainly arising from MGv (LV, OV) (Huang and Winer, 2000; Hackett, 2011; Saldeitis *et al.*, 2014), intracolumnar excitation through local intracortical recurrent microcircuits (Liu *et al.*, 2007), intercolumnar short- and long-range horizontal intracortical connections (Ojima *et al.*, 1991, 1992; Kadia and Wang, 2003; Kurt *et al.*, 2008; Moeller *et al.*, 2010) (Fig 4.3, intracortical activity is represented by blue arrows) . In addition, a fast-acting CTC-loop is involved. Thus, the contribution of the TC projections to spectral processing depends not solely on the ascending inputs from brainstem, but also on the influence by CT feedback. The infragranular TC terminals, on their turn, probably reflected by iS1 in the CSD pattern, could modulate directly and fast, i.e. by bypassing the sequential cascade of information processing, the activity of CT neurons (see 4.3.2).

Our results indicate that (under normal conditions) a recurrent transthalamic loop emanating from layer VI CT neurons projecting to MGv is most likely responsible for sharpening frequency tuning of S1, doing this particularly by amplifying BF responses, rather than by additionally enhancing suppressive mechanisms to inhibit nonBF responses (i.e., lateral inhibition). We nevertheless included an inhibitory connection providing lateral inhibition via the Rt or local inhibitory interneurons into our model, as it still may play a role in similar or other processes.

As aforementioned, the action of the recurrent transthalamic feedback loop becomes evident essentially for enhancing the ratio of BF to nonBF responses, while nearBF responses are not separately affected (i.e., at most along with a possible amplification of BF responses). This may be largely due to the divergence of TC projections (see 4.4.3).

Besides the involvement of CT neurons in frequency tuning of the initial input, they also seem to modulate the canonical interlaminar cascade of intracortical processing, which was manifested by a relative enhancement of the late extragranular sinks in lesioned animals. The influences they have on local intracortical processing may be accomplished by intrinsic collaterals to layer III-V (see 4.4.2).

4.4.2 Model of CTC interaction upon ICMS

To explain the electrically evoked phenomena or differences that occurred after layer VI and/or V lesions, any suggested connectivity model had to stand all constellations, i.e., to account for the respective activation patterns in both lesioned and non-lesioned animals, both before and after cortical silencing. There was no feasible model meeting all criteria that excludes the innervations of subcortical structures. Activation of AI via secondary auditory fields is also unlikely, since muscimol is expected to infuse and thus silence also the adjacent auditory fields.

Thus, we established a coherent explanatory model (Fig. 4.4) that includes the innervation of subcortical structures. How the different corticofugal circuitries interact is largely unknown. So, the model includes hypothetical mechanisms to both explain the generation of unreduced long-lasting (blurry) activity due to loss of layer V CT cells, and a mechanism which determines how the cortex represents this inherited activity.

We included in our model a further corticofugal target, namely the IC, in particular its cortices (in gerbil corresponding to DCIC/ECIC): (1) It receives considerable input from AC (Coleman and Clerici, 1987; Herbert *et al.*, 1991; Saldaña *et al.*, 1996; Druga *et al.*, 1997; Budinger *et al.*, 2000b, 2013). (2) MGB and IC are bidirectionally interconnected (Senatorov and Hu, 2002; Kuwabara and Zook, 2000; Mellott *et al.*, 2014). (3) Some of the CT axons that descend from layer V neurons (which are supposed to be eliminated here) may have collaterals that extend further to IC (Ojima, 1994; Lee *et al.*, 2011; Slater *et al.*, 2013). (4) IC neurons exhibit a row of distinct sustained firing patterns (Smith, 1992; Li *et al.*, 1998; Sivaramakrishnan and Oliver, 2001), which may be required for the sustained cortical activation. (5) There are inhibitory mechanisms within the IC (e.g., Merchán *et al.*, 2005; Nakamoto *et al.*, 2013).

According to our model, ICMS excites all types of present corticofugal neurons. When layer V CT cells are present, they will, via collaterals, activate GABAergic interneurons in IC, which in their turn will inhibit principle neurons of IC (projecting to MGB). As these neurons could also have been excited by an unbranched descending pathway to IC, they could shortly fire before being suppressed. In both cases of intact and lesioned layer V CT projections, the activated neuron will transmit its activity to AC via the thalamus, either in phasic

(possibly not distinguishable from direct CTC loop) or in more sustained manner, respectively. While MGd/MGm neurons can be driven by these colliculothalamic projections, the rather sparse projections from DCIC/ECIC to MGv (Mellott *et al.*, 2014) suggest that these colliculothalamic projections are unable to drive MGv neurons, but sufficient to modulate (i.e., prolong) their response when activated by layer VI CT projections. Thus, the elimination of both layer V and VI CT neurons may cause a non-lemniscal-like cortical activation pattern (i.e., no granular sink).

Alternatively, it is currently discussed to which extent branched projections to both MGB and IC exist (Lee *et al.*, 2011; Slater *et al.*, 2013), though they were frequently considered to represent only a minor fraction of largely independent auditory corticofugal projection streams (Wong and Kelly, 1981; Ojima, 1994). Therefore terminals of layer V CT cells could also activate thalamic inhibitory interneurons to quench the afferent signals from IC via presynaptic inhibition. However, the percentage of GABAergic neurons in MGB was found to be <1% in rodents – although it has not been investigated in gerbils – (Winer and Larue, 1996), which may decrease the likelihood and effectiveness of such a mechanism. The inclusion of additional synaptic relays, on the other hand, could make the circuitry too slow to account for the observed cortical patterns. In AC then, the afferent input could lead to both (direct) excitation of cortical (e.g., excitatory pyramidal) cells and (indirect) inhibition, e.g., disynaptic feed-forward shunting inhibition (Sun *et al.*, 2006) or feedback inhibition. This would explain why the elongated afferent input emerges only after muscimol (no intracortical inhibition anymore), and in layer V lesioned animals (generation of persisting activation). In non-lesioned animals, the afferent input will be weaker and shorter even without intracortical inhibition, thus the model works for both animal groups.

As mentioned above, the differential CSD patterns of animals that have layer VI lesions and those which have not could be mediated by Rt (or inhibitory interneurons of MGB). In detail, collaterals of layer VI CT neurons could innervate Rt sectors projecting to MGd/MGm (Crabtree, 1998; Yu *et al.*, 2004), which subsequently suppress these thalamic divisions. In this way, the electrically elicited cortical activity pattern of non-lesioned animals is largely determined by MGv inputs (acoustic-like appearance).

4.4.3 General principles governing auditory CT projections and functional implications for the CTC loops

Generally spoken, the CT system originating from layer VI neurons acts more locally (tonotopic, providing largely reciprocal feedback), while the system originating in layer V acts more globally (non-tonotopic, spreads activity widely across cortical fields in a feedforward manner) (see 1.2). Also their inputs (circumscribed vs. widespread; Llano and Sherman, 2009) and their intracortical axonal collaterals (vertical axonal arbors vs. horizontal wide ranging collaterals; e.g., Ojima *et al.*, 1992) fit into this scheme, as well as the distribution of terminals arising from the respective thalamic divisions (see 3.12 and 3.13).

Specifically, layer VI CT neurons are pivotal in providing fast feedback particularly to MGv. These CT cells, possibly being excited by direct TC synapses, are likely to mediate rapid adjustments related to various processing mechanisms (e.g., receptive field properties, gating, gain control, sound specific plasticity (see 1.1)). In particular, we found these cells to be involved in sharpening the frequency tuning in AI, probably via a CTC-loop through MGv (LV, OV).

Layer V neurons connecting to the non-lemniscal thalamus have for example been related to attentive functions (Yu *et al.*, 2004). For instance, slow oscillations in non-lemniscal thalamus can be altered by AC, thereby possibly controlling global alertness (He, 2003). Here, a supposed global role of layer V neurons may have appeared as the prolonged activity seen after cortical silencing in layer V lesioned animals, because they probably affected both lemniscal and non-lemniscal thalamus (nucleus-specific locations of electrically evoked cortical sinks depending on whether additional layer VI lesions were present or not). However, more animals with lesions restricted to layer V are required to ultimately confirm this effect.

Together, though the different CT systems hold specific functions (not at least determined by their distinct intra- and subcortical connectivities), they do not appear totally separable. This implies that an interaction of several corticofugal systems on the (intra- and) subcortical level exist (see Figs. 4.2 and 4.3).

4.5 Conclusion

Despite a host of literature devoted to the functional anatomy of the TC auditory system the fine details of this network are still not completely understood. Many of these details could not be disentangled by previous studies, for example, due to large tracer injections covering several MGB divisions and subdivisions, or due to limited knowledge about the organization of the AC. Overcoming these and other constraints in a well established animal model of auditory research, the Mongolian gerbil, we could show in this study, for instance, that the

(1) MGv consists of 3 subdivisions (LV, OV, and RP), each having conspicuous electrophysiological properties and very distinct projection patterns to the AC with respect to their field-specificity, topography (tonotopy, divergence, dorsoventral gradient), laminar preference, and spatial continuity or patchiness, respectively.

(2) MGd consists of at least 2 subdivisions, namely the MGd *proper* and DD. Both share many characteristics but differ significantly in their physiological responses and projections to cortical layers IV (MGd *proper*) and Va (DD), respectively.

(3) MGm neurons preferentially project to primary and secondary fields in a non-tonotopic although topographic manner; namely by forming repetitive column-like terminal clusters in the infragranular layers of the AC. Besides normal-sized terminals they also bear very large (“giant”) boutons.

(4) The ultrastructure of small and large terminals arising from MGm form multiple asymmetric (probably glutamatergic) contacts with dendritic spines and have abundant mitochondria. Their average size exceeds that of other intracortical and TC boutons, suggesting a powerful impact on the postsynaptic cell.

This and further knowledge about the cortical terminal patterns of the thalamic subdivisions will contribute to the understanding of the neuronal processing in the AC. Thereby, it has increasingly become clear that the auditory TC system is much more complex than previously expected and that probably each individual neuronal type of this system has its distinctive anatomy and function. Likewise, the contribution of recurrent CT feedback projections on cortical activity is largely unexplored so far. Thus, by retrograde labeling and

photolytical apoptosis of the CT projection neurons originating from layers V and VI of AI,

(5) we identified the laminar origins and thalamic targets of the CT projections in the Mongolian gerbil and revealed specific contributions of these cells to acoustically and electrically evoked cortical activity patterns.

In particular,

(6) layer VI CT neurons are considerably involved in spectrotemporal processing of tones, particularly in sharpening of frequency tuning (most likely) through interactions with the MGv (LV,OV).

(7) CT cells represent important neuronal generators of the electrically evoked laminar CSD profiles (layer VI CT neurons being required to produce a granular sink). The elimination of layer V and/or layer VI CT cells enabled us to formulate a model about the respective subcortical circuitries recruited.

Together, this work provides a comprehensive anatomical and functional characterization of the auditory TC and CT system and their interactions.

It can be concluded that spectrotemporal integration within AI is precisely orchestrated by the collaborative processing of TC and corticocortical connections, as well as by the CT system, which modulates the recurrent input the cortex obtains from the thalamus.

4.6 Outlook and future directions

MGm projection pattern and giant boutons

Our discoveries on the anatomical projection pattern and nature of terminals of MGm neurons has arisen a couple of new questions. For example: which thalamic cell types bear these large boutons? Which cortical cell types are targeted? How far do single axons distribute and do all of them form the conspicuous columnar pattern observed in our tracing studies? Which are the physiological correlates in the cortex? Which neurotransmitter receptors and transporters are involved, are there cotransmitters?

One approach to answer several of these questions would be to patch single MGm neurons on a physiological TC slice, stimulate them electrically, and simultaneously record at several sites of infragranular AC to test the hypothesis that and how MGm neurons simultaneously influence wide cortical areas. In the

end, a dye [biocytin, Lucifer yellow (Hanani, 2012)] would be injected to later identify thalamic cell type and reconstruct its axonal pattern.

To verify that the targeted spines (as seen in TEM) belong to pyramidal cells (rather than to spiny inhibitory neurons) they could be immunohistochemically labeled using a marker for neocortical pyramidal cells (e.g. Homeobox gene *Emx1*: Chan *et al.*, 2001; *CamKII*: McDonald *et al.*, 2002; *SMI-32*: Campbell and Morrison, 1989). Depending on recording method, also the recorded cortical cells could be intra- or juxtacellularly stained. The advantage of this approach would be to additionally obtain information about the proximity of the TC synapses to the soma, which may have implications for plastic changes of receptive field and reliability of synaptic transmission (Richardson *et al.*, 2009).

Since many features of the ultrastructure of small and large labeled boutons were similar, it would further be interesting to know if and in which manner these boutons, which are commonly located on the same axon, differ on the molecular/biochemical level. By post-embedding methods, questions respecting the involved pre- and postsynaptic receptor and transporter types for characterization of the transmission of the proposed neurotransmitter glutamate, identification of possible cotransmitters (dopamine, serotonin, VIP), and calcium binding proteins (PV, CB) could be investigated.

Investigations on the CTC loop

By selectively (but non-reversibly) deactivating the CT projections, we discovered some fundamental implications of these cells on cortical function.

To further unravel their roles, future approaches could include optogenetic tools (e.g., Boyden *et al.*, 2005; for review: Fenno *et al.*, 2011; Tye and Deisseroth, 2012) in order to reversibly and versatily manipulate targeted CT neurons (e.g., varying strength, duration, timing/temporal sequences of stimuli). Owing to the existence of both inhibitory and excitatory light dependent ion channels, we could also modulate these CT cells in both directions. To this aim, one would inject a retrograde virus (e.g., herpes simplex virus 1 (HSV1); Lima *et al.*, 2009) equipped with an opsin whose expression is dependent on a promoter specific for excitatory/pyramidal cells (e.g., *CamKII*-promoter) into a specified subdivision of the MGB and then illuminate AC to control their activity. In case that distinctive labeling of either layer V or layer VI CT pyramidal cells cannot be

achieved by division-specific injections, one could selectively express the desired opsin in one of these cell types. Layer VI CT neurons, for example, can be made sensitive to light by cre-dependent expression of opsins, if layer VI CT cells have been defined by *Ntsr1-cre* (Gong *et al.*, 2007; Olsen *et al.*, 2012; Bortone *et al.*, 2014; Kim *et al.*, 2014).

General anesthesia changes network dynamics (Cimenser *et al.*, 2011; Sellers *et al.*, 2013), influences tuning (Gaese and Ostwald, 2001; Felix *et al.*, 2012), and decreases the complexity of neuronal responses (Wang *et al.*, 2005). Ketamine-anesthesia, in particular, reduces the tonic drive by inhibition of the glutamatergic transmission through blockade of NMDA-receptors (Franks and Lieb, 1994; MacDonald *et al.*, 1987; Leong *et al.*, 2004). To circumvent these influences of anesthesia future studies should focus on electrophysiological techniques (e.g., CSD analysis) using unanesthetized animals. Alternatively, or in combination, cognitive tasks should be performed to understand the behaviorally relevant significance of the CT projections.

4.7 Figures

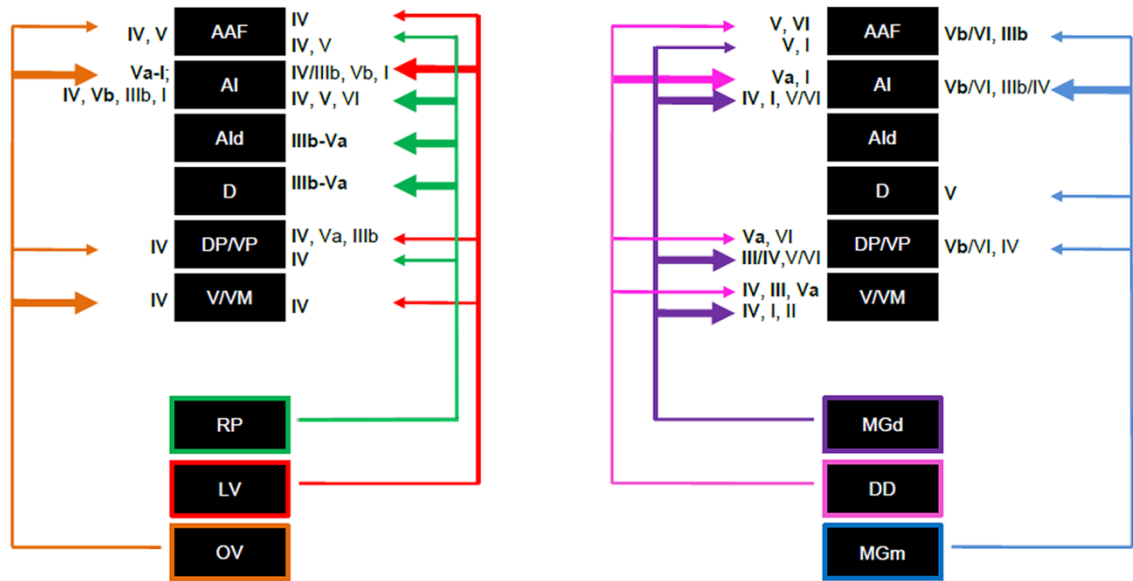


Figure 4.1: Summary diagram of the auditory TC connections between the different subnuclei of the MGB and the auditory cortical fields in the Mongolian gerbil. Each thalamic subdivision and cortical field is represented by a black box, the thickness of arrows indicates the relative strength of connections. The main target cortical layers as well as the relative strength of their respective thalamic innervation (by order) are also indicated.

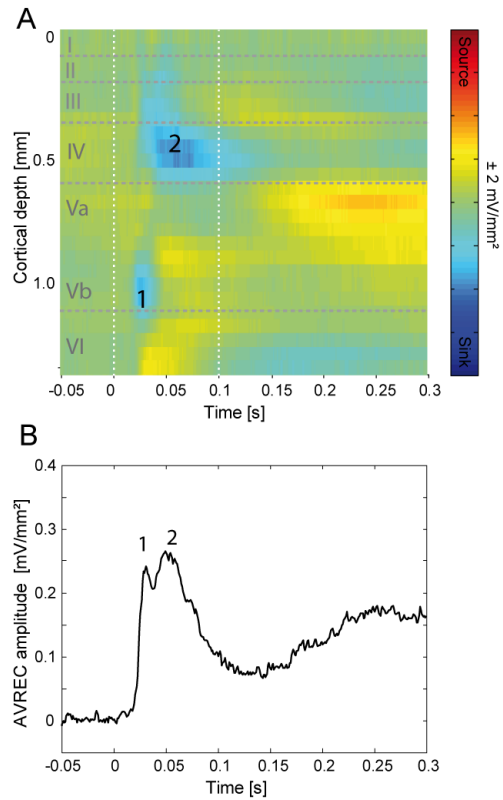


Figure 4.2: (A) CSD pattern at 3 octaves below BF and the corresponding AVREC curve (GLA19) in the untreated condition. (B) The latencies of the initial deep infragranular (1) and the granular (2) sink suggest that they are thalamically and intracortically generated, respectively. We speculate that the short latent infragranular sink far away from BF is evoked by the MGM, due to its widespread innervation of layer Vb (see also Fig. 3.6).

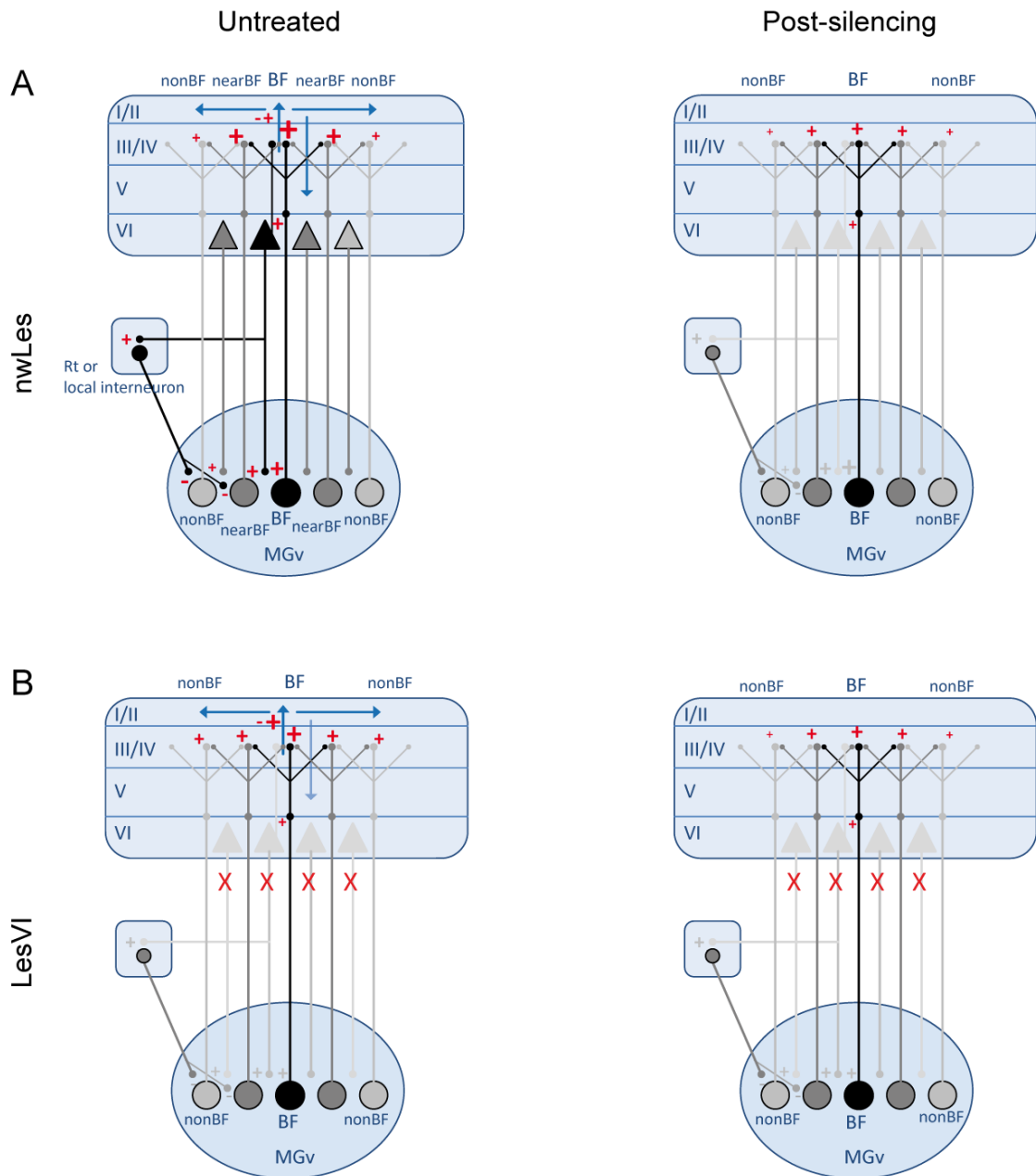


Figure 4.3: Proposed minimal model for the role of the CT system in processing of pure tones and sharpening frequency tuning. The mechanisms involved in spectrotemporal integration are shown for the non-lesioned (**A**) and layer VI CT lesioned (**B**) case. CT projections may amplify the activity of frequency-matched thalamic neurons, while the activity of frequency-non-matched neurons may be dampened by lateral inhibition via local interneurons or Rt neurons. With respect to our data, the enhancement of BF responses seems to contribute more to a modulation of the frequency tuning than the suppression of nonBF responses. TC and CT neurons project to BF and nearBF neurons. Intracortical collaterals of CT neurons may inhibit intracortical processing, as their loss led to a relative enhancement of late extragranular sinks. Active neurons are indicated by black, inactive neurons by grey outlines. The size of the signs represents the strength of excitation (+) or inhibition (-). X: lesion.

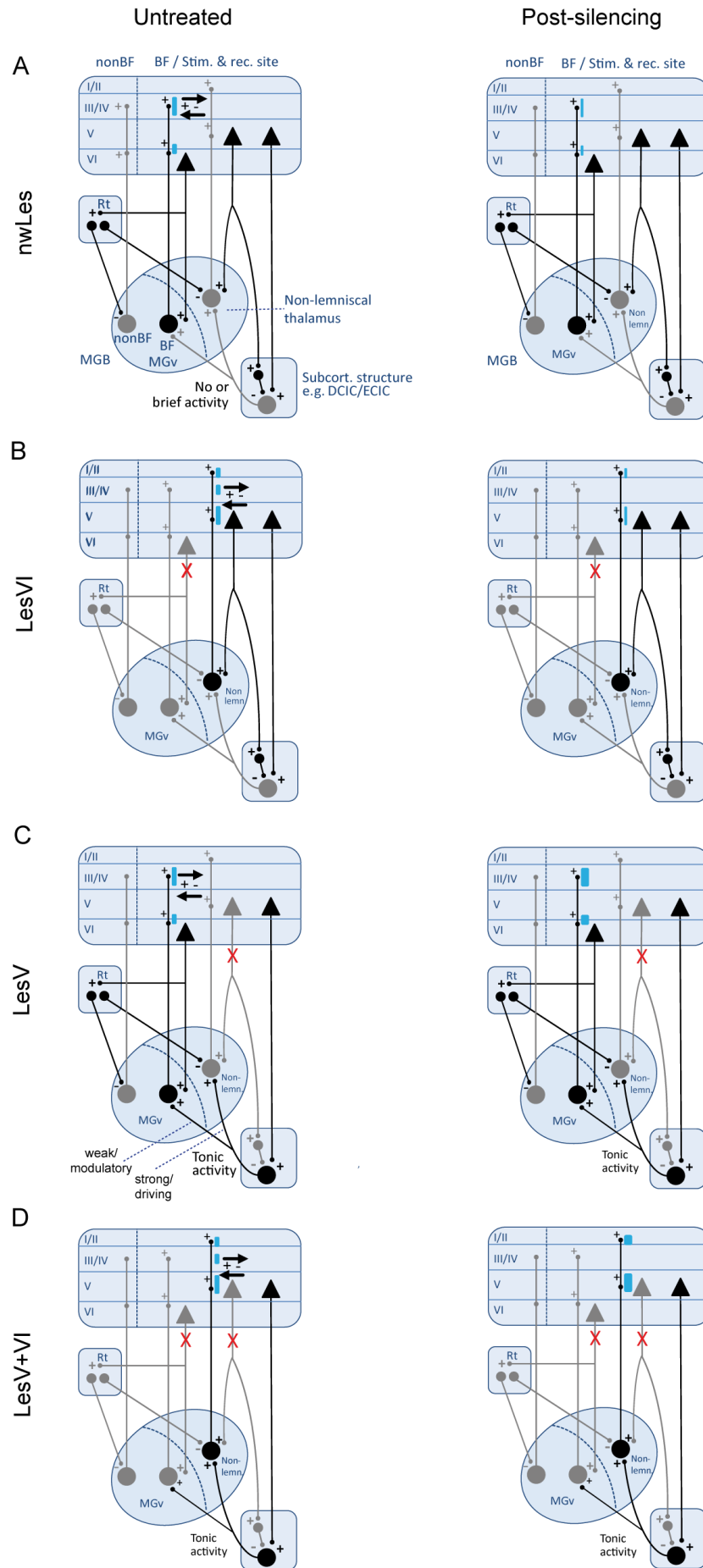


Figure 4.4 (preceding page): Current model explaining the electrically evoked CSD patterns observed in animals without **(A)** and with **(B-D)** elimination of CT projections. For the generation of S1 (after silencing), a feedback-loop via MGv involving layer VI CT neurons is required (B). These neurons may also indirectly (e.g., via Rt) inhibit non-lemniscal thalamic neurons projecting to extragranular cortical layers, explaining the absence of these sinks in non-lesioned animals (A). Other electrically excited corticofugal projection neurons, e.g., corticocollicular neurons, may account for the prolonged unreduced activity in animals with lesions of layer V CT neurons after cortical silencing (C, D), as their excitation of sustained-firing subcortical neurons is not quenched by collaterals of layer V CT projections (indirectly via interneurons) and intracortical inhibition. The blue bars represent the location of cortical sinks; their duration is indicated by the width. Intracortical activity is displayed by arrows. Active connections are drawn in black, inactive connections in grey. +: excitation; -: inhibition. X: lesion.

References

- Abrams DA, Nicol T, Zecker S, Kraus N. 2011. A possible role for a paralemniscal auditory pathway in the coding of slow temporal information. *Hear Res* 272(1-2):125-134.
- Ahissar E, Sosnik R, Haidarliu S. 2000. Transformation from temporal to rate coding in a somatosensory thalamocortical pathway. *Nature* 406(6793):302-306.
- Ainsworth M, Lee S, Cunningham MO, Roopun AK, Traub RD, Kopell NJ, Whittington MA. 2011. Dual gamma rhythm generators control interlaminar synchrony in auditory cortex. *J Neurosci* 31(47):17040-17051.
- Aitkin LM, Webster WR. 1972. Medial geniculate body of the cat: organization and responses to tonal stimuli of neurons in ventral division. *J Neurophysiol* 35(3):365-380.
- Alitto HJ, Usrey WM. 2003. Corticothalamic feedback and sensory processing. *Current Opinion in Neurobiology* 13(4):440-445.
- Andersen RA, Knight PL, Merzenich MM. 1980. The thalamocortical and corticothalamic connections of AI, AII, and the anterior auditory field (AAF) in the cat: Evidence for two largely segregated systems of connections. *J Comp Neurol* 194:663-701.
- Anderson LA, Linden JF. 2011. Physiological differences between histologically defined subdivisions in the mouse auditory thalamus. *Hear Res* 274(1-2):48-60.
- Anderson LA, Wallace MN, Palmer AR. 2007. Identification of subdivisions in the medial geniculate body of the guinea pig. *Hear Res* 228(1-2):156-167.
- Antunes FM, Malmierca MS. 2011. Effect of auditory cortex deactivation on stimulus-specific adaptation in the medial geniculate body. *J Neurosci* 31(47):17306-17316.
- Bajo VM, Moore DR. 2005. Descending projections from the auditory cortex to the inferior colliculus in the gerbil, *Meriones unguiculatus*. *J Comp Neurol* 486(2):101-116.
- Bajo VM, Nodal FR, Moore DR, King AJ. 2010. The descending corticocollicular pathway mediates learning-induced auditory plasticity. *Nat Neurosci* 13(2):253-260.
- Bajo VM, Rouiller EM, Welker E, Clarke S, Villa AE, de Ribaupierre Y, de Ribaupierre F. 1995. Morphology and spatial distribution of corticothalamic terminals originating from the cat auditory cortex. *Hear Res* 83(1-2):161-174.
- Bandyopadhyay S, Shamma SA, Kanold PO. 2010. Dichotomy of functional organization in the mouse auditory cortex. *Nat Neurosci* 13(3):361-368.
- Banks MI, Smith PH. 2011. Thalamocortical relations. In: Winer JA, Schreiner CE, editors. *The auditory cortex*. New York: Springer. p 75-98.
- Barone P, Clarey JC, Irons WA, Imig TJ. 1996. Cortical synthesis of azimuth-sensitive single-unit responses with nonmonotonic level tuning: a thalamocortical comparison in the cat. *J Neurophysiol* 75(3):1206-1220.
- Barth DS, MacDonald KD. 1996. Thalamic modulation of high-frequency oscillating potentials in auditory cortex. *Nature* 383(6595):78-81.

- Bartlett EL, Smith PH. 1999. Anatomic, intrinsic, and synaptic properties of dorsal and ventral division neurons in rat medial geniculate body. *J Neurophysiol* 81(5):1999-2016.
- Bartlett EL, Stark JM, Guillery RW, Smith PH. 2000. Comparison of the fine structure of cortical and collicular terminals in the rat medial geniculate body. *Neuroscience* 100(4):811-828.
- Bäuerle P, von der Behrens W, Kössl M, Gaese BH. 2011. Stimulus-specific adaptation in the gerbil primary auditory thalamus is the result of a fast frequency-specific habituation and is regulated by the corticofugal system. *J Neurosci* 31(26):9708-9722.
- Becker N, Wierenga CJ, Fonseca R, Bonhoeffer T, Nägerl UV. 2008. LTD induction causes morphological changes of presynaptic boutons and reduces their contacts with spines. *Neuron* 60(4):590-597.
- Bolz J, Gilbert CD. 1986. Generation of end-inhibition in the visual cortex via interlaminar connections. *Nature* 320(6060):362-365.
- Bordi F, LeDoux JE. 1994a. Response properties of single units in areas of rat auditory thalamus that project to the amygdala. I. Acoustic discharge patterns and frequency receptive fields. *Exp Brain Res* 98(2):261-274.
- Bordi F, LeDoux JE. 1994b. Response properties of single units in areas of rat auditory thalamus that project to the amygdala. II. Cells receiving convergent auditory and somatosensory inputs and cells antidromically activated by amygdala stimulation. *Exp Brain Res* 98(2):275-286.
- Bortone Dante S, Olsen Shawn R, Scanziani M. 2014. Translaminar inhibitory cells recruited by layer 6 corticothalamic neurons suppress visual cortex. *Neuron* 82(2):474-485.
- Bourassa J, Deschênes M. 1995. Corticothalamic projections from the primary visual cortex in rats: a single fiber study using biocytin as an anterograde tracer. *Neuroscience* 66(2):253-263.
- Bourassa J, Pinault D, Deschênes M. 1995. Corticothalamic projections from the cortical barrel field to the somatosensory thalamus in rats: a single-fibre study using biocytin as an anterograde tracer. *Eur J Neurosci* 7(1):19-30.
- Boyden ES, Zhang F, Bamberg E, Nagel G, Deisseroth K. 2005. Millisecond-timescale, genetically targeted optical control of neural activity. *Nat Neurosci* 8(9):1263-1268.
- Brandner S, Redies H. 1990. The projection from medial geniculate to field AI in cat: organization in the isofrequency dimension. *J Neurosci* 10(1):50-61.
- Brosch M, Budinger E, Scheich H. 2013. Different synchronization rules in primary and nonprimary auditory cortex of monkeys. *J Cogn Neurosci* 25(9):1517-1526.
- Budinger E, Brosch M, Scheich H, Mylius J. 2013. The subcortical auditory structures in the mongolian gerbil: II. Frequency-related topography of the connections with cortical field AI. *J Comp Neurol* 521(12):2772-2797.
- Budinger E, Heil P, Hess A, Scheich H. 2006. Multisensory processing via early cortical stages: Connections of the primary auditory cortical field with other sensory systems. *Neuroscience* 143(4):1065-1083.
- Budinger E, Heil P, Scheich H. 2000a. Functional organization of auditory cortex in the Mongolian gerbil (*Meriones unguiculatus*). III. Anatomical subdivisions and corticocortical connections. *Eur J Neurosci* 12(7):2425-2451.

- Budinger E, Heil P, Scheich H. 2000b. Functional organization of auditory cortex in the Mongolian gerbil (*Meriones unguiculatus*). IV. Connections with anatomically characterized subcortical structures. *Eur J Neurosci* 12(7):2452-2474.
- Budinger E, Klump GM. 2008. Proceedings of the International Workshop "The Mongolian gerbil as a model for auditory research". Magdeburg, Germany: docupoint Verlag.
- Budinger E, Laszcz A, Lison H, Scheich H, Ohl FW. 2008. Non-sensory cortical and subcortical connections of the primary auditory cortex in Mongolian gerbils: Bottom-up and top-down processing of neuronal information via field AI. *Brain Res* 1220:2-32.
- Budinger E, Scheich H. 2009. Anatomical connections suitable for the direct processing of neuronal information of different modalities via the rodent primary auditory cortex. *Hear Res* 258(1-2):16-27.
- Burton H, Jones EG. 1976. The posterior thalamic region and its cortical projection in New World and Old World monkeys. *J Comp Neurol* 168(2):249- 301.
- Caird D, Scheich H, Klinke R. 1991. Functional organization of auditory cortical fields in the Mongolian gerbil (*Meriones unguiculatus*): binaural 2-deoxyglucose patterns. *J Comp Physiol [A]* 168(1):13-26.
- Calford MB. 1983. The parcellation of the medial geniculate body of the cat defined by the auditory response properties of single units. *J Neurosci* 3(11):2350-2364.
- Calford MB, Aitkin LM. 1983. Ascending projections to the medial geniculate body of the cat: Evidence for multiple parallel auditory pathways through thalamus. *J Neurosci* 3:2365- 2380.
- Calford MB, Webster WR. 1981. Auditory representation within principal division of cat medial geniculate body: an electrophysiology study. *J Neurophysiol* 45(6):1013-1028.
- Campbell MJ, Morrison JH. 1989. Monoclonal antibody to neurofilament protein (SMI-32) labels a subpopulation of pyramidal neurons in the human and monkey neocortex. *J Comp Neurol* 282(2):191-205.
- Campolattaro MM, Halverson HE, Freeman JH. 2007. Medial auditory thalamic stimulation as a conditioned stimulus for eyeblink conditioning in rats. *Learning & Memory* 14(3):152-159.
- Cant NB, Benson CG. 2006. Organization of the inferior colliculus of the gerbil (*Meriones unguiculatus*): differences in distribution of projections from the cochlear nuclei and the superior olivary complex. *J Comp Neurol* 495(5):511-528.
- Cant NB, Benson CG. 2007. Multiple topographically organized projections connect the central nucleus of the inferior colliculus to the ventral division of the medial geniculate nucleus in the gerbil, *Meriones unguiculatus*. *J Comp Neurol* 503(3):432-453.
- Caviness VS, Frost DO. 1980. Tangential organization of thalamic projections to the neocortex of the mouse. *J Comp Neurol* 194(2):335- 367.
- Cetas JS, de Venecia RK, McMullen NT. 1999. Thalamocortical afferents of Lorente de No: medial geniculate axons that project to primary auditory cortex have collateral branches to layer I. *Netherlands: Brain Res.* p 203-208.

- Cetas JS, Price RO, Crowe J, Velenovsky DS, McMullen NT. 2003. Dendritic orientation and laminar architecture in the rabbit auditory thalamus. *J Comp Neurol* 458(3):307-317.
- Cetas JS, Price RO, Velenovsky DS, Crowe JJ, Sinex DG, McMullen NT. 2002. Cell types and response properties of neurons in the ventral division of the medial geniculate body of the rabbit. *J Comp Neurol* 445(1):78-96.
- Cetas JS, Price RO, Velenovsky DS, Sinex DG, McMullen NT. 2001. Frequency organization and cellular lamination in the medial geniculate body of the rabbit. *Hear Res* 155(1-2):113-123.
- Chan C-H, Godinho LN, Thomaidou D, Tan S-S, Gulisano M, Parnavelas JG. 2001. Emx1 is a Marker for Pyramidal Neurons of the Cerebral Cortex. *Cerebral Cortex* 11(12):1191-1198.
- Cimenser A, Purdon PL, Pierce ET, Walsh JL, Salazar-Gomez AF, Harrell PG, Tavares-Stoeckel C, Habeeb K, Brown EN. 2011. Tracking brain states under general anesthesia by using global coherence analysis. *Proc Natl Acad Sci USA* 108(21):8832-8837.
- Clerici WJ, Coleman JR. 1990. Anatomy of the rat medial geniculate body: I. Cytoarchitecture, myeloarchitecture, and neocortical connectivity. *J Comp Neurol* 297:14- 31.
- Clerici WJ, McDonald AJ, Thompson R, Coleman JR. 1990. Anatomy of the rat medial geniculate body: II. Dendritic morphology. *J Comp Neurol* 297:32-54.
- Coleman JR, Clerici WJ. 1987. Sources of projections to subdivisions of the inferior colliculus in the rat. *J Comp Neurol* 262(2):215- 226.
- Conti F, DeFelipe J, Farinas I, Manzoni T. 1989. Glutamate-positive neurons and axon terminals in cat sensory cortex: a correlative light and electron microscopic study. *J Comp Neurol* 290(1):141-153.
- Contreras D, Steriade M. 1996. Spindle oscillation in cats: the role of corticothalamic feedback in a thalamically generated rhythm. *J Physiol* 490:159-179.
- Crabtree JW. 1998. Organization in the auditory sector of the cat's thalamic reticular nucleus. *J Comp Neurol* 390(2):167-182.
- de Venecia RK, McMullen NT. 1994. Single thalamocortical axons diverge to multiple patches in neonatal auditory cortex. *Devel Brain Res* 81(1):135-142.
- DeFelipe j, Conti F, Van Eyck SL, Manzoni T. 1988. Demonstration of glutamate-positive axon terminals forming asymmetric synapses in cat neocortex. *Brain Res* 455(1):162-165.
- Deschênes M, Hu B. 1990. Membrane resistance increase induced in thalamic neurons by stimulation of brainstem cholinergic afferents. *Brain Res* 513(2):339-342.
- Destexhe A. 2000. Modelling corticothalamic feedback and the gating of the thalamus by the cerebral cortex. *J Physiol Paris* 94(5-6):391-410.
- Destexhe A, Contreras D, Steriade M. 1999. Cortically-induced coherence of a thalamic-generated oscillation. *Neuroscience* 92(2):427-443.
- Donishi T, Kimura A, Okamoto K, Tamai Y. 2006. "Ventral" area in the rat auditory cortex: A major auditory field connected with the dorsal division of the medial geniculate body. *Neuroscience* 141(3):1553-1567.
- Doucet JR, Rose L, Ryugo DK. 2002. The cellular origin of corticofugal projections to the superior olivary complex in the rat. *Brain Res* 925(1):28-41.

- Druga R, Syka J, Rajkowska G. 1997. Projections of auditory cortex onto the inferior colliculus in the rat. *Physiol Res* 46(3):215-222.
- Edeline J-M. 2011. Physiological Properties of Neurons in the Medial Geniculate Body. In: Winer JA, Schreiner CE, editors. *The auditory cortex*. New York: Springer. p 251-274.
- Eggermont JJ, Wang X. 2011. Temporal coding in auditory cortex. In: Winer JA, Schreiner CE, editors. *The auditory cortex*. New York: Springer. p 309-328.
- Ehret G, Schreiner CE. 1997. Frequency resolution and spectral integration (critical band analysis) in single units of the cat primary auditory cortex. *J Comp Physiol [A]* 181(6):635-650.
- Engel AK, Fries P, Singer W. 2001. Dynamic predictions: Oscillations and synchrony in top-down processing. *Nat Rev Neurosci* 2(10):704-716.
- Engel AK, Konig P, Singer W. 1991. Direct physiological evidence for scene segmentation by temporal coding. *Proc Natl Acad Sci U S A* 88(20):9136-9140.
- Engel AK, Singer W. 2001. Temporal binding and the neural correlates of sensory awareness. *Trends Cogn Sci* 5(1):16-25.
- Eyding D, Macklis JD, Neubacher U, Funke K, Worgotter F. 2003. Selective elimination of corticogeniculate feedback abolishes the electroencephalogram dependence of primary visual cortical receptive fields and reduces their spatial specificity. *J Neurosci* 23(18):7021-7033.
- Felix RA, II, Kadner A, Berrebi AS. 2012. Effects of ketamine on response properties of neurons in the superior paraolivary nucleus of the mouse. *Neuroscience* 201(0):307-319.
- Fenko L, Yizhar O, Deisseroth K. 2011. The development and application of optogenetics. *Annu Rev Neurosci* 34:389-412.
- Fishman YI, Steinschneider M. 2010. Neural Correlates of Auditory Scene Analysis Based on Inharmonicity in Monkey Primary Auditory Cortex. *J Neurosci* 30(37):12480-12494.
- Franklin KBJ, Paxinos G. 2008. *The Mouse Brain in Stereotaxic Coordinates*: Elsevier/Academic Press.
- Franks NP, Lieb WR. 1994. Molecular and cellular mechanisms of general anaesthesia. *Nature* 367(6464):607-614.
- Frost DO, Caviness VSJ. 1980. Radial organization of thalamic projections to the neocortex in the mouse. *J Comp Neurol* 194(2):369-393.
- Gaese BH, Nowotny M, Pilz PK. 2009. Acoustic startle and prepulse inhibition in the Mongolian gerbil. *Physiol Behav* 98(4):460-466.
- Gaese BH, Ostwald J. 2001. Anesthesia changes frequency tuning of neurons in the rat primary auditory cortex. *J Neurophysiol* 86(2):1062-1066.
- Games KD, Winer JA. 1988. Layer V in rat auditory cortex: projections to the inferior colliculus and contralateral cortex. *Hear Res* 34(1):1-25.
- Gilbert CD, Kelly JP. 1975. The projections of cells in different layers of the cat's visual cortex. *J Comp Neurol* 163(1):81-105.
- Goldschmidt J, Wanger T, Engelhorn A, Friedrich H, Happel M, Ilango A, Engelmann M, Stuermer IW, Ohl FW, Scheich H. 2010. High-resolution mapping of neuronal activity using the lipophilic thallium chelate complex TIDDC: protocol and validation of the method. *Neuroimage* 49(1):303-315.

- Goldschmidt J, Zuschratter W, Scheich H. 2004. High-resolution mapping of neuronal activity by thallium autometallography. *Neuroimage* 23(2):638-647.
- Gong S, Doughty M, Harbaugh CR, Cummins A, Hatten ME, Heintz N, Gerfen CR. 2007. Targeting Cre Recombinase to Specific Neuron Populations with Bacterial Artificial Chromosome Constructs. *J Neurosci* 27(37):9817-9823.
- Gray CM, Konig P, Engel AK, Singer W. 1989. Oscillatory responses in cat visual cortex exhibit inter-columnar synchronization which reflects global stimulus properties. *Nature* 338(6213):334-337.
- Gray EG. 1959. Axo-somatic and axo-dendritic synapses of the cerebral cortex: An electron microscope study. *Journal of Anatomy* 93(Pt 4):420-433.
- Grienberger C, Adelsberger H, Stroh A, Milos RI, Garaschuk O, Schierloh A, Nelken I, Konnerth A. 2012. Sound-evoked network calcium transients in mouse auditory cortex in vivo. *J Physiol* 590(Pt 4):899-918.
- Hackett TA. 2011. Information flow in the auditory cortical network. *Hear Res* 271(1-2):133-146.
- Hackett TA, Barkat TR, O'Brien BMJ, Hensch TK, Polley DB. 2011a. Linking topography to tonotopy in the mouse auditory thalamocortical circuit. *J Neurosci* 31(8):2983-2995.
- Hackett TA, Takahata T, Balaram P. 2011b. VGLUT1 and VGLUT2 mRNA expression in the primate auditory pathway. *Hear Res* 274(1-2):129-141.
- Hanani M. 2012. Lucifer yellow – an angel rather than the devil. *Journal of Cellular and Molecular Medicine* 16(1):22-31.
- Happel MF, Jeschke M, Ohl FW. 2010. Spectral integration in primary auditory cortex attributable to temporally precise convergence of thalamocortical and intracortical input. *J Neurosci* 30(33):11114-11127.
- Happel MFK, Deliano M, Handschuh J, Ohl FW. 2014. Dopamine-Modulated Recurrent Corticoefferent Feedback in Primary Sensory Cortex Promotes Detection of Behaviorally Relevant Stimuli. *The Journal of Neuroscience* 34(4):1234-1247.
- Harding GW. 1992. The currents that flow in the somatosensory cortex during the direct cortical response. *Exp Brain Res* 90(1):29-39.
- Harris Km, Sultan P. 1995. Variation in the number, location and size of synaptic vesicles provides an anatomical basis for the nonuniform probability of release at hippocampal CA1 synapses. *Neuropharmacology* 34(11):1387-1395.
- Harris KM, Weinberg RJ. 2012. Ultrastructure of synapses in the mammalian brain. *Cold Spring Harb Perspect Biol* 4(5).
- Hartigan JA, Hartigan PM. 1985. The Dip Test of Unimodality. *Ann Statist* 13:70-84.
- Hashikawa T, Molinari M, Rausell E, Jones EG. 1995. Patchy and laminar terminations of the medial geniculate axons in monkey auditory cortex. *J Comp Neurol* 362(2):195-208.
- Hazama M, Kimura A, Donishi T, Sakoda T, Tamai Y. 2004. Topography of corticothalamic projections from the auditory cortex of the rat. *Neuroscience* 124(3):655-667.
- He J. 1997. Modulatory effects of regional cortical activation on the onset responses of the cat medial geniculate neurons. *J Neurophysiol* 77(2):896-908.

- He J. 2003. Slow oscillation in non-lemniscal auditory thalamus. *J Neurosci* 23(23):8281-8290.
- He J, Yu YQ, Xiong Y, Hashikawa T, Chan YS. 2002. Modulatory effect of cortical activation on the lemniscal auditory thalamus of the Guinea pig. *J Neurophysiol* 88(2):1040-1050.
- Henschke JU, Noesselt T, Scheich H, Budinger E. 2015. Possible anatomical pathways for short-latency multisensory integration processes in primary sensory cortices. *Brain Struct Funct* 220(2):955-977.
- Herbert H, Aschoff A, Ostwald J. 1991. Topography of projections from the auditory cortex to the inferior colliculus in the rat. *J Comp Neurol* 304:103- 122.
- Herkenham M. 1980. Laminar organization of thalamic projections to the rat neocortex. *Science* 207(4430):532-535.
- Herrmann CS, Munk MHJ, Engel AK. 2004. Cognitive functions of gamma-band activity: memory match and utilization. *Trends in Cognitive Sciences* 8(8):347-355.
- Hu B. 1995. Cellular basis of temporal synaptic signalling: an in vitro electrophysiological study in rat auditory thalamus. *J Physiol* 483(Pt 1):167-182.
- Hu B. 2003. Functional organization of lemniscal and nonlemniscal auditory thalamus. *Exp Brain Res* 153(4):543-549.
- Huang CL, Winer JA. 2000. Auditory thalamocortical projections in the cat: laminar and areal patterns of input. *J Comp Neurol* 427(2):302-331.
- Imaizumi K, Priebe NJ, Crum PA, Bedenbaugh PH, Cheung SW, Schreiner CE. 2004. Modular functional organization of cat anterior auditory field. *J Neurophysiol* 92(1):444-457.
- Imig TJ, Adrian HO. 1977. Binaural columns in the primary field (A1) of cat auditory cortex. *Brain Res* 138:241- 257.
- Imig TJ, Brugge JF. 1978. Sources and terminations of callosal axons related to binaural and frequency maps in primary auditory cortex of the cat. *J Comp Neurol* 182:637- 660.
- Imig TJ, Morel A. 1983. Organization of the thalamocortical auditory system in the cat. *Ann Rev Neurosci* 6:95- 120.
- Imig TJ, Morel A. 1984. Topographic and cytoarchitectonic organization of thalamic neurons related to their targets in low, middle and high frequency representations in cat auditory cortex. *J Comp Neurol* 227:511- 539.
- Imig TJ, Morel A. 1985a. Tonotopic organization in lateral part of posterior group of thalamic nuclei in the cat. *J Neurophysiol* 53(3):836-851.
- Imig TJ, Morel A. 1985b. Tonotopic organization in the ventral nucleus of the medial geniculate body in the cat. *J Neurophysiol* 53:309- 340.
- Issa John B, Haeffele Benjamin D, Agarwal A, Bergles Dwight E, Young Eric D, Yue David T. 2014. Multiscale Optical Ca²⁺ Imaging of Tonal Organization in Mouse Auditory Cortex. *Neuron* 83(4):944-959.
- Ito T, Bishop DC, Oliver DL. 2011. Expression of glutamate and inhibitory amino acid vesicular transporters in the rodent auditory brainstem. *J Comp Neurol* 519(2):316-340.
- Jensen O, Kaiser J, Lachaux J-P. 2007. Human gamma-frequency oscillations associated with attention and memory. *Trends Neurosci* 30(7):317-324.
- Jeschke M. 2006. Untersuchungen zur laminaren Strom-Quelle-Dichte-Verteilung im primären auditorischen Kortex der Wüstenrennmaus nach

- akustischer oder intrakortikaler elektrischer Stimulation [Diploma]. Magdeburg: Otto-von-Guericke University. 96 p.
- Jeschke M, Lenz D, Budinger E, Herrmann CS, Ohl FW. 2008. Gamma oscillations in gerbil auditory cortex during a target-discrimination task reflect matches with short-term memory. *Brain Res* 1220:70-80.
- Jones EG, Burton H. 1976. Areal differences in the laminar distribution of thalamic afferents in cortical fields of the insular, parietal and temporal regions of primates. *J Comp Neurol* 168(2):197-247.
- Jones EG, Powell TPS. 1971. An analysis of the posterior group of the thalamic nuclei on the basis of its afferent connections. *J Comp Neurol* 143(2):185- 216.
- Kadia SC, Wang X. 2003. Spectral integration in A1 of awake primates: neurons with single- and multip peaked tuning characteristics. *J Neurophysiol* 89(3):1603-1622.
- Kaiser J, Lutzenberger W. 2005. Cortical oscillatory activity and the dynamics of auditory memory processing. *Rev Neurosci* 16(3):239-254.
- Kanold PO, Nelken I, Polley DB. 2014. Local versus global scales of organization in auditory cortex. *Trends Neurosci* 37(9):502-510.
- Kaur S, Lazar R, Metherate R. 2004. Intracortical pathways determine breadth of subthreshold frequency receptive fields in primary auditory cortex. *J Neurophysiol* 91(6):2551-2567.
- Kaur S, Rose HJ, Lazar R, Liang K, Metherate R. 2005. Spectral integration in primary auditory cortex: laminar processing of afferent input, in vivo and in vitro. *Neuroscience* 134(3):1033-1045.
- Kelly JP, Wong D. 1981. Laminar connections of the cat's auditory cortex. *Brain Res* 212(1):1- 15.
- Kharazia VN, Weinberg RJ. 1994. Glutamate in thalamic fibers terminating in layer IV of primary sensory cortex. *J Neurosci* 14(10):6021-6032.
- Khorevin VI. 1978. Responses of the neurons of the magnocellular portion of the medial geniculate body to acoustic and somatosensory stimulation. *Neirofiziologija* 10(2):133-141.
- Kim J, Matney CJ, Blankenship A, Hestrin S, Brown SP. 2014. Layer 6 Corticothalamic Neurons Activate a Cortical Output Layer, Layer 5a. *J Neurosci* 34(29):9656-9664.
- Kimura A, Donishi T, Okamoto K, Imbe H, Tamai Y. 2007. Efferent connections of the ventral auditory area in the rat cortex: implications for auditory processing related to emotion. *Eur J Neurosci* 25(9):2819-2834.
- Kimura A, Donishi T, Okamoto K, Tamai Y. 2004. Efferent connections of "posterodorsal" auditory area in the rat cortex: implications for auditory spatial processing. *Neuroscience* 128(2):399-419.
- Kimura A, Donishi T, Okamoto K, Tamai Y. 2005. Topography of projections from the primary and non-primary auditory cortical areas to the medial geniculate body and thalamic reticular nucleus in the rat. *Neuroscience* 135(4):1325-1342.
- Kimura A, Donishi T, Sakoda T, Hazama M, Tamai Y. 2003. Auditory thalamic nuclei projections to the temporal cortex in the rat. *Neuroscience* 117(4):1003-1016.
- Klemann CJHM, Roubos EW. 2011. The gray area between synapse structure and function—Gray's synapse types I and II revisited. *Synapse* 65(11):1222-1230.

- Klinge A, Klump GM. 2009. Frequency difference limens of pure tones and harmonics within complex stimuli in Mongolian gerbils and humans. *J Acoust Soc Am* 125(1):304-314.
- Kobbert C, Apps R, Bechmann I, Lanciego JL, Mey J, Thanos S. 2000. Current concepts in neuroanatomical tracing. *Prog Neurobiol* 62(4):327-351.
- Komura Y, Tamura R, Uwano T, Nishijo H, Ono T. 2005. Auditory thalamus integrates visual inputs into behavioral gains. *Nat Neurosci* 8(9):1203-1209.
- Kubota Y, Hatada S, Kondo S, Karube F, Kawaguchi Y. 2007. Neocortical Inhibitory Terminals Innervate Dendritic Spines Targeted by Thalamocortical Afferents. *J Neurosci* 27(5):1139-1150.
- Kurt S, Deutscher A, Crook JM, Ohl FW, Budinger E, Moeller CK, Scheich H, Schulze H. 2008. Auditory cortical contrast enhancing by global winner-take-all inhibitory interactions. *PLoS ONE* 3(3):e1735.
- Kuwabara N, Zook JM. 2000. Geniculo-collicular descending projections in the gerbil. *Brain Res* 878(1-2):79-87.
- Lakatos P, Karmos G, Mehta AD, Ulbert I, Schroeder CE. 2008. Entrainment of neuronal oscillations as a mechanism of attentional selection. *Science* 320(5872):110-113.
- Lakatos P, Shah AS, Knuth KH, Ulbert I, Karmos G, Schroeder CE. 2005. An oscillatory hierarchy controlling neuronal excitability and stimulus processing in the auditory cortex. *J Neurophysiol* 94(3):1904-1911.
- Lee CC. 2012. Thalamic and cortical pathways supporting auditory processing. *Brain and Language* 126(1):22-28.
- Lee CC, Imaizumi K, Schreiner CE, Winer JA. 2004a. Concurrent Tonotopic Processing Streams in Auditory Cortex. *Cereb Cortex* 14(4):441-451.
- Lee CC, Kishan AU, Winer JA. 2011. Wiring of Divergent Networks in the Central Auditory System. *Front Neuroanat* 5:46.
- Lee CC, Schreiner CE, Imaizumi K, Winer JA. 2004b. Tonotopic and heterotopic projection systems in physiologically defined auditory cortex. *Neuroscience* 128(4):871-887.
- Lee CC, Sherman SM. 2008. Synaptic properties of thalamic and intracortical inputs to layer 4 of the first- and higher-order cortical areas in the auditory and somatosensory systems. *J Neurophysiol* 100(1):317-326.
- Lee CC, Sherman SM. 2009. Modulator property of the intrinsic cortical projection from layer 6 to layer 4. *Front Syst Neurosci* 3:3.
- Lee CC, Sherman SM. 2010. Drivers and modulators in the central auditory pathways. *Front Neurosci* 4:79.
- Lee CC, Sherman SM. 2011. On the classification of pathways in the auditory midbrain, thalamus, and cortex. *Hear Res* 276(1-2):79-87.
- Lee CC, Sherman SM. 2012. Intrinsic modulators of auditory thalamocortical transmission. *Hear Res* 287(1-2):43-50.
- Lee CC, Winer JA. 2005. Principles Governing Auditory Cortex Connections. *Cereb Cortex* 15(11):1804-1814.
- Lee CC, Winer JA. 2008. Connections of cat auditory cortex: I. Thalamocortical system. *J Comp Neurol* 507(6):1879-1900.
- Lee CC, Winer JA. 2011a. Convergence of thalamic and cortical pathways in cat auditory cortex. *Hear Res* 274(1-2):85-94.
- Lee CC, Winer JA. 2011b. A synthesis of auditory cortical connections: thalamocortical, commissural and corticocortical system. In: Winer JA,

- Schreiner CE, editors. The auditory cortex. New York: Springer. p 147-170.
- Leong D, Puil E, Schwarz D. 2004. Ketamine blocks non-N-methyl-D-aspartate receptor channels attenuating glutamatergic transmission in the auditory cortex. *Acta Otolaryngol* 124(4):454-458.
- Li J, Guido W, Bickford ME. 2003. Two distinct types of corticothalamic EPSPs and their contribution to short-term synaptic plasticity. *J Neurophysiol* 90(5):3429-3440.
- Li Y, Evans MS, Faingold CL. 1998. In vitro electrophysiology of neurons in subnuclei of rat inferior colliculus. *Hear Res* 121(1-2):1-10.
- Lima SQ, Hromádka T, Znamenskiy P, Zador AM. 2009. PINP: A New Method of Tagging Neuronal Populations for Identification during In Vivo Electrophysiological Recording. *PLoS ONE* 4(7):e6099.
- Linke R, Schwegler H. 2000. Convergent and complementary projections of the caudal paralamina thalamic nuclei to rat temporal and insular cortex. *Cereb Cortex* 10(8):753-771.
- Liu B-h, Wu GK, Arbuckle R, Tao HW, Zhang LI. 2007. Defining cortical frequency tuning with recurrent excitatory circuitry. *Nat Neurosci* 10(12):1594-1600.
- Liu X, Basavaraj S, Krishnan R, Yan J. 2011. Contributions of the thalamocortical system towards sound-specific auditory plasticity. *Neurosci Biobehav Rev* 35(10):2155-2161.
- Llano DA, Sherman SM. 2008. Evidence for nonreciprocal organization of the mouse auditory thalamocortical-corticothalamic projection systems. *J Comp Neurol* 507(2):1209-1227.
- Llano DA, Sherman SM. 2009. Differences in intrinsic properties and local network connectivity of identified layer 5 and layer 6 adult mouse auditory corticothalamic neurons support a dual corticothalamic projection hypothesis. *Cereb Cortex* 19(12):2810-2826.
- Loskota WJ, Lomax P, Verity MA. 1974. A stereotaxic atlas of the Mongolian gerbil (*Meriones unguiculatus*). Michigan: Ann Arbor Science.
- Ma X, Suga N. 2009. Specific and nonspecific plasticity of the primary auditory cortex elicited by thalamic auditory neurons. *J Neurosci* 29(15):4888-4896.
- MacDonald JF, Miljkovic Z, Pennefather P. 1987. Use-dependent block of excitatory amino acid currents in cultured neurons by ketamine. *J Neurophysiol* 58(2):251-266.
- Macklis JD. 1993. Transplanted neocortical neurons migrate selectively into regions of neuronal degeneration produced by chromophore-targeted laser photolysis. *J Neurosci* 13(9):3848-3863.
- Madison RD, Macklis JD. 1993. Noninvasively induced degeneration of neocortical pyramidal neurons in vivo: selective targeting by laser activation of retrogradely transported photolytic chromophore. *Exp Neurol* 121(2):153-159.
- Malhotra S, Stecker GC, Middlebrooks JC, Lomber SG. 2008. Sound localization deficits during reversible deactivation of primary auditory cortex and/or the dorsal zone. *J Neurophysiol* 99(4):1628-1642.
- Malmierca MS, Anderson LA, Antunes FM. 2015. The cortical modulation of stimulus-specific adaptation in the auditory midbrain and thalamus: A potential neuronal correlate for predictive coding. *Front Syst Neurosci* 9:19.

- Malmierca MS, Merchán MA. 2004. Auditory system. In: Paxinos G, editor. The rat nervous system. San Diego: Elsevier Academic Press. p 997-1082.
- Malmierca MS, Merchán MA, Henkel CK, Oliver DL. 2002. Direct projections from cochlear nuclear complex to auditory thalamus in the rat. *J Neurosci* 22(24):10891-10897.
- Markram H, Toledo-Rodriguez M, Wang Y, Gupta A, Silberberg G, Wu C. 2004. Interneurons of the neocortical inhibitory system. *Nat Rev Neurosci* 5(10):793-807.
- McDonald AJ, Muller JF, Mascagni F. 2002. GABAergic innervation of alpha type II calcium/calmodulin-dependent protein kinase immunoreactive pyramidal neurons in the rat basolateral amygdala. *J Comp Neurol* 446(3):199-218.
- Mellott JG, Foster NL, Ohl AP, Schofield BR. 2014. Excitatory and inhibitory projections in parallel pathways from the inferior colliculus to the auditory thalamus. *Front Neuroanat* 8:124.
- Merchán M, Aguilar LA, Lopez-Poveda EA, Malmierca MS. 2005. The inferior colliculus of the rat: Quantitative immunocytochemical study of GABA and glycine. *Neuroscience* 136(3):907-925.
- Metherate R, Kaur S, Kawai H, Lazar R, Liang K, Rose HJ. 2005. Spectral integration in auditory cortex: mechanisms and modulation. *Hear Res* 206(1-2):146-158.
- Middlebrooks JC, Dykes RW, Merzenich MM. 1980. Binaural response-specific bands in primary auditory cortex (AI) of the cat: Topographical organization orthogonal to isofrequency contours. *Brain Res* 181:31-48.
- Middlebrooks JC, Zook JM. 1983. Intrinsic organization of the cat's medial geniculate body identified by projections to binaural response-specific bands in the primary auditory cortex. *J Neurosci* 3(1):203-224.
- Miller LM, Escabi MA, Read HL, Schreiner CE. 2001. Functional convergence of response properties in the auditory thalamocortical system. *Neuron* 32(1):151-160.
- Miller LM, Escabi MA, Read HL, Schreiner CE. 2002. Spectrotemporal receptive fields in the lemniscal auditory thalamus and cortex. *United States: J Neurophysiol.* p 516-527.
- Mitani A, Itoh K, Mizuno N. 1987. Distribution and size of thalamic neurons projecting to layer I of the auditory cortical fields of the cat compared to those projecting to layer IV. *J Comp Neurol* 257(1):105-121.
- Mitani A, Itoh K, Nomura S, Kudo M, Kaneko T, Mizuno N. 1984. Thalamocortical projections to layer I of the primary auditory cortex in the cat: a horseradish peroxidase study. *Brain Res* 310:347-350.
- Mitzdorf U. 1985. Current source-density method and application in cat cerebral cortex: investigation of evoked potentials and EEG phenomena. *Physiol Rev* 65(1):37-100.
- Moeller CK, Kurt S, Happel MFK, Schulze H. 2010. Long-range effects of GABAergic inhibition in gerbil primary auditory cortex. *Eur J Neurosci* 31(1):49-59.
- Molinari M, Dell'Anna ME, Rausell E, Leggio MG, Hashikawa T, Jones EG. 1995. Auditory thalamocortical pathways defined in monkeys by calcium-binding protein immunoreactivity. *J Comp Neurol* 362(2):171-194.
- Morel A, Imig TJ. 1987. Thalamic projections to fields A, AI, P, and VP in the cat auditory cortex. *J Comp Neurol* 265(1):119-144.

- Morel A, Rouiller E, de Ribaupierre Y, de Ribaupierre F. 1987. Tonotopic organization in the medial geniculate body (MGB) of lightly anesthetized cats. *Exp Brain Res* 69(1):24-42.
- Morest DK. 1965. The laminar structure of the medial geniculate body of the cat. *J Anat* 99:143-160.
- Mylius J, Brosch M, Scheich H, Budinger E. 2013. Subcortical auditory structures in the mongolian gerbil: I. Golgi architecture. *J Comp Neurol* 521(6):1289-1321.
- Nakamoto KT, Mellott JG, Killius J, Storey-Workley ME, Sowick CS, Schofield BR. 2013. Ultrastructural examination of the corticocollicular pathway in the guinea pig: a study using electron microscopy, neural tracers, and GABA immunocytochemistry. *Front Neuroanat* 7:13.
- Nicholson C, Freeman JA. 1975. Theory of current source-density analysis and determination of conductivity tensor for anuran cerebellum. *J Neurophysiol* 38(2):356-368.
- NIH. 2011. National Institute of Health: Guide for the care and use of laboratory animals. Washington, D.C.: The National Academic Press.
- Ogawa R, Itoh K, Kaneko T, Mizuno N. 1989. Co-existence of vasoactive intestinal polypeptide (VIP)- and cholecystokinin (CCK)-like immunoreactivities in thalamocortical neuron in the ventrolateral nucleus of the rat. *Brain Res* 490(1):152-156.
- Ojima H. 1994. Terminal morphology and distribution of corticothalamic fibers originating from layers 5 and 6 of cat primary auditory cortex. *Cereb Cortex* 4(6):646- 663.
- Ojima H, Honda CN, Jones EG. 1991. Patterns of axon collateralization of identified supragranular pyramidal neurons in the cat auditory cortex. *Cereb Cortex* 1:80- 94.
- Ojima H, Honda CN, Jones EG. 1992. Characteristics of intracellularly injected infragranular pyramidal neurons in cat primary auditory cortex. *Cereb Cortex* 2(3):197-216.
- Ojima H, Rouiller EM. 2011. Auditory cortical projections to the medial geniculate body. In: Winer JA, Schreiner CE, editors. *The auditory cortex*. New York: Springer.
- Oliver DL, Hall WC. 1978. The medial geniculate body of the tree shrew, *Tupaia glis*. II. Connections with the neocortex. *J Comp Neurol* 182(3):459-493.
- Olsen SR, Bortone DS, Adesnik H, Scanziani M. 2012. Gain control by layer six in cortical circuits of vision. *Nature* 483(7387):47-52.
- Paillart C, Li J, Matthews G, Sterling P. 2003. Endocytosis and vesicle recycling at a ribbon synapse. *J Neurosci* 23(10):4092-4099.
- Pandya DN, Rosene DL. 1993. Laminar termination patterns of thalamic, callosal and association afferents in the primary auditory area of the rhesus monkey. *Exp Neurol* 119(2):220- 234.
- Paxinos G, Watson C. 2007. *The rat brain in stereotaxic coordinates*. 6th ed. San Diego: Academic Press.
- Petrof I, Sherman SM. 2013. Functional significance of synaptic terminal size in glutamatergic sensory pathways in thalamus and cortex. *J Physiol* 591(13):3125-3131.
- Phillips DP, Irvine DR. 1979. Acoustic input to single neurons in pulvinar-posterior complex of cat thalamus. *J Neurophysiol* 42(1 Pt 1):123-136.

- Pitts W. 1952. Investigations on synaptic transmission. In: *Cybernetics-Transactions of the Ninth Conference of the Josiah Macy Foundation*, New York. p 159-166.
- Polley DB, Read HL, Storace DA, Merzenich MM. 2007. Multiparametric Auditory Receptive Field Organization Across Five Cortical Fields in the Albino Rat. *J Neurophysiol* 97(5):3621-3638.
- Prieto JJ, Winer JA. 1999. Layer VI in cat primary auditory cortex: Golgi study and sublaminar origins of projection neurons. *J Comp Neurol* 404(3):332-358.
- Qu L, Akbergenova Y, Hu Y, Schikorski T. 2009. Synapse-to-synapse variation in mean synaptic vesicle size and its relationship with synaptic morphology and function. *J Comp Neurol* 514(4):343-352.
- Read HL, Nauen DW, Escabí MA, Miller LM, Schreiner CE, Winer JA. 2011. Distinct core thalamocortical pathways to central and dorsal primary auditory cortex. *Hear Res* 274(1-2):95-104.
- Read HL, Winer JA, Schreiner CE. 2001. Modular organization of intrinsic connections associated with spectral tuning in cat auditory cortex. United States: *Proc Natl Acad Sci U S A*. p 8042-8047.
- Redies H, Brandner S. 1991. Functional organization of the auditory thalamus in the guinea pig. *Exp Brain Res* 86(2):384-392.
- Redies H, Brandner S, Creutzfeldt OD. 1989. Anatomy of the auditory thalamocortical system of the guinea pig. *J Comp Neurol* 282(4):489-511.
- Reichova I, Sherman SM. 2004. Somatosensory Corticothalamic Projections: Distinguishing Drivers From Modulators. *J Neurophysiol* 92(4):2185-2197.
- Richardson RJ, Blundon JA, Bayazitov IT, Zakharenko SS. 2009. Connectivity patterns revealed by mapping of active inputs on dendrites of thalamorecipient neurons in the auditory cortex. *J Neurosci* 29(20):6406-6417.
- Riedel A, Stober F, Richter K, Fischer KD, Miettinen R, Budinger E. 2013. VGLUT3-immunoreactive afferents of the lateral septum: ultrastructural evidence for a modulatory role of glutamate. *Brain Struct Funct* 218(1):295-301.
- Rodrigues-Dageaff C, Simm G, De Ribaupierre Y, Villa A, De Ribaupierre F, Rouiller EM. 1989. Functional organization of the ventral division of the medial geniculate body of the cat: evidence for a rostro-caudal gradient of response properties and cortical projections. *Hear Res* 39(1-2):103-125.
- Roger M, Arnault P. 1989. Anatomical study of the connections of the primary auditory area in the rat. *J Comp Neurol* 287:339-356.
- Romanski LM, LeDoux JE. 1993. Organization of rodent auditory cortex: anterograde transport of PHA-L from MGv to temporal neocortex. *Cerebral Cortex* 3:499-515.
- Rothschild G, Nelken I, Mizrahi A. 2010. Functional organization and population dynamics in the mouse primary auditory cortex. *Nat Neurosci* 13(3):353-360.
- Rouiller EM. 1997. Functional organization of the auditory pathways. In: Ehret G, Romand R, editors. *The central auditory system*. New York: Oxford University Press. p 3-96.

- Rouiller EM, de Ribaupierre F. 1985. Origin of afferents to physiologically defined regions of the medial geniculate body of the cat: ventral and dorsal divisions. *Hear Res* 19(2):97- 114.
- Rouiller EM, de Ribaupierre F. 1990. Arborization of corticothalamic axons in the auditory thalamus of the cat: a PHA-L tracing study. *Neurosci Lett* 108:29- 35.
- Rouiller EM, Durif C. 2004. The dual pattern of corticothalamic projection of the primary auditory cortex in macaque monkey. *Neurosci Lett* 358(1):49-52.
- Rouiller EM, Rodrigues- Dagaëff C, Simm G, de RY. 1989. The functional organization of the medial division of the medial geniculate body of the cat: tonotopic organization, spatial distribution of response properties and cortical connections. *Hear Res* 39:127- 142.
- Rouiller EM, Welker E. 1991. Morphology of corticothalamic terminals arising from the auditory cortex of the rat: A Phaseolus vulgaris- leucoagglutinin (PHAL-L) tracing study. *Hear Res* 56:179- 190.
- Rouiller EM, Welker E. 2000. A comparative analysis of the morphology of corticothalamic projections in mammals. *Brain Res Bull* 53(6):727-741.
- Ryan A. 1976. Hearing sensitivity of the mongolian gerbil, *Meriones unguiculatus*. *J Acoust Soc Am* 59(5):1222-1226.
- Ryan AF, Woolf NK, Sharp FR. 1982. Tonotopic organization in the central auditory pathway of the Mongolian gerbil: A 2-Deoxyglucose study. *J Comp Neurol* 207:369- 380.
- Ryugo DK, Killackey HP. 1974. Differential telencephalic projections of the medial and ventral divisions of the medial geniculate body of the rat. *Brain Res* 82(1):173-177.
- Ryugo DK, Spirou GA. 2009. Auditory system: giant synaptic terminals, endbulbs and calyces. In: *New Encyclopedia of Neuroscience*. Oxford: Academic Press. p 759-770.
- Saldaña E, Feliciano M, Mugnaini E. 1996. Distribution of descending projections from primary auditory neocortex to inferior colliculus mimics the topography of intracollicular projections. *J Comp Neurol* 371(1):15-40.
- Saldeitis K, Happel MFK, Ohl FW, Scheich H, Budinger E. 2014. Anatomy of the auditory thalamocortical system in the mongolian gerbil: Nuclear origins and cortical field-, layer-, and frequency-specificities. *J Comp Neurol* 522(10):2397-2430.
- Saldeitis K, Jeschke M, Happel MFK, Wetzel W, Scheich H, Ohl FW, Budinger E. 2013. Role of auditory interhemispheric connections in lateralized sound processing by Mongolian gerbils [Poster]. 10th Göttingen Meeting of the German Neuroscience Society. Göttingen.
- Scheel M. 1988. Topographic organization of the auditory thalamocortical system in the albino rat. *Anat Embryol* 179:181- 190.
- Scheich H, Brechmann A, Brosch M, Budinger E, Ohl FW. 2007. The cognitive auditory cortex: task-specificity of stimulus representations. *Hear Res* 229(1-2):213-224.
- Scheich H, Brechmann A, Brosch M, Budinger E, Ohl FW, Selezneva E, Stark H, Tischmeyer W, Wetzel W. 2011. Behavioral semantics of learning and crossmodal processing in auditory cortex: The semantic processor concept. *Hear Res* 271(1-2):3-15.

- Scheich H, Heil P, Langner G. 1993. Functional organization of auditory cortex in the Mongolian gerbil (*Meriones unguiculatus*). II. Tonotopic 2-Deoxyglucose. *Eur J Neurosci* 5:898- 914.
- Schoonover CE, Tapia J-C, Schilling VC, Wimmer V, Blazeski R, Zhang W, Mason CA, Bruno RM. 2014. Comparative strength and dendritic organization of thalamocortical and corticocortical synapses onto excitatory layer 4 neurons. *J Neurosci* 34(20):6746-6758.
- Schreiner CE, Froemke RC, Atencio CA. 2011. Spectral processing in auditory cortex. In: Winer JA, Schreiner CE, editors. *The auditory cortex*. New York: Springer. p 275-308.
- Schreiner CE, Sutter ML. 1992. Topography of excitatory bandwidth in cat primary auditory cortex: single-neuron versus multiple-neuron recordings. *J Neurophysiol* 68(5):1487-1502.
- Schreiner CE, Winer JA. 2007. Auditory cortex mapmaking: principles, projections, and plasticity. *Neuron* 56(2):356-365.
- Schroeder CE, Mehta AD, Givre SJ. 1998. A spatiotemporal profile of visual system activation revealed by current source density analysis in the awake macaque. *Cereb Cortex* 8(7):575-592.
- Schulze H, Langner G. 1997. Representation of periodicity pitch in the primary auditory cortex of the Mongolian gerbil. *Acta Otolaryngol Suppl* 532:89-95.
- Schulze H, Neubauer H, Ohl FW, Hess A, Scheich H. 2002. Representation of stimulus periodicity and its learning induced plasticity in the auditory cortex: Recent findings and new perspectives. *Acta Acoustica united with Acoustica* 88:399-407.
- Schulze H, Ohl FW, Heil P, Scheich H. 1997. Field-specific responses in the auditory cortex of the unanaesthetized Mongolian gerbil to tones and slow frequency modulations. *J Comp Physiol [A]* 181(6):573-589.
- Sellers KK, Bennett DV, Hutt A, Fröhlich F. 2013. Anesthesia differentially modulates spontaneous network dynamics by cortical area and layer. *J Neurophysiol* 110(12):2739-2751.
- Senatorov VV, Hu B. 2002. Extracortical descending projections to the rat inferior colliculus. *Neuroscience* 115(1):243-250.
- Sherman SM, Guillery RW. 1998. On the actions that one nerve cell can have on another: Distinguishing "drivers" from "modulators". *Proceedings of the National Academy of Sciences* 95(12):7121-7126.
- Sivaramakrishnan S, Oliver DL. 2001. Distinct K Currents Result in Physiologically Distinct Cell Types in the Inferior Colliculus of the Rat. *J Neurosci* 21(8):2861-2877.
- Slater BJ, Willis AM, Llano DA. 2013. Evidence for layer-specific differences in auditory corticocollicular neurons. *Neuroscience* 229(0):144-154.
- Smith PH. 1992. Anatomy and physiology of multipolar cells in the rat inferior collicular cortex using the in vitro brain slice technique. *J Neurosci* 12(9):3700-3715.
- Smith PH, Manning KA, Uhrich DJ. 2010. Evaluation of inputs to rat primary auditory cortex from the suprageniculate nucleus and extrastriate visual cortex. *J Comp Neurol* 518(18):3679-3700.
- Smith PH, Uhrich DJ, Manning KA, Banks MI. 2012. Thalamocortical projections to rat auditory cortex from the ventral and dorsal divisions of the medial geniculate nucleus. *J Comp Neurol* 520(1):34-51.

- Staiger JF, Zilles K, Freund TF. 1996. Recurrent axon collaterals of corticothalamic projection neurons in rat primary somatosensory cortex contribute to excitatory and inhibitory feedback-loops. *Anat Embryol* 194(6):533-543.
- Stecker GC, Harrington IA, Macpherson EA, Middlebrooks JC. 2005. Spatial Sensitivity in the Dorsal Zone (Area DZ) of Cat Auditory Cortex. *J Neurophysiol* 94(2):1267-1280.
- Stecker GC, Mickey BJ, Macpherson EA, Middlebrooks JC. 2003. Spatial Sensitivity in Field PAF of Cat Auditory Cortex. *J Neurophysiol* 89(6):2889-2903.
- Steinschneider M, Tenke CE, Schroeder CE, Javitt DC, Simpson GV, Arezzo JC, Vaughan HG, Jr. 1992. Cellular generators of the cortical auditory evoked potential initial component. *Electroencephalogr Clin Neurophysiol* 84(2):196-200.
- Steriade M, Llinás RR. 1988. The functional states of the thalamus and the associated neuronal interplay. *Physiol Rev* 68(3):649-742.
- Storace DA, Higgins NC, Chikar JA, Oliver DL, Read HL. 2012. Gene Expression Identifies Distinct Ascending Glutamatergic Pathways to Frequency-Organized Auditory Cortex in the Rat Brain. *J Neurosci* 32(45):15759-15768.
- Storace DA, Higgins NC, Read HL. 2010. Thalamic label patterns suggest primary and ventral auditory fields are distinct core regions. *J Comp Neurol* 518(10):1630-1646.
- Storace DA, Higgins NC, Read HL. 2011. Thalamocortical pathway specialization for sound frequency resolution. *J Comp Neurol* 519(2):177-193.
- Suga N. 2012. Tuning shifts of the auditory system by corticocortical and corticofugal projections and conditioning. *Neurosci Biobehav Rev* 36(2):969-988.
- Suga N, Gao E, Zhang Y, Ma X, Olsen JF. 2000. The corticofugal system for hearing: recent progress. *Proc Natl Acad Sci U S A* 97(22):11807-11814.
- Suga N, Ma X. 2003. Multiparametric corticofugal modulation and plasticity in the auditory system. *Nat Rev Neurosci* 4(10):783-794.
- Suga N, Yan J, Zhang Y. 1997. Cortical maps for hearing and egocentric selection for self-organization. *Trends Cogn Sci* 1(1):13-20.
- Sugimoto S, Sakurada M, Horikawa J, Taniguchi I. 1997. The columnar and layer-specific response properties of neurons in the primary auditory cortex of Mongolian gerbils. *Hear Res* 112(1-2):175-185.
- Sun Q-Q, Huguenard JR, Prince DA. 2006. Barrel cortex microcircuits: thalamocortical feedforward inhibition in spiny stellate cells is mediated by a small number of fast-spiking interneurons. *J Neurosci* 26(4):1219-1230.
- Szymanski FD, Garcia-Lazaro JA, Schnupp JWH. 2009. Current source density profiles of stimulus-specific adaptation in rat auditory cortex. *J Neurophysiol* 102(3):1483-1490.
- Szymanski FD, Rabinowitz NC, Magri C, Panzeri S, Schnupp JW. 2011. The laminar and temporal structure of stimulus information in the phase of field potentials of auditory cortex. *J Neurosci* 31(44):15787-15801.
- Takayanagi M, Ojima H. 2006. Microtopography of the dual corticothalamic projections originating from domains along the frequency axis of the cat primary auditory cortex. *Neuroscience* 142(3):769-780.

- Takei K, Mundigl O, Daniell L, De Camilli P. 1996. The synaptic vesicle cycle: a single vesicle budding step involving clathrin and dynamin. *J Cell Biol* 133(6):1237-1250.
- Taschenberger H, von Gersdorff H. 2000. Fine-tuning an auditory synapse for speed and fidelity: developmental changes in presynaptic waveform, EPSC kinetics, and synaptic plasticity. *J Neurosci* 20(24):9162-9173.
- Theyel BB, Llano DA, Sherman SM. 2010. The corticothalamocortical circuit drives higher-order cortex in the mouse. *Nat Neurosci* 13(1):84-88.
- Thiessen DD, Yahr P. 1977. The gerbil in behavioral investigations. Mechanisms of territoriality and olfactory communication. Austin and London: University of Texas Press.
- Thomas H, Tillein J, Heil P, Scheich H. 1993. Functional organization of auditory cortex in the Mongolian gerbil (*Meriones unguiculatus*). I. Electrophysiological mapping of frequency representation and distinction of fields. *Eur J Neurosci* 5:882- 897.
- Thomas O. 1908. The Duke of Bedford's zoological exploration in Eastern Asia. XI List of mammals from the Mongolian plateau. *Proc Zool Soc Lond*:104-110.
- Thomson AM. 2010. Neocortical layer 6, a review. *Front Neuroanat* 4:13.
- Traub RD, Whittington MA, Stanford IM, Jefferys JGR. 1996. A mechanism for generation of long-range synchronous fast oscillations in the cortex. *Nature* 383(6601):621-624.
- Tye KM, Deisseroth K. 2012. Optogenetic investigation of neural circuits underlying brain disease in animal models. *Nat Rev Neurosci* 13(4):251-266.
- Vaudano E, Legg CR, Glickstein M. 1991. Afferent and efferent connections of temporal association cortex in the rat: A horseradish peroxidase study. *Eur J Neurosci* 3:317- 330.
- Vaughan D. 1983. Thalamic and callosal connections of the rat auditory cortex. *Brain Res* 260(2):181- 189.
- Velenovsky DS, Cetas JS, Price RO, Sinex DG, McMullen NT. 2003. Functional subregions in primary auditory cortex defined by thalamocortical terminal arbors: an electrophysiological and anterograde labeling study. *J Neurosci* 23(1):308-316.
- Vercelli A, Repici M, Garbossa D, Grimaldi A. 2000. Recent techniques for tracing pathways in the central nervous system of developing and adult mammals. *Brain Res Bull* 51(1):11-28.
- Viaene AN, Petrof I, Sherman SM. 2011a. Synaptic properties of thalamic input to layers 2/3 and 4 of primary somatosensory and auditory cortices. *J Neurophysiol* 105(1):279-292.
- Viaene AN, Petrof I, Sherman SM. 2011b. Synaptic properties of thalamic input to the subgranular layers of primary somatosensory and auditory cortices in the mouse. *J Neurosci* 31(36):12738-12747.
- Villa AE, Rouiller EM, Simm GM, Zurita P, de Ribaupierre Y, de Ribaupierre F. 1991. Corticofugal modulation of the information processing in the auditory thalamus of the cat. *Exp Brain Res* 86(3):506-517.
- Wallace MN, Anderson LA, Palmer AR. 2007. Phase-locked responses to pure tones in the auditory thalamus. *J Neurophysiol* 98(4):1941-1952.
- Wallace MN, Kitzes LM, Jones EG. 1991. Intrinsic inter- and intralaminar connections and their relationship to the tonotopic map in cat primary auditory cortex. *Exp Brain Res* 86:527- 544.

- Wang X, Lu T, Snider RK, Liang L. 2005. Sustained firing in auditory cortex evoked by preferred stimuli. *Nature* 435(7040):341-346.
- Weedman DL, Ryugo DK. 1996. Projections from auditory cortex to the cochlear nucleus in rats: synapses on granule cell dendrites. *J Comp Neurol* 371(2):311-324.
- Wehr M, Metherate R. 2011. Synaptic integration in auditory cortex. In: Winer JA, Schreiner CE, editors. *The auditory cortex*. New York: Springer. p 235-250.
- Wenstrup JJ, Grose CD. 1995. Inputs to combination-sensitive neurons in the medial geniculate body of the mustached bat: the missing fundamental. *J Neurosci* 15(6):4693-4711.
- Wepsic JG. 1966. Multimodal sensory activation of cells in the magnocellular medial geniculate nucleus. *Exp Neurol* 15(3):299-318.
- Whitworth TL, Herndon LC, Quick MW. 2002. Psychostimulants differentially regulate serotonin transporter expression in thalamocortical neurons. *J Neurosci* 22(1).
- Wimmer VC, Bruno RM, de Kock CPJ, Kuner T, Sakmann B. 2010. Dimensions of a projection column and architecture of VPM and POr axons in rat vibrissa cortex. *Cereb Cortex* 20(10):2265-2276.
- Winer JA. 1985. The medial geniculate body of the cat. In: *Advances in Anatomy, Embryology and Cell Biology*. New York: Springer-Verlag.
- Winer JA. 1992. The functional architecture of the medial geniculate body and the primary auditory cortex. In: Webster DB, Popper AN, Fay RR, editors. *The mammalian auditory pathway: neuroanatomy*. New York: Springer-Verlag. p 222-409.
- Winer JA. 2006. Decoding the auditory corticofugal systems. *Hear Res* 212(1-2):1-8.
- Winer JA. 2011. A profile of auditory forebrain connections and circuits. In: Winer JA, Schreiner CE, editors. *The auditory cortex*. New York: Springer. p 41-74.
- Winer JA, Diehl JJ, Larue DT. 2001. Projections of auditory cortex to the medial geniculate body of the cat. *J Comp Neurol* 430(1):27-55.
- Winer JA, Kelly JB, Larue DT. 1999a. Neural architecture of the rat medial geniculate body. *Hear Res* 130(1-2):19-41.
- Winer JA, Larue DT. 1987. Patterns of reciprocity in auditory thalamocortical and corticothalamic connections: Study with horseradish peroxidase and audioradiographic methods in the rat medial geniculate body. *J Comp Neurol* 257:282- 315.
- Winer JA, Larue DT. 1996. Evolution of GABAergic circuitry in the mammalian medial geniculate body. *United States: Proc Natl Acad Sci U S A*. p 3083-3087.
- Winer JA, Lee CC. 2007. The distributed auditory cortex. *Hear Res* 229:3-13.
- Winer JA, Miller LM, Lee CC, Schreiner CE. 2005. Auditory thalamocortical transformation: structure and function. *Trends Neurosci* 28(5):255-263.
- Winer JA, Sally SL, Larue DT, Kelly JB. 1999b. Origins of medial geniculate body projections to physiologically defined zones of rat primary auditory cortex. *Hear Res* 130(1-2):42-61.
- Winkowski DE, Kanold PO. 2013. Laminar transformation of frequency organization in auditory cortex. *J Neurosci* 33(4):1498-1508.
- Wong D, Kelly JP. 1981. Differentially projecting cells in individual layers of the auditory cortex: a double labeling study. *Brain Res* 230(1-2):362- 366.

- Xiong Y, Zhang Y, Yan J. 2009. The neurobiology of sound-specific auditory plasticity: A core neural circuit. *Neurosci Biobehav Rev* 33(8):1178-1184.
- Yu YQ, Xiong Y, Chan YS, He J. 2004. Corticofugal gating of auditory information in the thalamus: an in vivo intracellular recording study. *J Neurosci* 24(12):3060-3069.
- Zhang Y, Suga N. 1997. Corticofugal amplification of subcortical responses to single tone stimuli in the mustached bat. *J Neurophysiol* 78(6):3489-3492.
- Zhang Y, Suga N. 2000. Modulation of responses and frequency tuning of thalamic and collicular neurons by cortical activation in mustached bats. *J Neurophysiol* 84(1):325-333.
- Zhang Y, Suga N, Yan J. 1997. Corticofugal modulation of frequency processing in bat auditory system. *Nature* 387(6636):900-903.
- Zhang Y, Yan J. 2008. Corticothalamic Feedback for Sound-Specific Plasticity of Auditory Thalamic Neurons Elicited by Tones Paired with Basal Forebrain Stimulation. *Cereb Cortex* 18(7):1521-1528.
- Zhang Z-W, Deschênes M. 1997. Intracortical axonal projections of lamina VI cells of the primary somatosensory cortex in the rat: a single-cell labeling study. *J Neurosci* 17(16):6365-6379.
- Zhang Z, Yu YQ, Liu CH, Chan YS, He J. 2008. Frequency tuning and firing pattern properties of auditory thalamic neurons: An in vivo intracellular recording from the guinea pig. *Neuroscience* 151:293-302.
- Zilles K, Wree A. 1995. Cortex: Areal and laminar structure. In: Paxinos G, editor. *The rat nervous system*. Sydney: Academic Press. p 649-685.

Appendix

A Buffer solutions

A.1 Phosphate buffered saline (PBS, 0.1 M, pH 7.4)

Stock solution (10 x Ca- and Mg-free PBS):

- 2 g/l KCl
- 2 g/l KH_2PO_4
- 80 g/l NaCl
- 12.7 g $\text{Na}_2\text{HPO}_4 \cdot 2 \text{H}_2\text{O}$

Utility solution (1 x PBS, 0.1 M, pH 7.4):

- Dilute stock solution 1:10 with aq. dest. and adjust pH value to 7.4.

A.2 Phosphate buffer (PB, 0.2 M, pH 7.4)

For 1 l: 200 ml solution I + 800 ml solution II

- Solution I (acid): 27.6 g $\text{NaH}_2\text{PO}_4 \cdot \text{H}_2\text{O}$ + 1 l aq. dest.
- Solution II (base): 35.6 g $\text{Na}_2\text{HPO}_4 \cdot 2\text{H}_2\text{O}$ + 1 l aq. dest.

A.3 Phosphate buffer (PB, 0.01 M, pH 7.4)

For 100 ml: 20 ml solution I + 80 ml solution II

- Solution I (acid): 0.138 g $\text{NaH}_2\text{PO}_4 \cdot \text{H}_2\text{O}$ + 100 ml aq. dest.
- Solution II (base): 0.178 g $\text{Na}_2\text{HPO}_4 \cdot 2\text{H}_2\text{O}$ + 100 ml aq. dest.

A.4 TRIS(hydroxymethyl)-aminomethan-HCl-buffer (Tris, 0.05 M, pH 7.6)

Stock solution (0.2 M):

- Add 24.2 g TRIS(hydroxymethyl)-aminomethane to 1 l aq. dest.

Utility solution (0.05 M, pH 7.6):

- 725 ml aq. dest.
- 775 ml 0.1 N HCl
- 500 ml 0.2 M TRIS(hydroxymethyl)-aminomethane

A.5 Tris-buffered saline (TBS, 0.05 M, pH 7.6):

- Dissolve 6.1 g TRIS in 50 ml aq. dest.
- 37 ml 1 N HCl
- 8.8 g NaCl
- Fill up with aq. dest. to 1 l end volume and adjust pH to 7.6.

B Tracer solutions

B.1 5% biocytin in TRIS-HCl buffer (pH 7.6)

For 50 μ l solution:

- Dissolve 2.5 mg biocytin (Sigma-Aldrich, USA, B4261-100 MG) in 50 μ l TRIS-HCl-buffer.
- Agitate for approx. 30 min.

B. 2 3% biocytin in 1.5 M NaCl

For 1 ml solution:

- 0.0877 g NaCl
- 1 ml aq. dest.
- 30 mg biocytin

B.3 Chlorin e₆ conjugated microbeads

- Prepare a 1 mM Chlorin e₆ (-monoethylenediamineamide) (Phytochlorin, Frontier Scientific CAS# 19660-77-6) (MW 596.68) solution in 3 ml 0.01 M phosphate buffer (PB, pH 7.4). Herefore vortex 1.79 mg Chlorin e₆ in 1 ml PB using an Eppendorf tube and transfer it to a centrifuge tube. Then add another 2 ml PB.
- Activation with 5 mg N-Cyclohexyl-N'-(2-morpholinoethyl)carbodiimide metho-p-toluenesulfonate (Sigma-Aldrich; product number C1011, CAS number: 2491-17-0) for 30 min at 4°C on a rocker table (70 rpm).
- Dissolve 50 μ l Red Retrobeads™ IX (Lumafuor) in 300 μ l 0.01 M PB (pH 7.4).
- Conjugate der Retrobead with the Chlorin e₆ through gentle agitation on a rocker table (70 rpm) for 1h at 4°C.
- Stop the reaction with 335 μ l 0.1 M glycine buffer (pH 8.0).
(Glycine: $m=75.07 \text{ g/mol} * 0.1 \text{ mol/l} * 0.04 \text{ l} = 300 \text{ mg glycine in } 40 \text{ ml aq. dest.}$)
- Produce a pellet by a series of ultracentrifugations (60 min at 45,000 rpm, 140,000 g, at 20°C). After each cycle, resuspendate with PB until the supernant is clear.
- Remove supernant, resuspendate the pellet in 50 μ l PB, transfer to a small Eppendorf tube and store at 4°C. The tracer solution is usable for at least 14 days.

C Anesthetic solutions

C.1 Anesthetic solution for surgery

For 1 ml solution:

- 0.45 ml Ketamin-ratiopharm, (50 mg/ml, Ratiopharm GmbH, Germany)
- 0.05 ml 2% Rompun (20 mg xylazin/ml, Bayer, Germany)
- 0.5 ml 0.9% NaCl (Braun, Germany)

Initial dosis: 0.45 ml /100 g body weight; maintenance dosis: 0.045 ml /100 g body weight.

C.2 Anesthetic solution for perfusion

For 1 ml solution:

- 0.9 ml Ketamin-ratiopharm
- 0.1 ml 2% Rompun

Dosis: 0.45 ml /100 g body weight

D Perfusion solutions

D.1 Fixative solution for light- and fluorescence microscopy

4% paraformaldehyde (PFA) incl. 0.1% glutaraldehyde (GA) (pH 7.4):

For 1 l solution:

- Add 40 g PFA to 1 l aq. dest.
- Dilute with alkaline (NaOH).
- 15.6 g $\text{Na}_2\text{HPO}_4 \cdot 2\text{H}_2\text{O}$
- Adjust pH to 7.4 using 10 M NaOH.
- Filtrate before using.
- Immediately before perfusion add 0.8 ml of 25% GA (for fixation of biocytin).
- Prewash with PBS, 20 ml.
- Perfusion rate: 3 min at 30 ml/min, then at 20 ml/min

D.2 Fixative solution for electron microscopy

4% PFA + 0.26% picric acid + 1% GA

For 300 ml solution:

- Add 12 g PFA to 105 ml aq. dest. (dilute with 10 N NaOH).

- 45 ml saturated picric acid
- 150 ml 0.2 M PB, pH 7.4
- Always prepare freshly and filtrate before using.
- Adjust pH to 7.2-7.4.
- Immediately before perfusion add GA: 12 ml GA (25%) per 300 ml, or 10 ml GA per 250 ml fixative.
- Perfusion rate: 3 min at 30 ml/min, then at 20 ml/min
- Prewash with saline (0.9% NaCl), 20 ml.

E Protocol for the biocytin stain

During the whole procedure slices are treated in microwells (free-floating)

Day 1: Blocking and conjugation to ABC complex

- Blocking of reactive aldehyde groups:
1% Natriumborohydrid (NaBH_4) in 0.1 M PBS; 20 min
- Rinse 3 x in 0.1 M PBS.
- Blocking of endogenous peroxidase:
Methanol plus 0.1 M PBS (1:1) + 1% hydrogen peroxide (30%);
20 min
- Rinse 3 x in 0.1 M PBS.
- Blocking of unspecific antibody binding:
5% bovine serum (BSA) in 0.1 M PBS + 0.3% Triton X (Sigma-Aldrich);
30-45 min
- Rinse 3 x in 0.1 M PBS.
- Bind avidin-biotin-peroxidase (ABC) complex to biocytin:
Add 1 drop of reagent A and 1 drop of reagent B of the Vectastain Elite-Kit solution (Vector; prepare 30 min before use) to 25 ml 0.1 M PBS, 0.3% triton and 1% BSA; over night

Day 2: DAB-reaction

- Rinse 2 x with PBS.
- Rinse 2 x with 0.05 M TRIS(hydroxymethyl)aminomethane-HCl buffer (Tris).
- DAB reaction:

Add 5 mg diaminobenzidine to 10 ml Tris + 100 µl of 1 M imidazol solution + 5 µl 30% hydrogen peroxide (pre-delute DAB in aq. dest.; prepare in the dark); incubate 8-10 min.

- Rinse 2 x with 0.05 M Tris.
- Rinse 2 x with 0.1 M PBS.
- Mount the slices on gelatine-coated object slides and let them dry overnight.
- Counterstain (see F) and coverslip with Merckoglass (MERCK).

F Protocols for counterstains

F.1 Methyl green stain

- | | |
|-----------------------------------|-----------|
| • 40% ethanol | 5 min |
| • Methyl green (1% in aqua dest.) | 7 min |
| • Aq. dest. (pH 4.0) | 3 min |
| • 70% ethanol | 2 min |
| • 100% ethanol | 1 min |
| • Roticlear (Roth) | 3 x 5 min |

F.2 Nissl stain

- | | |
|---|-----------|
| • 0.05 M sodium acetate buffer (pH 4.0 – 4.2) | 5 min |
| • Cresyl violet (0.5 g Cresyl violet acetate + 100 ml aqua dest.) | 15-20 s |
| • 50% ethanol | 2 min |
| • 70% ethanol | 2 min |
| • 96% ethanol | 2 min |
| • Isopropanol : ethanol (2:1) | 2 x 5 min |
| • Roticlear | 3 x 5 min |

G Protocol for Neuronal Nuclei (NeuN) stain

During the whole procedure slices are treated in microwells (free-floating).

Day 1: Blocking, incubation of primary antibody

- Blocking of reactive aldehyde groups: 1% sodium borohydride (NaBH₄) in PBS; 20 min
- Rinse 2 x in PBS.

- Blocking of endogene peroxidase: methanol + PBS (1:1) + 1% hydrogen peroxide (30%); 20 min
- Rinse 2 x in PBS.
- Blocking of unsepecific antibody bindings: 5% bovine serum (BSA) in PBS; 0.1-0.3% Triton X; 30-45 min
- Rinse 2 x in PBS.
- Incubate primary antibody (NeuN: anti-mouse 1:500-1000; 300 µl per microwell), in antibody dilution solution (= PBS with 0.1-0.3% Triton and 1% BSA); controls without primary antibody; at room temperature on a shaker, overnight - 2 d

Day 2: Incubation of secondary antibody, DAB reaction, mounting

- Rinse 2 x in PBS.
- Incubate seondary antibody: biotinylated anti-host (1:200; 300 µl per microwell), in antibody dilution solution; 2 h
- Rinse 2 x in PBS.
- Biotin detection reaction (500 µl per microwell): add 2 drops of A and 2 drops of B of Vectastain Elite-Kit (VECTOR; prepare 30 min before use) to 50 ml PBS; 0.3% Triton; 1% BSA; 2 h
- Rinse 2 x in PBS.
- Rinse 1 x in 0.05 M Tris(hydroxymethyl)aminomethane-HCl buffer
- DAB-reaction: 5 mg diaminobenzidine to 10 ml TRIS + 100 µl 1M Imidazol solution + 5 µl hydrogen peroxide (30%); 5-10 min
- Rinse 1 x in TRIS.
- Rinse 2 x in PBS.
- Mount slices on gelatine coated glass slides (tap water), allow to dry overnight.

Day 3: Dehydration, coverslipping

- Dehydration:
 - Isopropanol; 2 min
 - Roticlear (ROTH); 3 x 5 min
- Coverslip with Merckoglas (MERCK); let dry; 2d

H Protocol for TEM pre-embedding

Day 1: Cut brain and prepare brain slices

- Cut with vibratome, 60µm, horizontally: Glue brain with Roti Coll (ROTH), collect in 0.1 M PB (dilute 0.2 M PB 1:1 with aq.dest.) in 6 x 4 microwells.
- Rinse slices in 0.1 M PB; 3 x 30 min (i.e., wait 30 min between each wash).
- Transfer 12 selected slices into 3 x 4 microwells, agitate overnight at 4°C in 0.1 M PB. Freeze remaining slices in cryoprotection solution (CPS; for 50 ml solution: 15 ml glycerol + 15 ml ethylene glycol + 20 ml PBS).

Day 2: Freeze-thawing and incubation in ABC

- Rinse slices in 0.1 M PB, pH 7.4; 3 x 30 min (wait 30 min between each wash)
- Incubate in 1% NaBH₄ in double distilled water for 30 min.
- Rinse in 0.1 M PB, pH 7.4 ; 3 x, afterwards 3 x 30 min
- Preincubation in 25% sucrose + 10 % glycerol in 0.05 M PB; 20-30 min
- Freeze-thawing: transfer slices with some preincubation solution to aluminium foil, put it on dry ice. Let them freeze and thaw (4-5 x).
- Rinse in 0.1 M PB, pH 7.4; 3 x 30 min
- Rinse in 0.05 M Tris buffered saline (TBS), pH 7.4; 2 x 20 min
- Blocking: 5% BSA in TBS; 40 min
- Rinse in TBS; 3 x 30 min.
- ABC Vector (1:500), Standard- kit (PK-4000) (do not use ELITE-Kit)
 - 1 drop of A + 1 drop of B in 25 ml TBS (approx. 2 ml per slice).
 - Incubate at 4°C for 2-3 days (e.g. weekend).

Day 3: DAB reaction

- Rinse in TBS; 3 x 20 min
- Rinse in 0.05 M Tris (pH 7.6); 2 x 10 min (NOT TBS)
- Add 2 ml of 0.05% DAB solution (25 mg DAB in 50 ml 0.05 M Tris; filtrate; adjust pH to 7.6) to each slice. Incubate for 20-30 min.
- Add 20 µl H₂O₂ for development.
- Stop reaction with 0.05 M Tris and rinse 3 x 30 min.
- Store slices in PB (0.1 M, pH 7.4) until processing for TEM.

Day 4: Embedding (excute all steps under hood)

- Transfer slices into bottles with snap-on caps; rinse in 0.1 M PB (pH 7.4), 2 x 20 min
- Incubate in 1% OsO₄ in PB (pH 7.4) for 1 h at room temperature in the dark. Herefore add 2 ml 0.2 M PB and 2 ml 2% OsO₄ stock solution (1:1) separately with plastic Pasteur pipettes and cover the bottle to prevent evaporation.
- Rinse in 0.1 M PB (pH 7.4); 2 x 10 min (dispose OsO₄ as hazardous waste)
- Rinse in double distilled water.
- Incubate in 50% ethanol for 10 min.
- Incubate in 1% uranyl-acetate (for contrast enhancement; for 12 slices: 0.4 g uranyl-acetate in 40 ml ethanol (70%), stir under a hood, afterwards put the stir bar in acetone; filtrate) for 40 min (in case the slices go wavy weigh them down using a bottle with snap-on caps).
- 90% ethanol for 10 min
- 94% ethanol for 10 min
- Absolute alcohol for 2 x 10 min (99.5%; dry at least 24 h)
- Propyleneoxide 2 x 10 min; removal of the old and adding of the new propyleneoxide must occur simultaneously to prevent drying
- Embedding in Durcupan: prepare 1 h before usage. 20 g of component A, 20 g of B, 0.6 g of C, 0.6 g of D; stir under a hood. Incubate slices (freely floating), overnight, at room temperature.

Day 5: Mounting and coverslipping

- Tilt the bottles such that the slices come off the bottom and swim towards the opening. Pick up the slices using a spatula and mount them on an uncoated object slides. Remove surplus Durcupan. Coverslip (eventually weigh them down with a metal block). The coverslips must have been treated with liquid release agent (Electron microscopy sciences, cat# 70880) before.
- Incubate object slides and Durcupan bottles in a heating chamber at 60°C overnight (polymerization of Durcupan).

Day 6: Light microscopy, selection of ROIs

I Brief theoretical background of CSD analysis

The current source density (CSD) analysis is a means of analyzing local field potentials (LFP) to obtain precise spatiotemporal information about neuronal activity on a mesoscopic level (Pitts, 1952; Freeman & Nicholson, 1975; Mitzdorf, 1985; Lakatos *et al.*, 2007) (Fig. J.1). Mathematically, it entails a second-derivative approximation of the voltage gradient from a profile of field potentials. Viewed from the extracellular space, transmembrane currents flowing into the cell during neuronal activity are called sinks, currents flowing out of the cell are called sources. The evoked sinks and sources mainly represent grouped (excitatory) synaptic activities summing up within a spatially restricted area. Current source distributions obtained from the described experimental approach are assumed to mainly reflect excitatory activation of pyramidal cells. Due to the electrical properties of the membrane, active (e.g., inward) currents (extracellular sink) become balanced by loop-closing passive (largely capacitive) compensation (e.g., outward) currents of the opposite sign at more distant locations (extracellular sources) (Fig. J.1 E). In this way, postsynaptic potentials generate source and sink triplets: EPSPs form source-sink-source triplets, whereas IPSPs form sink-source-sink triplets. If synapses are, for example, located near the cell bodies, compensation currents can be observed only on one side leading to source-sink duplets, due to the higher capacity of neuronal somata. Because of the ambiguity of CSD patterns (e.g., due to canceling effects) an anatomical and/or physiological model of the investigated structures must be available before the results can be interpreted (Fig. J.1 D).

J Figures

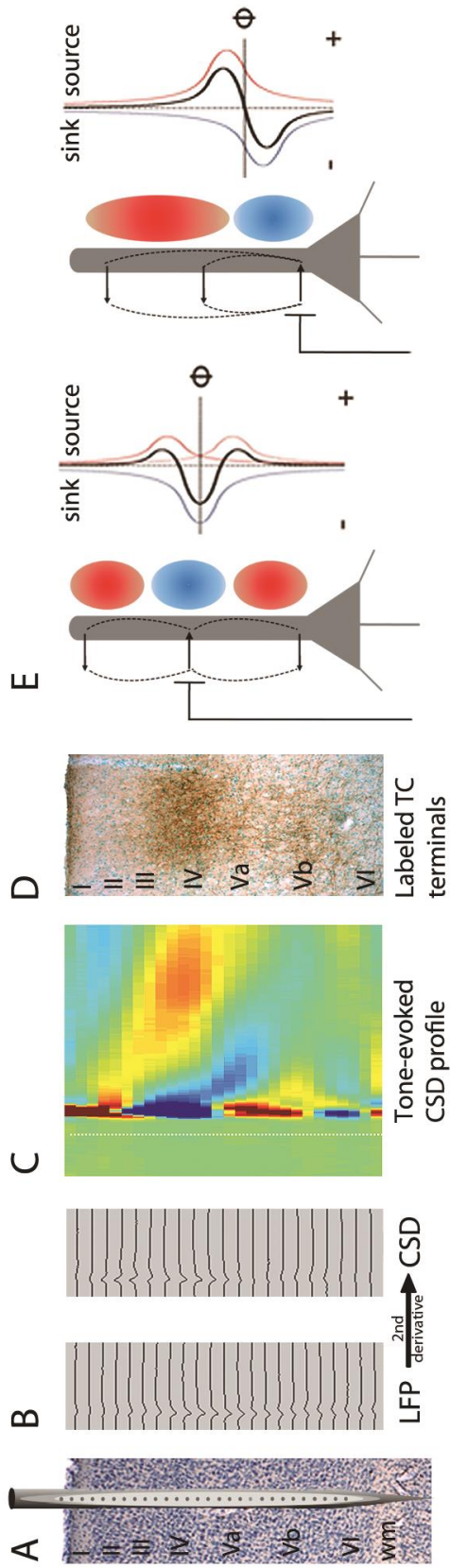


Figure J.1 (preceding page): Theoretical and exemplary CSD distributions of different neuronal activities. **(A)** Laminar local field potentials are recorded by multichannel shaft-electrodes. **(B)** CSD profiles are computed from the second derivation of the laminar LFP. Acoustically evoked CSD patterns in AI **(C)** are believed to reflect TC input from MGv, in accord with their laminar distribution of terminals **(D)**. **(E)** Depending on the location of an excitatory synapse on a neuron either sink-source-sink triplets (left) or source-sink duplets (right) arise. For visualization, extracellular sources and sinks are depicted in red and blue, respectively.

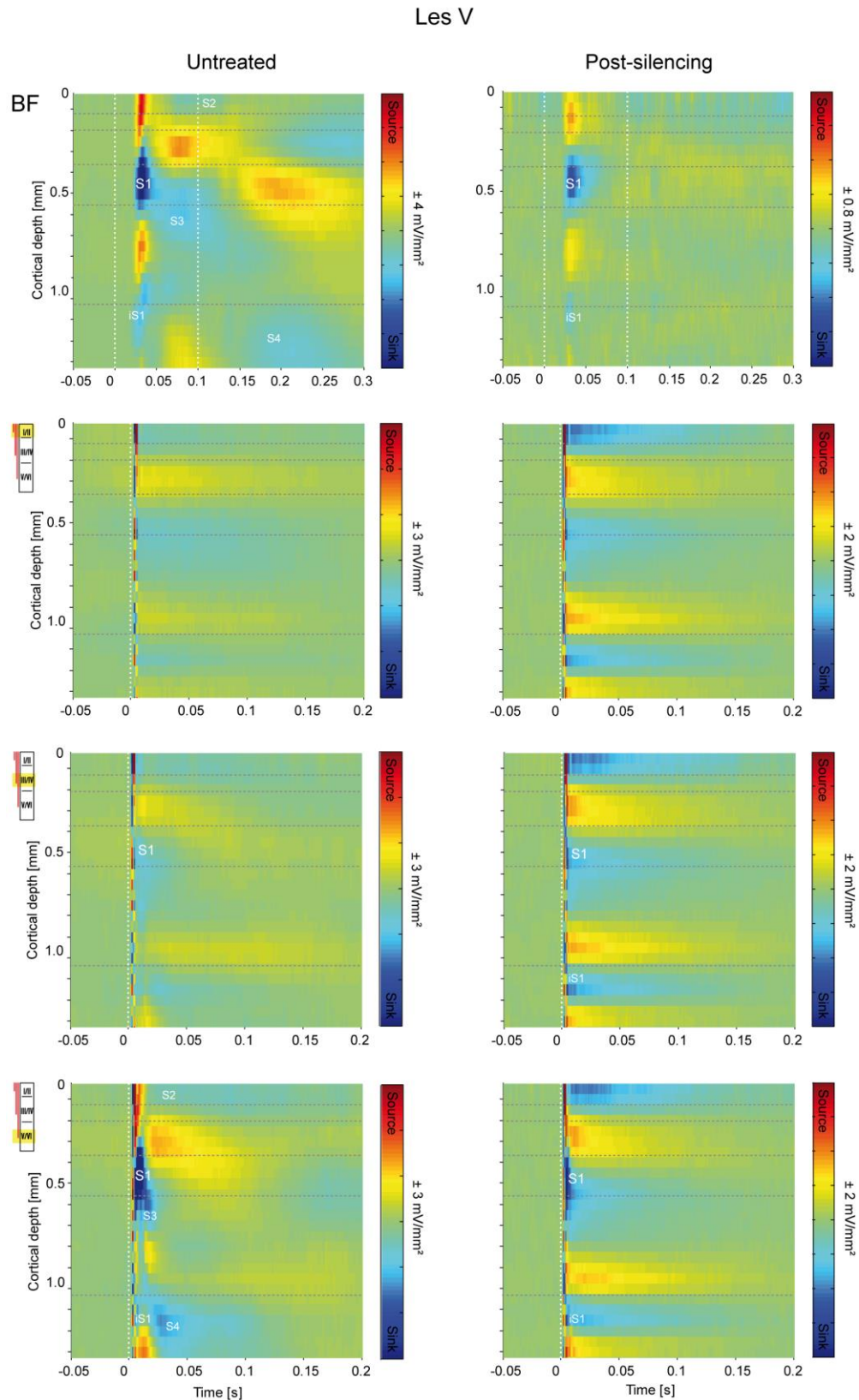


Figure J.2: CSD profiles of an animal (GLA16) with loss of layer V CT neurons only. The first row represents acoustically (at BF), the others electrically evoked (SGstim, Gstim, IGstim) activity patterns, both before (left column) and after (right) cortical silencing. Note that ICMS is able to produce a granular sink, because layer VI CT cells are undamaged. After application of muscimol, the sinks and sources are more sustained than in cases without lesion.

Summary of the doctoral thesis of Dipl.-Biol. Katja Saldeitis

Thalamocortical and corticothalamic interactions of the auditory cortex in the Mongolian gerbil (*Meriones unguiculatus*)

The auditory cortex (AC) holds a key role in the neuronal bottom-up and top-down processing of auditory as well as of non-auditory information. The medial geniculate body (MGB) of the thalamus is the major source of subcortical input to the AC. Thus, the neuronal spectro-temporal response properties of auditory cortical neurons depend highly on their thalamocortical (TC) connectivities. Thalamic neurons, in turn, are also massively innervated by corticothalamic (CT) neurons. The cortex is thus able to dynamically influence thalamic processing and ultimately adjust its own input via recurrent corticoefferent feedback. In the Mongolian gerbil (*Meriones unguiculatus*), a frequently used animal model in auditory research, the detailed anatomy of the TC and CT system has not yet been worked out. Furthermore, many questions about how the transthalamic feedbackloop actually contributes to cortical activation patterns *in vivo* are still unanswered. This thesis therefore had the following objectives: (1) to investigate the anatomy of the TC system by iontophoretic injections of the anterograde tract tracer biocytin into the MGB, (2) to characterize the ultrastructure hitherto unknown “giant” TC terminals arising from the medial (MGm) division [which were discovered during (1)], and (3) to examine the cortico-thalamo-cortical (CTC) interactions by means of current source density (CSD) analysis after a selective photolytic apoptosis of CT neurons.

Our data reveal highly specific features of the TC connections regarding their nuclear origin in the subdivisions of the MGB and their termination patterns in the auditory cortical fields and layers. Besides tonotopically organized projections to the AC, a large number of axons diverge across the tonotopic gradient. In particular, neurons of the MGm project in a columnar fashion to several auditory fields. They bear small and large boutons, which are rich in mitochondria and form asymmetric synapses with dendritic spines. It is conceivable that their transmission has a strong, temporally precise influence on the postsynaptic neurons, which may enable the MGm neurons to orchestrate and synchronize the activity of multiple cortical ensembles. As revealed by acoustic stimulation, the elimination of layer VI CT feedback neurons led to slightly reduced initial sinks, to relatively enhanced late sinks, and to a broader frequency tuning in the AC. The granular sink, which is normally also evoked by infragranular intracortical microstimulation (ICMS), was reduced in layer VI CT lesioned animals upon ICMS, indicating that it recruits a CTC-loop via MGv. In contrast, the overall activation after cortical silencing with muscimol was strongest in layer V lesioned

animals, suggesting the involvement of distinct subcortical circuitries. Together, this dissertation provides a comprehensive anatomical and functional characterization of the auditory TC and CT systems and their interactions, which will enable a better understanding of the neuronal processing in the auditory cortex and thalamus.

Zusammenfassung der Dissertationsschrift von Dipl.-Biol. Katja Saldeitis

Thalamocortical and corticothalamic interactions of the auditory cortex in the Mongolian gerbil (*Meriones unguiculatus*)

Thalamokortikale und kortikothalamische Interaktionen des auditorischen Kortex der Mongolischen Wüstenrennmaus (*Meriones unguiculatus*)

Der auditorische Kortex (*auditory cortex*, AC) befindet sich in einer Schlüsselposition zwischen aufsteigender (bottom-up) und absteigender (top-down) Verarbeitung auditorischer und nicht-auditorischer Informationen. Das mediale Genikulatum (*medial geniculate body*, MGB) des Thalamus ist die Hauptquelle subkortikalen Inputs zum AC. Demzufolge hängen die spektrotemporalen Antwortigenschaften der kortikalen Neurone stark von den thalamokortikalen (*thalamocortical*, TC) Konnektivitäten ab. Das Wissen über deren Anatomie ist also fundamental, um die auditorische Informationsverarbeitung im Gehirn verstehen zu können. Thalamische Neurone werden ihrerseits nicht nur durch das aufsteigende auditorische System innerviert, sondern auch massiv von kortikothalamischen (*corticothalamic*, CT) Feedback-Neuronen. Über die kontinuierliche Kommunikation mit dem Thalamus ist der Kortex in der Lage, die thalamische Informationsverarbeitung dynamisch zu beeinflussen und folglich durch rekurrenten kortikoefferenten Feedback seinen eigenen Input anzupassen bzw. zu verbessern (egozentrische Selektion). In der Mongolischen Wüstenrennmaus (*Meriones unguiculatus*), einem häufig genutzten Tiermodell in der auditorischen Forschung, wurde die detaillierte Anatomie des TC Systems bisher nicht untersucht. Während desweiteren die Einflüsse der CT Projektionen auf thalamische Antworten schon relativ gut erforscht sind, sind viele Aspekte, die die vollständige kortiko-thalamo-kortikale (*cortico-thalamo-cortical*, CTC) Schleife betreffen, d.h. wie die kortikal modulierten TC Eingänge wiederum die kortikale Aktivität *in vivo* beeinflussen, weitgehend ungeklärt. Diese Arbeit verfolgte daher die folgenden Ziele: (1) Die detaillierte anatomische Untersuchung des TC Systems durch elektrophysiologisch geleitete iontophoretische Injektionen des anterograden Trakt-Tracers Biocytin in den MGB. (2) Die Charakterisierung der Ultrastruktur eines besonderen Typs von präsynaptischen Terminalien des medialen MGB (MGm), die während (1) entdeckt wurden. (3) Die Untersuchung der CTC Interaktionen mittels Stromquellendichte-Analyse nach selektiver photolytischer Apoptose der CT Neurone.

Die Ergebnisse zeigen, dass die TC Verbindungen hochspezifisch sind hinsichtlich ihres Ursprungs in einer der Untereinheiten [ventraler MGB (MGv): *pars lateralis* (LV),

pars ovoidea (OV), rostraler Pol (RP); dorsaler MGB (MGd): MGd *proper*, deep dorsal nucleus (DD); MGm] und ihrer Terminationsmuster in den verschiedenen auditorischen kortikalen Feldern und Schichten. Das impliziert, dass trotz gewisser Ähnlichkeiten jedes Verbindungssystem spezifische Funktionen bei der TC Informationsverarbeitung besitzt. Neben tonotop (topographisch) organisierten Projektionen (insb. LV, OV) gibt es auch zahlreiche nicht-tonotope (über den tonotopen Gradienten divergierende) Axone (insb. RP, MGd *proper*, MGm). Neurone des MGm z.B. terminieren in kolumnärer Form in mehreren auditorischen Feldern. Anders als die Neurone der anderen Untereinheiten bilden sie neben kleinen auch sehr große Terminalien aus (bis zu 5 μm^2 Querschnittsfläche), deren Ultrastruktur durch einen hohen Anteil von Mitochondrien und asymmetrische, wahrscheinlich glutamaterge synaptische Kontakte mit dendritischen Spines charakterisiert ist. Die Eigenschaften der MGm Neurone prädestinieren sie für eine schnelle, präzise und zuverlässige Informationsübertragung, die es ihnen ermöglichen könnte, die Aktivität multipler kortikaler Ensembles zu koordinieren und zu synchronisieren.

Die Eliminierung der CT Neurone aus den Schichten V und/oder VI schlug sich in Veränderungen der kortikalen Aktivitätsmuster nach akustischer sowie nach schichtspezifischer elektrischer Stimulation (intrakortikale Mikrostimulation) nieder. Alle Versuche wurden vor und nach topischer Applikation von Muscimol (GABA-Agonist) durchgeführt, um TC und intrakortikale Eingänge zu dissoziieren. Die Stimulation mit Reintönen zeigte, dass der Verlust von Schicht VI CT Neuronen zu leicht schwächeren initialen Senken in den thalamischen Haupteingangsschichten, zu relativ verstärkten späten extragranulären Senken sowie zu einem breiteren kortikalen Frequenztoning führt. Die granuläre Senke, die normalerweise durch infragranuläre Elektrostimulation evoziert wird, war nach dieser in Tieren mit Schicht VI lädierten Projektionsneuronen stark reduziert. Das lässt auf eine notwendige Rekrutierung dieser Neurone schließen, infolge derer eine Rückkopplungsschleife über den MGv aktiviert wird. Diese CT Zellen hemmen möglicherweise auch (indirekt) nicht-lemniskale thalamische Kerne, da nach ihrer Eliminierung stattdessen extragranuläre Senken auftraten. Die Apoptose der Schicht V CT Neurone, andererseits, hatte nach Blockade der intrakortikalen Aktivität eine relativ langandauernde, unreduzierte Gesamtaktivierung des Cortex zur Folge. Diese kommt vermutlich durch eine subkortikale Disinhibition zustande, welche normalerweise durch die CT Zellen aus Schicht V vermittelt wird.

Schlussfolgernd kann gesagt werden, dass die vorliegende Dissertationsschrift eine umfassende anatomische und funktionelle Charakterisierung des TC und CT Systems sowie ihrer Interaktionen liefert, die zu einem besseren Verständnis kortikaler und thalamischer Verarbeitungsmechanismen beiträgt.

Acknowledgements

No scientific study is ever done in isolation even if one is not always aware of it. Therefore, I would like to thank everyone who contributed to this thesis may it be scientifically, mentally or emotionally: my family, my friends and my colleagues whom I had the pleasure to meet *along* the way. Among the latter I would particularly like to thank Prof. Frank Ohl, Dr. Eike Budinger, Dr. Max Happel, Anja Gürke, and Dr. Karin Richter. My special thanks go to my boyfriend Marcus for supporting me in many ways and enduring all my moods.

Selbstständigkeitserklärung

Hiermit erkläre ich, dass ich die von mir eingereichte Dissertation mit dem Thema

Thalamocortical and corticothalamic interactions of the auditory cortex in the Mongolian gerbil (*Meriones unguiculatus*)

selbstständig verfasst, nicht schon als Dissertation verwendet und die benutzten Hilfsmittel und Quellen vollständig angegeben habe.

Weiterhin erkläre ich, dass ich weder diese noch eine andere Arbeit zur Erlangung des akademischen Grades *doctor rerum naturalium* (Dr. rer. nat.) an anderen Einrichtungen eingereicht habe.

In dieser Dissertation wurde von mir für ein fließenderes Englisch das Personalpronomen „we“ verwendet. Die Arbeit wurde jedoch entsprechend der oben verfassten Erklärung von mir selbstständig durchgeführt und verfasst.

Magdeburg, 28.4.2015

Katja Saldeitis

List of publications

Saldeitis K, Happel MFK, Ohl FW, Scheich H, Budinger E. 2014. Anatomy of the auditory thalamocortical system in the mongolian gerbil: Nuclear origins and cortical field-, layer-, and frequency-specificities. *Journal of Comparative Neurology* 522(10):2397-2430.